Spin phenomena can influence the tunnel current through quantum dot systems. Here, Pauli spin blockade effects are experimentally observed here in the clear-cut transport spectrum of a serial double quantum dot device based on an individual single-walled carbon nanotube in the regime of capacitive and weak tunnel inter dot coupling. With a simple model, based on a sequential tunneling description of the double quantum dot as *two interacting artificial atoms*, spin blockade is used as a means of spectroscopy on spin and charge interdot transitions. This spin blockade spectroscopy reveals the evolution of the interdot transitions with different energy scales. Singlet-triplet spin blockade is lifted when a linear combination of interdot detuning gate energy and Zeeman energy is equal or greater than the singlet-triplet splitting. The resulting *spin blockade triangles* are experimentally observed also at finite interdot detuning and symmetrically at finite magnetic fields. Controllable trapping of single spins by means of spin blockade requires an accurate characterisation of its energy scales. The present results can provide a working point for spin blockade in a double quantum dot that is used as a module in forthcoming spintronics circuits. Two other potential spintronics modules, based on a spin valve configuration and on Kondo effects, are also investigated.

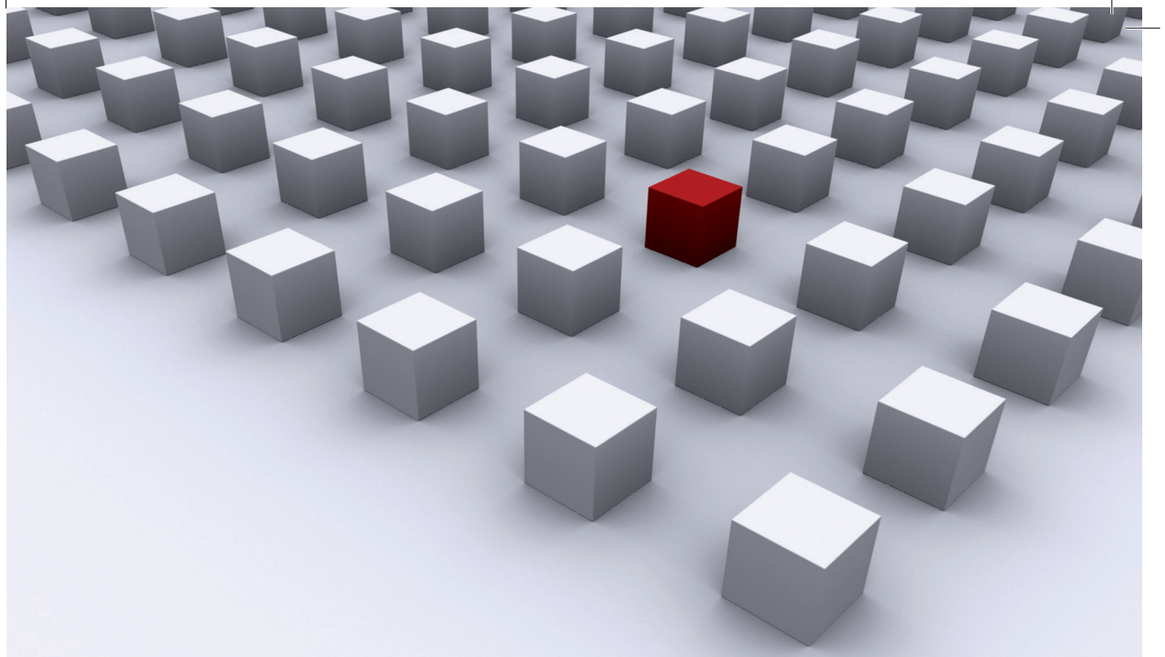

Dominik Oliver Preusche-Rogstad

Spin Blockade Spectroscopy in a Carbon Nanotube Double Quantum Dot Transistor

Universitätsverlag Regensburg

Dissertationsreihe Physik - Band 24

ISBN 978-3-86845-083-5

gefördert von:

Alumni der physikalischen Fakultät der Universität Regensburg e.V.

Universität Regensburg

Dominik Oliver Preusche-Rogstad

24

Dissertationsreihe Physik

Universitätsverlag Regensburg

Dominik Oliver
Preusche-Rogstad

Spin Blockade Spectroscopy in a Carbon Nanotube Double Quantum Dot Transistor

Spin Blockade Spectroscopy in a Carbon Nanotube Double Quantum Dot Transistor

Dissertation zur Erlangung des Doktorgrades der Naturwissenschaften (Dr. rer. nat.)
der Fakultät für Physik der Universität Regensburg
vorgelegt von

Dominik Oliver Preusche-Rogstad

aus Heidelberg

Juli 2011

Die Arbeit wurde von Prof. Dr. C. Strunk angeleitet.
Das Promotionsgesuch wurde am 02.05.2011 eingereicht.
Das Kolloquium fand am 26.09.2011 statt.

Prüfungsausschuss:

Vorsitzende:	Prof. Dr. Milena Grifoni
1. Gutachter:	Prof. Dr. Christoph Strunk
2. Gutachter:	Prof. Dr. Jascha Repp
weiterer Prüfer:	PD Dr. Tobias Korn

Dissertationsreihe der Fakultät für Physik der Universität Regensburg, Band 24

Herausgegeben vom Präsidium des Alumnivereins der Physikalischen Fakultät:
Klaus Richter, Andreas Schäfer, Werner Wegscheider, Dieter Weiss

Dominik Oliver
Preusche-Rogstad

Spin Blockade Spectroscopy in a Carbon Nanotube Double Quantum Dot Transistor

Universitätsverlag Regensburg

Bibliografische Informationen der Deutschen Bibliothek.
Die Deutsche Bibliothek verzeichnet diese Publikation
in der Deutschen Nationalbibliografie. Detailierte bibliografische Daten
sind im Internet über http://dnb.ddb.de abrufbar.

1. Auflage 2011

Leibnizstraße 13, 93055 Regensburg

Konzeption: Thomas Geiger
Umschlagentwurf: Franz Stadler, Designcooperative Nittenau eG
Layout: Dominik Oliver Preusche-Rogstad
Druck: Docupoint, Magdeburg
ISBN: 978-3-86845-083-5

Weitere Informationen zum Verlagsprogramm erhalten Sie unter:
www.univerlag-regensburg.de

Spin Blockade Spectroscopy in a Carbon Nanotube Double Quantum Dot Transistor

Dissertation
zur Erlangung des Doktorgrades der Naturwissenschaften
(Dr. rer. nat.)
der Fakultät für Physik
der Universität Regensburg
vorgelegt von
Dominik Oliver Preusche-Rogstad
aus Heidelberg

Juli 2011

Die Arbeit wurde von Prof. Dr. C. Strunk angeleitet.
Das Promotionsgesuch wurde am 02.05.2011 eingereicht.
Das Kolloquium fand am 26.09.2011 statt.

Prüfungsausschuss:	Vorsitzende:	Prof. Dr. Milena Grifoni
	1. Gutachter:	Prof. Dr. Christoph Strunk
	2. Gutachter:	Prof. Dr. Jascha Repp
	weiterer Prüfer:	Prof. Dr. Dominique Bougeard

à la famille

Contents

List of Tables

List of Figures

Introduction

The *spin degree of freedom* is a quantum mechanical concept [1, 2] with direct technological applications; spin-based information storage is industrially established, in particular since the discoveries of the giant magnetoresistance effect (Nobel prize in 2007, [3–6]) and an industrially significant tunnelling magnetoresistance (TMR) [7]. However, today's information *processing* technology relies on the charge degree of freedom only. The electronic spin is a physical *two-level system* in which the concept of *bits* can be implemented, i. e. by mapping $(-\frac{1}{2}, +\frac{1}{2}) \mapsto (0, 1)$. The spin degree of freedom has attracted particular attention as a potential building block of a quantum bit (qubit) in a solid state-based quantum computer [8, 9].
Spintronics [10–13], or spin-electronics, is a fast evolving, application-oriented field of both industrial and fundamental research. It seeks to tap the full potential of electromagnetical interaction between electrons that may lead to novel functionalities conventional electronics are not feasible or unable to supply [14]. An exemplary spintronics application that is already in the industrial 'pipeline' today is a magnetic random access memory (MRAM), performance-enhanced by the spin-momentum-transfer effect (SMT) [15]; STM-MRAM has the additional advantage over the current *CMOS*-technology of non-volatility and low power consumption [12]. The technological prerequisite and the experimental challenge of spintronics is the ability to isolate spins and to control and manipulate their spin orientation. A directly derived requirement for the suitability of a physical system to operate as a spintronics device - or building block of a potential quantum computer - is a sufficient coherence of the spin states [8, 9, 16].

A suitable experimental setup to isolate and manipulate spins are *quantum dots*: single electrons can be spatially confined within a *small* piece of conductive matter. If, e. g., a metallic cube is reduced in all three spatial dimensions below the coherence length of the confined electron, the electronic wave function discretises due to length quantisation, in analogy to discrete electronic states in atoms. The metallic cube effectively becomes a 'zero-dimensional' *quantum dot* or *artificial atom* [17]. Similarly, *artificial molecules* [18] or *artificial solids* can be devised from arrays

of coherently tunnel-coupled quantum dots. To access the single electron charging regime, all coupling to the environment, e. g. the temperature $k_{\mathrm{B}}T$, must be smaller than the quantised level spacing, requiring cooling to cryogenic temperatures [19]. Advances in nanoscale fabrication have provided the tools for sufficient miniaturisation to tailor customised quantum dots in experiment. Apart from the technological interest, quantum dot devices in this so-called *mesosocopic* length scale (i. e. 'medium-sized' [20] with respect to macroscopic and atomic length scales) of particle confinement are highly tunable, experimentally wieldable model systems to investigate the fundamental physics of atoms and molecules. The industrial miniaturisation has already reached integrated circuit dimensions of down to 22 nm [21]. If the industrial standard is to keep up with the pace set by *Moore's Law* [22], it will soon be driven below the quantum limit [23, 24] - at which point topics of fundamental, quantum mechanical research will coincide with the practical issues for state-of-the-art electronics [23]. Furthermore, the research interests in atomic and condensed matter physics converge in the concept of quantum information [24].

Quantum dots have been fabricated from a wide range of conductive condensed matter systems; to cite only a few examples, there are quantum dots based on small metallic islands (e. g. self-assembled gold nanoparticles [25]), on semiconductors (e. g. by an electrostatically defined potential well in a 'two-dimensional electron' gas in semiconductor systems, like the group-III-V semiconductors GaAs/$\mathrm{Al}_x\mathrm{Ga}_{(1-x)}As$ [10, 18, 20, 26, 27] or group-IV semiconductors Si/SiGe [28–30]), on semiconductor quantum wires (e. g. a one-dimensional InAs nanorod segment [31, 32]) or on single atoms and molecules (e. g. a patch of graphene [33], segments of a carbon nanotube [19, 34, 34, 35] or C_{60}-'bucky balls' [36]).

The discovery of carbon nanotubes (CNTs) [37], and in particular of individual single-walled carbon nanotubes (SWCNTs) [38], has inspired and triggered an entire field of research with the promises of their extraordinary electronic, mechanical and optical properties [39–42]. A single-wall carbon nanotube can be pictured as a patch of graphene honeycomb lattice 'wrapped' around some axis in the graphene sheet plane and fused by carbon-carbon bonds into a seamless, cylindrical, *tubular* molecule [43]. Depending on the orientation of this 'wrapping axis', that defines the so-called *chiral angle*, a SWCNT has a finte energy gap between conductance and valence bands and behaves like a semiconductor, while certain chiral angles result in zero-band gap tubes that exhibit the properties of a quasi-metal. Carbon nanotubes are considered the prototypical one-dimensional conductors exhibiting ballistic transport [19].

The hope that a carbon-based transistor technology may eventually succeed the current silicon technology was recently expressed by the award of the Nobel prize for the discovery of the 'sister material' of carbon nanotubes, graphene [44]. Within carbon nanotube quantum dots, standard field effect transistors [34], novel integrated circuits [45, 46], fast [47] or flexible transistors [48], nanomechanical oscillators [49–52] and photoactive devices [53], nano-SQUIDs [54] or spin valves [55–57] have been realised.
Ultraclean, individual SWCNT can be synthesised by, e. g., chemical vapour deposition (CVD) with high structural integrity [58, 59]. Their synthesis process is in principle compatible with the industry standard semiconductor fabrication, although at present CNT-semiconductor transistors are at a prototype stage. Significant engineering progress is required for an industrially viable and scalable carbon-based transistor technology. Half a century ago, the now highly developed semiconductor technology faced similar - pessimists said insurmountable - challenges; the optimists are now amongst the technology leaders. While merely few nanometers in diameter, SWCNTs can grow into molecules of extreme, mesoscopic-scale length (tens of nm to few mm [60]). These extreme aspect ratios make CNTs particularly suitable for the fabrication of molecular transistors on standard semiconductor wafer material, acting as 'bridges between the molecular and crystalline quantum worlds' [61]. A major engineering challenge of mesoscopic quantum circuits is a sufficient isolation from the environment, as coupling is a major source of decoherence [62]. Significant interaction with the environment suppresses the quantum nature of the states. With their large coherence lengths devices based on high-quality CNTs fullfill this important prerequisite for spintronics [61] or quantum information applications [16].

The fundamental research interest of this thesis is to experimentally explore spin phenomena in carbon nanotube-based quantum dot systems as a contribution to the fields of spintronics. Moreover, it is motivated by the prospective of spin-based quantum computation applications in condensed matter chips. The discussion treads along the following line:
as a precursor to the experimental findings, relevant theoretical and experimental concepts are reviewed and developed. In particular, chapter 1 investigates the double quantum dot theory, with a focus on serial double quantum dots. The two-dimensional double dot formalism for capacitances and energies is formulated with full consideration of cross capacitances in matrix formalism which takes the same form as the scalar formalism of a single quantum dot. The matrix notation also is convenient for data analysis and computerised measuring.
Chapter 2 reviews some relevant theoretical concepts of all-carbon molecules, starting from bulk carbon down to the quantum dots implemented in SWCNT segments.

Chapter 3 describes how a SWCNT-based double quantum dot device have been fabricated and measured.

Manipulation of a spin state requires an understanding of a spin effect mechanism along with a sufficient experimental control over the device. Three types of spin effects measured in SWCNT-based quantum dot systems are investigated in this thesis:

- Magnetoresistance effects, in particular the TMR effect, can occur in individual quantum dots in a *spin-valve configuration*, where two ferromagnetic electrodes serve as spin injector and spin detector. For the spin valve operation, injector and detector electrode must have different coercive field values to switch their relative magnetisation from parallel to anti-parallel. TMR is not a single spin effect but based on spin polarisation of a current, i. e. an average spin over a great number of electrons. Chapter 4 presents results on how suitable different designs of ferromagnetic electrodes, varied in shape and ferromagnetic alloy composition, are for lateral CNT-based spin valves.

- Kondo features are spin effects intrinsic to quantum dots with transparent electrical contacts; these higher-order tunnelling effects require some energetic level degeneracy, e. g. of spin, orbital or spin singlet-triplet states. Appendix C provides an exemplary measurement of a SWCNT-based quantum dot exhibiting the characteristic four-fold level degeneracy and various Kondo effects in its transport spectrum.

- Pauli-spin blockade is a phenomenon of devices in serial double quantum dot setup. Although energetically allowed, the transport is blockaded due to spin selection rules. An energy difference between spin states, e. g. a singlet and triplet spin state, is a prerequisite for Pauli-spin blockade. Spin blockade can be used as a spectroscopic method to analyse the spin state of a double quantum dot. Chapter 5 demonstrates the operation of a SWCNT-based double quantum dot with highly tunable interdot coupling. Capacitances and energy scales are evaluated for the weak interdot coupling regime where the device can be described as *two interacting atoms*. The evaluation is based on the theory developed in Chapter 1. Chapter 6 characterises the excited state spectrum of the double quantum dot, in preparation of the results in chapter 7; Chapter 7 presents the main (and eponymous) results of this thesis. Pauli-spin blockade is demonstrated around zero and finite magnetic field. Spin blockade spectroscopy is shown to relate experimental features to the double quantum dot transition spectrum via a simple model. In particular, it is demonstrated how

a single spin on the double quantum dot system can be trapped and released again by tuning different energy scales.

This thesis is a contribution towards integrating the above spin effects in a single spin transistor, the *CNT-based double quantum dot spin valve in the Kondo regime*. Possible extensions to this device setup are substitution of the middle gate electrode in the DQDot configuration by a superconducting electrode in order to split Cooper pairs into coherent, entangled Einstein-Podolsky (EPR) spin pairs [63,64], microwave irradiation to prepare, manipulate and read out the spin-charge state on the DQDot [65, 66] and tunable nano-mechanical resonances, in particular coupled to single electron tunneling, by suspending the carbon nanotube segments like an oscillating string between the contact electrodes [50–52]. The fundamental research interest in the interplay of multiple spin effects in a single experimental device (cf. [67]) has the potential to trigger concepts for novel spintronics and quantum computation applications (e. g. [68]).

Chapter 1

Quantum dots

When a small enough piece of electrically conductive matter confines electrons in a potential well, the electronic states on such a *quantum dot* discretise just like in an *artificial atom*. In analogy, an array such of mesoscopical conductors behaves - depending how strongly they are coupled to each other - like an *artificial molecule* or like an *artificial solid*.
Aside from introducing the conceptual prerequisites of the subsequent transport experiments in chapters 5, 6 and 7, this chapter formulates the a model for a serial double quantum dot (i. e. source electrode, then first, then second quantum dot, then drain electrode) with full consideration of cross capacitances between all conductors (i. e. the gate electrodes or the two dots) - which allows to accurately translate the experimentally applied voltages into energies of the quantum dot system, i. e. the quantities of physical interest. In particular, an the ansatz is presented to collect the relevant capacitances on a capacitance matrix; it leads to a formalism for the weakly interdot-coupled double quantum dot that is consistently formulated in matrix notation where the equations take the same form as the scalar formalism of individual quantum dot but the objects are matrices on $\mathbb{R}^2 \times \mathbb{R}^2$ instead of scalars. The formulae here are consistent with references [20, 24, 26] which have been used throughout this chapter.

1.1 Single quantum dots and Coulomb blockade

1.1.1 Coulomb blockade

Charging a conductive island that is weakly coupled to source and drain electron reservoirs, such as sketched in figure 1.1, requires energy in order to overcome the Coulomb repulsion between electrons. Mesoscopically small islands are called quantum dots because of quantum mechanical discretisation of the electronic levels, so

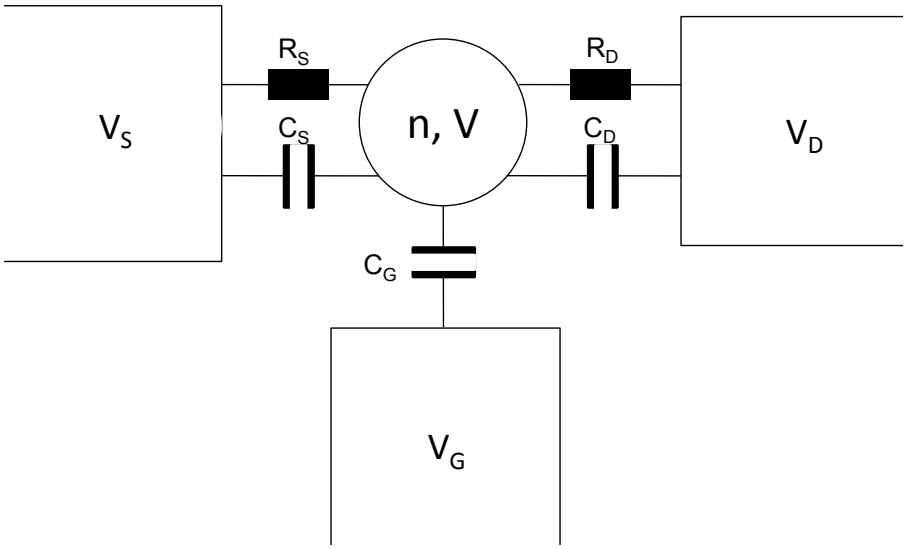

Figure 1.1: Equivalent circuitry of a capacitively coupled quantum dot.

an additional amount of energy must be paid to overcome the quantum mechanical level spacing E_{QM}. The (total) addition energy

$$E^{add} \approx E^C + E^{QM} \tag{1.1}$$

can be provided experimentally from a charge reservoir of suitable electrostatic potential eV_G applied via a gate electrode. For now, the discussion shall be limited to the case of $E^C >> E^{QM}$ where the system behaves in good approximation as a classically big metallic island. The charging energy is then given by

$$E^C = \frac{e^2}{C_{dot}}, \tag{1.2}$$

where $C_{dot} := C_S + C_D + C_G$ is total capacitance of the dot.
Figure 1.2 (a,b,c) sketches the charateristic energy, conductance and charge state dependencies of a classical dot as a function of the gate voltage. Typical for classical dots is the equidistant spacing of the Coulomb peaks (see figure 1.2 (b)). By ramping the gate voltage V_G up to negative (positive) values, a dot can be successively charged (depleted), as sketched in figure 1.2 (c). Whenever an unoccupied level comes into the bias window $eV_{SD} = \partial\mu_{SD}$, an electron is added (figure 1.2 (c)), corresponding to a *Coulomb peak* in conductance G. This situation is sketched in figure 1.2 (e) for finite bias. If no state lies within the bias window, transport is *Coulomb-blockaded*, as shown for the linear response regime, i. e. near zero bias, in figure 1.2 (d).
As the temperature smears out the levels of source and drain electrodes and hence the Coulomb peaks, $k_{\mathrm{B}}T$ must be small against the features to be observed, i. e.

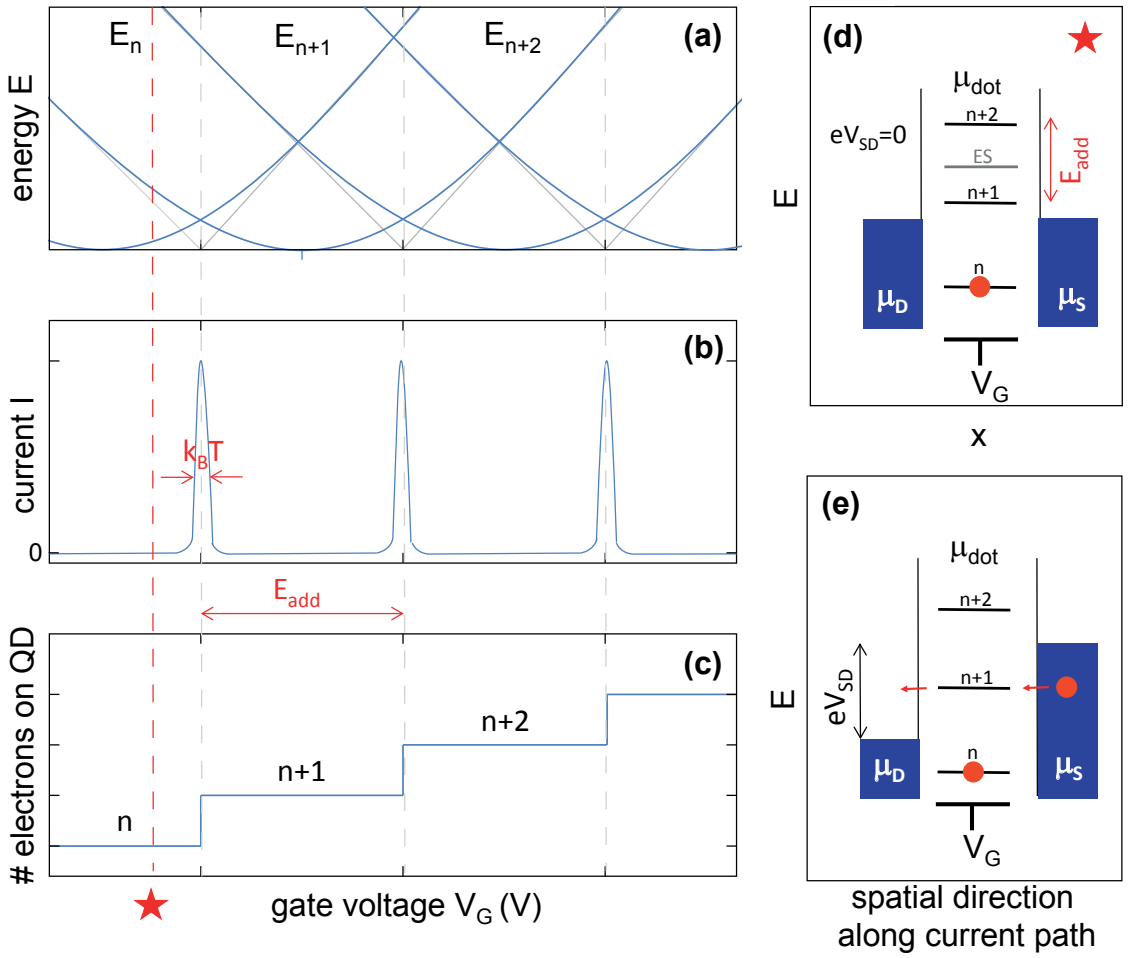

Figure 1.2: (a) Energy, (b) conductance and (c) excess charges on the dot plotted against the gate potential at zero bias. Illustration of Coulomb blockade (d) at zero bias and (e) at finite bias V_{SD}: a current can flow via elastic or inelastic (as sketched here) sequential tunnelling through the QDot whenever a level is within the bias window. The star (★) relates the level schematics to the equivalent physical situations in charge number, current and energy.

$k_{\mathrm{B}}T << E_C, E_{QM}$. For this reason, cryogenic temperatures are required for transport experiments on CNT-based quantum dots.

1.1.2 Linear response: $\mu_D \approx \mu_{dot} \approx \mu_S$

The probability of dot being charged with n electrons is, from the grand canonical ensemble [69]

$$P_n = \frac{1}{Z} e^{-\frac{\Omega(n)}{k_{\mathrm{B}}T}} = \frac{1}{Z} e^{-\frac{F(n)-\mu n}{k_{\mathrm{B}}T}}. \tag{1.3}$$

where Z is the partition function. At low electron temperature, the free energy $F(n)$ can be approximated with the ground state energy E_n of the dot [24].
A tunnel current through the dot can occur only if the number of electrons can fluctuate by $|\Delta n| \geq 1$. For single electron tunnelling ($\Delta n = 1$), linear response (near zero bias) and in the zero temperature limit, this condition can be equivalently expressed (for increasing the charge number on the dot) as

$$P_n \stackrel{!}{=} P_{n\pm1} \Leftrightarrow \mu_S \equiv \mu_D \stackrel{!}{=} E_{n+1} - E_n =: \mu_{dot}, \tag{1.4}$$

where the last equality is the definition of the electro-chemical potential of a quantum dot. The *constant interaction model* approximates the system as an effective single particle picture. In this model, the ground state energy, as sketched in figure 1.2 (a), of a level on the quantum dot is

$$E_n = \underbrace{\frac{1}{2C_{dot}}[en + C_G V_G]^2}_{E^C(n,V_G)} + \underbrace{\sum_{i=1}^{n} \epsilon_i}_{E^{QM}}, \tag{1.5}$$

where the ϵ_i are quantum mechanical single particle energies. The addition energy to add an electron to a quantum dot has two contributions. The first, $E^C(n, V_G)$, is an effective classical energy that accounts for electrostatics plus electron interaction. The second, E^{QM}, describes a single particle in a potential well quantum mechanically.
Depending on experimental device and setup parameters - like thickness and properties of the dielectric, shape of local gate electrodes and their distance to the CNT as lithographically patterned (see chapter 3) - only a portion $0 < \alpha_G < 1$ is effectively 'felt' by the electrons on the dot. This so called *gate efficiency* $\alpha_G := \frac{\partial \mu_{dot}}{\partial e V_G}$ converts gate voltage into energy scales of the quantum dot and is related to the capacitive contribution of a gate G to the total dot capacitance C_{dot}:

$$\alpha_G := \frac{C_G}{C_{dot}}. \tag{1.6}$$

The condition for the transition from quantum dot charge state n to $n+1$ in equation 1.4 can then be rewritten in an experimentally meaningful way:

$$\begin{aligned} \mu_{dot} + \epsilon_{n+1} &= e\alpha_G V_G + \frac{e^2}{C_{dot}}[n + \frac{1}{2}] \\ &= e\alpha_G V_G + E_C[n + \frac{1}{2}]. \end{aligned} \tag{1.7}$$

Equivalently, to add the $(n+1)^{th}$ electron, the voltage of the gate electrode must be increased by

$$\Delta V_G^{n\to n+1} = \frac{1}{e\alpha_G}[\epsilon_{n+1} - \epsilon_n]V_G + \frac{e}{C_{dot}} \tag{1.8}$$

1.1.3 Finite bias: $\mu_{D/S} < \mu_{dot} < \mu_{S/D}$

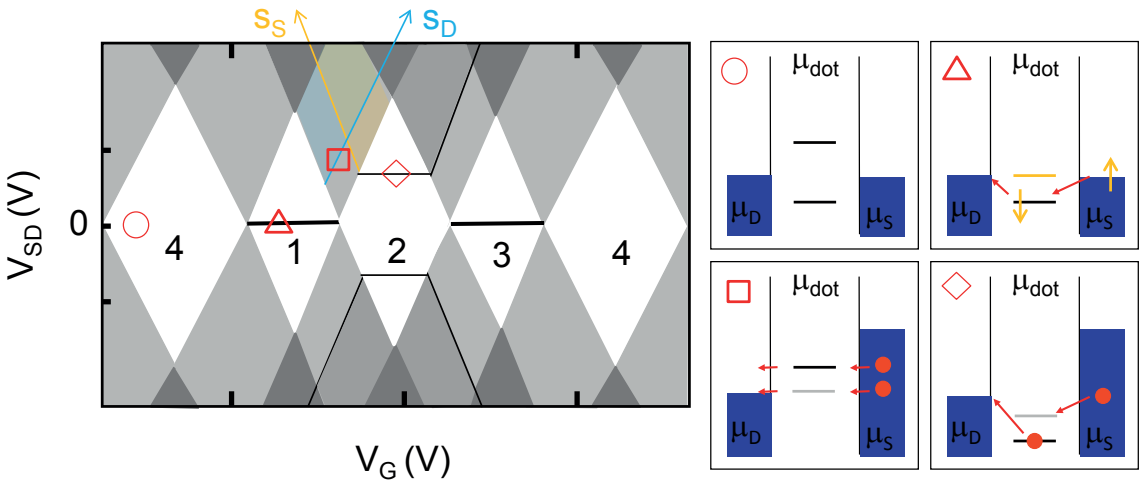

Figure 1.3: Sketch of a typical SWCNT-based quantum dot stability diagram. Current as function of bias and gate voltages. White areas are Coulomb blockaded, light grey areas mark finite current due to single electron tunneling, dark grey corresponds to multiple electron tunneling. Examples of possible higher order, inelastic or exited state processes are highlighted: ◯: Coulomb blockade. □: increased current as an exited state (grey) enters the bias window. △: zero bias Kondo anomaly. Lead and dot electron hybridise to a virtual state, opening a co-tunnelling conductance channel. ◊: inelastic cotunneling.

At finite bias the electrochemical potential in source and drain is altered and the response of the current is not linear to the bias anymore. Also, the capacitive action of source and drain electrodes, with respective capacitances C_S and C_D, must be included into the model, as indicated in figure 1.6.
The condition for single electron tunnelling becomes

$$\mu_D \overset{!}{\leq} \mu_{dot} \overset{!}{\leq} \mu_S \tag{1.9}$$

or reverse for negative bias. Figure 1.3 sketches a 2D map of the current as a function of bias $eV_{SD} = \mu_S - \mu_D \equiv \mu_{SD}$ and gate voltage V_G.
As indicated by the (overlapping) orange and blue areas in figure 1.3, the tunnel current can increase when exited states open additional transport channel within the bias window - but need not. If, for instance, the source electrode coupling to the dot outweighs the drain coupling, an electron can readiliy tunnel onto the dot via the exited state channel. Due to the lower tunnel coupling to the drain, it remains on the dot, blocking further sequential tunnelling by Coulomb repulsion [24].
Equation 1.9 defines the white areas, dubbed *Coulomb diamonds*, wherein the current is blocked by Coulomb repulsion. Would no quantum effects come into play,

i. e. in the classical limit, the Coulomb diamonds were all of equal size. The sketch, however, illustrates the typical signature of four-fold level degeneracy in SWCNT quantum dots, a big diamond followed by three smaller ones, which will be discussed in depth in section 2.4. The borders of the Coulomb diamonds with positive/negative slope $s_{S/D}$ mark that the electrochemical potential of the $(n+1)^{th}$ electronic single particle state is aligned to source/drain potential; they fulfill the conditions

$$\mu_S - e[(1-\alpha_S)V_{SD} + \alpha_G V_G] + \frac{e^2}{C_{dot}}[n+\frac{1}{2}] + \epsilon_n \equiv \text{const.} \tag{1.10}$$

$$\mu_D - e[\alpha_S V_{SD} + \alpha_G V_G] + \frac{e^2}{C_{dot}}[n+\frac{1}{2}] + \epsilon_n \equiv \text{const.} \tag{1.11}$$

The addition energy to place one more charge on the quantum dot can either be provided in gate voltage, where only the portion α_G of the voltage portion is effectively 'felt' by the charges, or in bias voltage or a combination of both. The height of the Coulomb diamonds, is equal to the experimentally applied bias and corrensponds innately to a physical energy scale. Hence, the bias serves as a gauge to obtain absolute energy scales of the quantum dot system: comparison of width and height of the Coulomb diamonds quantifes the gate efficiency

$$\alpha_G = \frac{\text{Coulomb diamond width}}{\text{Coulomb diamond height}} \tag{1.12}$$

from an experimental stability diagram, see figure 1.4. The gate efficiencies of the bias nodes $\alpha_{S/D} := \frac{C_{S/D}}{C_{dot}}$ are defined as previously with the gate nodes. Extraction of the slopes $s_{S/D}$ from experimental data allows to quantify α_S via

$$s_S = \frac{\partial V_G}{\partial V_{SD}}|_{S\equiv\text{const.}} = -\frac{\alpha_S}{\alpha_G} = -\frac{C_S}{C_G} \tag{1.13}$$

$$s_D = \frac{\partial V_G}{\partial V_{SD}}|_{D\equiv\text{const.}} = \frac{(1-\alpha_S)}{\alpha_G} = \frac{C_D}{C_G} \tag{1.14}$$

where the drain potential is assumed to be constant relative to the dot states. Solving equations 1.13 and 1.14 for α_S, setting them equal provides an alternative extraction method of α_G via

$$\alpha_G = \frac{1}{\frac{1}{|s_S|} + \frac{1}{|s_D|}}. \tag{1.15}$$

Typical features in the stability diagram

Whenever an electronic level of the quantum dot enters the bias window, Coulomb blockade is lifted as a conductance channels opens through which sequential single

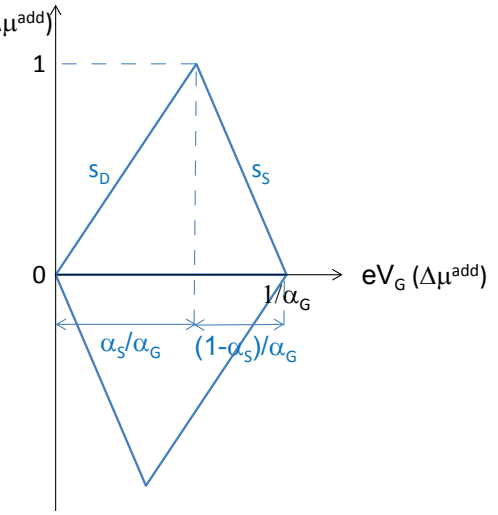

Figure 1.4: Sketch of a *Coulomb diamond*, i. e. the characteristic, diamond-shaped area of transport blockade, in the (gate,bias)-plane in units of its height - which corresponds the addition energy $\Delta\mu^{add}$. From the slopes of SQD Coulomb diamonds, the capacitive coupling coefficents can be extracted independently from any quantum mechanical effect.

electron can tunnel. Light grey areas in figure 1.3 signify the areas of single electron tunneling. The cross marks a situation where additional currrent can be carried through an excited state. The star marks a possible two-electron, zero bias anomaly in odd Coulomb diamonds, the spin-$\frac{1}{2}$-Kondo effect. Briefly speaking, Kondo correlations stem from a magnetic exchange interaction between a localised magnetic moment and free conduction electrons - 'Kondo ridges' are counted amongst the anomalous (anomalous w. r. t. first order processes) conductance features (for details see appendix C). Attempting to minimise the exchange energy, the conduction electrons tend to screen the magnetic moment and the ensemble forms a spin singlet, hybridised state [54]. The Coulomb diamond labelled with excess charge occupancy $n = 2$ in figure 1.3 features an inelastic co-tunnelling process.
If the differential conductance were plotted in the stability diagram figure 1.3 instead of the current, only the changes in current, i.e. the outlines of the areas defined by the onset of a condutance channel would be visible. Experimentally, the differential conductance can be measured as $\frac{\mathrm{d}I^{dc}(V_{SD}^{dc})}{\mathrm{d}V_{SD}^{dc}} \equiv \frac{I^{ac}(V_{SD}^{dc})}{V_{SD}^{ac}}$ with lock-in techniques.

1.1.4 Effects of magnetic fields in current spectroscopy

Electronic spins ($\hat{\vec{S}}$) couple to an external magnetic field $\vec{B}$ via the Zeeman interaction

$$\hat{H}_Z = g\mu_B \vec{B} \cdot \hat{\vec{S}} \tag{1.16}$$

and the energy levels are *Zeeman-shifted*, as illustrated in figure 1.5, by

$$\begin{aligned} S_z \Delta E_Z &= S_z g \mu_B B_z \\ &\approx S_z \times 116 \frac{\mu eV}{T} B_z \end{aligned} \tag{1.17}$$

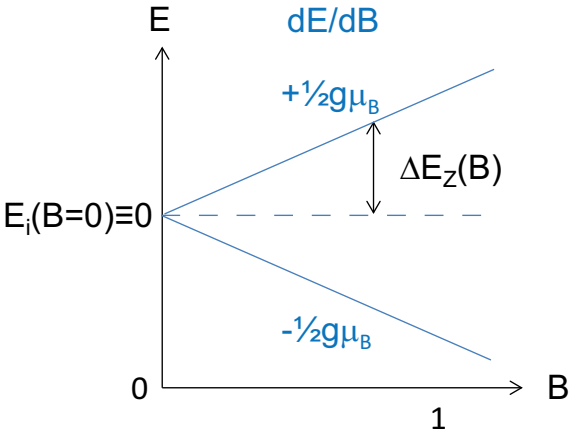

Figure 1.5: Sketch of Zeeman splitting $2 \times \Delta E_Z$, i. e. the magnetic field dependence on the energy of a spin-$\frac{1}{2}$ electronic state.

with the a *Landé factor* $g \approx 2$ (for, e. g., carbon nanotubes [70, 71]) and Bohr's magneton $\mu_\mathrm{B} \approx 5.789 \times 10^{-5} \frac{eV}{T}$. Effects of the external magnetic field that can be observed in current spectroscopy are, for example, the Zeeman-splitting of an (in zero magnetic field) spin-degenerate state or ground state transitions at higher magnetic fields.

1.2 Double quantum dots (DQDots)

The equivalent circuit in figure 1.6 models a serial double quantum dot weakly coupled to source and drain electrodes, i. e. in the Coulomb blockade regime. The two circles represent left and right quantum dot; they are charged with n_l and n_r electrons respectively. The notation attributes capital letter subscripts to quantities related to the macroscopic electrodes and lowercase subscripts to left and right quantum dot. V_l (V_r) is the voltage on the left (right) quantum dot and V_L (V_R) the voltage on the left (right) local gate, and V_S and V_D are the source and drain voltages. All voltages refer to the same reference potential. The capacitance, for instance, between **L**eft local gate to the **l**eft dot is denoted as C_{Ll}. C_{Lr} stands for the *cross-capacitance* between the **L**eft gate to the **r**ight dot. For source and drain electrode, only the capacitances to the adjacent dot are considered, reducing the notation to $C_S := C_{Sl}$ and $C_D := C_{Dr}$. The current path from source over the dots to drain is marked by 'tunnel resistors' R_S, R_{lr} and R_D.

First, the phenomenology of the double quantum dot transport spectrum is presented as a guideline for the ensuing derivations from more basics principles.

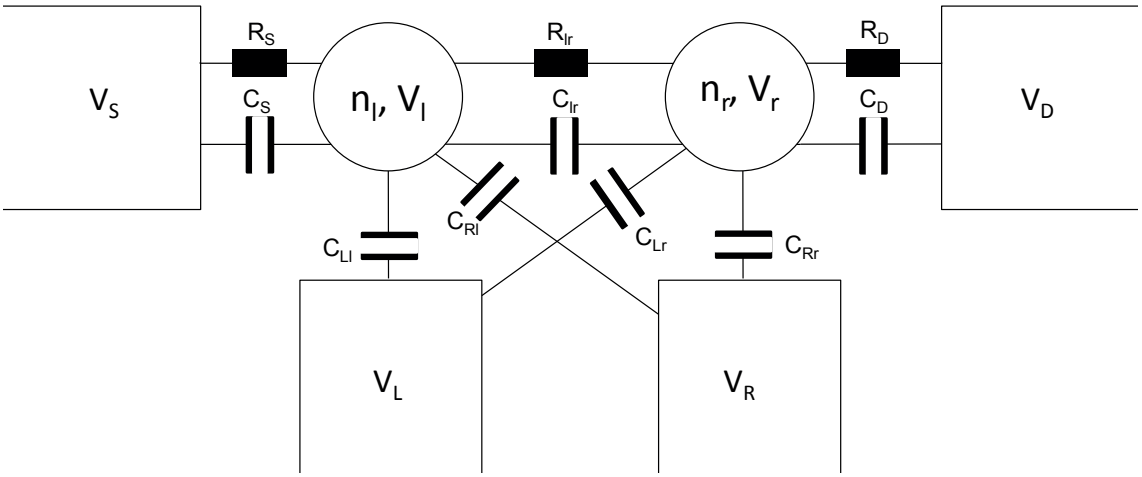

Figure 1.6: Equivalent circuitry of a capacitively coupled serial double quantum dot. Each *charge node* (i. e. the source (subscript S), drain (D), left local gate (L), middle local gate (M) and right local gate (R) electrodes as well as left (l) and right (r) quantum dots are each at a relative electrostatic potential (i. e. can be assigned to a voltage V). Additionally, the quantum dots carry a finite number of excess charge carriers n. All charge nodes are in principle capacitively coupled. The capacitance C_{Lr} is, e. g., a measure for the coupling of **L**eft local gate to **r**ight quantum dot. The standard device architecture of a DQDot requires that only source, dots and drain are tunnel-coupled (indicated by resistances R) but the gate electrodes are not (for modified architectures refer to [63, 64]).

Classes of interdot coupling regimes

The *gate stability diagram* of a double quantum dot - in analogy to the line trace of current $I(V_{gate})$ of an individual quantum dot exhibiting, e. g., Coulomb peaks - refers to a two-dimensional map of current (or differential conductance) plotted as a function of left and right local gate voltages, $I(V_L, V_R)$. For small enough tunnel coupling between source and drain electrode and low enough temperature, a double quantum dot can be operated in the Coulomb blockade regime, too. The 2D-Coulomb pattern is further characterised by two 'classes' of *interdot coupling regimes*: the classical regimes of capacitive interdot coupling and the quantum mechanical regimes of interdot tunnel coupling.

Experimental 'knob' to tune the interdot coupling

The middle topgate, as fabricated on the real device shown in figure 3.1, has the prime impact on the potential barrier that divides, in the present case, the carbon nanotube section into two quantum dots. In theory, the middle gate electrode can drive the double dot to the different interdot coupling regimes. V_M does not enter

the model because ideally, once the interdot coupling is conveniently tuned, it is kept constant during the measurements. However, other charge nodes often have a non-negligible impact on the shape of the double potential well that defines the DQDot.

Capacitive interdot coupling regimes

As illustrated in figure 1.6, each charge node is capacitively coupled to the adjacent nodes. This means that, in a double quantum dot, each dot acts like a gate electrode to the other. The capacitive interdot coupling is a measure of the reciprocal gate capacitance. In a different wording, the interdot capacitance C_{lr} eppresses the Coulomb repulsion of charge carriers on different dots and therfore corresponds to an interdot charging energy.

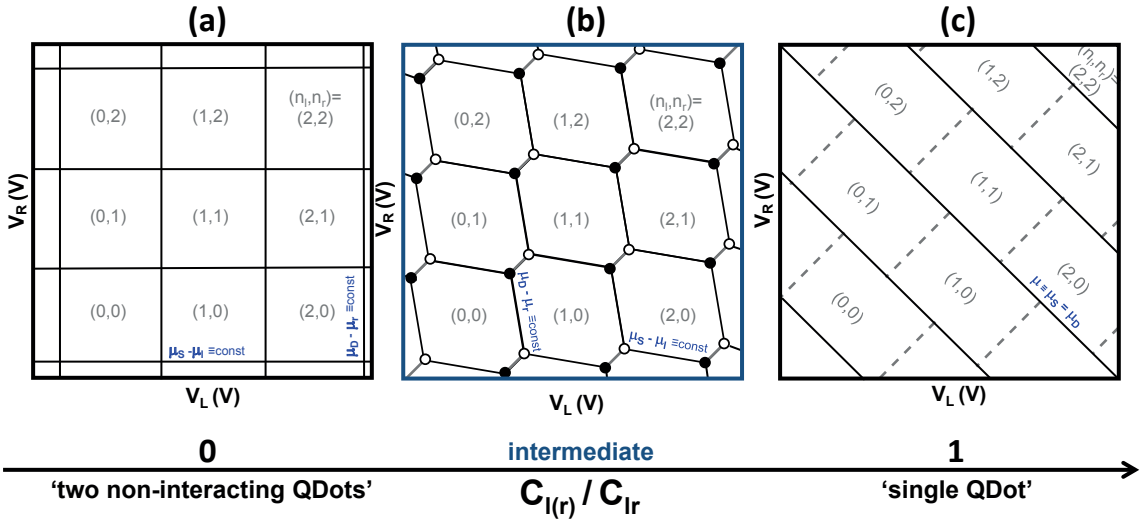

Figure 1.7: Capacitive interdot coupling regimes: characteristic Coulomb blockade patterns in the DQDot stability diagram, i. e. a 2D-map of the tunnel current as a function of left and right local gate voltages (V_L, V_R) for the regimes of (a) very weak (b) intermediate and (c) strong capacitive interdot coupling. The sketches are valid only in the limit of the very weak interdot tunnel coupling regime.

If two quantum dots l and r are coupled neither electrostatically nor by tunneling, they each exhibit a Coulomb peak pattern in $I(V_L)$ and $I(V_R)$ independently from each other. The stability diagram of these 'two uncoupled quantum dots' is only characterised by the charging energies corresponding to the total capacitance in left

and right dot

$$C_l := C_S + C_{Ll} + C_{Rl} + C_{lr}\ (+C_{BG} + C_{rest}) \qquad (1.18)$$
$$C_r := C_D + C_{Lr} + C_{Rr} + C_{lr}\ (+C_{BG} + C_{rest}).$$

The resulting stability diagram falls into rectangular quadrants of constant charge, as sketched in figure 1.7 (a). The sketch additionally assumes that the cross-capacitances C_{Lr} and C_{Rl} of the local gates L and R are negligible. At the black-outlined borders of two or four quadrants, the charge states are energetically degenerate and the charge can fluctuate.
If the capacitive interdot coupling is increased, the interdot charging energy has an increasing contribution to the total charging energies of the individual dots, causing the *quadruple points* to split into two *triple points* of three energetically degenerate charge states (n_l, n_r). A characteristic hexagonal pattern arises in the stability diagram, as illustrated in figure 1.7 (b). Sequential tunnelling through the double quantum dot is possible only at these four- or three-fold degenerate intersections.
In the limit of interdot charging energy becoming the dominating contribution to charging energies of left and right dot ($C_i/C_{lr} \to 1,\ i \in \{l, r\}$ [26]), the system behaves effectively like a single quantum dot with charge $n = n_l + n_r$. Characteristic for this limit is a Coulomb blockade pattern of negatively-sloped, parallel lines in the stability diagram, see figure 1.7 (b).

Interdot tunnel coupling regimes

Up this point in discussion, the tunnel coupling was assumed to be very weak. In this limit, the double quantum dot behaves like two individual 'artificial atoms'. Figure 1.8 (a) illustrates this physical situation with probability distributions that are spatially localised over the sites of each individual dot without overlap. In this case, the DQDot can be described in a classical electrostatic theory. In the stability diagram, the lines - that mark the border of constant charge areas - are consequently straight because the electro-chemical potentials are linear in the gate voltages. For finite tunnel coupling between the dots, the probability distribution is finite over the entire DQDot system, as illustrated in figure 1.8 (b). The eigenbasis that describes the system can then be thought of as 'hybridised' from 'atomic states', and the DQDot system effectively behaves like an 'artificial molecule'. In the limit of interdot total transparency $t_{lr} \to 1$, the entire system behaves like an individual quantum (see figure 1.8 c)) dot where charge carriers are confined not in a double but a single, unmodulated potential well. The quantum mechanical tunnel coupling between the dot in the stability diagram effects avoided crossings at the triple points (see figure 1.12), i. e. non-linear curves. A finite tunnel interdot coupling always entrails a

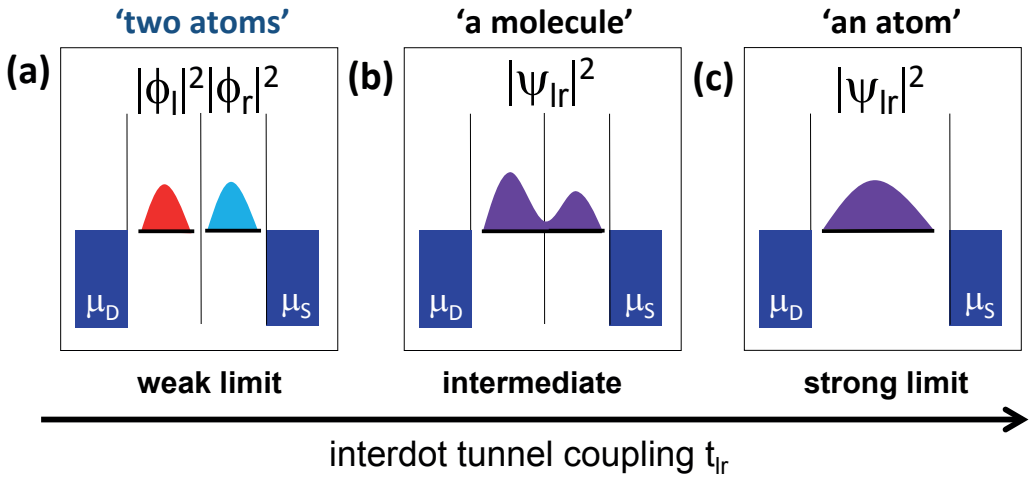

Figure 1.8: Interdot tunnel coupling regimes: the double quntum dot system behaves like (a) 'two artificial atoms' in the weak tunnel coupling limit, (b) like an 'artificial molecule' for intermediate interdot opacity or (c) as a 'single atrificial atom' in the limit of full interdot transparency. The sketch indicates this by schematic probability distribution on the dot system.

finite capacitive interdot coupling because the states have a finite probability to be in 'both quantum dots'.

Relevant regime for this work

The targeted and relevant regime for the subsequently presented experiments is

- the Coulomb blockade regime with respect to the coupling of source and drain electrodes to their adjacent quantum dots,
- the regime of weak interdot tunnel coupling, and
- the regime of intermediate capacitive interdot coupling.

In this experimental situation, the double quantum dot behaves like 'two interacting atoms' and its stability diagram corresponds to the sketch in figure 1.7 (b). The ratios of tunnel-versus-capacitive coupling can vary significantly with the material system that hosts the double quantum dot (e. g. GaAs/AlGaAs [24,72,73] or CNTs). How suitable CNTs are to implement widely tunable double quantum dot systems was demonstrated, e. g., by an nearly ideal-typical stability diagram of weak interdot coupling and tunnel coupling in reference [54].

1.2.1 Weak tunnel coupling in linear response: $\mu_D \approx \mu_{dot} \approx \mu_S$

If the tunnel coupling is sufficientlly weak, a double quantum dot behaves like two atoms that interact only electrostatically. A purely diagonal two-particle Hamiltonian and non-overlapping, single particle states $|\psi_l\rangle$ and $|\psi_r\rangle$ on left and right dot

$$\begin{aligned} \hat{\mathcal{H}}_{\mathbf{0}}|\vec{\psi}\rangle &= \mathbf{E}^{QM}|\vec{\psi}\rangle \\ \begin{pmatrix} \hat{\mathcal{H}}_l & 0 \\ 0 & \hat{\mathcal{H}}_r \end{pmatrix} \begin{pmatrix} |\psi_l\rangle \\ |\psi_r\rangle \end{pmatrix} &= \begin{pmatrix} E_l^{QM}|\psi_l\rangle \\ E_r^{QM}|\psi_r\rangle \end{pmatrix} \end{aligned} \tag{1.19}$$

with eigenenergies E_l^{QM} and E_r^{QM} describes the quantum mechanics of the system well. If the electronic wavefunctions sufficiently localise over the the site of only a single quantum dot, the double dot can thus be modelled as two separate islands with separate charge states (n_l, n_r) and separate quantum mechanical energy eigenstates. The corresponding stability diagram of 'two interacting atoms' is featured in the center of figure 1.8 (a).

Energy of a non-tunnel coupled double quantum dot

In analogy to the single quantum dot the energy ot the double quantum dot reads

$$E = E^C + E^{QM} \tag{1.20}$$

where the quantum part is

$$E^{QM} = E_l^{QM} + E_r^{QM} \approx E_l^{CNT} + E_r^{CNT} \tag{1.21}$$

and the classical electrostatic part

$$E^C(n_l, n_r; V_l, V_r) = E_l^C + E_r^C + E_{lr}^C \tag{1.22}$$

with left, right and interdot energies

$$\begin{aligned} E_l^C(n_l; V_l, V_r) &= \frac{\frac{1}{2}C_r}{C_l C_r - C_{lr}^2}\left[en_l + C_{Ll}V_L + C_{Rl}V_R\right]^2 \\ E_r^C(n_r; V_l, V_r) &= \frac{\frac{1}{2}C_l}{C_l C_r - C_{lr}^2}\left[en_l + C_{Lr}V_L + C_{Rr}V_R\right]^2 \\ E_{lr}^C(n_l, n_r; V_l, V_r) &= \frac{C_{lr}}{C_l C_r - C_{lr}^2}\left[en_l + C_{Ll}V_L + C_{Rl}V_R\right]\left[en_l + C_{Lr}V_L + C_{Rr}V_R\right]. \end{aligned} \tag{1.23}$$

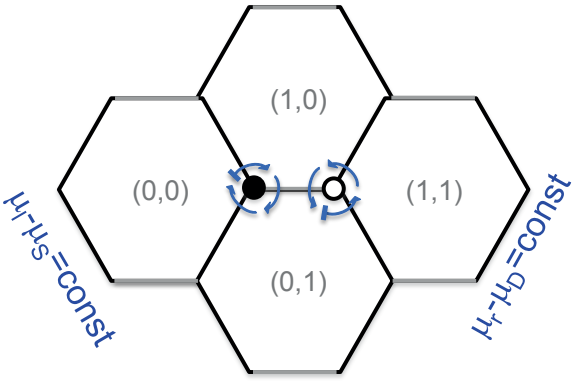

Figure 1.9: Sequential charge transport mechanism at the triple points in linear response. As indicated, the current can be described as sequential tunnelling between isoenergetic charge configurations (n_l, n_r).

Like for the single dot in equation 1.4, the electro-chemical potentials for left and right dot can be defined as the energy difference for adding one electron

$$\begin{aligned} \begin{pmatrix} \mu_l \\ \mu_r \end{pmatrix} &:= \begin{pmatrix} E^C(n_l+1, n_r; V_l, V_r) - E^C(n_l, n_r; V_l, V_r) \\ E^C(n_l, n_r+1; V_l, V_r) - E^C(n_l, n_r; V_l, V_r) \end{pmatrix} \\ &= \begin{pmatrix} \mu_l^C \\ \mu_r^C \end{pmatrix} + \begin{pmatrix} \mu_l^{QM} \\ \mu_r^{QM} \end{pmatrix} \end{aligned} \tag{1.24}$$

Triple points

With finite capacitive interdot coupling, the *quadruple points* in the zero coupling limit, where the charge state on the double dot can fluctuate between four isoenergetic configurations of (n_l, n_r), are split into a pair of points in the gate plane (V_l, V_R). In the stability diagrams in figure 1.8, the quadratic lattice of quadruple points morphs into two offset sublattices of *triple points*. On these triple resonances $\mu_S \stackrel{!}{=} \mu_l \stackrel{!}{=} \mu_r \stackrel{!}{=} \mu_D$, the charge state can correspondingly fluctuate between three configurations (n_l, n_r) and sequential charge transport through the serial double dot can occur only here. Within a pair of triple points, the sequence of charge transport discriminates between a *clockwise* and a *counter-clockwise* triple point, as illustrated in figure 1.9. The terminology was chosen because at positive finite bias, the transport process for three sequential electron tunnel events corresponding to the curved arrows in figure 1.9 must be described with opposite helicities for the two points. Bias reversal reverses the helicity. Consequently this labelling is non-defined for zero bias. In literature, a triple point pair is often named *electron* and *hole* triple point [26]. The present discussion does not follow the latter categorisation because both triple points can be alternatively described by either hole or electron transport sequences.

Within this formalism, the electrostatic potential of a dot is, strictly, only well-defined for constant charge on the other dot. Exactly at the 'points of experimental

interest', the *triple points*, this condition is violated. If it were not violated, there would be no sequential tunnelling accross the double dot. However, the formalism proves powerful also to describe also the transport phenomena [24, 26].

Conversion of the experimentally applied voltages to energy

To obtain quantitative information on the physical energy scales, experimental stability diagrams must be mapped from the gate plane (V_L, V_R) to the energy plane (μ_L, μ_R)

$$\begin{aligned} \vec{\mu} &= e\mathbf{A}\vec{V} \\ \begin{pmatrix} \mu_l \\ \mu_r \end{pmatrix} &= e\underbrace{\begin{pmatrix} \alpha_{Ll} & \alpha_{Rl} \\ \alpha_{Lr} & \alpha_{Rr} \end{pmatrix}}_{=:\mathbf{A}} \begin{pmatrix} V_L \\ V_R \end{pmatrix} + \underbrace{\frac{e^2}{C_l C_r - C_{lr}^2} \begin{pmatrix} (n_l + \frac{1}{2})C_r + n_r C_{lr} \\ (n_r + \frac{1}{2})C_l + n_l C_{lr} \end{pmatrix}}_{\text{negligible offset}} \end{aligned} \tag{1.25}$$

The dimensionless gate coefficient α_{Xy} in $\mathbf{A}$ express what effect a gate X has on a dot y. They are related to the *Gate to dot-capacitances*

$$\mathbf{C}_{Gd} := \begin{pmatrix} C_{Ll} & C_{Rl} \\ C_{Lr} & C_{Rr} \end{pmatrix} \tag{1.26}$$

by a linear transformation composed of the total dots capacitances and the interdot capacitance $C_{lr} \equiv C_{rl}$, which shall be called *dot total capacitance matrix* $\mathbf{C}_{dot}$, defined as

$$\begin{aligned} \mathbf{C}_{dot} &= \begin{pmatrix} C_l & -C_{lr} \\ -C_{lr} & C_r \end{pmatrix} \\ \mathbf{C}_{dot}^{-1} &= \frac{1}{C_l C_r - C_{lr}^2} \begin{pmatrix} C_r & C_{lr} \\ C_{lr} & C_l \end{pmatrix} = \frac{1}{\det \mathbf{C}_{dot}} \mathrm{adj}\mathbf{C}_{dot}. \end{aligned} \tag{1.27}$$

The gate coeffients written as ratios of capacitances are then

$$\begin{aligned} \mathbf{A} &:= \mathbf{C}_{Gd}\mathbf{C}_{dot}^{-1} \\ \begin{pmatrix} \alpha_{Ll} & \alpha_{Rl} \\ \alpha_{Lr} & \alpha_{Rr} \end{pmatrix} &= \frac{1}{C_l C_r - C_{lr}^2} \begin{pmatrix} C_{Ll}C_r + C_{Lr}C_{lr} & C_{Rr}C_r + C_{Rl}C_{lr} \\ C_{Ll}C_l + C_{Lr}C_{lr} & C_{Ll}C_l + C_{Rl}C_{lr} \end{pmatrix}. \end{aligned} \tag{1.28}$$

In analogy to the 1D-formalism of a single dot (compare equation 1.6), equation 1.28 intuitively amounts to dividing the gate to dot capacitance by the dot total capacitance scalars. The matrix elements have the dimension [1/F]. Given that the gate coefficients can be extracted more readiliy and with less ambiguity from experimental data than the capacitances, the inverse conversion

$$\mathbf{C}_{Gd} = \mathbf{A}\mathbf{C}_{dot} \tag{1.29}$$

will more likely find application.

'Honeycomb-like lattice' of single resonance lines

Single resonances, where the electrochemical potentials of either left dot and source or right dot and drain are aligned, appear as lines in the zero bias stability diagram, see e. g. figure 1.10. On these lines, the charge state n_i, $i = l, r$, can fluctuate on only one dot and its electrochemical potential is constant with respect to V_L and V_R. The slopes for left and right dot alignment can be directly obtained from experimental raw data in the (V_L, V_R) plane and yield, by expanding the conditions $\mu_{l/r} = \mu_{S/D}$ to first order as $\frac{\partial \mu_{l/r}}{\partial V_L} V_L + \frac{\partial \mu_{l/r}}{\partial V_R} V_R = \mu_{S/D}$ and deriving by V_R, two conditions on the gate coupling ratios

$$\left(\frac{dV_R}{dV_L}\right)_{\mu_l=\mu_S=\text{const.}} = -\frac{\alpha_{Ll}}{\alpha_{Rl}} \tag{1.30}$$

$$\left(\frac{dV_R}{dV_L}\right)_{\mu_r=\mu_D=\text{const.}} = -\frac{\alpha_{Lr}}{\alpha_{Rr}}. \tag{1.31}$$

Consistently, the slope for left dot alignment diverges and the slope for right dot alignment converges to zero in the limit of zero cross-capacitances and interdot coupling, as illustrated in figure 1.7 (a).

Retrieving the dot addition energies

The total addition energies $\Delta\mu_l$ for the left and $\Delta\mu_r$ for the right dot

$$\begin{aligned} \Delta\vec{\mu} &:= \Delta\vec{\mu}^C + \Delta\vec{\mu}^{QM} \\ &= \begin{pmatrix} \mu_l(n_l+1, n_r; V_l, V_r) - \mu_l(n_l, n_r; V_l, V_r) \\ \mu_r(n_l, n_r+1; V_l, V_r) - \mu_r(n_l, n_r; V_l, V_r) \end{pmatrix} \end{aligned} \tag{1.32}$$

are given by the distance of two parallel, neighbouring lines in the stability diagram in (μ_l, μ_r) coordinates - provided the charge remains constant on the repective other dot. The values can be directly extracted from the raw data in (V_l, V_r) coordinates and, with knowledge of the gate coefficients $\mathbf{A}$, converted into energy via $\Delta\vec{\mu} = e\mathbf{A}\Delta\vec{V}$.

The classical parts are the electrostatic charging energies for left and right dot. So, the hexagon size differs in (μ_l, μ_r) directions only by the quantum mechanical energy contributions, mainly given by the carbon nanotube level spacings μ_l^{CNT} and μ_r^{CNT} as detailed in section 2.4.

The three relevant electrostatic charging energies for left dot, right dot and interdot

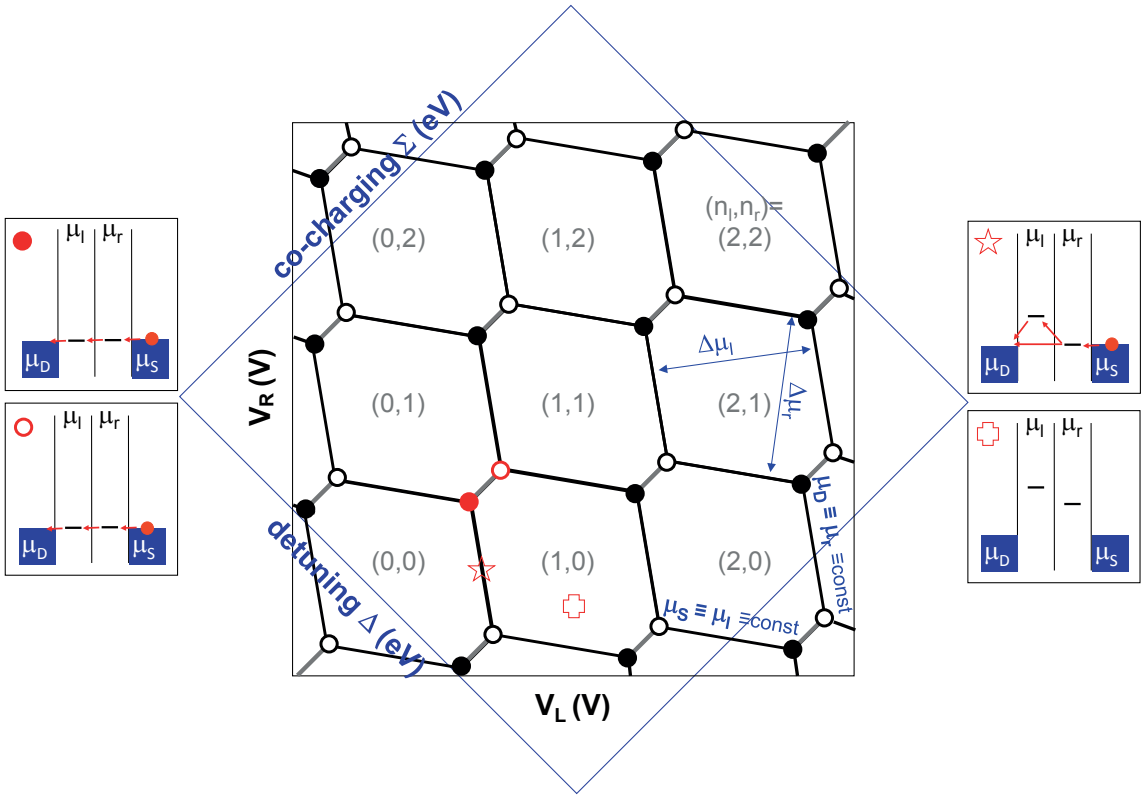

Figure 1.10: Sketch: Stability diagram of a capacitively coupled serial double quantum dot at near zero bias (linear response).

charging can be conveniently expressed in terms of the total dots capacitances as

$$\Delta\mu_l^C = e^2\frac{C_r}{\det\mathbf{C}_{dot}} = e^2\left[1-\frac{C_{lr}^2}{C_lC_r}\right]^{-1}1/C_l =: e^2/C_l^* \tag{1.33}$$
$$\Delta\mu_r^C = e^2\frac{C_l}{\det\mathbf{C}_{dot}} = e^2\left[1-\frac{C_{lr}^2}{C_lC_r}\right]^{-1}1/C_r =: e^2/C_r^*$$
$$\Delta\mu_{lr}^C = e^2\frac{C_{lr}}{\det\mathbf{C}_{dot}} = e^2\left[\frac{C_lC_r}{C_{lr}^2}-1\right]^{-1}1/C_{lr} =: e^2/C_{lr}^*$$

The *interdot charging energy* corresponds to 'distance' between the triple dots within a pair, again assuming that all quantum effects can be neglected. It accounts for the extra energy to add a charge on one dot due to one charge on the other [20, 26]. More useful for data evaluation are, obtained through some straightforward algebra helped by the ratio comparisons of energy and capacitances (from pairwise division of equations 1.33)

$$\frac{C_r}{C_l}=\frac{\Delta\mu_l^C}{\Delta\mu_r^C};\quad \frac{C_{lr}}{C_r}=\frac{\Delta\mu_{lr}^C}{\Delta\mu_l^C};\quad \frac{C_{lr}}{C_l}=\frac{\Delta\mu_{lr}^C}{\Delta\mu_r^C}. \tag{1.34}$$

(or alternatively by simply swapping $\Delta\mu^C \leftrightarrow C$) the capacitances in terms of charging energies are obtained

$$C_l = 1/e^2 \frac{\Delta\mu_r^C}{\det\mathbf{M}^C} = 1/e^2 \left[1 - \frac{\Delta\mu_{lr}^{C\,2}}{\Delta\mu_l^C \Delta\mu_r^C}\right]^{-1} 1/\Delta\mu_l^C \tag{1.35}$$

$$C_r = 1/e^2 \frac{\Delta\mu_l^C}{\det\mathbf{M}^C} = 1/e^2 \left[1 - \frac{\Delta\mu_{lr}^{M\,2}}{\Delta\mu_l^C \Delta\mu_r^C}\right]^{-1} 1/\Delta\mu_r^C$$

$$C_{lr} = 1/e^2 \frac{\Delta\mu_{lr}^C}{\det\mathbf{M}^C} = 1/e^2 \left[\frac{\Delta\mu_l^C \Delta\mu_r^C}{\Delta\mu_{lr}^{C\,2}} - 1\right]^{-1} 1/\Delta\mu_{lr}^C$$

because the energies $\Delta\vec{V} = \frac{1}{e}\mathbf{A}^{-1}\Delta\vec{\mu}$ can be drawn directly from the raw data but the capacitances cannot. The *electrostastic charging energy matrix* $\mathbf{M}^C$ is defined analogously as its conjugate $\mathbf{C}_{dot}$, see equation 1.27, and is obtained by just exchanging $\Delta\mu^C \leftrightarrow C$.

'Natural' double dot gate energy coordinate system (Σ, Δ)

A second coordinate transformation $\mathbf{T}$ allows to present the data in the 'natural' double dot coordinates

$$\begin{pmatrix} \Sigma \\ \Delta \end{pmatrix} := \underbrace{\begin{pmatrix} \frac{1}{2} & \frac{1}{2} \\ -1 & 1 \end{pmatrix}}_{=:\mathbf{T}} \begin{pmatrix} \mu_l \\ \mu_r \end{pmatrix} + \text{const} \tag{1.36}$$

$$= e \begin{pmatrix} \frac{1}{2} & \frac{1}{2} \\ -1 & 1 \end{pmatrix} \begin{pmatrix} \alpha_{Ll} & \alpha_{Rl} \\ \alpha_{Lr} & \alpha_{Rr} \end{pmatrix} e \begin{pmatrix} V_L \\ V_R \end{pmatrix} + \text{const}' \tag{1.37}$$

$$=: \mathbf{TA}e\vec{V} + const'.$$

Note that this transformation has $\det\mathbf{T} = 1$ and preserves the absolute energy scale. $\Delta := \mu_r - \mu_l$ is defined as the difference of left and right dot potentials. Along its direction, no charge is added to the total double dot system, rather are the charges 'shuffled' or redistributed from one dot to the other. The dot potentials are shifted or 'detuned' around a fixed centre, hence the name *detuning*.
$\Sigma := \frac{1}{2}(\mu_l + \mu_r)$ is defined as the arithmetic mean of left and right dot potentials. In Σ-direction, the potentials of left and right dot do not shift relatively to each other, but jointly. Notably, the interconnection of a triple point pair, where $\mu_l = \mu_r$ are aligned, is parallel to it. It shall be called *average charging direction*, because along it the net charge on the total double dot increases.
Figure 1.10 shows a stability diagram framed in black by the gate coordinates (V_L, V_R) and in blue by the natural energy coordinates (Σ, Δ). This sketch can

not convey that the coordinate transformation not only tilts but also streches and skews the hexagons, depending on the gate coeffients **A**. The side boxes illustrate the relative position of electrode and dot potentials for the triple dot pair (full and empty circle) and within a Coulomb-blockaded hexagon area (cross). The star marks a single resonance where transport is either carried by co-tunnelling (long arrow at Fermi level) or e. g. thermally exited inelasic sequential tunnelling (two short arrows up and down).

Relation of the interdot detuning Δ and the electronic states at the triple points

In the follwing the magnetic field dependence of the observable Δ, the interdot detuning, is related to the electronic states, using a model of non-tunnel coupled "atomic" quantum dots.
The free energy F of a system, like a quantum dot, is defined as [69]

$$F(n) =: \mu n$$

A change in free energy ∂F can be expanded as

$$dF = \frac{\partial F}{\partial n} dn.$$

The chemical potential μ is thus a measure how the free energy F changes (by dF) when the particle number n changes by dn:

$$\mu = \frac{dF}{dn}$$

The particles in question for electronic transport in quantum dots are electrons. The electronic charge is quantised in units of e=1.062×10^{-19} C. Consider adding a charge to a quantum dot with m charges; this correnspponds to the transition from an initial charge state $n_{|i\rangle} = m$ to a final charge state $n_{|f\rangle} = m+1$. Then the change in charge is

$$dn = n_{|f\rangle} - n_{|i\rangle} = (m+1) - m = 1$$

Analogously, when reducing charge of quantum dot with m charges by one, the transition goes from an initial charge state $n_{|i\rangle} = m$ to a final charge state $n_{|f\rangle} = m-1$. The change in charge number is then

$$dn = n_{|f\rangle} - n_{|i\rangle} = (m-1) - m = -1.$$

At low electron temperature, the free energy $F(n)$ can be approximated with the ground state energy E_n of the dot [24,69]. The energy differenve between the charge

state with $m+1$ and m electrons is $\partial F = E_{m+1} - E_m$, in terms of the ground state energies E_k of the charge states k (see section 1.1.1). The electrochemical potentials for adding a charge to a thermally isolated system (here: a quantum dot at cryogenic temperatures) are then

$$\mu_{m\to m+1} = \frac{\partial F}{\partial n} = \frac{E_{m+1} - E_m}{n_{|f\rangle} - n_{|i\rangle}} = \frac{E_{m+1} - E_m}{+1} = E_{m+1} - E_m$$

and for taking off a charge from a quantum dot

$$\mu_{m\to m-1} = \frac{\partial F}{\partial n} = \frac{E_m - E_{m-1}}{n_{|f\rangle} - n_{|i\rangle}} = \frac{E_m - E_{m-1}}{-1} = E_{m-1} - E_m.$$

In the wording of reference [69], adding a particle to one system implies taking it from another; what is measurable is then the difference between chemical potentials; the common zero-point of all μ's is hence an arbitrary definition.
An interdot charge transition between two quantum dot implies that, e. g. for negative bias, a charge is taken from the right dot r and added to the left dot l, i. e.

$$(m_l + 1, m_r - 1) \leftarrow (m_l, m_r).$$

The interdot detuning Δ is defined as the difference between the electrochemical potentials of left and right dot (see equation 1.36), i. e. the measured quantity is separated into contributions of left and right quantum dot according to equation 1.26 and the difference is taken. The detuning for an interdot transition, e. g. of a single charge going from right to left dot is expressed in terms of single electron energies as

$$\Delta_{(m_l+1,m_r-1)\leftarrow(m_l,m_r)} = -[E_{m_l+1} - E_{m_l}] + [E_{m_r-1} - E_{m_r}]$$

The evolution of the interdot detuning with the magnetic field is then

$$\Delta' := \frac{\partial \Delta}{\partial B} = \frac{\partial}{\partial B}\left\{-[E_{m_l+1} - E_{m_l}] + [E_{m_r-1} - E_{m_r}]\right\},$$

dropping the bulky subscript. Denoting the partial derivative by the magnetic field as dash, this rewrites

$$\Delta' = -[E'_{m_l+1} - E'_{m_l}] + [E'_{m_r-1} - E'_{m_r}] \tag{1.38}$$

1.2.2 Weak tunnel coupling at finite bias: $\mu_{D/S} < \mu_{dot} < \mu_{S/D}$

When a finite bias window $\mu_{SD} := \mu_S - \mu_D \equiv eV_{SD} > 0$ is opened, the condition for sequential transport through the double dot is given by the inequation

$$\mu_D \overset{!}{\leq} \mu_{dot} \overset{!}{\leq} \mu_S \tag{1.39}$$

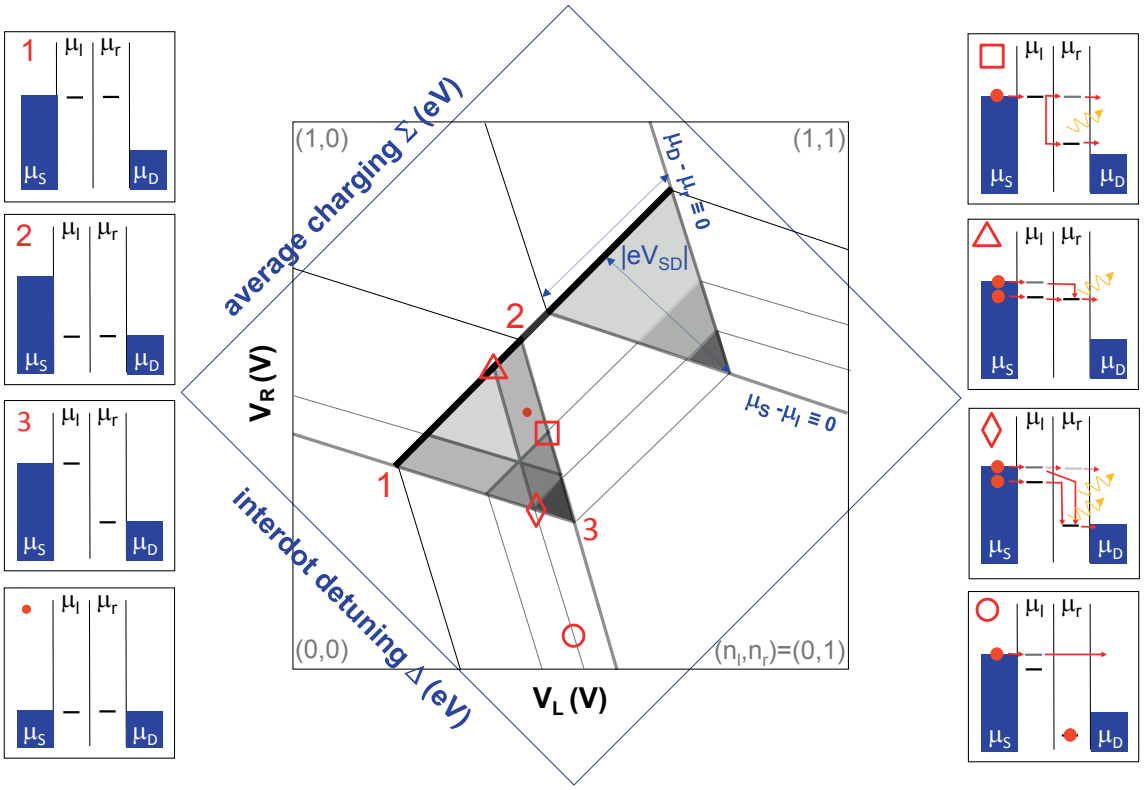

Figure 1.11: Stability diagram of a capacitively coupled, weakly tunnel coupled serial double quantum dot at finite bias in the Coulomb blockade regime. Numbers 1-3 mark the triple triangle points and their corresponding configurations of electro-chemical potential. Symbols □△◊◯ identify the transport mechanism behind the various resonance lines in the stability diagram (refer to the main text for details).

Figure 1.11 sketches a double dot stability diagram for positive bias. Compared to a single dot situation, the area of conductance is further restricted because now, not only both dot potential need to within the bias window. Additionally, a left dot state must be equal or higher/lower in energy than a right dot state for positive/negative bias.

These conditions confine sequential tunnelling to an (in energy coordinates) equilateral *triple triangle* with a baseline length $\overline{12}$ and a height from baseline to tip (figure 1.11 3) of $|eV_{SD}|$ - this is an important point for the parameter evaluation, as the bias is an experimental parameter that, unlike the gate voltages, directly relates the data to a physical energy scale. For negative bias, the triangle tip points upwards.

On the features in the stability diagram

Resonant sequential tunnelling through the electronic ground states of both quantum dots is possible only along the line that interconnects the points $\overline{12}$ in figure 1.11, where the dot potentials $\mu_l = \mu_r$ are aligned. The length of this *base line* is given by the size of the bias window $e|V_{SD}|$. At the end points of the triple triangle base line, both dot potentials are aligned with source (figure 1.11 2) or drain Fermi edges (figure 1.11 1). Inelastic sequential tunnelling is possible until the detuning Δ is so large that (for negative bias) both quantum dots have their electro-chemical potentials aligned to the Fermi edges of the adjacent electrodes, which marks the triangle tip (figure 1.11 3). If the two quantum dots are detuned beyond this point, the double quantum dot system is driven into Coulomb blockade. In energy coordinates, these *triple triangles* are equal-sided. Their base line and orthogonal distance from baseline to tip are set by the bias. The small red dot in figure 1.11 marks the position the zero bias triple point; the position is sample-dependent and arbitrarily chosen for purposes of the example. This point could be called the 'seed point' for the 'triple triangle growth with bias'. If source and drain electrode had no capacitve action on the quantum dot, the 'seed point' would be at point 2. Refer to section 5.7 for experiment-backed details.
Whenever an exited state (e. g. on the left dot) aligns within the bias window to some ground or exited state in the other dot (e. g. figure 1.11 $\square$), a second base line appears parallel to ground state one (figure 1.11 $\overline{12}$). Some potential configurations are exemplified on a line, stemming from an exited state on the right dot, that shows inelastic sequential tunnelling within the triple triangle (figure 1.11 $\triangle$ and $\Diamond$) and co-tunnelling at the single resonance (figure 1.11 $\bigcirc$). Off the triple points, the double dot can be thought of as a single quantum dot, with the off-resonance dot as part of the opposite current electrode [74].
The, partly overlapping, shaded areas indicate that every supplementary transport channel can change the tunnel current via inelastic processes - although, as already noted in the discussion of single dots in section 1.1.3, the tunnel current need not necessarily increase and can possibly even decrease. All sketched features have been observed experimentally in the subsequent chapters.

How to extract the set of gate couplings α_{Xy} from the data

The zero bias stability diagram only reveals two relations (equations 1.31 and 1.31) on the ratio of gate couplings α_{Xy}/α_{Yy}; it lacks a global gauge that allows to convert gate voltage into absolute energy scales. Such a gauge is given by a finite bias V_{SD}. The finite bias stability allows to extract the full set of gate couplings α_{Xy} from gate electrodes L, R to the dots l, r . Six conditions can be set by subtracting the each

left and right dot potentials at the points 1, 2 and 3 depicted in figure 1.11. The originating point is indicated on a quantity by a supercript 1,2,3.

$$\begin{aligned}
(1-2)_l:\ \mu_l^1-\mu_l^2 &= \mathrm{e}V_{SD} & \qquad (1-2)_r:\ \mu_r^1-\mu_r^2 &= \mathrm{e}V_{SD} \\
(2-3)_l:\ \mu_l^2-\mu_l^3 &= -\mathrm{e}V_{SD} & \qquad (2-3)_r:\ \mu_r^2-\mu_r^3 &= 0 \\
(3-1)_l:\ \mu_l^3-\mu_l^1 &= 0 & \qquad (3-1)_r:\ \mu_r^3-\mu_r^1 &= -\mathrm{e}V_{SD}
\end{aligned} \tag{1.40}$$

By using the coordinate transformation in equation 1.26, they can be expressed in terms of gate voltages and gate couplings α_{Xy}.

$$\begin{aligned}
(1-2)_l:\ \alpha_{Ll}\Delta V_L^{12}-\alpha_{Rl}\Delta V_R^{12} &= V_{SD} & \qquad (1-2)_r:\ \alpha_{Lr}\Delta V_L^{12}-\alpha_{Rr}\Delta V_R^{12} &= V_{SD} \\
(2-3)_l:\ \alpha_{Ll}\Delta V_L^{23}-\alpha_{Rl}\Delta V_R^{23} &= -V_{SD} & \qquad (2-3)_r:\ \alpha_{Lr}\Delta V_L^{23}-\alpha_{Rr}\Delta V_R^{23} &= 0 \\
(3-1)_l:\ \alpha_{Ll}\Delta V_L^{31}-\alpha_{Rl}\Delta V_R^{31} &= 0 & \qquad (3-1)_r:\ \alpha_{Lr}\Delta V_L^{31}-\alpha_{Rr}\Delta V_R^{31} &= -V_{SD}
\end{aligned}$$

with $\Delta V_X^{ab} := V_X^a - V_X^b$, $X \in \{L,R\}$ and $a,b \in \{1,2,3\}$, that can be directly measured in the $I(V_L,V_R)$ stability diagram. Solving for α_{Ll} and α_{Rr} and inserting

$$(3-1)_l \text{ into } (1-2)_l:\ \alpha_{Ll} = \frac{V_{SD}}{\Delta V_L^{12}(1-\frac{\Delta V_L^{31}}{\Delta V_R^{31}}\frac{\Delta V_R^{12}}{\Delta V_L^{12}})} \tag{1.41}$$

$$(2-3)_r \text{ into } (1-2)_r:\ \alpha_{Rr} = \frac{V_{SD}}{\Delta V_R^{12}(1-\frac{\Delta V_L^{12}}{\Delta V_R^{12}}\frac{\Delta V_R^{23}}{\Delta V_L^{23}})} \tag{1.42}$$

gives the experimental absolute value of two gate coefficients. This set of four gate coefficients is completed by the cross-gate coeffients from

$$(2-3)_r:\ \alpha_{Lr} = -\alpha_{Rr}\frac{\Delta V_R^{23}}{\Delta V_L^{23}} \text{ and} \tag{1.43}$$

$$(3-1)_l:\ \alpha_{Rl} = -\alpha_{Ll}\frac{\Delta V_L^{31}}{\Delta V_R^{31}}. \tag{1.44}$$

It is important to note that the ratio $\frac{V_{SD}}{\Delta V_{L/R}^{12}}$ relate the gate coefficients to physical energy scales but do not depend on the absolute bias value (because $\Delta V_{L/R}^{12}$ is linearly bias-dependent). Hence, the gate couplings are bias-independent, and the same set of gate coefficients is valid for stability diagrams taken at different bias voltages.

1.2.3 Strong tunnel coupling

Whether coherent electron tunnelling is non-negligible can be directly read off from the stability diagram, as sketched in figure 1.12, at the vicinity of where the triple points would have been in a weakly coupled double dot. Now, the electronic states

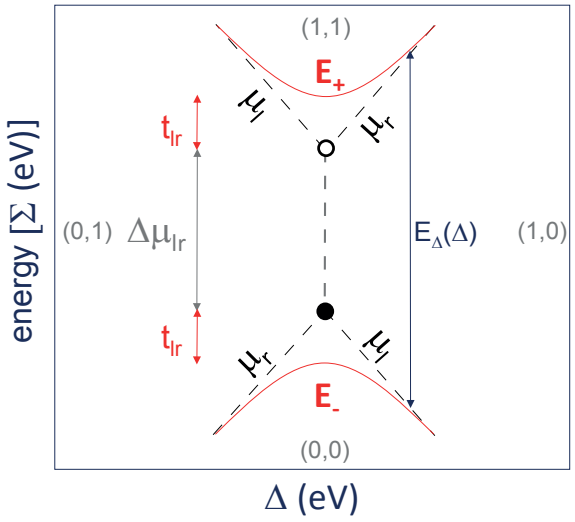

Figure 1.12: At strong interdot coupling, the single-particle states hybridise to a molecular two-particle state. This gives rise to a bonding and an antibonding state with energies E_- and E_+, and an anticrossing at the former sites of the triple dots with a repulsion of twice the interdot tunnel coupling t_{lr} on top of the interdot charging energy $\Delta\mu_{lr}$.

hybridise to a 'molecular' state with a probability density delocalised over the entire double dot system. This gives rise to an avoided crossing, and the current resonances lie no longer on the 'single particle' energy lines E_l and E_r (black in figure 1.12) but rather on the lines of a bonding and antibonding energies of a molecular state. A simple two level system serves to explain the basic mechanism qualitatively. The tunnel coupling can be expressed by an interaction Hamiltonian $\hat{\mathcal{T}}$ in the Schrödinger equation

$$(\hat{\mathcal{H}}_\mathbf{0} + \hat{\mathcal{T}})|\vec{\phi}\rangle = \mathbf{E}^{QM}|\vec{\phi}\rangle \tag{1.45}$$

with the bonding and antibonding molecular eigenstate $|\phi_-\rangle$ and $|\phi_+\rangle$

$$(\hat{\mathcal{H}}_\mathbf{0} + \hat{\mathcal{T}}) \begin{pmatrix} |\phi_-\rangle \\ |\phi_+\rangle \end{pmatrix} = \begin{pmatrix} E_- |\phi_-\rangle \\ E_+ |\phi_+\rangle \end{pmatrix} \tag{1.46}$$

with eigenenergies

$$E_- = \Sigma - \sqrt{\frac{1}{4}\Delta^2 + |t_{lr}|^2} \tag{1.47}$$

$$E_+ = \Sigma + \sqrt{\frac{1}{4}\Delta^2 + |t_{lr}|^2} \tag{1.48}$$

with the *charging* $\Sigma := \frac{1}{2}(\mu_l + \mu_r)$ and the *detuning* $\Delta := \mu_l - \mu_r$ which is nothing but the definition of the 'natural DQD' coordinate system in equation 1.36. The notations for electrochemical potentials $\mu_{l/r}$ and energies $E_{l/r}$ have been set equal because, in the experiment, energy differences are extracted from data plots in these coordinates.

The energy difference between bonding and antibonding state resonance is then

$$E'_{\Delta}(\Delta) = E_{+} - E_{-} = \sqrt{\Delta^2 + 4|t_{lr}|^2} \tag{1.49}$$

in the exemplary two-level system. At zero detuning, the interdot tunnel coupling causes a repulsion of $2|t_{lr}|$. In a double dot system, the spread is additionally increased by the classical interdot charging energy $\Delta\mu_{lr}$

$$E_{\Delta}(\Delta) \equiv \delta\Sigma(\Delta) = \Delta\mu_{lr} + \sqrt{\Delta^2 + 4|t_{lr}|^2} \tag{1.50}$$

as illustrated in figure 1.12.

Chapter 2

Carbon nanotubes

Carbon nanotubes are an outstanding material in many ways; they are macromolecules with respect to their length while their diameter is on the sun-nanometer scale, down to only few atoms around their circumference [75]. Mechanically, they are stronger yet lighter than steel. Electrically, they are the prototypical example of a one-dimensional, ballistic quantum wire, with the capacity to carry far higher current densities than normal metals. Technologically, they are particularly suitable for applications in molecular electronics, because they are relatively easy to handle, can be integrated in existing mesoscopic device architectures and are both chemically stable and mechanically robust.
The remarkable electronic behavior of carbon nanotubes (CNTs) originates from a particular combination of the symmetry properties of the graphene band structure and the quantization of momentum imposed by periodic boundary conditions along the nanotube circumference. Many properties stem directly from the carbon atom. This symmetry results in a four-fold degenerate shell structure in the energy spectrum of CNT quantum dots (QDots).

This chapter first presents the theory on some basic electronic properties of carbon nanotubes, following the concept how quantum dots can be implemented by 'stripping off' dimensions from all-carbon molecules down to the 0D case.

2.1 3D: carbon

The basis properties of the carbon atom allow to conclude to the existence of fullerenes, such as carbon nanotubes. It is the sixth element in the periodic system, where it is listed at the top of the fourth group. Of its six electrons, two fill all states with main quantum number $n = 1$ (the He shell $1s$); these tightly bound

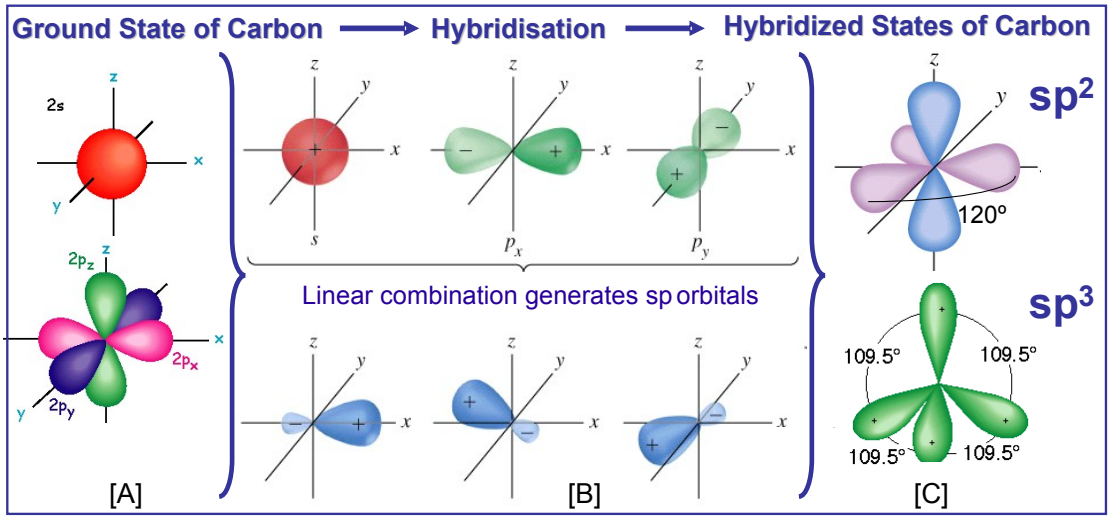

Figure 2.1: (a) Ground state electronic distribution (orbitals) of the free carbon atom. (b) Hybridisation of sp^2 states and (c) and the sp^2 orbitals (the carbon configuration in graphite) sp^3 orbitals (the carbon configuration in diamonds). Assembled from [76] and [77].

'core electrons' do not participate in transport. The remaining four, more weakly bound 'valence electrons' occupy half the shell of the next inert gas (Ne) with the main quantum number $n = 2$, can accommodate $2n^2 = 8$ electrons. From the simple 'octet rule' which states that each atom seeks to minimise its energy by chemical bonds that grant the inert gas shell of either the next lower or next higher core number Z, it is directly evident that elements of the fourth group (such as C, Si or Ge) can form one-element molecules or crystals.

Electronic structure: Hybridisations of carbon

The spatial orientation of the bond in all carbon molecules can be easily read from its electronic configuration; in the ground state of a free carbon atom, the electronic configuration is $1s^2$, $2s^2$, $2p^2$ (figure 2.1 (a)). The shape of each orbital depends on the angular momentum quantum number l[1]. Hybrid sp^n orbitals arise from linear combination of one s and n p orbitals. The orbitals are oriented such that the charge distribution is as isotropic as possible.

For $n = 3$, four sp^3 orbitals are separated by the tetrahedral angle $\theta_{sp^3} = 109.5°$ to each other; this the configuration of diamonds and Si and Ge crystals. For $n = 2$,

[1] where $s := l \equiv 0$, $p := l \equiv 1$ (l=-n,...,n)

however, the electron distribution is $p_z^1 sp^2$. With the p_z orbital pointing w.l.o.g. in z-direction, the three sp^2 orbitals are evenly spaced in the xy-plane by an angle $\theta_{sp^2} = \frac{2\pi}{3} = 120°$. This simple observation already predicts the plane, hexagonal lattice structure of graphite. Equivalence of the carbon atoms in the hexagon also predict the delocalisation of the bonding π or anti-bonding π^* bonds between $p_z - p_z$ orbitals and, by symmetry, allow to reduce the description to an angle segment of 30°, the triangle marked by the points of high symmetry $\overline{\Gamma KM}$ in figure 2.3 (b). The lack of sp and sp^2 hybridisation in higher elements in the fourth group (Si, Ge) can be related to the more complicated core shells. σ-bonds of sp^2 are covalent in all carbon molecules and can therefore be neglected in the escripion of electronic transport.

Nuclear structure: isotopes of carbon

In nature, there are two stable isotopes of carbon (setting aside the decaying ^{14}C), the predominant ^{12}C (98.9% [24]), which has an even number of hadrons in its nucleus and therefore - simply put - no nuclear spin, and ^{13}C, which has a non-zero nuclear spin. Carbon nanotubes can be made from both isotopes, and the impact of the carbon isotope on transport through a tube has been observed, e. g., in reference [71]. Together with the weak spin-orbit coupling, this qualifies ^{12}C nanotubes as an material for spintronics because hyperfine coupling of coherent electron spins is a dominant source for spin decoherence - although hyperfine interaction can be exploited if controlled [71].

2.2 2D: graphene

This chapter mainly excerpts from references [39], [40], [78] and [79], developing an own, self-contained notation. The basic idea is to consistently describe the the problem in *transversal coordinate* (along the tube axis) and *circumferential coordinate* (around the tube's circumference).

Positional lattice structure

The carbon-carbon σ bonds of sp^2 orbitals form the planar graphene lattice; the problem is thus reduced by one dimension to $2D$. The two lattice vectors are

$$\vec{a}_1 = a \begin{pmatrix} \frac{\sqrt{3}}{2} \\ \frac{1}{2} \end{pmatrix}, \vec{a}_2 = a \begin{pmatrix} \frac{\sqrt{3}}{2} \\ -\frac{1}{2} \end{pmatrix}, \tag{2.1}$$

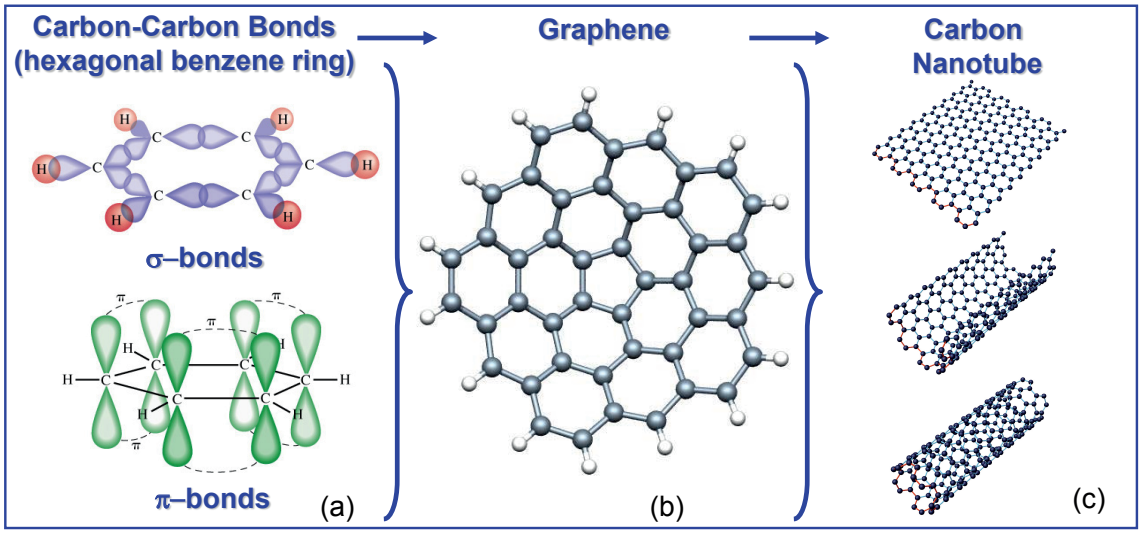

Figure 2.2: (a) σ bonds form, by the sp^2 symmetry, the hexagonal lattice seen in (b). (c) 'Theoretical synthesis' of a carbon nanotube by rolling up a graphene sheet into a seamless cylinder. Assembled from [76].

where $a = |\vec{a}_1| = |\vec{a}_2| = 2.46\,\mathring{A}$ is the lattice constant. They span the unit cell (a rhombus-shaped area depicted in figure 2.3 (a)) which contains two carbon atoms.

Reciprocal lattice structure

Obeying

$$\vec{a_i} \cdot \vec{b_j} = 2\pi\delta_{ij}; \quad i,j = 1,2 \tag{2.2}$$

the reciprocal lattice vectors are found to be

$$\vec{b}_1 = \frac{2\pi}{a}\begin{pmatrix} \frac{1}{\sqrt{3}} \\ 1 \end{pmatrix}, \vec{b}_2 = \frac{2\pi}{a}\begin{pmatrix} \frac{1}{\sqrt{3}} \\ -1 \end{pmatrix}. \tag{2.3}$$

Because the periodicity of the lattice in positional space is inherited ito the reciprocal space, all physics can be described within the (hexagonal) unit cell of the reciprocal space, the first Brioullin zone. It is shown in figure 2.3 (b), where the points of high symmetry Γ, K and M are indicated in red colour.

Electronic dispersion relation

The out-of-plane p_z orbitals hybridise and form a delocalised π band that dominates the electronic properties of graphite [39]. In good approximation, the tightly bound σ bonds can be neglected in graphene electronic transport properties.

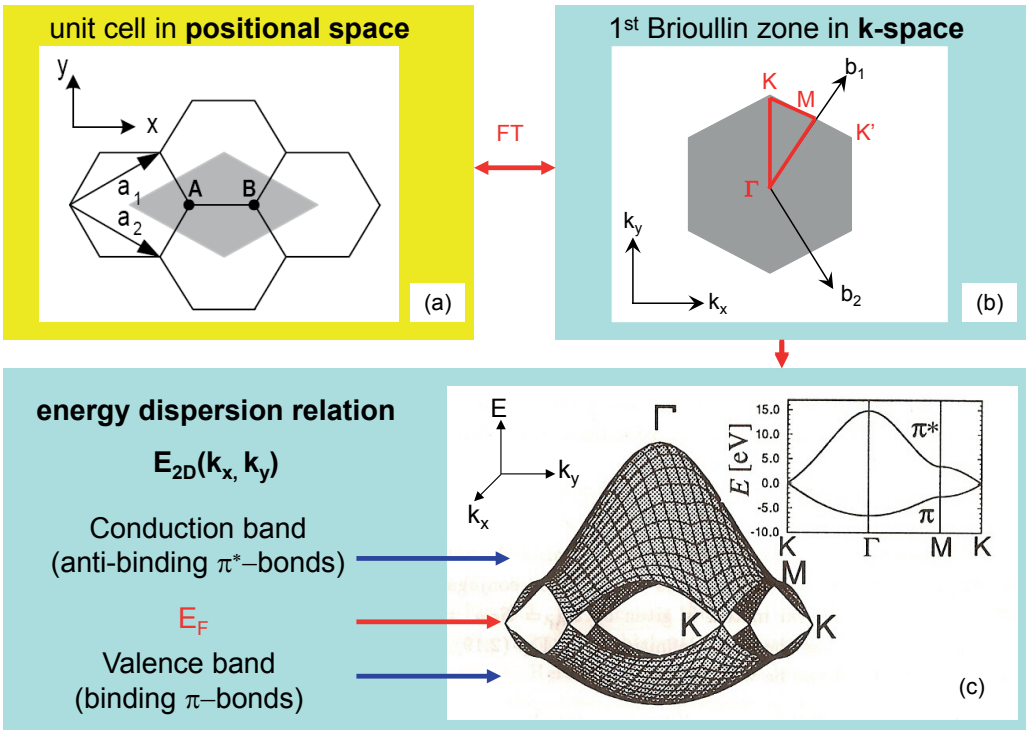

Figure 2.3: (a) Unit cell of graphene in positional space (b) first Brillouin zone (in k-space) (c) energy dispersion $E_{2D}(k_x, k_y)$ plotted over the first Brillouin zone. Inset: Dispersion relation along connections between points of high symmetry $K\Gamma KM$ (see the dashed red triangle in (b)). Grey areas mark the unit cells in positional and reciprocal spaces. Partly taken and adapted from [78].

A simple tight binding approach with three nearest neighbours (at lattice coordinates $\vec{R}_1$, $\vec{R}_2$ and $\vec{R}_3$) has a very high accuracy compared to *ab initio* DFT calculations [40] and matches well with experiments (e.g. ref [56]):

The lattice periodicity suggests a Bloch wave ansatz

$$\begin{aligned} \Phi_j(\vec{k},\vec{r}) &= \frac{1}{\sqrt{N}} \sum_{\alpha=A,B} \sum_{i=1}^{N} e^{i\vec{k}\vec{R}_{\alpha,i}} \varphi_j(\vec{r}, \overrightarrow{R}_\alpha) \\ &= \Phi_j(\vec{k}, \vec{r} + \vec{a}_m);\ m = 1,2 \end{aligned} \tag{2.4}$$

normalised by the number of unit cells $N \approx 10^{24}$ [39, 78]. n is the number of $2p$-eigenfunctions φ_j for each atom $\alpha = A, B$ in the unit cell weighted with a phase factor $e^{i\vec{k}\vec{R}_\alpha}$. The second equality states the periodic boundary condition for lattice vectors $\overline{a}_m$ (and their integer multiples).

Expanding the eigenfunctions $\Psi_l(\vec{k},\vec{r})$ into these Bloch functions

$$\Psi_l(\vec{k},\vec{r}) = \sum_{m=1}^{n} C_{lm}(\vec{k})\Phi_m(\vec{k},\vec{r}) \tag{2.5}$$

the task is reduced to determining the coefficients $C_{lm}(\vec{k})$ and minimising the energy functional

$$E_l(\vec{k}) = \frac{\langle\Psi_l|\hat{\mathcal{H}}|\Psi_l\rangle}{\langle\Psi_l|\Psi_l\rangle} \tag{2.6}$$

by solving the eigenvalue problem (i.e. the Schrödinger equation)

$$det[\hat{\mathcal{H}} - E\hat{\mathcal{S}}] = 0 \tag{2.7}$$

where $\hat{\mathcal{H}}$ is the Hamilton operator and $\hat{\mathcal{S}}$ the overlap integral. In nearest neighbour approximation for graphite, $n = 2$ unit cells are taken into account because for any atom A, its three direct neighbours B in adjacent unit cells are equivalent et vice versa, allowing to write the operators as 2×2 matrices

$$\mathcal{H}_{lm} = \langle\varphi_l|\hat{\mathcal{H}}|\varphi_m\rangle = \begin{pmatrix} \epsilon_{2p} & tf(\vec{k}) \\ tf(\vec{k})^* & \epsilon_{2p} \end{pmatrix}_{lm} \tag{2.8}$$

$$\mathcal{S}_{lm} = \langle\varphi_l|\varphi_m\rangle = \begin{pmatrix} 1 & sf(\vec{k}) \\ sf(\vec{k})^* & 1 \end{pmatrix}_{lm} \tag{2.9}$$

where

$$f(\vec{k}) = e^{ik_x a/\sqrt{3}} + 2e^{-ik_x a/2\sqrt{3}} cos(\frac{k_y}{2}) \tag{2.10}$$

$$\gamma_0 = \langle\varphi_l(\vec{r} - \vec{R}_A)|\hat{\mathcal{H}}|\varphi_m(\vec{r} - \vec{R}_B)\rangle \tag{2.11}$$

$$s = \langle\varphi_l(\vec{r} - \vec{R}_A)|\varphi_m(\vec{r} - \vec{R}_B)\rangle \tag{2.12}$$

and γ_0 and s are called the transfer and overlap integrals respectively.

The (ground state) eigenvalues are then given by

$$E_{2D} = \frac{\epsilon_{2p} \pm \gamma_0|f(\vec{k})|}{1 \pm s|f(\vec{k})|} \tag{2.13}$$

where the "+" sign gives the bonding π-band (valence band) and the "-" sign the anti-bonding π^*-band (conduction band). As the two electrons per unit cell fill up the π-band and leave the π^*-band empty, this point is also called *charge neutrality point* (CNP). When scaling ϵ_{2p} to zero by convenience and taking $\gamma_0 = -3.033eV$ and $s = 0.129$ from first principle calculations [39], the dispersion relation over the

first Brillouin zone matches well with first principle calculations. For $s = 0$, in the Slater-Kloster scheme [78], the π and π^* bands become symmetric [39] and the energy reads

$$E_{2D}(k_x, k_y) = \pm\gamma_0\{1 + 4\cos(\frac{\sqrt{3}k_x a}{2})\cos(\frac{k_y a}{2}) + \cos^2(\frac{k_y a}{2})\}^{\frac{1}{2}}. \tag{2.14}$$

Near the K-points (in k space and energy) the bands can be approximated as straight lines (*light cone approximation*), and

$$E_{2D}(\overrightarrow{k}) = \pm\hbar v_F|\vec{k} - \vec{k}_F| \tag{2.15}$$

holds well with a Fermi velocity $v_F = 8 \cdot 10^5 \frac{m}{s}$ [80].

2.3 1D: Single-walled carbon nanotubes (SWCNTs)

The electronic structure of CNTs can be derived from the two-dimensional band structure of a graphene sheet. The continuity of the electron wave function around the CNT circumference imposes the quantisation of the wave vector component perpendicular to the CNT axis. This leads to a set of one-dimensional subbands in the longitudinal direction. These subbands are two-fold spin-degenerate.

Positional Space Lattice Structure

In figure 2.2 (c), the 'theoretical synthesis' of carbon nanotubes is depicted. The orientation of the graphene layer (depicted in figure 2.2 (b)) before being 'wrapped' into a cylindric tube is uniquely identified by the chiral vector $(n\vec{a}_1, m\vec{a}_2) \equiv (n, m)$, where $\vec{a}_i$ are the lattice vectors of graphene and n, m integers; the same information is contained in the tube's diameter and chiral angle (d, θ) , i.e.

$$d = \frac{|\vec{C}|}{\pi} = a\sqrt{n^2 + m^2 + nm} \tag{2.16}$$

$$\theta = mod_{\frac{\pi}{6}}(\arccos(\frac{\vec{C}}{|\vec{C}|} \cdot \frac{\vec{a}_1}{|\vec{a}_1|})) = mod_{\frac{\pi}{6}}(\arccos(\frac{2n + m}{2\sqrt{n^2 + m^2 + nm}})) \tag{2.17}$$

where the translation vector $\vec{T}$ and the circumference vector $\vec{C}$, as exemplified for a (n,m)=(4,2) nanotube in figure 2.4, are

$$\begin{pmatrix} \vec{T} \\ \vec{C} \end{pmatrix} = \begin{pmatrix} \vec{OB} \\ \vec{OA} \end{pmatrix} = \begin{pmatrix} t_1 & t_2 \\ c_1 & c_2 \end{pmatrix} \begin{pmatrix} \vec{a}_1 \\ \vec{a}_2 \end{pmatrix} = \begin{pmatrix} \frac{2m+n}{\mathcal{R}} & \frac{2n+m}{\mathcal{R}} \\ n & m \end{pmatrix} \begin{pmatrix} \vec{a}_1 \\ \vec{a}_2 \end{pmatrix} \tag{2.18}$$

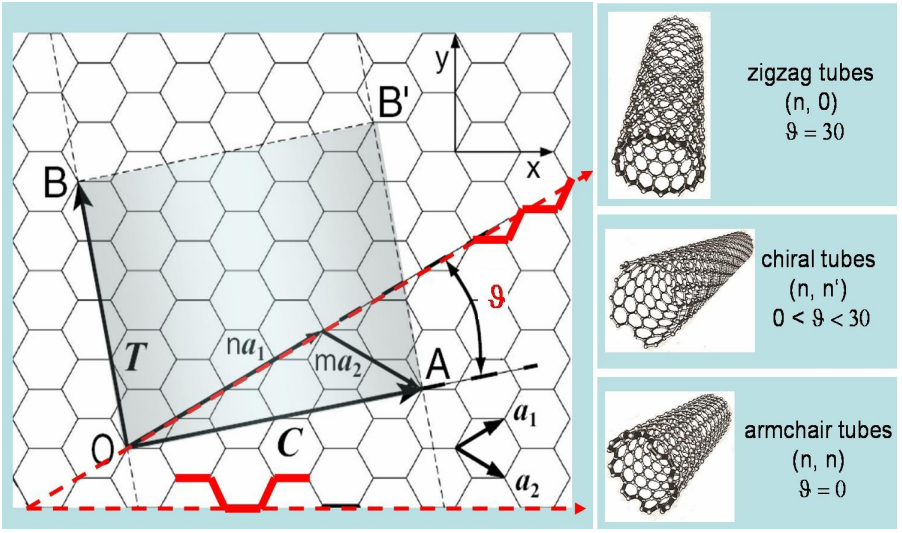

Figure 2.4: Depending on the orientation of the graphene honeycomb lattice when 'rolling it up' and fusing it into seamless cylinder (where, e.g., the atoms at 0 and A as well as at B and B' coincide), the chiral angle θ will be different and yield a zigzag, chiral or armchair nanotube. $\vec{T}$ points in the direction of the tube axis and its length is the transversal length of the CNT unit cell. $\vec{C}$ points in 'circumferential' direction and its length is the circumferential length of the unit cell. The unit cell area is shaded in light blue.

where $\mathcal{R}$ is 3 if $mod_3(n-m) \neq 0$, i.e. 3 for metallic nanotubes, else 1.

This means that the 2D cylinder surface in 3D space, described by the 'directions' $\vec{T}, \vec{C}$ can be mapped equivalently to the flat coordinates $\vec{a}_1, \vec{a}_2$ of the graphene sheet, which grants a more convenient description.

The two special cases for minimal chiral angle ($\theta = 0°$) and maximal chiral angle ($\theta = 30°$) were baptised *zigzag* and *armchair* for the pattern of the carbon bonds around their circumference. This can be seen from the bold red lines in figure 2.4. All other geometries ($0° < \theta < 30°$) are referred to as *chiral* nanotubes.

The unit cell is a (2D) cylinder surface segment spanned by $\vec{T} \times \vec{C}$, which is shown, in its unrolled form, by the shaded area in figure 2.4. The unit cell of a nanotube contains

$$N := \frac{|\vec{T} \times \vec{C}|}{|\vec{a}_1 \times \vec{a}_2|} = \frac{2(n^2 + nm + m^2)}{n\mathcal{R}} \tag{2.19}$$

graphene unit cells and correspondingly $2N$ carbon atoms. Because each carbon atom has one p_z orbital contributing to conductance, N coincides with the number of subbands of the nanotube.

Reciprocal Lattice Structure

Via the condition for reciprocal lattice vectors

$$\vec{K}_i \cdot \vec{j} = 2\pi\delta_{ij};\ i,j = T,C \tag{2.20}$$

the reciprocal lattice vectors are given by

$$\begin{pmatrix} \vec{K}_T \\ \vec{K}_C \end{pmatrix} = \frac{1}{N} \begin{pmatrix} -t_2 & t_1 \\ m & n \end{pmatrix} \begin{pmatrix} \vec{b}_1 \\ \vec{b}_2 \end{pmatrix}. \tag{2.21}$$

The folding of the graphene sheet into a closed cylinder imposes, by symmetry of the molecular lattice, a periodic boundary condition along the tube circumference $\vec{C}$:

$$\vec{k}_{C,l} \cdot \vec{C} = 2\pi \cdot l \tag{2.22}$$

where the integer l denotes the number of nodes around the circumference; all other wavelengths $\lambda = \frac{2\pi}{k}$ vanish by interference [40]. This quantises the $\vec{k}_C$ in direction of $\vec{K}_C$ into subbands (also called *channels* or *electrical modes* [81]) with a spacing

$$\Delta\vec{k}_C = \frac{2\pi}{|\vec{C}|} = \frac{2}{d}. \tag{2.23}$$

Note that one more dimension (in the sense of an electronic degree of freedom in space) has been lost, achieving 1-dimensional transport; along the tube, in $\vec{T}$-direction $\vec{k}_T$ is still continuous, at least for infinitely long tubes. For nanotubes of finite length L, e.g. if contacted with metal leads or simply kinking it, the transport is stripped of yet another dimension, i.e. the sample is a (0D) nanotube quantum dot. The allowed k vectors are then spaced by $\frac{2\pi}{L}$ in direction $\vec{K}_T$.

The first Brillouin zone of the nanotube is obtained by taking (1D) line segments out off the (2D) Brillouin surface of graphene. This is depicted in figure 2.5. The length $\Delta\vec{k}_T$ of these lines is given by the translation vector:

$$-\frac{\pi}{|\vec{T}|} > \vec{k}_T > \frac{\pi}{|\vec{T}|} \tag{2.24}$$

The number of line segments, i.e. subbands, that make up the 1st Brillouin zone is given by the number of p_z-orbitals $2N$ (one per atom) in the nanotube's unit cell

$$1 \leq l \leq 2N \tag{2.25}$$

The (1D) volume of the 1st Brillouin zone is then

$$2N|\vec{K}_T| = \frac{4\pi d}{\sqrt{3}a}. \tag{2.26}$$

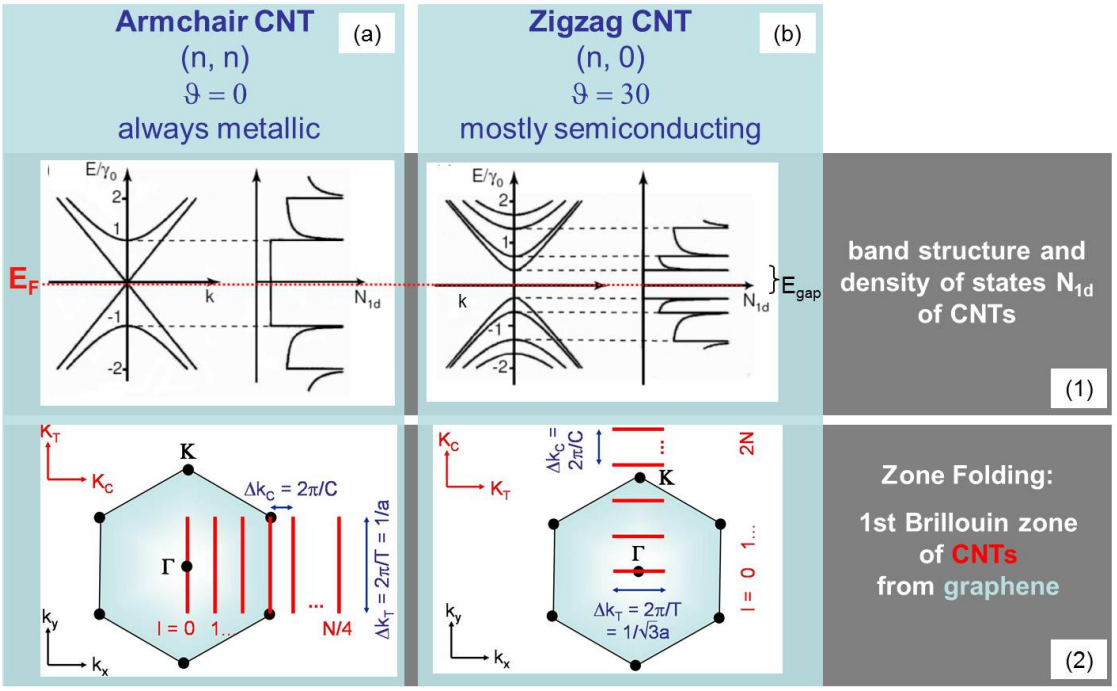

Figure 2.5: Schematic band structure and density of states (1) and first Brioullin (2) zone from graphene for armchair (a) and zigzag (b) carbon nanotubes.

The first Brillouin zone can be pictured as a $2N$ line segments in k-space parallel to $\vec{K}_T$ within an rectangle of length $2N \cdot \frac{2\pi}{|\vec{C}|}$ and width $\frac{2\pi}{|\vec{T}|}$.

Energy dispersion in carbon nanotubes

In the *zone folding* or *confinement* approximation [40], the basic idea is that the electronic band structure of a carbon nanotube is given by the energy dispersion of graphene along its allowed k_T-lines; the carbon nanotubes the first Brioullin zone of carbon nanotubes was obtained by taking slices out of the 1st Brioullin of graphene. Similarly, the energy dispersion of carbon nanotubes is retrieved by taking traces $E_l(k_x, k_y)$ out of the energy $E_{2D}(k_x, k_y)$ of graphene, where n denotes the l^{th} sub-band (see figure 2.6).

Near the K-points (in k space and energy) the bands can be approximated as straight lines (*light cone approximation*), i. e.

$$E_{1D,l}(\vec{k}_l) = \pm\gamma_0 \frac{\sqrt{3}a}{2} |\vec{k}_l - \vec{k}_F| \tag{2.27}$$

where $\gamma_0 = \frac{2\hbar v_F}{d}$ with a typical Fermi velocity $v_F = 8 \cdot 10^5 \frac{m}{s}$ [80]. Expressed in

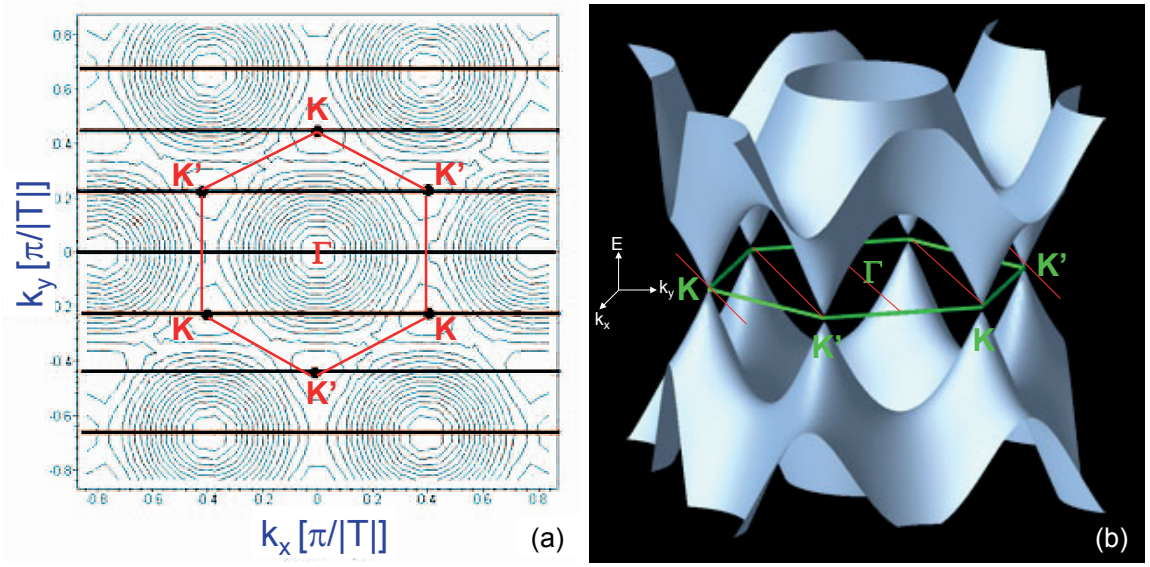

Figure 2.6: The principle of the Zone Folding Approximation; contour-plot of the bonding π-band of graphene. If the lines of allowed k-vectors for a carbon nanotube (here a metallic (3,0) zigzag nanotube) 'hit' a K-point in the first Brillouin zone of graphene then the nanotube is metallic. Adapted from [78]

coordinates parallel and circumferential to the tube the allowed k-values for the l^{th} subband are

$$\vec{k}_l = \begin{pmatrix} k_T \\ k_C \end{pmatrix} = \begin{pmatrix} k_T \\ \Delta k_c \cdot l \end{pmatrix} = \begin{pmatrix} k_T \\ \frac{4}{d}|l - \frac{1}{3}(n-m)| \end{pmatrix}. \tag{2.28}$$

For 1D transport, the Fermi wave vector then has a non-zero component only along the tube axis. Then the energy of the l^{th} subband becomes

$$E_{1D,l}(k_T) = \pm\gamma_0 \frac{\sqrt{3}a}{2}\sqrt{l \cdot \Delta k_C^2 + (k_T - k_F)^2}. \tag{2.29}$$

From this, one can directly see that the minimum of the π^*-band and the maximum of the π-band

$$\begin{aligned} E_{1D,l}^M &= E_{2D,l}(\vec{k}_l = 0) \\ &= \pm\gamma_0 \frac{\sqrt{3}a}{2}\sqrt{l \cdot \Delta k_C^2 + (k_T - k_F)^2} \\ &= \pm\gamma_0 \frac{\sqrt{3}a}{2}\sqrt{l \cdot \frac{4}{d}|l - \frac{1}{3}(n-m)|} \end{aligned} \tag{2.30}$$

are...

- both zero and therefore degenerate for
  - all armchair tubes $(n,m) = (n,n)$ for the first subband $l = 0$.
  - those zigzag tubes $(n,0)$ and chiral tubes (n,m) for which $l - \frac{1}{3}(n-m) = 0$ for some subband l, i.e. $n-m$ is a multiple of three.

  In both cases, one valence subband is degenerate with a subband above Fermi energy. These carbon nanotubes have zero bandgap. Because they are expected to show metallic behaviour, they are also called *quasi metals*. More accurately, they could be called 'zero gap-semiconductors'.

- both finite with opposite sign. This is the case for all other tubes (n,m). They are thus semiconducting with a finite band gap [78]

$$E_{\text{gap}} = \gamma_0 \frac{\sqrt{3}a}{d}. \tag{2.31}$$

At (near) zero bias excitation, current can flow through a CNT via two conductance channels because bands are pairwise degenerate. Together with spin degeneracy, this leads to the four-fold level degeneracy of carbon nanotubes and a quantum limit to conductance of

$$G_{max}^{CNT} = 2 \cdot 2 \cdot \frac{e^2}{h}. \tag{2.32}$$

Due to curvature, the smallest CNT possible is a $(3,3)$ armchair nanotube [75]. By simply counting all possible combinations (n,m), it is found that one third of the CNTs are metallic and two thirds are semiconducting.
From figure 2.5 (b1) and (b2) it is seen that $(\vec{k}_C || \vec{k}_x)$ for armchair and $(\vec{k}_C || \vec{k}_y)$ for zigzag nanotubes. Inserting the respective quantisation conditions along the circumference (equation 2.22)

$$k_x = k_{C,l}^{armchair} = \frac{2\pi}{N\sqrt{3}a} \cdot l \tag{2.33}$$

$$k_y = k_{C,l}^{zigzag} = \frac{2\pi}{Na} \cdot l \tag{2.34}$$

into the energy dispersion found for graphene (2.3) expressions in (k_x, k_y)-coordinates can be obtained straightforwardly:

$$E_{1D,l}^{armchair}(k_y) = \pm\gamma_0 \{1 + 4cos(\frac{\pi \cdot l}{N}) \cos(\frac{k_y a}{2}) + cos^2(\frac{k_y a}{2})\}^{\frac{1}{2}}, \tag{2.35}$$

$$E_{1D,l}^{zigzag}(k_x) = \pm\gamma_0 \{1 + 4cos(\frac{k_x}{2}) \cos(\frac{\pi \cdot l}{N}) + cos^2(\frac{\pi \cdot l}{N})\}^{\frac{1}{2}}. \tag{2.36}$$

In the unit cell of a nanotube, two of the $2N$ carbon atoms are equal in pairs. In reciprocal state this means simply that, e.g. a metallic tube touches two equivalent K-points. This leads to a two-fold degeneracy of each subband.

Density of states

Instead of providing a derivation of the density of states (DoS) (e. g. [40]), a brief comment on the density of states for a free electron gas in d-dimensions may be found instructive.
The number of occupied states Z for a d-dimensional electron gas at E_F is obtained by counting all k-states within the $(d-1)$-dimensional Fermi surface of constant energy in reciprocal space. Consequently, Z is proportional to k^d

$$Z_{dD}(k) \propto k^d. \tag{2.37}$$

Expressed as a function of energy, using the parabolic energy dispersion of a free electron gas $E(k) \propto k^2$, the partition function spells

$$Z_{dD}(E) \propto E^{\frac{d}{2}}. \tag{2.38}$$

The density of states (per energy) $D_{dD}(E)$ is given by derivation of $Z_{dD}(E)$ with respect to E

$$D_{dD}(E) = \frac{dZ_{dD}}{dE} \propto E^{\frac{d}{2}-1}. \tag{2.39}$$

For a 1-dimensional system ($d = 1$) this leads to

$$D_{1D}(E) = \frac{dZ_{1D}}{dE} \propto E^{-\frac{1}{2}}. \tag{2.40}$$

Note that because $Z_{1D} \propto k$ the DoS can be written as $D_{1D} \propto |\frac{dE}{dk}|^{-1}$. This holds for any, not only parabolic energy dispersions. Features corresponding to the divergence of the inverse square root at $E = 0$ can be observed experimentally in 1-dimensional systems, such as carbon nanotubes (e.g. [40]), and are named *van Hove*-singularities.

For semiconducting carbon nanotubes, the energy dispersion can be parabolically approximated around the minima and maxima to second order, i.e. $E_{1D}^{CNT} \propto cos^2(k) \approx 1 + k^2$, so the DoS is expected to have a $\frac{1}{\sqrt{E}}$-behaviour.
For metallic carbon nanotubes, the linear *light cone* approximation 2.29 describes well the lowest, two-fold degenerate subband. Thus, its DoS $D_l(E) = const$ and there is no van Hove-singularity. All other bands are distinctly parabolic around their extrema so that the divergence appears at the points $\vec{k} = (k_T, \delta k_C \cdot l)$ tangential to them.

The l^{th} contributes a density of states

$$D_l(E) = \frac{1}{N|\vec{K}_T|} |\frac{\partial E_l}{\partial k_T}|^{-1} \tag{2.41}$$

normalised by the unit volume (from 2.26) [78].
In the light cone approximation, the inverse partial derivative is

$$\left|\frac{\partial E_l}{\partial k_T}\right| = \frac{\sqrt{3a}}{2}\gamma_0 \frac{|(\frac{E_l}{E_l^M})^2|}{\sqrt{(\frac{E_l}{E_l^M})^2 - l^2}}. \tag{2.42}$$

The total DoS results from summing up all subband contributions with an offset equal to its extremal energy, i.e.

$$D(E) = 2 \cdot 2 \cdot \frac{2}{N|\vec{K}_T|} \sum_{l=0}^{N} D_l(E') \operatorname{sgn}(E_M) \int_{-\infty}^{\infty} dE' \theta(|E_l'| - |E_l^M|). \tag{2.43}$$

The first factor 2 accounts for the two-fold channel degeneracy, the second for the two spin orientations - granted that they are degenerate.

The density of states can be experimentally probed by scanning tunnelling spectroscopy (STS), using a scanning tunnelling microscope (STM); roughly speaking, the differential conductance is proportional to the DoS [39, 79].

2.4 0D: Electronic transport in SWCNT-based quantum dots

By patterning metallic electrodes with distance L onto a CNT, a mesoscopic "*0D*"-CNT segment is defined that can act as a *quantum dot* or *artificial atom*. Along the tube axis, the energies of electronic states quantise

$$\Delta\mu^L = \frac{h v_F}{d\, L}, \tag{2.44}$$

stemming from the electron confinement within the CNT section of length L, with h Planck's quantum and $v_F \approx 8{\cdot}10^5 \frac{m}{s}$ the Fermi velocity in carbon nanotubes. The constant d is 1 for orbital and spin degeneracies, 2 for only spin degeneracy and 4 for no level degeneracy, if e. g. a magnetic field lifts the spin degeneracy, too [54].
When all dimensions of a wire are reduced below the mean free path of the electrons passing through, the electronic transport is no longer diffusive but ballistic. Simply put, an electron meets no scatterer on its path through the wire and thus meets no electrical resistance. An example of a mesoscopic wire in the ballistic transport regime is a mesoscopic section (up to several μm) of a SWCNT. Experimentally, such a mesoscopic section can be fabricated by depositing source and drain electrodes onto or underneath the tube. The Landau-Büttiker formalism [74, 82] describes the

electrical current through a mesoscopic conductor connected to source (S) and drain (D) reservoirs as

$$I = \frac{e}{h} \int \mathrm{d}\epsilon [f_S - f_D] T(\epsilon) \tag{2.45}$$

with the Fermi-Dirac distribution $f_{S,D} = \frac{1}{1+e^(E-\mu_{S,D}/k_\mathrm{B}T)}$ and channel transmission probability T. Setting the electro-chemical potential in source and drain to $\mu_S := \mu_{SD}$ and $\mu_D := 0$, the conductance becomes

$$\begin{aligned} G(\mu_{SD}) &= e\frac{\partial I}{\partial \mu_{SD}} \\ &= \frac{e^2}{h} \int \mathrm{d}\epsilon F_T(\epsilon - \mu_{SD}) T(\epsilon) \end{aligned} \tag{2.46}$$

and the thermal broadening $F_T = \frac{\partial}{\partial \mu_{SD}} f_{SD}$. In the zero temperature limit, F_T becomes a δ-function and the expression for the conductance simplifies to

$$G(\mu_{SD}) = \frac{e^2}{h} T(\epsilon). \tag{2.47}$$

$\frac{e^2}{h} = \frac{1}{25.8\mathrm{k}\Omega}$ is then the quantum limit of conductance per channel. The total conductance is obtained by summing over all channels (or, named equivalently, electron energy levels) within the bias window μ_{SD}. The *quantum resistance* or *von Klitzing constant* of 25.8 kΩ per channel is fundamental cannot be overcome and is, in particular, not in contradiction to "loss-free" ballistic transport. For a short enough, defect-free section of a metallic SWCNT (so that transport is in the ballistic regime) at the Dirac point with four-fold level degeneracy (two from the K and K' branches in the dispersion relation times two for spin degeneracy) and full transparency to the electrodes ($T = 1$) per level, the maximum conductance is thus

$$G_\mathrm{max}^\mathrm{SWCNT} = 4\frac{e^2}{h} = \frac{1}{6.45\mathrm{k}\Omega}. \tag{2.48}$$

In the case of nearly perfect interface resistance of electrodes and a defect-free tube, propagating electron waves interfere like in a Fabry-Pérot interferometer [83] with the tube acting as coherent waveguide and the electrodes forming the resonant cavity. As the electonic probability density $|\Psi|^2$ is not localised over the tube section, the number of electrons in the tube is not fixed [74]. In the other extreme of high interface resistance and tunnel coupling between electrodes and nanotube, wave functions are localised on the dot and the number of electrons on the CNT section

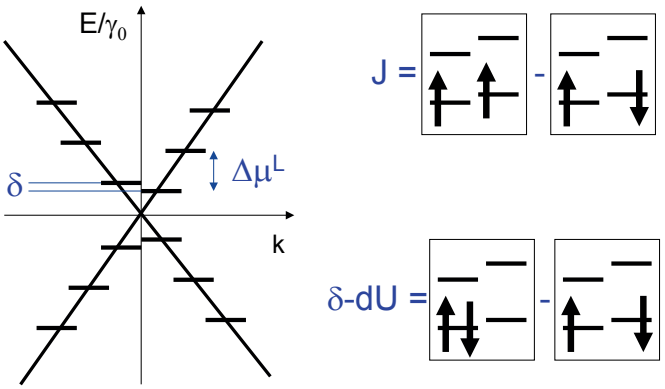

Figure 2.7: Corrections to fourfold energy level degeneracy in SWCNTs.

can be fixed. This allows to observe Coulomb blockade. Of particular interest is the lower resistance limit in the Coulomb blockade regime (typically $20 - 50\text{k}\Omega$) where the wave functions of electrodes and CNT still overlap but an electron number on the nanotube is reasonably well-defined. A typical feature of this regime are, e. g., Kondo effects (e. g. [70] or chapter C).

Corrections to four-fold level degeneracy

The four-fold level degeneracy of carbon nanotubes is somewhat idealising. To describe real CNT specimen more accurately, corrections to the spin and orbital degeneracies must often be included. Figure 2.7 sketches the typical light cone-shaped energy dispersion $E(k)$ of a quasi-metallic carbon nanotube near a K-point. Shown are corrections for the cases of one and two effective charges on a CNT-based quantum dot (the case of, e. g., 3 net excess electrons is equivalent to one excess hole; four electrons on the dot correspond to a filled shell and thus to zero effective charges).

For instance, there can be a mismatch δ between the orbital branches [84]. Another correction is due to electrostatic repulsion on the island (here the CNT-based quantum dot): double occupancy of one orbital level has an energy higher compared to single occupancy by an amount δU. Also, the total spin of (e. g.) two spin-$\frac{1}{2}$ electrons can take values $S = |s_1 - s_2|, |s_1 - s_2| + 1, ..., |s_1 + s_2| = 0, 1$, thus there is a singlet ($S = 0$, $S_z = 0$) and triplet ($S = 1$, $S_z = -1, 0, +1$). The triplet state can be higher in energy compared to the singlet state by an exchange energy term J, the singlet-triplet splitting. Taking into account the corrected dispersion, the addition energies $\Delta\mu_i^{add} = \Delta\mu^C + \Delta\mu_i^{QM}$ to for filling up the four states on a CNT-based

quantum dot then read

$$\Delta\mu_1 = \Delta\mu^C + dU + J \tag{2.49}$$

$$\Delta\mu_2 = \Delta\mu^C + \delta - dU \tag{2.50}$$

$$\Delta\mu_3 = \Delta\mu_1 \tag{2.51}$$

$$\Delta\mu_4 = \Delta\mu^C + \Delta\mu^L + \delta - dU \tag{2.52}$$

in zero magnetic field [84]. $\Delta\mu^C$ is the classical electrostatic charging energy. A typical mean magnitude of these corrections can be estimated to

$$\overline{\Delta\mu}^{QM} \approx 0.4\Delta\mu^L \tag{2.53}$$

in units of the length quantisation $\Delta\mu^L$ (see equation 2.44) from empiry (cf. [85], [86], chapter C). The above quantum corrections can be recognised in and evaluated from a stability diagram $dI/dV(V_{SD}, V_{gate})$ by a periods of four Coulomb diamonds. In each period, a medium Coulomb diamond ($\Delta\mu_2$) is flanked by two smaller ones ($\Delta\mu_1 \equiv \Delta\mu_3$). The three of them are be flanked by big diamonds ($\Delta\mu_0 \equiv \Delta\mu_4$). Exited states appear as additional lines features in the stability diagram.

Chapter 3

Fabricating a double quantum dot from a single-walled carbon nanotube

The notion of a *double quantum dot* is strictly speaking a idealising concept. The subject of this chapter is how this concept can be implemented in experiment. In particlar, an experimental procedure is presented to fabricate from a single wall carbon nanotube (section 3.1) a spintronics device (section 3.2) that can be electrically tuned (section 3.3) to behave like a double quantum dot at cryogenic temperatures.

Figure 3.1 shows a SEM micrograph of the SWCNT-based double quantum dot device; measurements on this sample are presented in the subsequent chapters. The sketch in figure 3.2 gives a step-by-step overview of how this sample was fabricated, starting with the synthesis of the carbon nanotubes (see figure 3.2 (a)).

3.1 Synthesis of SWCNTs

Carbon nanotubes can be synthesised by various methods [87, 88], e. g. by arc discharge [89], laser ablation [90] or chemical vapour deposition (CVD) [58]. CVD is the method of choice to grow individual, ultra-clean single-walled carbon nanotubes of high structural quality and to integrate them in standard fabrication of mesoscopic transistor devices on silicon substrates.
The CVD process was set up in the course of the work resulting in this thesis with technical support from the group of Herre van der Zant, and in particular by Benoit

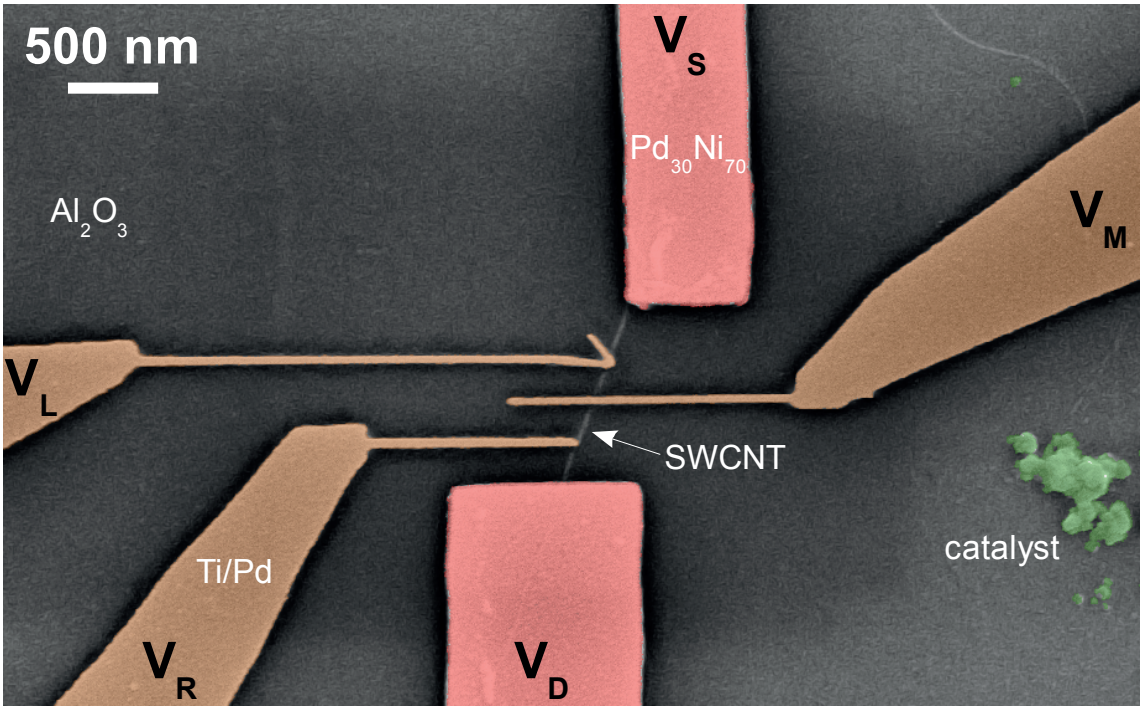

Figure 3.1: SEM image of the investigated CNT double quantum dot with ferromagnetic electrodes. Colourised are the left, middle and right top gates (V_L, V_M and V_R) defining and running the double quantum dot, the ferromagnetic source and drain electrodes (V_S and V_D) to bias the sample and the granular catalyst particles for CNT growth by CVD. For details refer to figure 3.2.

Witkamp, TU Delft. The exact growth parameter can vary strongly between individual experimental setups (compare e. g. [74]). Optimisation of our setup (see figure 3.3 (a)) yielded isolated carbon nanotubes of up to several hundreds of microns. Typical diameters of around 1 nm (see figure 3.3 (c)) indicate that SWCNTs are obtained (and no bundles, double- or multi-walled CNTs). The single shell structure of our tubes was also confirmed by difraction measurements in a transmission electron microscope (TEM) on suspended carbon nanotubes, performed by Christian Huber and in cooperation with the group of Josef Zweck, Universität Regensburg (for details refer to appendix B). A quality fingerprint for the structure of our home-grown SWCNTs is the observation of the typical four-fold periodicity in the Coulomb blockade stability diagram (see chapter C).

Our growth process is based on a recipe from reference [58]. Starting from a clean chip of p-doped Si wafer topped with 300 nm of insulating thermal silicon oxide, catalyst island of about 2 μm in diameter are patterned, by deposition from suspension onto a lithographically defined mask, where the CNTs are to grow. Subsequently, these samples are heated in a tubular furnace up the 900°C in an argon atmo-

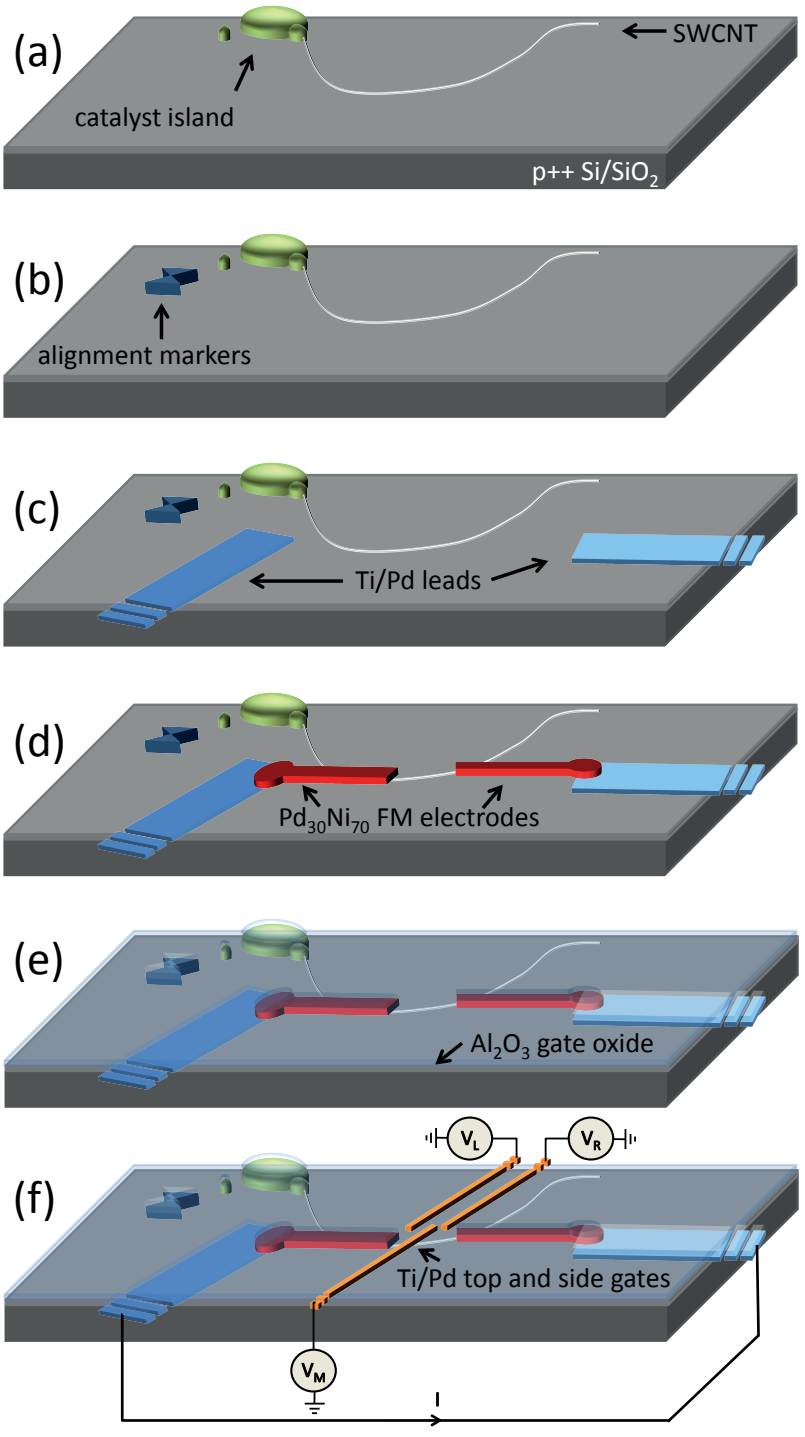

Figure 3.2: Sample fabrication step by step. (a) Electron Beam Lithography (EBL) patterning and deposition of catalyst granulat from suspension, then CVD growth of SWCNTs. The highly p-doped Si substrate topped with 300 nm thermal oxide can serve as a backgate. (b) EBL and metallisation of Ti/Pd (10 nm/40 nm) alignment markers. The tubes are then detected by SEM or AFM microscopy. Their position is recorded with respect to these markers for the subsequent lithography. (c) EBL patterning of on-chip Ti/Pd (10 nm/ 40 nm) leads and bonding pads with respect to the predefined markers. (d) EBL pattering the ferromagnetic $Pd_{30}Ni_{70}$ (45 nm) electrodes of different width onto tube and Pd leads with respect to markers defined in the previous process. (e) Atomic layer deposition (ALD) of an Al_2O_3 (20 nm) gate oxide layer over the entire sample surface, indicated by the semitransparent layer. (f) EBL patterning of Ti/Pd (10 nm/20 nm) top and side gate fingers with respect to markers defined in the $Pd_{30}Ni_{70}$ step. Consequently, the chip is glued into a chip carrier with conductive silver glue and bonded to the pins with and Al wire. The path of the electrical current I is indicated. Via the gate fingers electrostatic potentials V_L, V_M and V_R can be applied, defining and driving the double quantum dot.

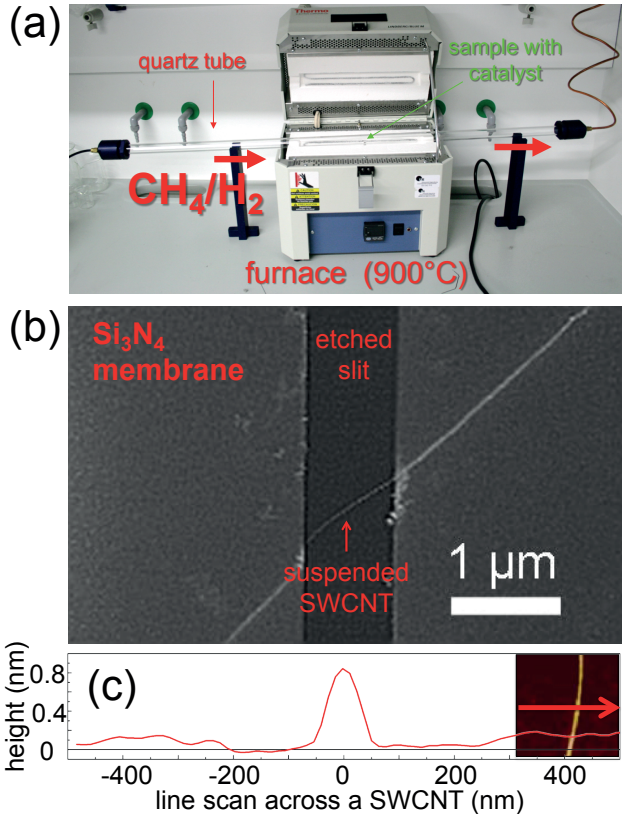

Figure 3.3: (a) Chemical Vapour Deposition (CVD) setp for SWCNT growth: methane is catalytically decomposed and assembled into a tubular, all carbon lattice. (b) SEM micrograph of a SWCNT suspended over a slit etched into a 50 nm thick silicon nitride membrane. (c) AFM height profile across to the length of a SWCNT. The height of about 0.8 nm provides a good estimate for the SWCNT diameter. Inset: AFM micrograph around the region of the line scan (indicated by the red arrow). Figure (c) is taken and adapted from [88].

sphere. The SWCNT growth is initiated by the supply of a carbon feedstock, in our case methane. The availability of isotopically very clean $^{12}CH_4$ (natural ratio $\approx 98.8\%$ [24]) or $^{13}CH_4$ provides an easy means to produce either ^{12}SWCNTs with net nuclear spin $I = 0$ or ^{13}SWCNTs with net nuclear spin $I = \frac{1}{2}$ [71].

Table 3.1: Composition of our catalyst for CVD growth of CNTs (after [58])

Ingredient (powder)	quantity	comment
$MoO_2(acac)_2$	4-10 mg (best 8.5 mg)	governs ammount of CNTs
$Fe(NO_3)_3.9H_2O$	40 mg	catalytically active ingredient
Al_2O_3	30 mg	mean particle size 14 nm
methanol	30 ml	sonicate mixture 30 min to suspend

Catalysed by the *catalyst nanoparticles* (see table A.1), methane decomposes and, via various C_xH_y precursors, builds up the tubular all-carbon lattice. The catalytically active ingredient are commonly feromagnetic nanoparticles like Ni, Co (e. g. [94]) or, as in the present case, Fe (cf. [58]) - or combinations of e. g. Fe and Co [91].

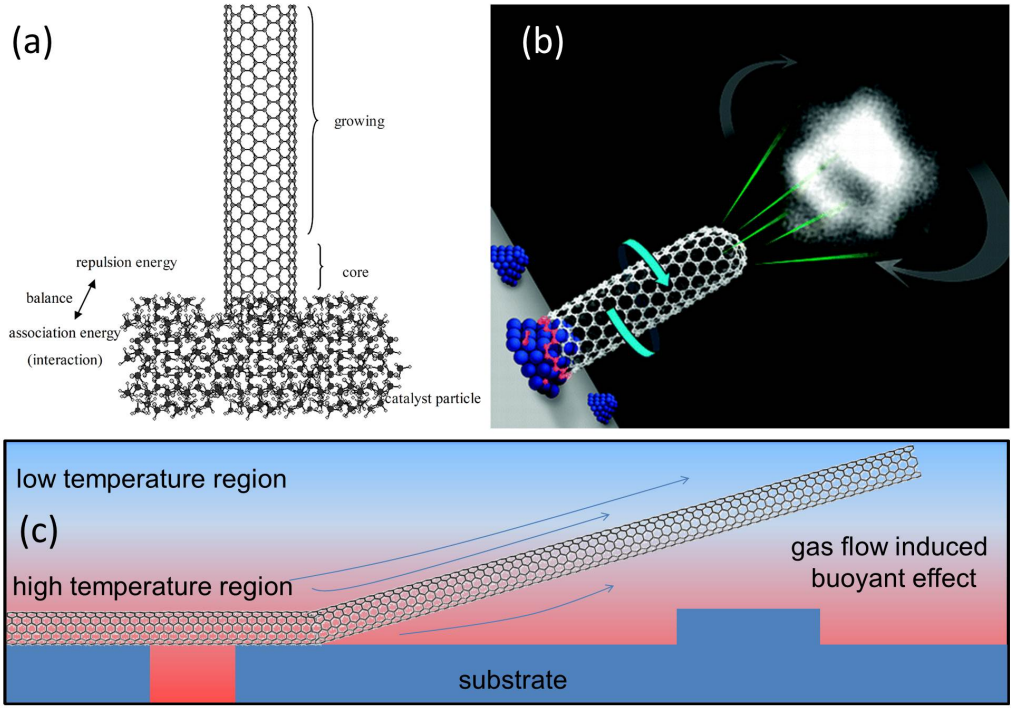

Figure 3.4: (a) Simple *bottom-up* growth mechanism of SWCNTs: the *core* is nucleated on the catalyst particles and supported against the distorted energy of sp^2 orbits. The diameter of the core is determined by balancing of energy in terms of size of catalyst particle, temperature, and the interaction between the catalyst and carbon atoms (caption text and figure from [91]). (b) Field emission microscopy (FEM) has directly revealed that SWCNT indeed grow out of the catalyst particles perpendicularly to the substrate surface; in particluar, FEM videos show how SWCNTs spiral about 15 times per minute around their own axis during their growth. One rotation has been related to the assembly of a single carbon dimer into the SWCNT lattice [92]. Figure taken from [92]. (c) The SWCNTs grow away from the substrate until they eventually fall and attach to the surface. Laminarising the process gas flow can align the SWCNT orientation on the substrate, which is convenient for many applications and scalability. Figure after [93].

The admixture of catalyst support substances such as MoO_2 and Al_2O_3 nanoparticles serves to effectively increase the surface area of the catalyst nanoparticles and enhances the yield of SWCNTs. The exact, pressure-dependent ratio of CH_4 and an additional H_2 is a crucial process parameter (cf. [93]). Oxygen contamination is especially detrimental, 'burning' the tubes. When the carbon feedstock is cut off after typically 10-15 min, the CNT growth is stopped.

According to one hypothesis, an individual tube grows vertically out of the catalyst particle (bottom-up growth) and more carbon atoms are absorbed into the catalyst and then built into the nanotube lattice while it floats in the gas stream (see

figure 3.4); as soon as it attaches to the SiO_2 surface, the strong *van-der-Waals* forces suppress the growth [95]. To give an experimental example of nanotubes growing while floating and then falling onto the substrate surface, figure 3.3 (b) shows a SWCNT suspended over slit. Recent progress [93] and current efforts in our group [88] have been made to prolong the time a CNT floats by laminarising the gas flow by means of ultralow gas flow and making use of a temperature gradient-induced bouyance effect. While CVD synthesis is a relatively inexpensive and conceptually straightforward process, its success depends very delicatly on the exact process parameters; few groups world-wide have achieved satisfactory results (e. g. [19, 54, 58, 63, 96, 97]). For process details refer to appendix A.

3.2 Device design and fabrication

A *quantum dot* can be produced from an individual carbon nanotube by mechanically or electrostatically defining a segment, with a length below typical coherence lengths. In the present case, this is achieved by simply fabricating two sufficiently (electrically) opaque electrodes onto the nanotube. The spacing these *source* and *drain* electrodes defines a 1.25 μm-long SWCNT segment (see figure 3.1). Additionally, they make the so-defined CNT-based quantum dot an electrically adressable device. The electrodes are defined by electron beam lithography (EBL). While not as scalable as optical lithography, EBL suits the need for versality in fundamental research to iteratively vary the design of prototype devices. The basic principle of EBL is to coat a piece of wafer material (here p-Si/300 nm-thick SiO_2) with a homogenous layer of long-chained polymere (here PMMA, vulgo plexiglass). In a negative process, a beam of electrons focussed on the scale of few nm can selectively fracture polymere chains. Shorter chains can be selectively removed due to their higher solubility in a suitable developer (here MIBK 1:3 propanol). In this way, a mask is defined on the wafer chip. For the technical principles of EBL refer to reference [98]. Metal films can be nanofabricated by evapourating a thin metal film on top of the EBL mask; the excess metal can be washed away together with the unfractured polymere chains (here lift-off with aceton) such that a metal film only remains where the metal attaches directly on the sample surface.

In order to make the device a transistor, gate electrodes are additionally required; they must be electrically insulated from the SWCNT. For operation as a single quantum dot transistor, the device can be gated via the highly p-doped Si substrate, where the 300 nm SiO_2 act as dielectric. For operation as a double quantum dot transistor, the device requires multiple gate electrodes that act locally on the

SWCNT segment.

Following figure 3.2, the fabrication steps are briefly presented.

Alignment markers (figure 3.2 (a))

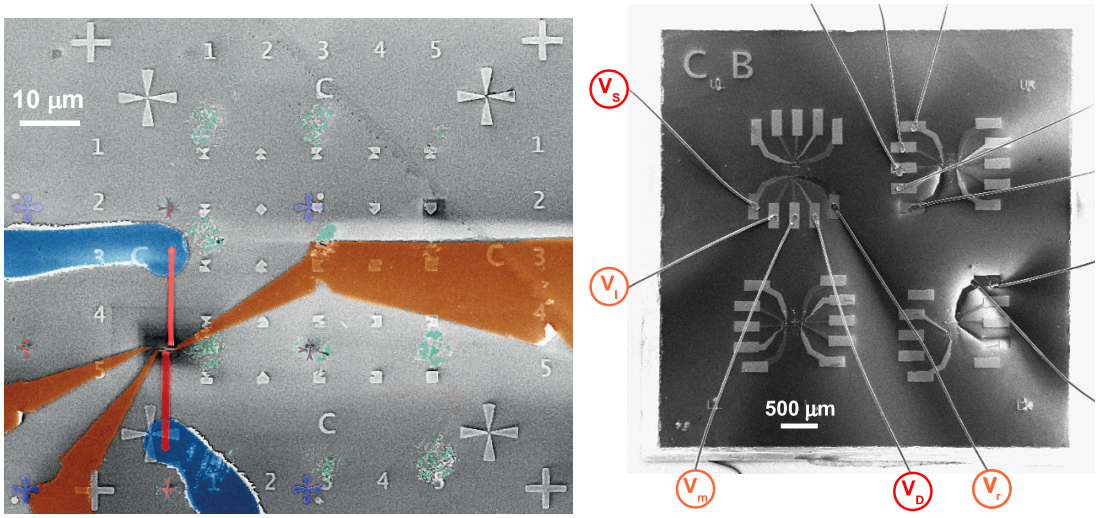

Figure 3.5: Larger SEM image of the investigated CNT double quantum dot with ferromagnetic electrodes and alignment marker field. Colourised are the left, middle and right top gates defining and running the double quantum dot, the ferromagnetic source and drain electrodes to bias the sample, the non-ferromagnetic leads and the granular catalyst dots for CNT growth by CVD.

The alignment marker layout was optimised for easy bookkeeping in mass production of multi-step SWCNT samples and to have as many tubes as possible on one chip during sample fabrication and crystate cool down to save work and measurement time. It has been taken up as a common standard within our nanotube subgroup. It follows the CVD process, despite of every lithography step entrailing contamination for the CNTs, because most metals melt in the hydrogen/methane atmossphere at 900°C, even much below their bulk melting point. on a double resist layer (200K/7%, 950K/2%) 40 nm of Pd for high SEM material contrast with a 10 nm Ti adhesion layer. Ti is used rather than Cr because Cr is near-ferromagnetic.
16 mm × 16 mm pieces are cut out of the 4” wafer, which are later cut into 16 4 mm × 4 mm samples that fit into the chip carriers of our cryostats, as sketched in figure 3.6. Big chips proved very work-efficient for up to the tricky CVD process and SWCNT detection, because one successful run yields a multitude of samples whereas the work is per sample and almost independent of sample size. For convenience, they

are by row and column from AA to DD. This label is written in the right corner to indicate the oreintation to the bare eye and to facilitate alignment to an external magnetic field. On Upper/Lower and Left/Right corners, big markers (UL, UR, LR, LL) allow adjustment to the stage coordinates and focus point of an SEM. As the markers are far the structures to be written in EBL, high charge doses can be applied for better accuracy at no risk of an overexposition. Each $4\,\mathrm{mm} \times 4\,\mathrm{mm}$ chip hosts four alignment crosses, labelled 11, 12, 21, 22 by row and coloumn, around which there are four alignment marker fields A, B, C, D, as shown in 3.5 (a). A field is structured by 5×5 alignment markers that fit into $2\ \mu\ \mathrm{m} \times 2\ \mu\mathrm{m}$ squares; the form of the top (bottom) part indicates the row (coloumn) such that position and orientation of a SWCNT can be read off unambiguously from only two markers, see figure 3.5 (a). This comes particularly handy on typically small-area AFM images given that beyond $20\ \mu\ \mathrm{m} \times 20\ \mu\,\mathrm{m}$ image area SWCNTs are hard to detect with a *digital instruments Nanoscope IIIa*.

Localising CNTs

Atomic Force Microscopy in tapping mode allows to detect SWCNTs and localise them with respect to alignment with very little contamination. The drawback of this method is the relatively time-consuming.

SEM is a more time-efficient method to localise SWCNTs. The principal problem is, however, that the electron beam contaminates the sample surface with a layer of amorphous carbon from residual carbon-containing gases in the SEM high vaccum chamber, as to be seen in figure 3.5 (a) as a blackened area where a zoom image of the active sample region has been taken. This problem can be solved conveniently by decreasing the accelleration voltage and distance from cathode to sample using the in-lense electron detector. These settings also enhance the SEM's topographical resolution. Best results have been obtained with cathode-sample distance of 5 mm and $0.5 - 1$ kV. As can be seen in figure 3.5 (a), SWCNTs can be seen on large scale images. Contamination is occurs only in the short space of time 1-2 s of the image scan and is reduced with decreasing voltage.

In SEM images the SWCNT appear, depending on the magnification and scan speed, about 8 times larger in diameter than on reference AFM pictures. This is because in fact not the tube itself appears in the low-kV SEM images, but its 'charge shadow' on the SiO_2 substrate. An indication for this is that the long SWCNT in figure 3.5 (b) has a darker charge contrast than the substrate in one section and a brighter one in the other.

Leads and bonding pads (figure 3.2 (c))

The outer leads are patterned near the individual CNT with respect to the predefined alignment markers, see figure 3.2 (c). On a 200K/7% PMMA mask, 40 nm of non-ferromagnetic, chemically inert Pd with a 10 nm Ti adhesion layer are deposited by e-gun evaporation.

Ferromagnetic source and drain electrodes (figure 3.2 (d))

The SWCNT is finally contacted and electrically connected to the leads in the third litography step (200K/7% PMMA mask) with 45 nm $Pd_{30}Ni_{70}$ after the CNT growth. To reduce contaminations, the alloy was fabricated by our supplier, *Mateck*, by inductive heating and without contact to the crucible. To rid the tube of adsorbates as to obtain a clean metal-CNT interface, the sample is pumped in a UHV chamber (low 10^{-8} mbar region) for at least 24 hours before metalisation. Their spoon-shaped form that is shown in figures 3.2 (d) and 3.5 (a) is intended to stabilise the magnetic switching, see section 4.2.3 for details. Both 16 μm in length, one ferromagnetic contact is, in the case of sample CB11C, 1250 nm, the other 800 nm in width in order to obtain a difference in the strips' coercive fields by form anistosopy. Our patterned $Pd_{30}Ni_{70}$ thin films has their magnetically easiest axis perpendicular inplane to its long side [99]. Because the external magnetic field should be aligned both in parallel to electrode easy axis and perpendicular SWCNT axis, to avoid orbital effects, electrode and tube are aligned as colinearly as possible. Because the accurate alignment of external field to ferromagnetic electrodes has priority for the purposes of the experiment, the electrodes are aligned to the chip (which can in turn be aligned to the magnet in the cryostat) rather than the tube. Also, given that the CNTs grow in random direction, no two devices could be precisely aligned on any one chip simultaneously.

Topping gate oxide (figure 3.2 (e))

Next, the entire sample surface is covered with 200 monolayers (corresponding to 20 nm) of Al_2O_3 that act as a dielectric for the topgates defining the double quantum dot. It is produced by atomic layer deposition (ALD): The ALD chamber is flooded with a pulse of water vapour which lubricates every (hydrophilic) surface. After a 5 s purge with N_2 (6.0, i. e. 99.9999% purity) a pulse of $Al(CH_3)_3$ that reacts with the water layer as

$$3H_2O + 2Al(CH_3)_3 \longrightarrow Al_2O_3 + 6CH_4, \tag{3.1}$$

forming a high quality monolayer of aluminum oxide per cycle. Following a recommendation of Prof. Peide Ye the purge time was chosen a short 5 s because

more purge time would tendentially imply more contamination owed to the high pressure ($2{\cdot}10^{-2}$ mbar) in our commercially available ALD chamber. Unlike with more extended graphene flakes this process can easily cover CNTs even if they are hydrophobic because they are thin enough to be overgrown laterally after few ALD cycles. A relatively high process temperature of 250°C was chosen for three reasons: First, film quality tends to improve with higher temperature, second, the sample was cleaned in neutral nitrogen atmosphere from adsorbates that could act as charge traps in later cryogenic experiments or dope the SWCNT, and third, it serves as an annealing step in a gas that does not chemically react with CNTs to enhance the electrical transparency of the $Pd_{30}Ni_{70}$-SWCNT interface.

Top gate fingers (figure 3.2 (f))

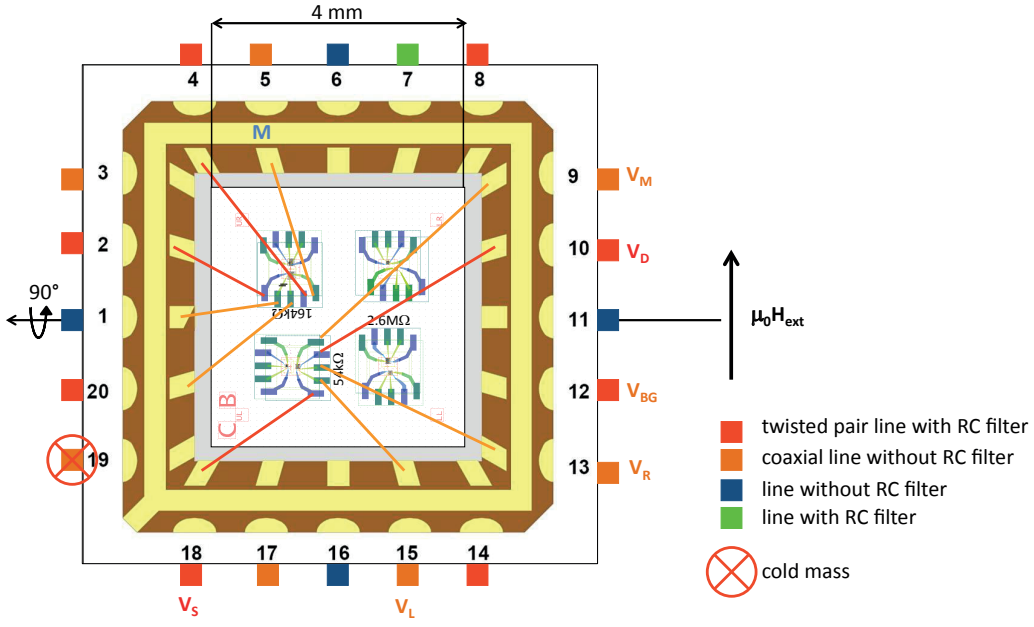

Figure 3.6: Sketch of chip carrier with bonded sample: The lines cryostat lines are labelled from 1 to 20. They are coloured to indicate their filtering scheme and use as source, drain (red font) or gate (orange font) electrode. Structures CB11C and CB12D are bonded. Room temperature 2-point resistances are indicated for three SWCNT spin valves.

Structuring the the top and side gates, as sketched in figure 3.2 (f), is the last of five lithograpy steps and the most delicate one.
A thin, more liquid resist (PMMA 200K/4% (75 nm)) was used to obtain a more homogenous resist layer. From dose tests, best results were obtained by writing the gate fingers as lines rather than rectangles with a dose of 4000 pC/cm and a

pixel spacing of 10 nm. Subsequently, a quite thin bilayer of 10 nm Ti/20 nm Pd was evaporated to facilitate the lift-off. Because these 30 nm metal thickness are difficult to bond on, the outer ponding pads were underlayed with Ti/Pd during the previous lithography of the leads(figure 3.2 (d)). With these settings, the lines become 39 nm wide strips after metallisation as measured by SEM. Dose values differed significantly for on Si/SiO_2 substrate versus Si/SiO_2 substrate with 20 nm Al_2O_3 topping layer.

Testing and interfacing to the cryostat

Subsequently, the samples are tested for promising resistance with a probe station at room temperature, then glued with conductive silver paste into a chip carrier (to connect the backgate), then bonded with an aluminum wire, connecting the bond pads to chip carrier pins, as sketched in figure 3.6. The chip carrier pins interface with the electrical lines of the crystat inset.

Post-experiments SEM-measuring of the sample

As carbon nanotubes can be contaminated (e. g. the electron beam can polymerise residual carbon in the UHV-SEM chamber) or structurally damaged. It is therefore recommendable to measure all relevant spacings after the transport experiments have been performed. The length of the carbon nanotube section between source and middle gate (middle gate to drain) define the size of the left (right) quantum dots:

$$L_l \approx 597 \text{ nm} \tag{3.2}$$

$$L_r \approx 659 \text{ nm} \tag{3.3}$$

as extracted from figure 3.1. Charge carries can be further confined electrostatically.

3.3 Setup for cryogenic transport measurements

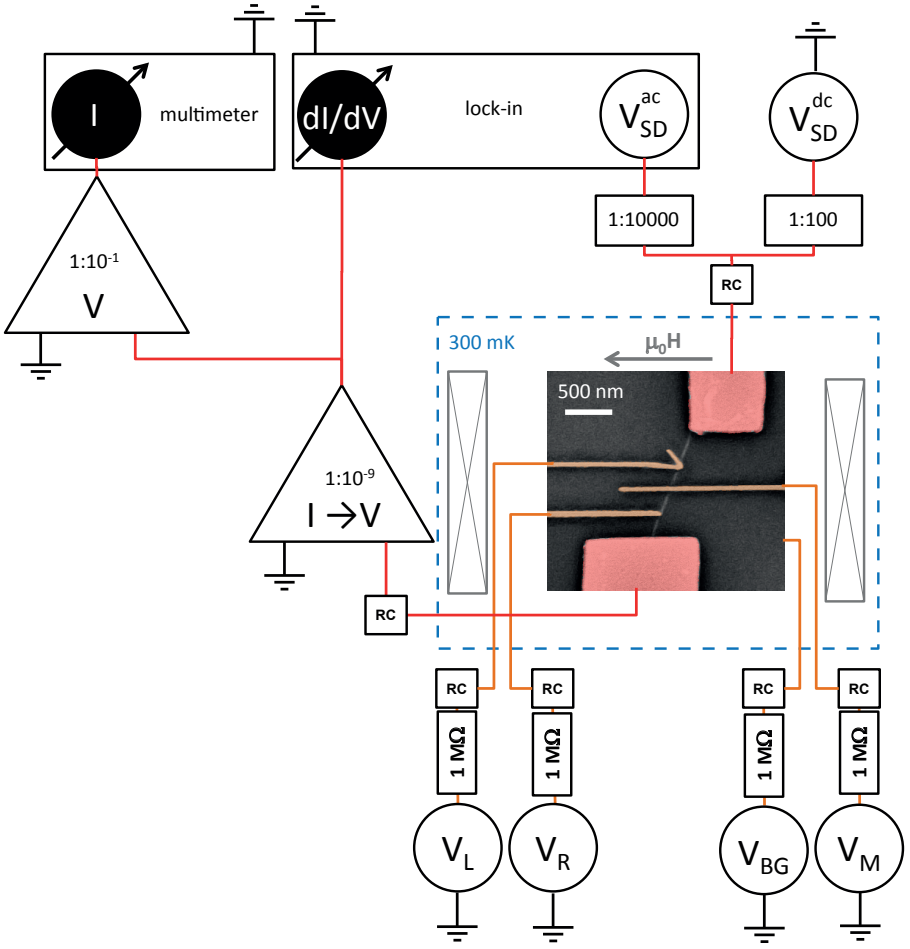

Figure 3.7: ACDC circuitry of double dot measurement setup: the ferromagnetic electrodes (coloured red in SEM micrograph) are biased at 300 mK with a superposition of a dc voltage and a small ac voltage, the sample's response is ampllified and both dc current and differental conductance are simultaneously protocolled as a function of dc bias, external magnetic field $\mu_0 H$ and gate voltages. The current path is marked with red connectors. The gate voltages are applied to the active sample region as indicated by the orange connectors.

Figure 3.7 sketches the circuitry of our cryogenic transport measurement setup of a SWCNT double dot with ferromagnetic contacts.
Measurements were performed in a ^{3}He cryostat with a bath temperature $T = 280$ mK $= 24\,\mu\text{eV}/k_\text{B}$. The elecron temperature was determined to $T = 431$ mK $= 37\,\mu\text{eV}/k_\text{B}$ from a zero bias Coulomb peak FMHW (cf. figure 6.4). Cryogenic temperatures are required because the sample temperature must be smaller than

the features of interest to be resolvable.
The ferromagnetic electrodes are biased with a dc voltage superposed with a small ac voltage (10 μV root mean square, 105 Hz). Ac and dc voltage are divided by appropriate, shielded voltage divider by a factor of 1:10000 and 1:100 respectively. All dc voltages, including the gate voltages, are applied by *Yokogawa 7651* voltage sources. The ac is excitation powered by a *Stanford Research Systems SR830* lock-in. All lines into the cryostate are filtered with low pass and π filters to atenuate noise. The sample's response is amplified by a current to voltage-converting *Ithaco* amplifier by a factor of 10^9 to 10^{10}. The differential conductance $\mathrm{d}I/\,\mathrm{d}V \equiv \frac{\mathrm{d}I^{dc}(V^{dc}_{SD})}{\mathrm{d}V^{dc}_{SD}} = \frac{I^{ac}(V^{dc}_{SD})}{V^{ac}_{SD}}$ is measured with standard lock-in techniques. The lock in intregration time time constant is set to 100 ms in order to comprise at least 10 oscillations of the 105 Hz excitation. The *Agilent 34420A* multimeter that measures the voltage equivalent to the dc current through the sample has a higher overload threshold than the lock-in amplifier and can therefore be additionally postampliflied by a *Stanford Research Systems SR560* voltage amplifier by a factor of 10. Its high input resistance of 10 GΩ also ensures that the lock-in operation is not disturbed by the simultaneous dc measurement.
The 1 MΩ resistors on the gate form, together with the capacitances in the lines, RC filters that significantly suppress the noise and enhance the resolution of the signal to the gate voltages, as monitored on an oscilloscope. The ground of all devices, voltage divider and cryostat are connected with copper cables to the house ground in a starlike grounding scheme to avoid parasitic signals. Likewise, every electrical consumer is plugged into insulating transformers rather than directly to the 50 Hz net. Substantial effort was invested in avoiding ground loops. For testing purposes during the setup of the experiment, the signals are piecewise, then jointly monitored on an oscilloscope. Only coaxial BNC cables are used and twisted together as to minimise the area between them to avoid magnetic inductances.
A magnetic field of up to 7 T has been applied by running a current through a superconducting coil around the sample powered by an *OXFORD Instruments IP 120-10* current supply. The sample was bonded and mounted into the cryostat such that the long side is in-plane perpendicular to the $Pd_{30}Ni_{70}$ electrodes, thus in-plane parallel to their magnetically easy axis. An in situ rotator allows to change the orientation by 90° of the magnetic field to out-of-plane with respect to the electrodes [100]. In this way, the effect of two magnetic field orientations can be studied in the same cooldown.

Chapter 4

Micromagnetic structure of ferromagnetic thin-film electrodes for SWCNT spin valves

This chapter presents an micromagnetic investigation [55, 101] of different thin-film evaporated ferromagnetic materials for their suitability as electrodes in individual single-wall and multi-wall carbon nanotube-based spin valve devices. Various electrode shapes made from permalloy ($Ni_{81}Fe_{19}$), the diluted ferromagnet PdFe, and PdFe/Fe bilayers are studied for both their micromagnetic properties and their contact formation to carbon nanotubes.
After section 4.1 has established some introductionary concepts, section 4.2 presents Lorentz microscopy investigations on the domain structure of varied thin-film ferromagnetic electrodes and their evolution while sweeping an external magnetic field. Varied parameters comprise different ferromagnetic materials and layer structures, with a focus on *Pd* alloys, electrode shape and temperature. This work was published in reference [55].

Pseudo spin valve geometry

A typical pseudo spin valve geometry is investigated, [57, 102–104] as shown in Fig. 4.1(a) for a multi-wall carbon nanotube (MWCNT) and in (b) for a single-wall carbon nanotube (SWCNT). Two ferromagnetic electrodes F1 and F2 are designed such that they have a different coercive field. This is achieved here by making use of shape anisotropy, which can be tuned via the sample geometry. In magnetoresistance measurements, a sufficiently large external magnetic field is applied to saturate and align the magnetisation of both contacts in parallel to it. A magnetic field sweep to opposite field direction will first switch the magnetisation of the contact with smaller

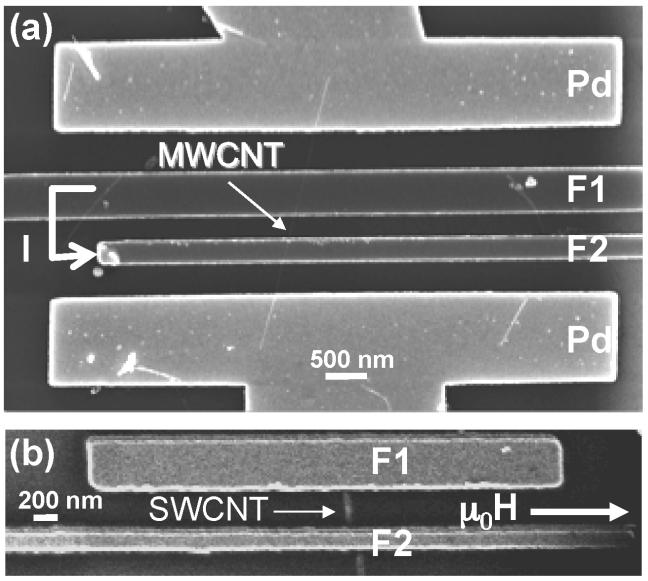

Figure 4.1: (a) Scanning electron microscopy (SEM) image of a multiwall carbon nanotube (MWCNT) contacted by two ferromagnetic electrodes, forming a pseudo-spin valve device. The electrodes F1 and F2 are fabricated from permalloy (Py, or $Ni_{81}Fe_{19}$); in addition two non-ferromagnetic Pd electrodes to allow four-terminal measurements are shown. (b) SEM image of a single-wall carbon nanotube (SWCNT) contacted by two ferromagnetic electrodes F1 and F2 made from the dilute ferromagnet $Pd_{60}Fe_{40}$. An arrow indicates the direction of an externally applied magnetic field. Because of shape anitrosopy, the different electrode aspect ratios result in a differing coercive field.

coercive field, thereby achieving antiparallel configuration, and then the magnetisation of the second, resulting in a parallel configuration with polarity opposite to the initial one.

Requirement profile of ferromagnetic electrodes in carbon nanotube-based spintronics devices

This work aims at an improvement of the switching properties of the ferromagnetic electrodes, i. e. obtaining reliable reversal of the magnetisation at reproducible coercive field values, with a focus on PdFe alloys. Simultaneously, the electrical interface quality from ferromagnet to nanotube is considered, including low-temperature magnetotransport measurements. Here, reliable control of magnetic switching is of particular importance as there are no direct means to check the magnetic domain structure once the sample is mounted in a cryostat for transport measurements.

4.1 Theoretical prerequisites for ferromagnetic contacts

This section motivates the following experiments with some relevant theoretical prerequisits and concepts.

4.1.1 Magnetostatics: ferromagnetism and form anisotropy

Origin of ferromagnetism in transition metals

The permanent magnetic moment in $3d$ transition metals stems from the spatial distribution of the $3d$ orbitals. Their density of states $D_F^{3d}(\vec{k})$ deviates much from the spherical distribution of a free electron gas, giving the spins orientation. Occupying the electronic orbitals following *Hund's rule*, the *majority spins* (those making up for the net magnetisation of the solid) are below Fermi energy and are thus assumed not to contribute to transport; they are effectively screened by the energetically higher orbitals scattering events.

Exchange Energy

From this exchange symmetry together with the Coulomb interaction arises, in the Heisenberg model, an additional term in the Hamiltonian the *exchange energy*:

$$H = -2\sum_{i,j} J_{ij}\vec{s}_i \cdot \vec{s}_j \tag{4.1}$$

In a external magnetic field this becomes

$$H = -2\sum_{i,j} J_{ij}\vec{s}_i \cdot \vec{s}_j - \sum_i \mu_B \vec{s}_i \cdot \vec{B}_{ext} \tag{4.2}$$

Depending on the sign of the coupling constant J, the system is in the

- $J > 0$: ferromagnetic phase
- $J < 0$: antiferromagnetic phase
- $J \propto R_{ij}\cos(R_{ij})$: spin glass phase, RKKY interaction, occurring e. g. in dilute ferromagnets.

The exchange lifts the degeneracy of the two spin orientations in the density of states. As to be seen in fig. 4.3, the density of states for the minority spins are the majority spins shifted by the exchange energy. This is important to spin injection

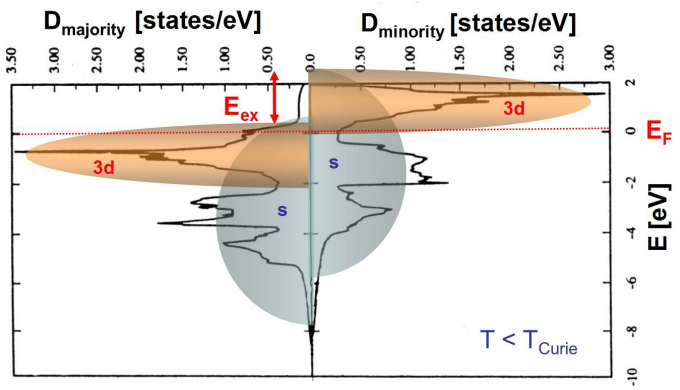

Figure 4.2: Schematic density of states (DoS) of a transition metal. The minority spin DoS is shifted against the majority DoS by the exchange energy. The underlying graph is a DFT calculation of the DoS for Fe from [105]. $3d$ and s orbital DoSs are highlighted by colour.

experiments; a high exchange energy yields a high spin polarisation P at Fermi energy, given by:

$$P_F(E_F) := \left| \frac{D_\uparrow(E_F) - D_\downarrow(E_F)}{D_\uparrow(E_F) + D_\downarrow(E_F)} \right| \tag{4.3}$$

A high P_F is important when injecting a spin-polarised current into a non-ferromagnetic conductor because the spin polarisation will decay exponentially with the mean spin flip length l_s over the sample length L like $P_N = P_F e^{-\frac{l_s}{L}}$. This suggests that either a ferromagnet with strong exchange coupling, as Fe, or a non-ferromagnetic material with long l_s, as carbon nanotubes, should be chosen - or both, as in the case of this work. Ref. [106] offers a detailed discussion of spin polarisation in ballistic and diffusive conductors.

Magnetisation and spin valves

Expressing the effective interaction of the microscopic magnets, the spins, by a mean field, the Hamiltonian spells

$$H = -\sum_i \mu_B \vec{s}_i \cdot (\vec{B}_{ext} + \vec{B}_m) \tag{4.4}$$

leading to an expression for the free energy

$$F(T, H) = U - TS - MH \tag{4.5}$$

where the magnetisation is the canonical force of the magnetic field

$$M(T, H) = -(\frac{\partial F}{\partial H})_T. \tag{4.6}$$

Minimizing a ferromagnet's free energy $F(T, H) = F(T, H, M(T, H)) \propto (T - T_C)M^2 + \mathcal{O}(M^4)$ at $H = 0$ with respect to the magnetisation, which, in the language of the

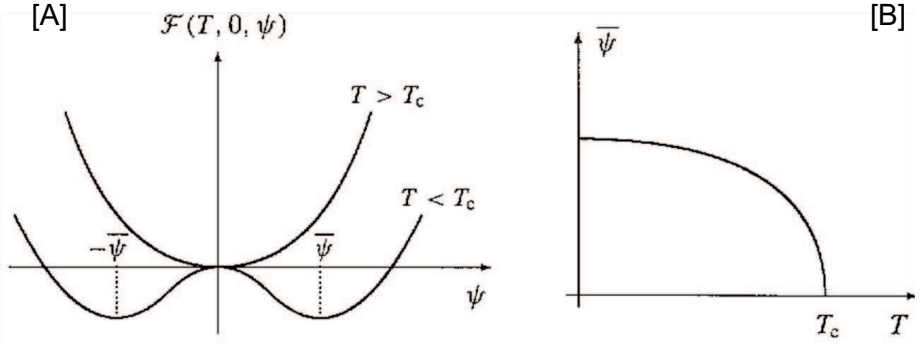

Figure 4.3: Landau theory of phase transitions: [A] Free energy as function of the order parameter $\Psi \equiv M(T, H)$ at zero external field H. The equilibrium value $\overline{\Psi}$ (here the remanent magnetisation M_s) is obtained by minimizing F. [B] A slice out of the 'full phase diagram fig. 4.4 at $H = 0$. From [69].

Landau formalism, is the order parameter of the systems phase transition, a spontaneous magnetisation M_S is found, which describes the permanent magnetic moment of e.g. Fe. Above a certain temperature, the Curie temperature T_C, this effect 'drowns in thermal disorder', i.e. entropy S. A full phase diagram is shown in figure 4.4. As $M(T)$ is continuous, this is a phase transition of second order from ferro- to paramagnetism. $M(T, H)$ will be measured for ferromagnetic PdFe strips in section 4.3.1 as function of T (Curie temperature measurements) and H (magnetic hysteresis measurements).

Via $k_\mathrm{B}T_C \approx E_{ex} = \mu_B B_{ex}$ an estimate for the (enormous) ferromagnetic exchange fields can be made, see table 4.1.

Table 4.1: Estimate for exchange fields in Fe, Ni and Co (from [108])

Metal	T_C [K]	$k_\mathrm{B}T_C$ [meV]	B_{ex} [T]
Fe	1043	89.907	1552.79
Ni	631	54.392	939.42
Co	1393	120.077	2073.86

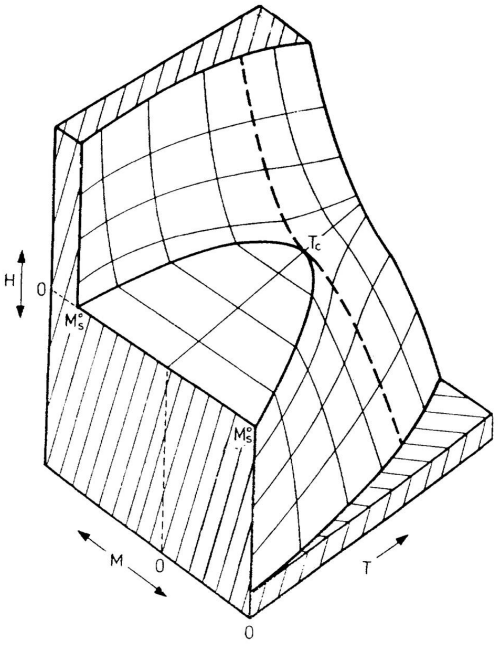

Figure 4.4: Schematic phase diagram of an idealised ferromagnet. At $T = T_C$ there is a phase transition of second order (M(T) is continuous). At M_s, the magnetic susceptibility $\xi := -(\frac{\partial^2 F}{\partial H^2})_T = (\frac{\partial M}{\partial H})_T$ diverges (phase transition of first order), corresponding to an infinitely sharp switching of the magnetisation in an increasing magnetic field. Real metals have finite ξ, as will be seen in section 4.3.1. From [107].

Crystal and form anisotropy

Depending on the crystalline symmetry, the magnetisation can be different in different direction, i.e. the magnetic moment matrix has, in orthonormal coordinates, different matrix elements. The directions corresponding to the smallest matrix element is called *magnetically easy axis* and the other (in 3D) two *magnetically hard axes*. In these experiments, crystalline anisotropy is negligible because the evaporated PdFe has a granular structure.

The orientation of the magnetization depends also on the form of, e.g., a ferromagnetic contact strip. The magnetic surface quasi-charges of the strip will create a stray field $\vec{H}_{stray}$. The reaction of the magnetic moments to their own stray field H_{stray} is a demagnetizing field within the strip, $\vec{H}_d$. In their own stray field, the magnetic moments have a total energy

$$E_{stray} = \frac{1}{2} \int dV \vec{M} \cdot \vec{H}_d \tag{4.7}$$

The magnetically easy axis of a strip is expected to lie within the sample plane parallel to its long axis. Section 4.3.2 will be checking this for the PdFe strips used in this work.

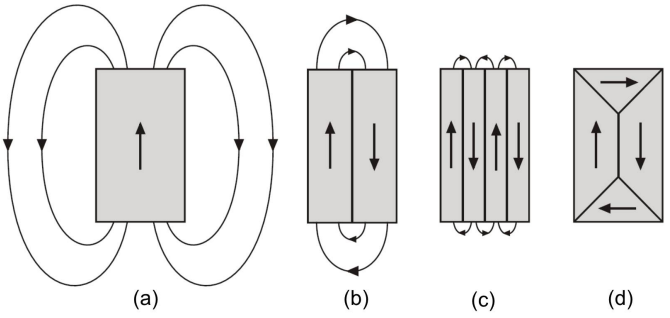

Figure 4.5: (a)-(d) Counting the number of stray field lines gives a notion how high the stray field energy of a domain configuration is (the more the higher). (d) The lowest, *Landau-Lifshitz* configuration with respect to stray field energy (but not necessarily w.r.t. minimizing the total energy). From [109]

.

Magnetic domains

A ferromagnetic solid is in a single or many domain configuration depending on what is energetically more favourable. The magnetic moments will adopt a configuration that minimises the sum of $E_{ex} + E_{stray}$ (see fig. 4.5) plus possibly a Zeeman energy $E_Z = -\mu_0 \int dV \vec{M} \cdot \vec{H}_{ext}$ (see fig. 4.6).
A deeper discussion, also taking into account corrections to this continuum model for the case of thin layers and interface anisotropy, is found in reference [105].

4.1.2 Magnetotransport: spintronics

The discoveries of giant magnetoresistance and tunnelling magnetoresistance in metallic spin valves have revolutionised applications such as magnetic recording and memory, and launched the new field of spin electronics or *spintronics*.

A *lateral spin valve*, which shall be investigated here, is a layered structure of magnetic and non-magnetic (spacer) materials whose electrical resistance depends on the spin state of electrons passing through the device and so can be controlled by an external magnetic field. The underlying magnetoresistive effect is the *tunnelling magnetoresistance* (TMR, in the case of tunnel contacts, the case of section 2.2.1) or the *giant magnetoresistance* (GMR, in the case of transparent contacts, the case of section 2.2.3) or something in between, as the two effects are in principle the same.

Additional magnetoresistive effects may account for a *background magnetoresistance* like *negative magnetoresistance* (NMR, for the CNT see section 2.3.2), Kondo effect or zero bias anomalies. In the contacts, anisotropic magnetoresistance may occur.

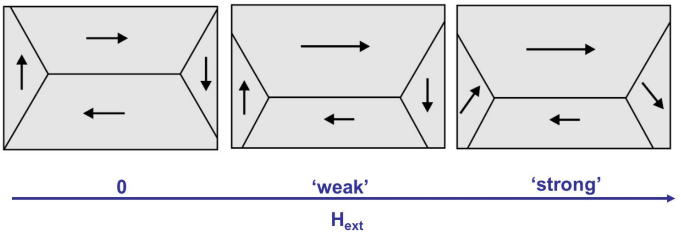

Figure 4.6: $H_{ext} = 0$: An unmagnetised sample. $H_{ext} = low$: The domain walls start moving. On a mesoscopic scale, some are growing at the expense of others; microscopically, some spins flip. $H_{ext} = strong$: Every domain gradually rotates into the direction of the external field. Adapted from [110].

GMR The giant magnetoresistance is observed in two ferromagnetic conductors separated by a thin non-ferromagnetic, normal-conducting layer where 'thin' stands for the condition that conductance electrons (at Fermi energy) pass through this layer without being scattered [106].
Spin valves made from only one ferromagnetic material use form anisotropy; when choosing different aspect ratios for two magnetic contacts $F1$ and $F2$ of the same granular material (here PdFe), the two contacts will have different coercive fields.

This allows to control the relative magnetisation configuration of the two ferromagnetic contacts $\{\vec{M}_{F1}, \vec{M}_{F2}\} \in \{\uparrow\uparrow, \uparrow\downarrow, \downarrow\uparrow, \uparrow\uparrow\}$ from parallel ('ferromagnetic coupling') to antiparallel ('antiferromagnetic coupling') by means of an external magnetic field. The GMR is defined as the difference in resistance between parallel and antiparallel configuration in units of the parallel case resistance.

$$GMR := \frac{R_{\uparrow\downarrow} - R_{\uparrow\uparrow}}{R_{\uparrow\uparrow}} \tag{4.8}$$

TMR The tunnelling magneto resistance is defined analogously to the GMR:

$$TMR := \frac{R_{\uparrow\downarrow} - R_{\uparrow\uparrow}}{R_{\uparrow\uparrow}} \tag{4.9}$$

The basic setup is similar to the one of the GMR: If the non-ferromagnetic layer is insulating and still 'thin' in the sense that conduction electrons can cross this tunnel barrier without undergoing scattering events the tunnel magnetoresistance (TMR) is observed. This most basic setup is readily expanded by replacing the single insulating layers by two insulating layer with a conductor in between, e.g. a carbon nanotube. Experimental implementations of this tunnel barriers are e.g. thin oxide layers - or the not totally transparent contact at a metal-CNT interface.

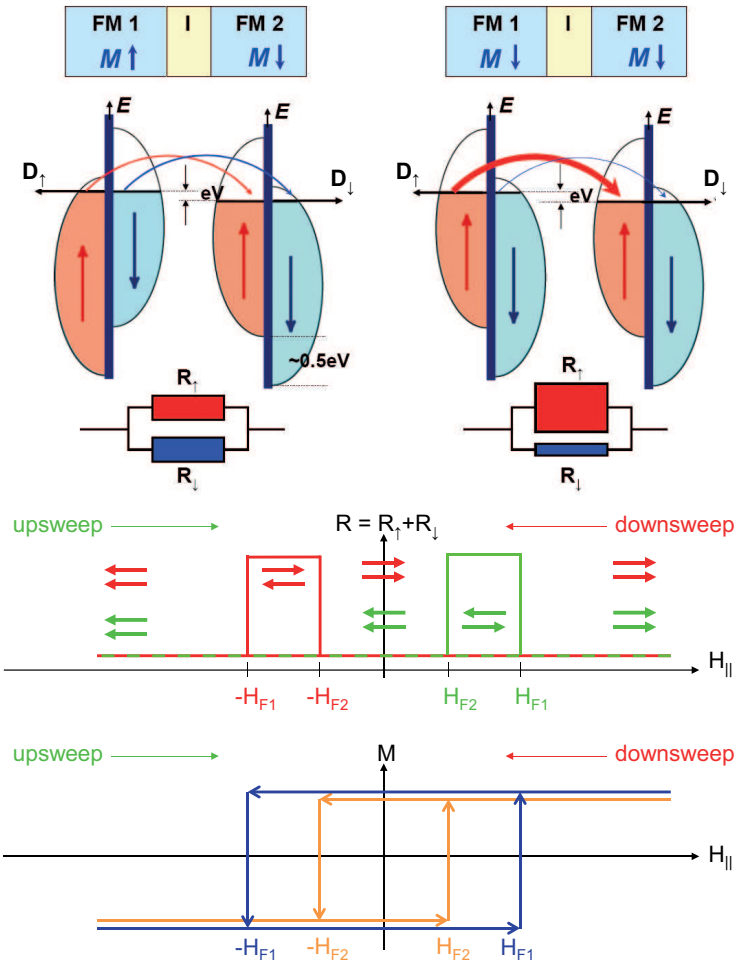

Figure 4.7: Tunnelling magnetoresistance (TMR): Magnetic field dependence in alignment of ferromagnetic source and drain electrode $FM1$ and $FM2$ magnetisation orientations, densities of state, resistance and magnetisation. Both the resistance R and mangetisation M are hysteretical w. r. t. the sweep direction of the magnetic field $\mu_0 H$. Partly from [106].

Electrons can tunnel through these insulating layer between the two ferromagnetic (FM) contacts. For a given source drain voltage, the tunnel current depends on the relative orientation of the FM contacts. This relative orientation can be controlled by an external magnetic field $\vec{H} = \mu_0 \vec{B}$. Thus, the conductance (and equivalently its inverse, the resistance) depends on $\vec{H}$.

The Jullière model provides an easy description of the tunnelling conductivity in F-I-F-junctions based on the following assumptions:

1. No spin-changing scattering events occur in the tunnelling process. Resistance depends on the tunnel probability for spin down and spin up separately.

2. The tunnel probability is proportional to the density of occupied states in the source close to Fermi level times the density of unoccupied states in the drain below Fermi level.

These two non-interacting spin channels can be pictured as two resistors in parallel (see fig. 4.7). In parallel configuration, one spin orientation is in majority in both source and drain, the other in minority. This corresponds to a small and a big resistor in parallel, thus a small resistor. In antiparallel configuration, however, both spin orientations are in majority in the source (drain) and in minority in the drain (source). This corresponds to two comparable, intermediate resistors, thus a higher resistance than in the parallel case.

AMR The anisotropic magnetoresistance (AMR) is a low-field effect occuring in ferromagnetic materials. Due to spin-orbit interaction the conductivity depends on the angle ϕ between current $\vec{I}$ and magnetisation $\vec{M}$ [106]. The AMR can be described with

$$\rho = \frac{\rho_{\parallel} + \rho_{\perp}}{2} + (\rho_{\parallel} + \rho_{\perp})(cos^2\phi - \frac{1}{2}) \tag{4.10}$$

Its effect in an $R(B)$ plot is thus symmetric and non-hysteretic.

4.2 Lorentz microscopy on the micromagnetic domain structure of various ferromagnetic electrode designs

For carbon nanotube magnetotransport experiments, the ferromagnetic contact electrodes are required to have a difference in coercive field large enough to be resolvable in transport measurements, e.g. 10 mT or more. A second requirement for reliable and reproducible magnetic switching is that the segment of the electrode contacting the carbon nanotube be in a well-defined single domain state to allow experimental control over injecting a spin-polarized current. Transmission electron microscopy (TEM) in Lorentz microscopy mode provides a powerful tool to investigate these properties of thin ferromagnetic films.

4.2.1 Methods

Lorentz microscopy [111–113] allows direct observation of the magnetic domain structure of a ferromagnetic structure and its evolution in an external magnetic field by sending a parallel (out of focus) electron beam through a magnetic specimen. The deflection of the beam due to the Lorentz force can be visualized by defocusing the objective lens. At the walls enclosing a magnetic domain, the electrons are deflected as they transverse the ferromagnetic film and form either a convergent or a

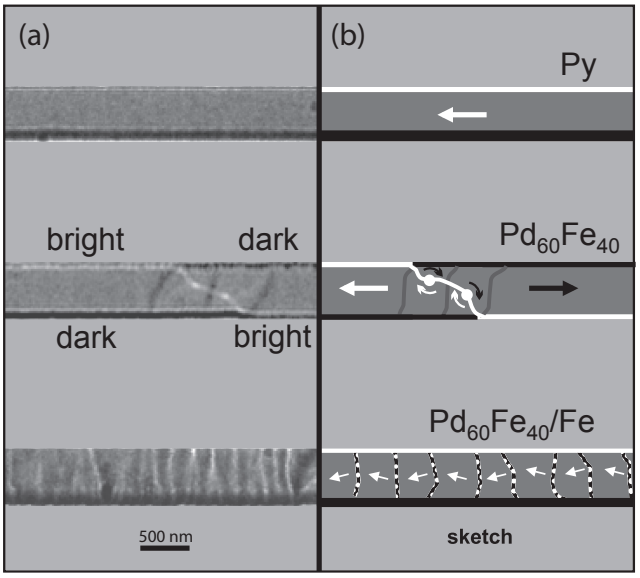

Figure 4.8: (a) Comparison of Lorentz microscopy images of rectangular electrodes made from different ferromagnetic materials. An external magnetic field is tuned close to the coercive field. All strips have lateral dimensions of 500 nm × 16 μm; the film thickness is 45 nm. (b) Sketch pointing out the observed micromagnetic features. The magnetisation direction (big black and white arrows) can be be determined by the position of the dark and bright contrast. Solid black and white lines, as seen in the $Pd_{60}Fe_{40}$ strip, are caused by magnetic domain walls with full magnetisation reversal. Cross-tie domain walls (grey lines) enclose a magnetic vortex (white dot with curved white and black arrows). Weak contrast lines, drawn dotted in the sketch, correspond to ripple domain walls with only small changes in magnetisation direction (small white arrows).

divergent set of partial electron waves. Correspondingly, an increase or a decrease of the electron beam intensity is detected at the location of domain walls. It should be noted that not only domain walls but also other variations in the magnetic induction within the specimen can be visualized by this technique.

If the specimen is magnetized homogeneously, every transmitted electron will be deflected to the same side. In this case, a brightly contrasted feature forms on the edge of the specimen where the deflected beam through it overlaps with the undeflected beam passing next to it. On the opposite side, the deflection of the electrons will partially deplete the edge region which manifests in a dark contrast line on the detector. These dark and bright contrast features can, for instance, be seen within the permalloy strip shown in the topmost panel of Fig. 4.8. Magnetic domain walls, where spins oppose each other in frustration, appear as dark or bright features within the strip area (see middle panel of Fig. 4.8). A detailed discussion of Fig. 4.8 will be given below.

Driving the electron beam focus from above to below the sample plane reverses the Lorentz-force induced contrast, providing a consistency test as to whether observed features are indeed of magnetic origin. A magnetisation reversal due to an external magnetic field can be detected by observing subsequent images during a field sweep when a structure's edge contrast is inverted. Note that on the borders of the observed ferromagnetic structures, the dark Lorentz contrast appears more pronounced than the bright one. This is partly owed to a superposition with a bright contrast all around the observed structures stemming from Fresnel edge diffraction. The magnetisation structure can therefore be read off most clearly by tracing structures of dark edge contrast.

In the TEM used for the work at hand, an external magnetic field $\mu_0 H$ can be applied only in parallel to the electron beam, i. e. perpendicular to the sample plane. An in-plane field component $\mu_0 H_{||} = \mu_0 H \sin\alpha$ with respect to the sample plane can be tuned by maintaining this field at constant magnitude and tilting the sample by an angle α. At a maximum tilt angle of $\pm 25°$, the in-plane component reaches about half the value of the out-of-plane component. Rotating the sample and thereby sweeping the in-plane field from saturation through zero field to saturation in opposite direction allows to monitor the magnetisation reversal process of the ferromagnetic specimen.

Electron transmission microscopy requires samples to be prepared on a grid or thin film membrane with low electron beam contrast. The metal test structures were patterned by electron beam lithography (EBL) and thermally evaporated in vacuum onto 50 nm thin low-stress PECVD silicon nitride membranes. Owing to shape anisotropy, Néel walls, i. e. with the frustrated spins being confined to the film plane, occur in sufficiently thin ferromagnetic films. Above a material-specific thickness, which is smaller for weaker magnetisation, Bloch walls dominate. Here, the spins form domain walls by gradually turning out of the film plane. According to our experience, the threshold thickness of permalloy (Py, $Ni_{81}Fe_{19}$) films is about 50 nm. The film thickness is therefore kept below that value. Also the large aspect ratio of film thickness compared to the lateral electrode dimensions is expected to favour an in-plane orientation of the magnetisation. [114] The discussion therefore starts with the effect of this in-plane magnetic field component. In any case, effects of magnetisation and magnetic field components parallel to the electron beam are not imaged in Lorentz microscopy, due to the cross product in the Lorentz force.

4.2.2 Material dependence of the magnetic domain structure

The investigated materials are chosen for their magnetic properties or expected contact transparency to carbon nanotubes. Permalloy (Py, $Ni_{81}Fe_{19}$) is considered and the giant paramagnet Pd diluted with Fe; the expectation was that diluted ferromagnetic PdFe alloys combine the benefits of the strong ferromagnetism of iron and the transparent contacts of palladium-carbon nanotube interfaces. [115, 116] The composition of the PdFe alloy is adjusted by setting the evaporation rates from two confocal thermal evaporation sources appropriately. In addition, magnetic bilayer structures with 10 nm of $Pd_{60}Fe_{40}$ and a 35 nm-thick Fe layer – to stabilize the magnetisation of the magnetically soft PdFe by the magnetically hard Fe – are discussed. To prevent the iron from oxidation and for improved interface resistance with the Pd leads, these bilayers were additionally capped with 5 nm of Pd.
In figure 4.8 (a), rectangular strips of equal dimensions made from these three polycrystalline materials are compared. To allow comparison of the domain structure in different ferromagnets, the Lorentz microscopy images are taken at the field values close to magnetisation reversal in the specific material. Consider first the central segment of the strip, where the contacted carbon nanotube would be placed in transport measurements. The majority spin orientation and magnetic domain structure of this portion determines spin orientation and polarisation of an injected current. The sketches of figure 4.8 (b) point out the relevant magnetic features of the Lorentz images.

Permalloy

Permalloy (Py alias $Ni_{81}Fe_{19}$) was a chosen as a ferromagnetic material for its high magnetic permeability, low coercive field, and large magnetic anisotropy. [114, 117, 118] From the homogeneity of the entire Py strip in figure 4.8 (a) it can be concluded that the observed segment is in a single domain state. In the Lorentz image the magnetic domain appears bordered by a continuous bright contrast line on the top side and a dark one on the bottom side. The corresponding arrow in figure 4.8 (b) symbolizes this uniform magnetisation orientation of the single domain. Note that the absolute direction of the magnetisation can only be determined from the dynamics during a full magnetic sweep by comparing subsequent Lorentz images.

PdFe alloy

In contrast to Py, the $Pd_{60}Fe_{40}$ strip segment in figure 4.8 (a) is in a two-domain state at a small field increase beyond magnetisation reversal but not yet saturated.

The black and white arrows in the sketch of Fig. 4.8(b) highlight the opposite magnetisation orientation of the domains. The border contrast changes from bright to dark where the sharp white line connects to the strip boundary. In addition, three dark-contrasted, roughly parallel lines can be made out crossing the bright line. Such so-called cross-tie wall structures are typical for samples between Néel and Bloch phase [114] where a successive row of in-plane (Néel) and out-of-plane (Bloch) type walls occurs. For our polycrystalline specimen, a vanishing crystalline anisotropy is expected, so the magnetic dipolar (or shape) anisotropy is dominant. Due to the small magnetisation of $Pd_{60}Fe_{40}$ compared to stronger ferromagnetic materials, also the shape anisotropy is small. This means that even low magnetic fields perpendicular to the film can lead to relatively large normal components M_z of magnetisation. In any case, magnetic multi-domain and cross-tie wall configurations of the $Pd_{60}Fe_{40}$ strip render its magnetisation configuration ill-defined for the operation of a CNT pseudo spin-valve. Furthermore, the specific domain wall pattern is often different for any two magnetic sweeps. Occurrence of magnetoresistance in a pseudo spin valve fabricated from this material is therefore prone to a random domain configuration and the position of magnetic pinning centers.

PdFe alloy with a Fe magnetisation stabilisation layer

The $Pd_{60}Fe_{40}$/Fe bilayer strips display a more uniform overall magnetisation, as indicated by a continuous dark, respectively bright, contrast along the entire borderlines of the strip. In addition, a fine structure appears in figure 4.8 (a), which signals the presence of ripple domains, i.e. areas in which the spins deviate from the overall magnetisation direction by a small angle as sketched in the bottom structure of figure 4.8 (b). The formation of ripple domains is a well-known phenomenon for thin film materials with a high saturation magnetisation like Fe, [114] suggesting that the Fe layer dominates the magnetic properties of the strip.
Figure 4.9 compares the switching behaviour of $Pd_{60}Fe_{40}$/Fe and Py strips of equal lateral dimension and total thickness of 45 nm. While the $Pd_{60}Fe_{40}$/Fe magnetic bilayer switches at higher fields than permalloy, it does so with a much higher margin of error.

4.2.3 Shape dependence of the coercive field

Next, the magnetic switching behaviour of rectangular, needle-shaped [119,120] and spoon-shaped [121] electrode structures is compared in order to identify the optimal geometry parameters for magnetic switching reproducibility and controllability. It is well-known that by choice of very high aspect ratio of length to width, the smaller

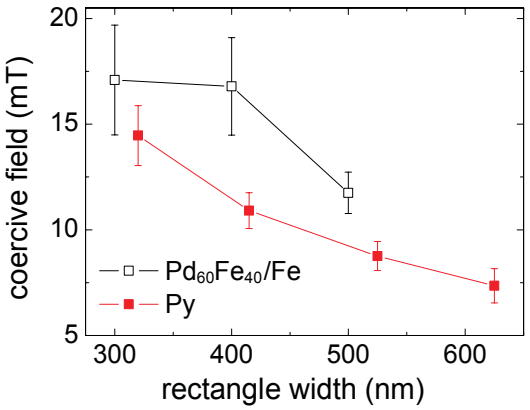

Figure 4.9: Comparison of the coercive field of Py and $Pd_{60}Fe_{40}$/Fe strips. Data points are retrieved from room temperature Lorentz microscopy measurements and averaged over three strips of same dimensions fabricated in the same EBL and metallisation process. While the absolute switching field is higher for strips of $Pd_{60}Fe_{40}$/Fe than of Py, the deviation from strip to strip is much larger. Py displays a more reliable switching (smaller error bars).

of the two parameters dominates the switching behaviour via shape anisotropy. By setting the length to 16 μm for all structures, investigations can be reduced to varying the electrode widths in the range from 200 nm up to $\sim 1\,\mu$m. Lorentz microscopy allows to determine whether a structures is of suitable dimensions to be in a single domain configuration.

Rectangles

Figure 4.10 shows four $Pd_{60}Fe_{40}$/Fe contact strips of different width at different values of the external magnetic field $\mu_0 H_{||}$. Coming from saturation, where all strip magnetisations are aligned along $-\mu_0 H_{||}$ (blue arrows, top image row), the external field is swept to opposite field direction $\mu_0 H_{||}$. As indicated by the arrow on the edge, subsequent image rows are recorded at increasing field values during a magnetic field sweep. The images show that the rectangular strips flip their magnetisation consecutively at coercive fields increasing in order of decreasing strip width.

An interesting feature visible in figure 4.10 is the formation of a magnetic end domain at the upper end of the electrode. Its evolution can be monitored by following the magnetic features at increasing field values. It indicates that the magnetic end domains nucleate the magnetic switching of the whole strip. Otherwise, the strips all show a clear single magnetisation direction as desired for a pseudo spin valve contact electrode.

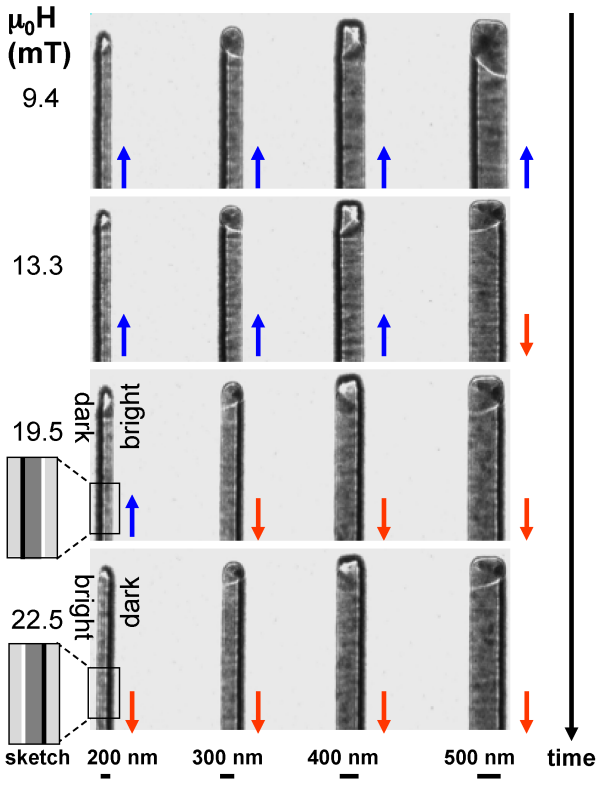

Figure 4.10: Lorentz microscopy images of four $Pd_{60}Fe_{40}$/Fe (10 nm/35 nm thick) strips of different width (200 nm, 300 nm, 400 nm, 500 nm). The length (16 μm) is chosen large enough for the width only to govern the shape anisotropy. The strips have been fully saturated in a magnetic field parallel to the long strip axis (blue arrows, top row). When applying an increasing external field in opposite direction (subsequent lower image rows), magnetic switching takes place, see the red and blue arrows next to the strips. The required coercive field clearly decreases with increasing strip width. The black arrow indicates how images were taken subsequently in time during a single magnetic field sweep. Insets: sketches of the observed edge features, cf. figure 4.8.

Needle-shaped structures

In figure 4.11, three $Pd_{60}Fe_{40}$/Fe needle-shaped structures of different width are Lorentz-imaged. A magnetisation reversal analogous to figure 4.10 is found. Compared to rectangles, switching in needles is also governed by the structure width but occurs at higher coercive field. This may be explained by fewer magnetically frustrated spins within the pointed structure tips, i. e. fewer and smaller end domains, see figure 4.11 compared to the rectangles of figure 4.10. As the magnetisation reversal is initiated by these end domains, their suppression also should translate into higher magnetisation stability.

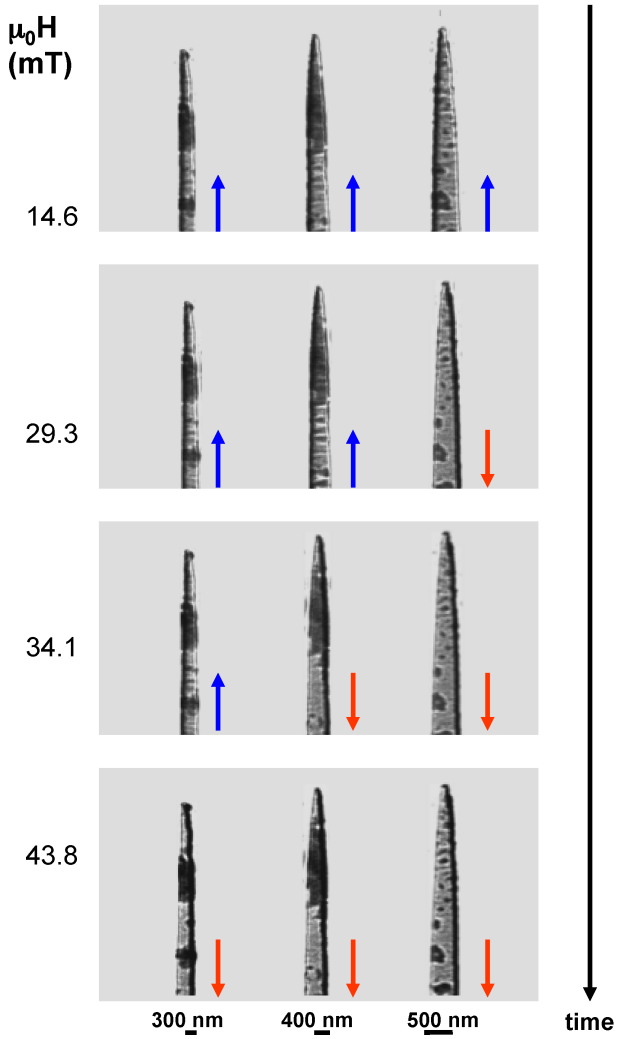

Figure 4.11: Lorentz microscopy images detailing the magnetisation reversal of needle-shaped $Pd_{60}Fe_{40}$/Fe (10 nm/35 nm) structures differing in width (300 nm, 400 nm, 500 nm), analogous to the data of Fig. 4.10. From upper to lower image row, an increasing magnetic field directed opposite to the original saturation magnetisation is applied. The irregular spots on the image stem from non-magnetic process contamination.

Spoon-shaped structures

In figure 4.12, TEM Lorentz microscopy images of spoon-shaped structures, i. e. rectangular strips with attached disk, are presented. The disk diameter dependence of the magnetisation reversal of attached rectangular strips is investigated. All strips have equal dimension, only the disk diameters are varied.

In a disk made from a ferromagnetic material, the spins can align in a vortex configuration. [114] Depending on whether the vortex chirality is clockwise or counter-

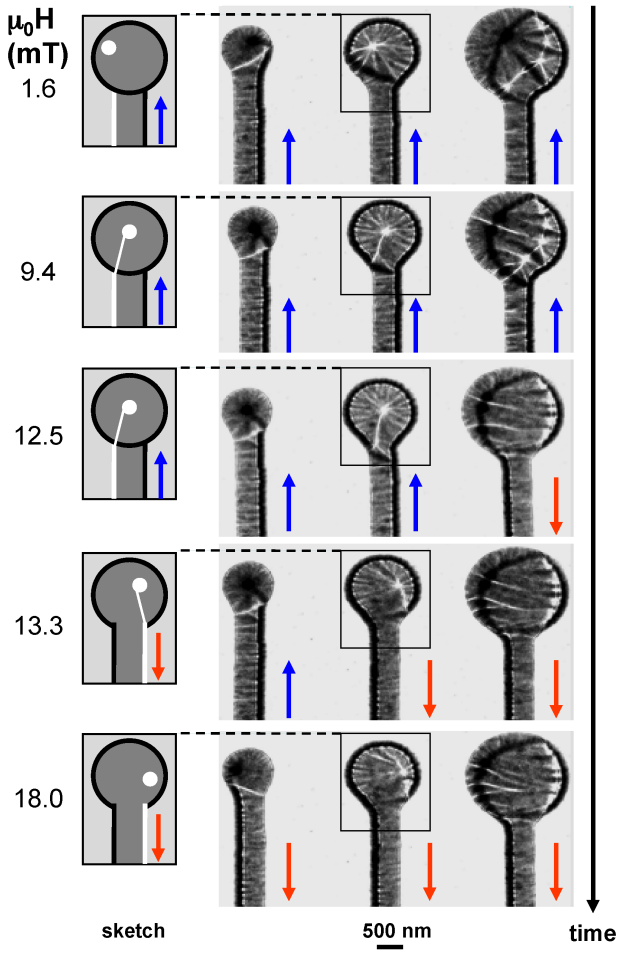

Figure 4.12: Lorentz microscopy images showing the magnetisation reversal of three spoon-shaped structures. Each of the identical, 16 μm $\times$ 500 nm, $Pd_{60}Fe_{40}$/Fe rectangular strips has a disc-shaped structure of different diameter (1.0 μm, 1.5 μm, 2.0 μm) attached at its upper end. The lower part of the strip (not shown, at large distance) has a rectangular ending. Inside the disk, the contrasts structure indicates the formation of a magnetic vortex. The magnetic switching of the strip with increasing external field (descending in image rows) is triggered when a domain wall originating from this vortex is driven into the rectangle.

clockwise, the vortex core appears in the Lorentz image as either a dark spot (structure in the first column of figure 4.12) or as a bright spot (second column). At zero external magnetic field, the vortex core is near the center of the disk. An external magnetic field along the strip "shoves" the bright (dark) vortex core to the right-hand side (left-hand side).

This behaviour can be observed most clearly in the example of the second column of

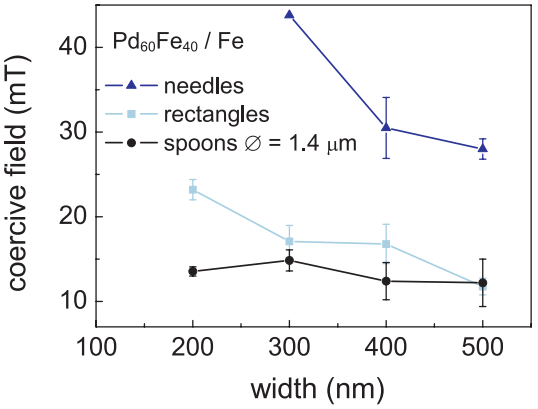

Figure 4.13: Shape influence on coercive field. The coercive field obtained from Lorentz microscopy images is plotted for spoon-shaped, rectangular, and needle-shaped structures made from $Pd_{60}Fe_{40}$/Fe. In the case of the spoon shapes, the 16 μm-long rectangular 'handles' are topped with identical disks of diameter 1.4 μm. For all structures, the (handle) strip width is varied (x-axis in the graph). Coercive field values are averaged over 4 magnetic field sweeps of the same structure and shown with respective error bars. The coercive field of the needles shows the strongest increase with decreasing width. Whereas the rectangles still display a sizeable strip width dependence of the coercive field, the disk dominates the magnetic switching of the spoon structures, nearly equalizing the coercive field for all strip widths.

figure 4.12, where the magnetisation reversal of a "spoon" with a 1.5 μm diameter disc is shown. A domain wall, seen as a bright line in the images, originates from the vortex core for all magnetic field values. Sweeping up from negative values of $\mu_0 H$, the vortex core is still shifted at +1.6 mT to the left-hand side, owing to the magnetic remanence of the structure. The domain wall ends at the left-hand side of the disk. A field of 9.4 mT is required to counter the magnetic remanence so the vortex is moved to the disk center. The white domain wall ends now near the joining of disk and strip as the domain to its left is expanding under the effect of the increasing magnetic field. At 12.5 mT the vortex core is shifted to the right-hand side and the domain left to the said white domain wall is on the brink of expanding into the rectangular strip beneath; a small increase to 13.3 mT is sufficient to cause the domain wall to pass through the rectangular strip, thereby initiating a magnetisation reversal. At 18.0 mT, the vortex core is almost 'pushed' out of the disk and the entire spoon-shaped structure is saturated. The switching field of the total spoon structure is lowered when the disk diameter is increased. It can be concluded that the disk can thus trigger the magnetisation switching of the strip structure in a controlled way, independent of random end domains. However, as can be seen in the third

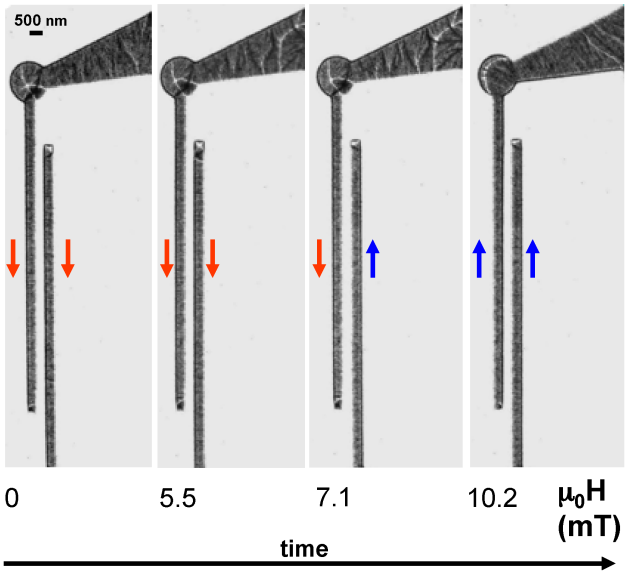

Figure 4.14: Lorentz microscopy images of a detached rectangular electrode compared to an electrode with attached large-area ferromagnetic leads. The electrode width is in both cases 500 nm. Following the images from left to right, it can be observed how an external magnetic field initiates a magnetisation reversal. The ferromagnetic leads change the switching field since the magnetisation reversal can be initiated by the increasing external field driving a domain wall from the lead into the rectangular electrode.

column of figure 4.12, at large disk diameters no clear vortex forms but strong ripple domain structures typical for Fe thin films appear, [122] counteracting the expected stabilising effect on magnetic switching.
Both effects are illustrated by the data of figure 4.13, where the coercive fields of strips ranging from 200 nm to 500 nm with and without an attached disc of diameter 1.4 μm, or a needle tip are plotted. The disc clearly dominates the switching of the spoon-shaped structures and equals the coercive field of all strips around 12.5 mT. However, for larger structures a stronger scatter in measured values can be observed. The needles show the strongest width dependence on the coercive field.

Effect of ferromagnetic supply lines

Fabricating contact electrodes together with supply lines and bond pads in a single metallisation process would simplify chip processing significantly. To investigate the effect of attaching large ferromagnetic supply lines on the magnetisation reversal of the contact electrodes, two identical $Pd_{60}Fe_{40}$/Fe strips with and without attached typical supply lines and bond pad (not shown) geometry attached are compared in figure 4.14. To reduce the magnetic coupling between electrode and supply lines

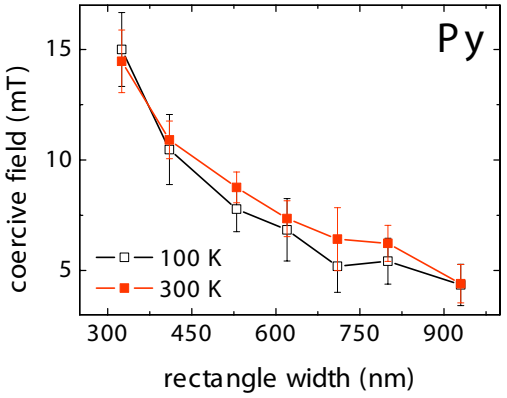

Figure 4.15: Comparison of the coercive field of rectangular Py strips of different width and with a length of 16 μm at room temperature (300 K, red) and close to liquid nitrogen temperature (100 K, white). Data points are retrieved from Lorentz microscopy measurements, averaging over three rectangular Py strips of same dimension fabricated in the same EBL and metallisation process.

a disk is placed at their junction. This disk typically forms a strongly diameter-dependent vortex, as discussed above.

Coming from saturation at high negative field, at 0 mT (left panel in figure 4.14) both contacts have their magnetisation aligned downwards (red arrows). At 7.1 mT, initiated by edge domains, the strip without attachment aligns along the external field (blue arrow). The strip with attachment follows at a coercive field of 10.2 mT – in this particular case at a higher rather than at lower field value, as also observed with an attached disc structure. Still, there is a difference in coercive field of 3.1 mT indicating that the magnetisation reversal is triggered by the multi-domain configuration in the supply lines. Switching is rendered irreproducible due to the random domain structure in the bulky supply line.

4.2.4 Temperature dependence

Low temperatures are still an important prerequisite to many fundamental studies of spintronics devices. This raises the question whether the results obtained by room temperature Lorentz microscopy remain valid in the low-temperature regime. For this purpose, figure 4.15 compares the coercive fields of rectangular Py strips obtained at room temperature with those at 100 K, the lowest accessible temperature in our TEM sample holder. Coercive field values agree, within the margin of error, for both temperatures, justifying an extrapolation of our findings to the low-temperature limit.

4.3 Summary

Various aspects of carbon nanotube-based pseudo spin valves with diluted ferromagnetic contacts have been investigated.
Ferromagnetic contact electrodes of different shapes and materials were studied for their suitability as contacts for carbon-nanotube based pseudo spin valves using TEM Lorentz microscopy. This allowed the identification of materials and shapes that are in a magnetic single domain state and whose magnetisation switches at a sharp, reproducible and shape-tunable coercive field.
Permalloy structures displayed the required single-domain magnetisation reversal. Its electrical interface to our MWCNT was, however, highly resistive and TMR traces were noise-ridden (see [55]). Transparent Py-SWCNT spin transistors have been realised with comparable contact qualities to Pd-ferromagnet alloys [123]. In comparison, PdFe alloy strips switched their magnetisation via multi-domain configurations. This can account for the comparatively lower reproducibility in magnetisation reversal. Furthermore, cross-tie domain walls were observed as indication of a non-negligible out-of-plane magnetisation. Multiple fine ripple domains appeared in magnetic double layer structures made from PdFe/Fe.
For all electrode shapes investigated, it holds that a larger width lowers the coercive field. End domains were identified to act as seeds for magnetisation reversal and thereby to decrease the coercive field. Out of the $Pd_{60}Fe_{40}$/Fe electrode shapes investigated here, rectangular strips exhibited the most reliable magnetisation reversal, although a more pronounced end domain structure was observed compared to pointy and circular end shapes. Large-area ferromagnetic appendices to electrode strips, as in the case of attached disks or supply lines, were found to strongly impact the magnetic switching, and to lead to unpredictable behaviour.
The giant paramagnet Palladium seems the obvious base material for carbon nanotube-based spintronics devices. Yet, the thin film magnetic properties of different ferromagnet-Pd alloys can vary strongly, in particular concerning the out-of-plane magnetisation, and require further optimisation.
This work was published in 2009 [55], also demonstrating the TMR effect occuring in SWCNT-based spin valves. Since then, the sample fabrication was further investigated, as shall be briefly outlined here: as a next iteration in sample fabrication, inspired by previous experiments [56, 124], a different ferromagnetic palladium alloy, PdNi [99]. It was found that the magnetic preferential direction of high aspect ratio $Pd_{0.3}Ni_{0.7}$ thin film contact strips behaves quite differently compared to the previously investigated Pd_xFe_{1-x} contacts [55, 101]. The strips feature a magnetically harder axis along the strip length. Unlike simple consideration of form anitrosopy may suggest, the in-plane transverse direction is the the magnetically easiest. MFM

measurements directly show that our PdNi strips spontaneously form magnetic domains in this direction. For application in CNT based spin devices it is therefore recommended to apply external magnetic fields in transverse direction in order to obtain a more distict switching behaviour. In addition, the difference in the electrode coercivities and thus the difference in electrode width has to be sufficently high to be resolved during measurement. However, the hysteretical effects in spin valves with our PdNi material based on both single and double quantum dots could not be unambiguously attributed to TMR.
Meanwhile, ongoing work in the research group could resolve the contact resistance issues of Py to CNTs by lower pressures (few 10^{-8} mbar) during e-gun evaporation (compare also [123]). Py has been shown here to exhibit clearer and very reliable magnetic domain switching and low contact resistances close to the unitary limit. Future spin valve devices should therefore be made from permalloy.

Chapter 5

Characterisation of energy scales and capacitances in a SWCNT-based double quantum dot

While introducing the characteristic measurements of a double quantum dot, this chapter takes up the evaluation guideline developed in chapter 1. Figure 5.1 (a) shows in a SEM micrograph of the investigated double quantum dot, where the voltages for left, middle, right local gate voltages (V_L, V_M, V_R), the backgate voltage V_{BG} and the bias voltage ($V_S - V_D$) are applied. The room temperature resistance of the device was 53 kΩ and its low-temperature resistance of about a MΩ when the device is operated as a double quantum dot. This resistance is in the lower range of similar CNT-based DQDot devices (with non-ferromagnetic electrodes) reported in literature (e. g. [19, 35, 71, 97]).

Figure 5.1 (b) represents the corresponding electrostatic replacement circuit. In particular, a new ansatz to extract the source and drain to dot capacitances is proposed. Note that the proposed ansatz allows to extract C_S and C_D directly from the data and independently of each other and possible parasitic capacitances relying on the position shift of the triple triangles with bias; in literature, e. g. [125], they are often coursely approximated by the difference of total dot capacitance minus all determined capacitances. The consideration of the cross-capacitances adds to the complexity of the evaluation. In figure 5.2, a consistent method for the data analysis is provided in form of a flow chart diagram. The arrows indicate what quantity depends on which previously evaluated one. The remainder of this section will undertake the evaluation steps depicted in figure 5.2 in detail. Along the way,

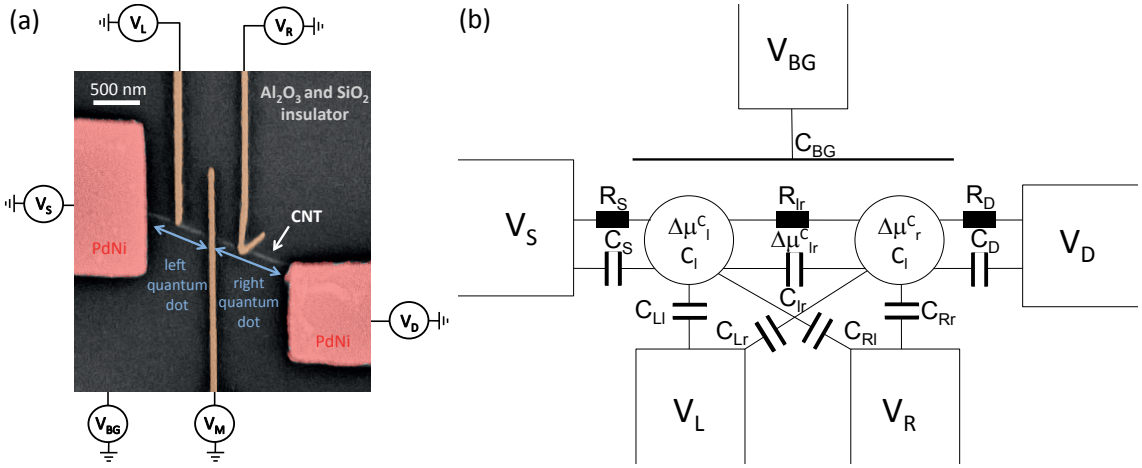

Figure 5.1: (a) Double quantum dot sample with electrode designation, as layed out in chapter 3. (b) Corresponding replacement circuit with all with capacitances (including cross-capacitances C_{Xy} and source and drain to dot capacitances) and charging energies to be evaluated.

some characteristic measurements of the studied CNT DQDot will be presented.

The sample in shown in figure 5.1 (a) is a (single) quantum dot even if no local gates were in use. To drive the sample as a double quantum dot, however, the CNT section between source and drain electrodes must be separated in two by means of a suitable electrostatic potential landscape. The prime impact on the definition of the double dot has the middle gate finger (V_M), but all other voltages or the magnetic field contribute to shaping the potential double well. The experimental challenge lies in its fine tuning in a large parameter space. Owing to the parameter inter-dependence, a specific behaviour (e. g. a weakly coupled DQDot) can often be observed only in small parameter regions (e. g. in the (V_L, V_R)-plane). The measurement in figure 5.3 exemplify three interdot coupling regimes. For all measurements throughout this chapter, the cryostat bath temperature was T=280 mK=25 μeV/k_B. Plotted is the tunnel current I as a function of, in graphs (b), left and right local gate voltages (V_L, V_R) at constant bias. Subplots (a) show the current depending on the bias V_{SD} and one gate voltage; subplots (a1) and (a2) are plotted against the global backgate voltage V_{BG} with the local gates (V_L, V_R) set to ground, while subplot (a3) shows the bias dependence along the green line in subplot (b3), obtained by a superposition of V_L and V_R. Subplots (b) are measured at low bias excitation (V_{SD}=100 μV) and are, for clarity, overstated tenfold in current ($\times$10). Via the middle local gate voltage V_M, as indicated along the black arrow to the right, the interdot coupling can be tuned from an effective single quantum dot at V_M=0. The SQDot resonances appear as straight lines in the (V_L, V_R) gate plane, cf. figure 5.3 (b1). Likewise, the stability

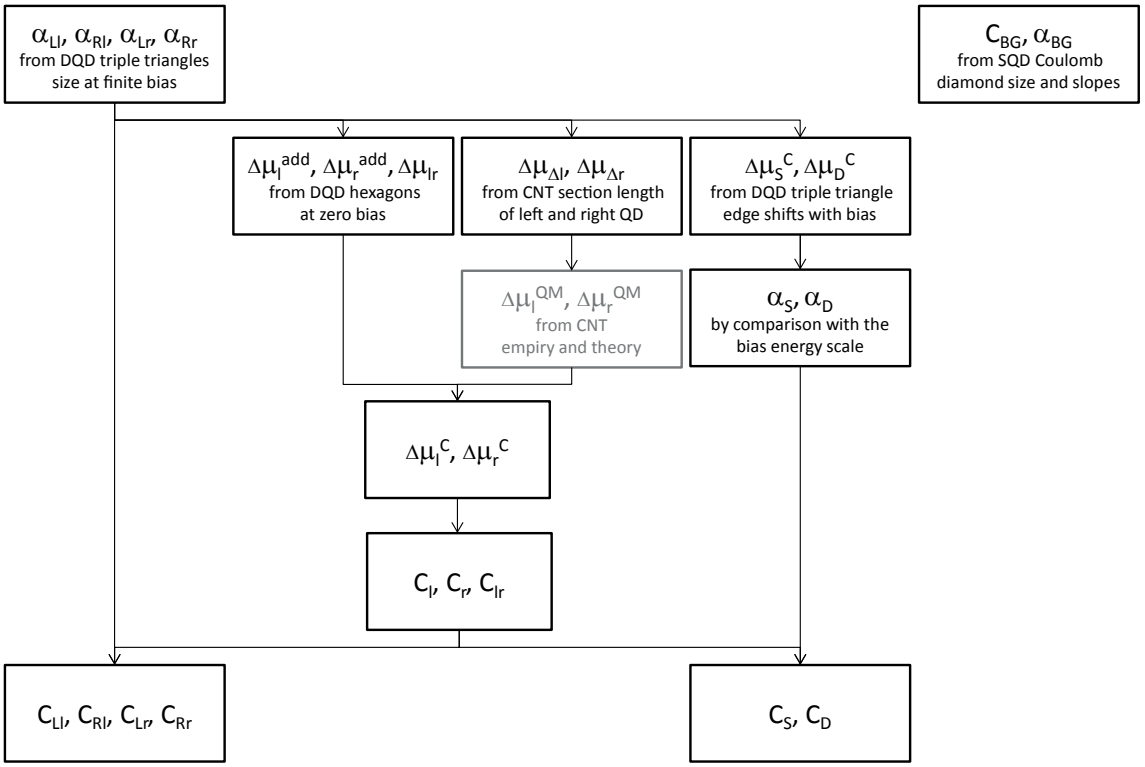

Figure 5.2: Flow chart of full double quantum dot capacitor and addition energy characterisation. Any evaluated quantity depends on all evaluations of above quantities that connect to it with arrows.

diagram in figure 5.3 (a1) consists of regular 'Coulomb diamonds'.

At V_M=-50 mV, the electrostatic potential landscape defines a strongly inter-coupled quantum dots. Its resonance lines in figure 5.3 (b2) become more irregular and undulated. Where two neighbouring waves approach, a triple point pair starts forming. The Coulomb diamonds can be understood as slices through the gate plain with bias dependence. They are more irregular in figure 5.3 (a2) compared with (a1) . Correspondingly, the onset of 'pair building' can be observed in some sequences of small and big diamonds.

At V_M=-100 mV, the sample shows a hexagonal triple point lattice in figure 5.3 (b3) which is characteristic for weakly inter-coupled double dot. The bias dependence (a3) through two pairs of triple dots (green line) in (b3) shows a period of a small diamond within a triple point pair and a big diamond between two pairs. The zero bias resonances correspond to the triple points. The Coulomb diamond sizes can be additionally modultated according to the CNT energy levels. Tests identified value of V_M=-100 mV as optimal for weak interdot coupling accross a sizeable (V_L, V_R) region, cf. figure 5.7.

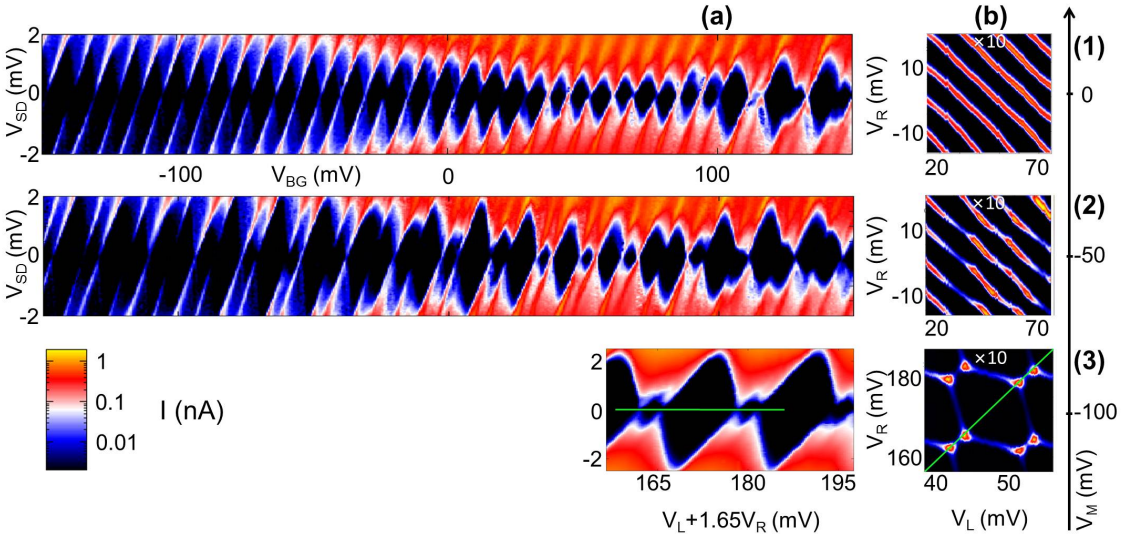

Figure 5.3: Interdot coupling regimes in the CNT-based DQDot: plotted is the tunnel current I as a function of, in graphs (b), left and right local gate voltages (V_L, V_R) at constant, small bias (V_M =-100 mV) or, in graphs (a), of the bias V_{SD} and different gate voltages; subplots (a1) and (a2) are plotted against the global backgate voltage with the local gates (V_L, V_R) set to ground, while subplot (a3) shows the bias dependence along the green line in subplot (b3), obtained by a superposition of V_L and V_R. Subplots (b) are measured at low bias excitation (V_{SD}=100 μV) and are overstated tenfold in current (×10). Via the middle local gate voltage V_M, as indicated along the black arrow to the right, the interdot coupling can be tuned from an effective single quantum dot at V_M=0, with straight resonance lines in the (V_L, V_R) gate plane (b1) and regular 'Coulomb diamonds' in the stability diagram (a1) - via a strong DQDot coupling regime at V_M=-50 mV, with irregular lines (b2) and Coulomb diamonds (a2) - to weakly inter-coupled double dot at V_M=-100 mV, with the characteristic hexagonal triple point lattice (b3). The bias dependence (a3) through two pairs of triple dots (green line) in (b3) shows a period of a small diamond within a triple point pair and a big diamond between two pairs.

All subsequent measrements in this work stem from this parameter region.

5.1 Backgate capacitance

By grounding all local gates and sweeping the backgate potential and bias the device can be driven as a single quantum dot. The stability diagram $\mathrm{d}I/\mathrm{d}V(V_{BG}, V_{SD})$ figure 5.3 (a1) shows indeed a very regular pattern of Coulomb diamonds typical for a single quantum dot.

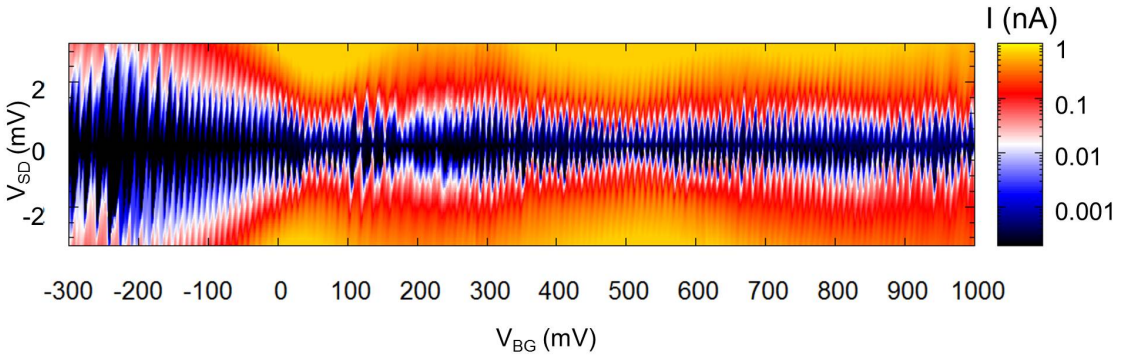

Figure 5.4: Stability diagram $\mathrm{d}I/\,\mathrm{d}V(V_{BG}, V_{SD})$ of bias and backgate. The measurement is a repetion of figure 5.3 (a1) with larger backgate range. More than 50 excess electrons on the dot can be observed.

For positive backgate, where current is carried by electrons, the conductivity is higher by orders of magnitude compared to the negative bias side. Although a band gap has not been observed over a large gate range from ±1 V. Figure 5.4 shows a large-range backgate scan than than the similar measurement in figure 5.3 (a1). The CNT can be thus to be considered metallic. The conductance is asymmetric with respect to bias, being enhanced for positive voltages. On the wider backgate scale in figure 5.4, an oscillating envelope of the Coulomb diamond tips is observed. Such an envelope can arise from a superimposed Coulomb diamond structure stemming from a residual electrostatic landscape, e. g. impurities.
In the present case, the backgate voltage is not used as a parameter to define a DQ-Dot and is held constant. Figure 5.3 (a1) allows to identify a regular, low-on-noise region with respect to V_{BG} as to avoid backgate noise. By choice, all subsequent data have therefore been taken at zero backgate potential. From its length $L = 1250$ nm, and using equation 2.44, a level spacing in the CNT of $\Delta\mu^{QM} = 1.3\mu$eV can be estimated. The Coulomb diamond size displays a two-fold symmetry (every second diamond is smaller by about 7% compared to the preceeding and following one).

Two sets of four diamonds both above and below zero backgate were investigated and averaged over 4×4 Coulomb diamonds for a more meaningful evaluation of $\langle\alpha_{BG}\rangle$. Equation 1.15 obtains the electrostatic backgate efficiency coefficient

$$\langle\alpha_{BG}\rangle = \frac{1}{\frac{1}{|s_S|} + \frac{1}{|s_D|}} = 0.195 \pm 2.9\% \tag{5.1}$$

from the diamond slopes. Half the diamond heigth gives the addition energy $\Delta\mu_{add}$ and by equation 1.2, having substacted quantum effects, the total dot capacitance

$C_{dot} = 1.38 \pm 4.2\%$. The backgate capacitance is then, by equation 1.6

$$C_G = \alpha_{BG} C_{dot} = 19.5\,\text{aF} \pm 7.1\%. \tag{5.2}$$

5.2 Local gates to dots coefficients α_{Xy}

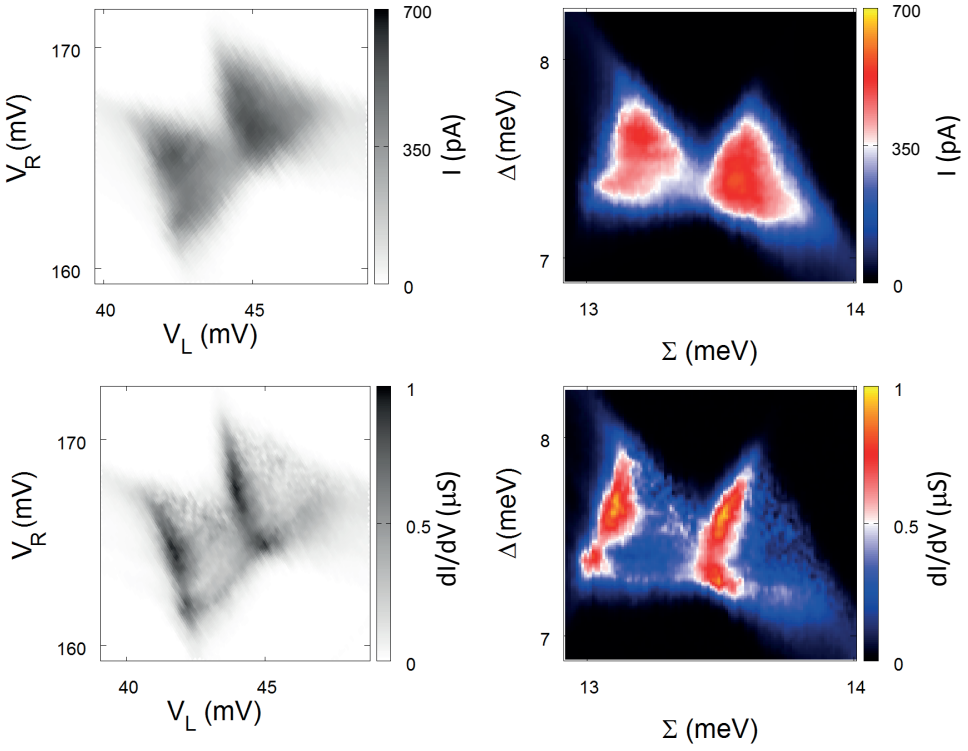

Figure 5.5: A triple dot pair in both the (V_L, V_R) and (Σ, Δ) planes, and each in I and $\mathrm{d}I/\mathrm{d}V$ at 280 mK. A field of 2 T ensures that the triangle base line is visible so that the gates to dot can be extracted.

The four local gate efficiency coefficients α_{Xy} to dot, defined in equation 1.26, are essential because they translate what the experimental voltage sources apply to left and right quantum dot into physical energy scales. The evaluation flow chart in figure 5.2 displays how important precise evaluation is here as the entire subsequent data evaluation grounds on them. They can be extracted via equations 1.41, 1.42, 1.43 and 1.44 by comparing the triangle side lengths to the bias and amount to

$$\mathbf{A} = \begin{pmatrix} \alpha_{Ll} & \alpha_{Rl} \\ \alpha_{Lr} & \alpha_{Rr} \end{pmatrix} = \begin{pmatrix} 0.144 & 0.017 \\ 0.06 & 0.107 \end{pmatrix} \tag{5.3}$$

- for the gate range presented in figure 5.5. The subsequent experiments were performed in this gate region. Figure 5.5 presents a triple triangle pair both in the 'raw

data' (V_L, V_R)- versus the 'natural DQD coordinate' (Σ, Δ)-planes. A consistency test for correct evaluation is to check whether the triangles are indeed equilateral of side length eV_{SD} in the (Σ, Δ)-plane. Furthermore, the same data is each shown in current and differential conductance that were measured simultaneously as sketched in the measurement setup (figure 3.7); one can observe that the triangle outline is much better defined in the $\mathrm{d}I/\mathrm{d}V$ data. Moreover, comparison of a statistically relevantnumber of triangles in I versus $\mathrm{d}I/\mathrm{d}V$ colour scales unveils that the base line often does not appear in the current, due to transport blockade effects that will be discussed later. Differential conductance data are thus better suited for evaluation.

5.3 Linear growth of triangles with bias

As detailed in section 1.2.2, the triple triangle side lengths depends linearly on the applied bias. Figure 5.6 confirms this experimentally. Figure 5.6 (a) shows a zoom on a hexagon in the (V_L, V_R) plane. The $I(V_L, V_R)$ map diplays the characteristic pattern of a capacitively, weakly tunnel coupled double quantum dot, cf. figure 5.1 (a). With the bias, the cornerpoints of each hexagon, i. e. the triple points, grow into 'triple triangles'. Figure 5.6 (b) verifies whether this growth is indeed linear. The three side lengths of the triple triangle, $\overline{12}$, $\overline{23}$ and $\overline{31}$, are evaluated in energy coordinates (Σ, Δ) and plotted against a large bias range from -1.5 mV to +1.5 mV. The correspondingly colour-coded linear fits match the data points well. For positive bias (not shown), the analogous pattern appears mirrored w. r. t. the axis defined by the interconnection line of a triple triangle pair. Simply put, the triangle tip points in the opposite direction upon bias reversal.

The second message of figure 5.6 (b) is that the triple triangle side lengths are given by the bias. The linear fit slopes s_{kl} are close to unity (times the electron charge e):

$$s_{12} = 0.89\ \mathrm{e} \pm 5\% \tag{5.4}$$

$$s_{23} = 0.86\ \mathrm{e} \pm 6\% \tag{5.5}$$

$$s_{31} = 0.96\ \mathrm{e} \pm 6\% \tag{5.6}$$

The procentual error comprises both data reading errors and fit error. Note the conversion from gate coordinates (V_L, V_R) to energy coordinates (Σ, Δ) requires the gate coeffiencts α_{Xy} as an input. Consequently, the absolute slope values are no direct measurement results. Rather they provide a measure, when compared to the theoretically postulated unity time e, for the quality of the data evaluation.

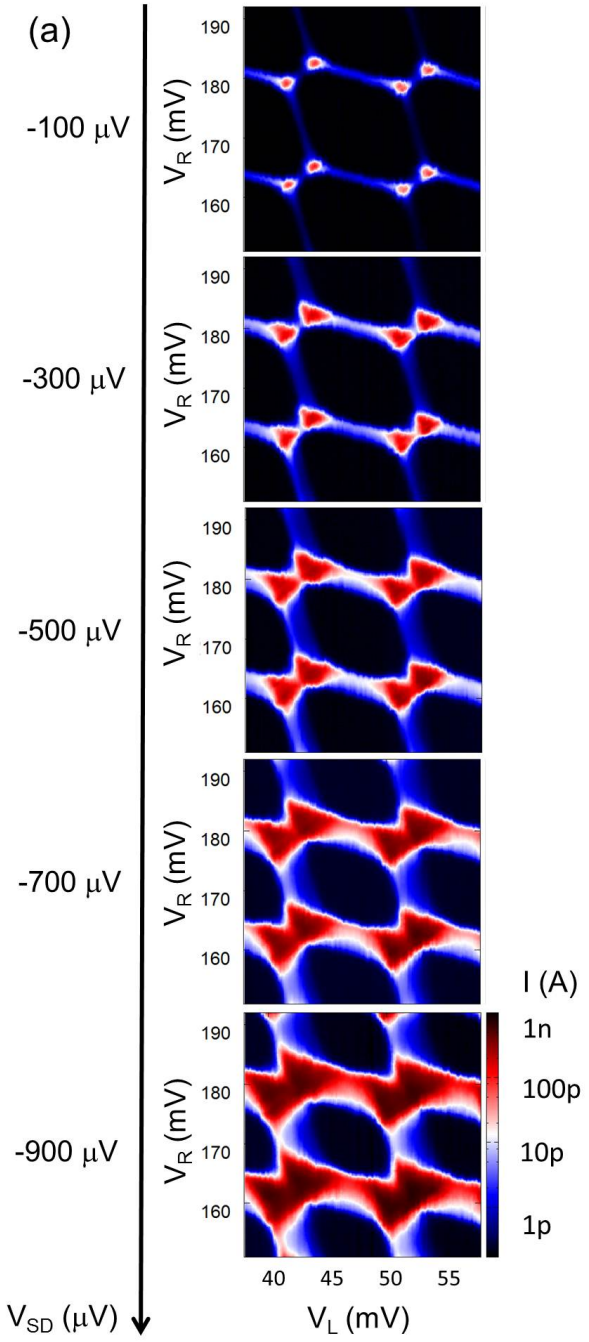

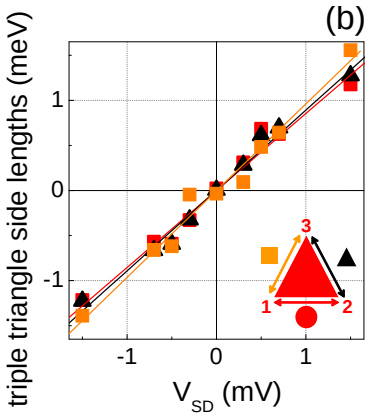

Figure 5.6: Bias dependence of triple triangle side lengths: (a) Zoom on a hexagon in the (V_L, V_R) plane that is characteristic for a capacitively, weakly tunnel coupled double quantum dot (V_M=-100 mV). With the bias, the cornerpoints of each hexagon, i. e. the triple triangles, grow into triple triangles. (b) The three side lengths of the triple triangle, $\overline{12}$, $\overline{23}$ and $\overline{31}$, are evaluated in energy coordinates (Σ, Δ) and plotted against a large bias range from -1.5 mV to +1.5 mV. The correspondingly colour-coded linear fits match the data points well, confirming that the triple triangle side length is given by the bias. Their slopes are close to unity, as expected for correct gate to energy scaling α_{Xy}.

5.4 Left, right and interdot addition energies

Figure 5.7 shows the typical hexagonal pattern of a weakly coupled DQD over a large gates range.

Of physical interest is that the interdot coupling varies over this large gate region from weak (stars in figure 5.7) to strong (crosses in figure 5.7). Our experiments aim

at the weak coupling regime, so the subsequent experiments were performed around the area marked by the red dashed square. A zoom of this region (figure 5.8) displays the ideal typical double quantum dot stability diagram with increased conductance at the triple point pairs, interconnected by co-tunnelling lines.

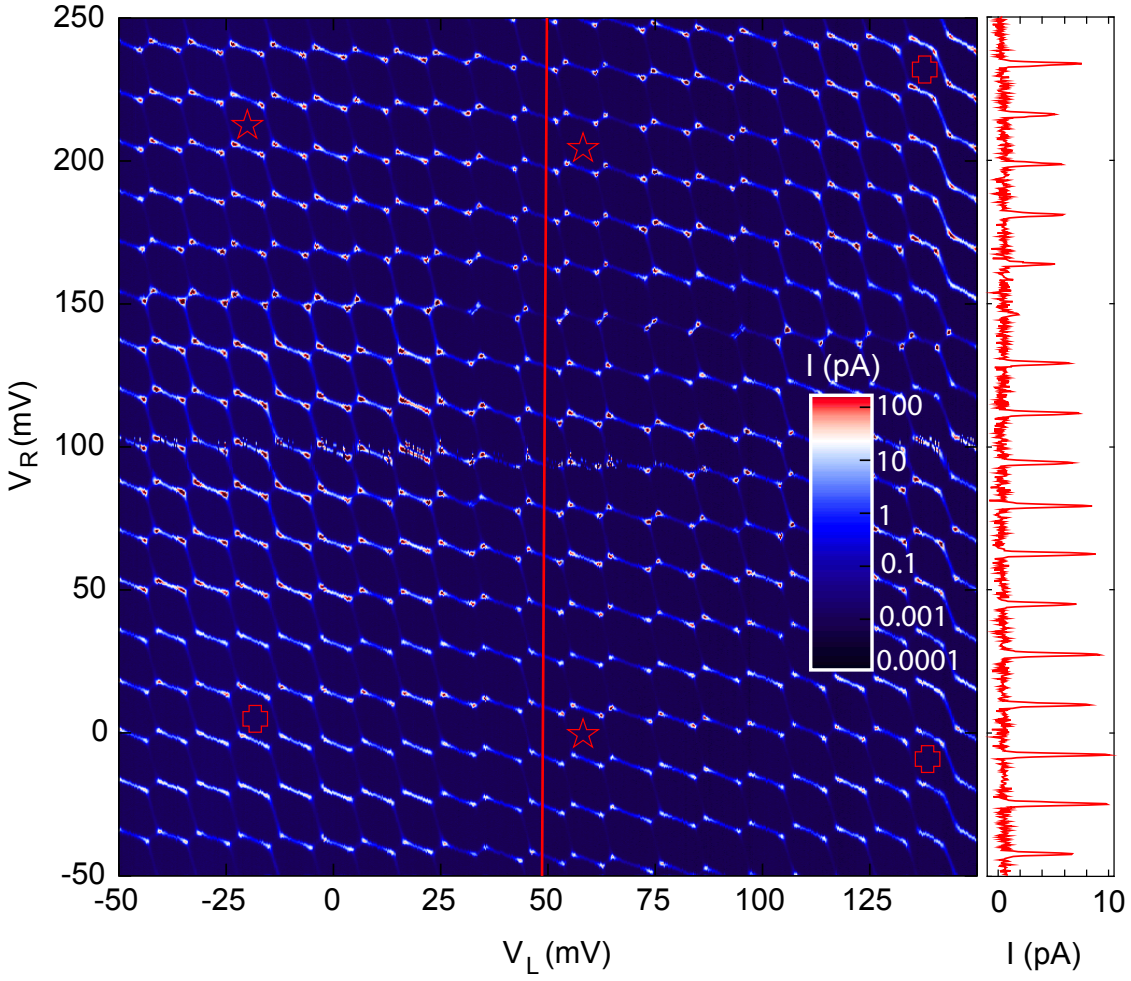

Figure 5.7: Double quantum dot hexagonal stability diagram, taken at an external magnetic field perpendicular to the CNT of 2 T and low bias excitation of -50 μV. The weak coupling regime is accessed by applying $V_M = -100$ mV to the middle local gate.The backgate is here and furthermore set to zero by default. Stars (crosses) mark regions of weak (strong) interdot coupling. The red line marks the position on the right-hand side line scan; it shows regular, very clearly defined Coulomb peaks. These peaks stem from 'single resonances', where only one dot is aligned to its adjacent bias electrode and transport occurs via co-tunnelling events.

A four-fold [71] or two-fold [126] periodicity in the double QD hexagons is a typical feature for a single CNT QD of length L and corresponding level spacing $\Delta\mu^L \propto \frac{1}{L}$, as

detailed in section 2.4. Here, a large, statistically viable square area of $(4\times4)\times(4\times4)$ hexagons was investigated at zero external field. However, no periodicity in addition energies could be deduced.

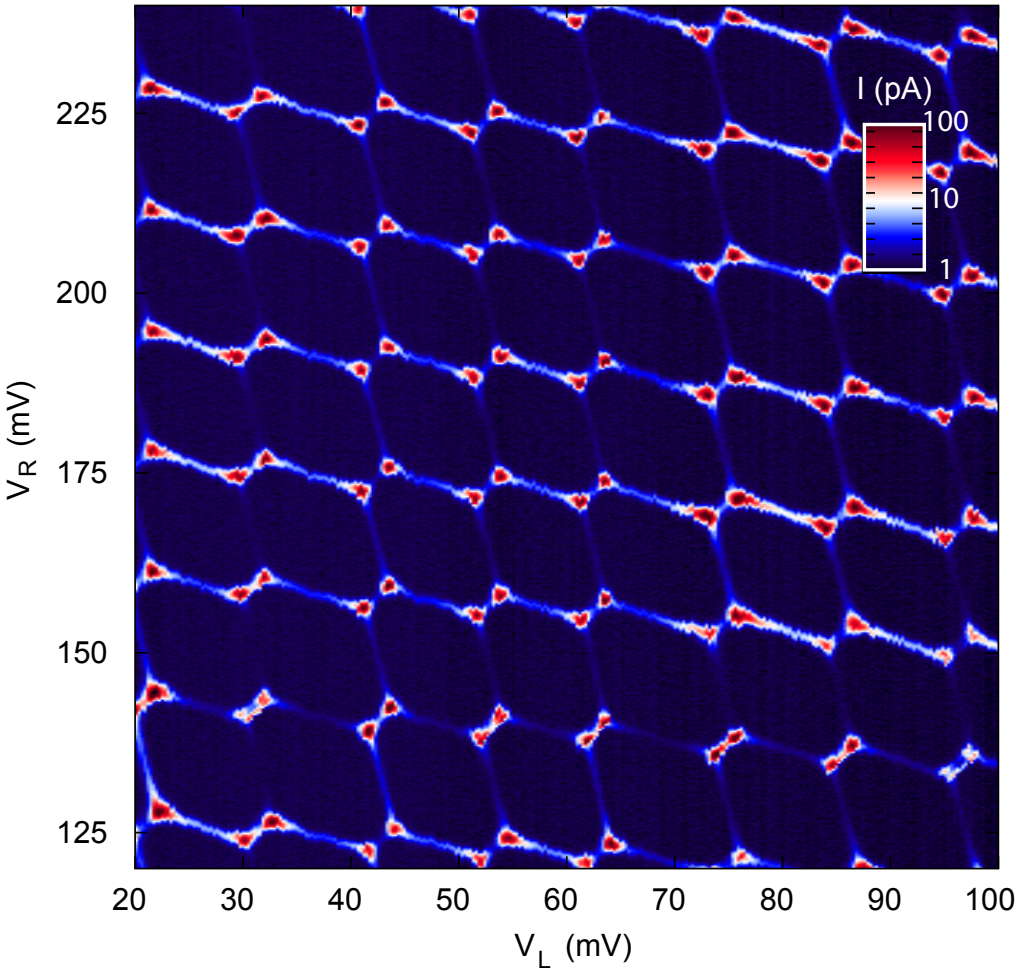

Figure 5.8: Double quantum dot hexagonal stability diagram, i. e. the dc current over the gate plane (V_L, V_R) at constant bias V_{SD}=-50 μV, V_{BG}=0 and V_M=-100 mV, in a region of weak coupling, cf. figure 5.3. Our subsequent measurements target this parameter region.

It is therefore reasonable to assume that both spin and orbital degeneracies are lifted. Without periodicity, the problem arises how the quantum mechanical part of the addition energy is to be quantified. Section 2.4 developed how to approximate $\Delta\mu^{QM}$ by an average of the theoretical fine structure of four given Coulomb peaks, empiry and reasonable assumptions, boiling down to 0.4 times the dots level spacing $\Delta\mu^{L}$. This energy scale is individual for each dot and can be quantified for our left and right dots from the length of the CNT sections, as measured in figure 5.1 (a) by

equation 2.44 to be

$$\begin{pmatrix} \Delta\mu_l^L \\ \Delta\mu_r^L \end{pmatrix} = \begin{pmatrix} \frac{hv_F}{4\times 597\,\mathrm{nm}} \\ \frac{hv_F}{4\times 659\,\mathrm{nm}} \end{pmatrix} = \begin{pmatrix} 1.40\,\mathrm{meV} \\ 1.27\,\mathrm{meV} \end{pmatrix} \tag{5.7}$$

The addition energies are then taken from the average of heights and widths of $(4 \times 4) \times (4 \times 4)$ hexagons at zero external field in the gate plane and translated into energy via the α_{Xy} from equation 5.3, yielding $\Delta\mu_l^{add} = 1.70\,\mathrm{meV} \pm 5.7\%$ and $\Delta\mu_r^{add} = 2.45\,\mathrm{meV} \pm 4.4\%$.

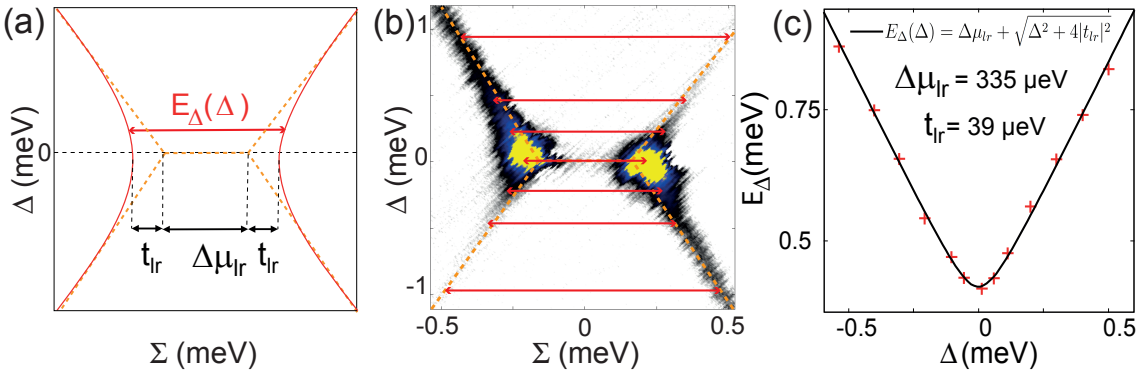

Figure 5.9: (a) Sketch of the tunnel current across the DQDot plotted as a function of (Σ.Δ). The Σ-distance between the two red curves at zero detuning is given by the interdot charging energy μ_{lr} plus twice the interdot tunnel coupling t_{lr}. (b) Equivalent measurement to (a), taken at near zero bias ($V_{SD} = 0.5$ μeV). The evaluated quantity, $E_\Delta(\Delta)$ is illustrated by the red arrows, e. g. the Σ-distance of the the two yellow triple point centres at zero detuning Δ. (c) Values for $E_\Delta(\Delta)$ as extracted from the data overlayed with a fit to equation 1.26.

The interdot charging energy $\Delta\mu_{lr}^C$ can be obtained, together with the interdot tunnelling energy t_{lr}, from the Σ-spacings $E_\Delta(\Delta)$ between the co-tunnelling lines for several values of the detuning Δ around a triple point pair. To do this, the extracted values for $E_\Delta(\Delta)$ must be fitted to equation 1.26 This is demonstrated in figure 5.9. For precision's sake, the meaurement is taken at extremely low, near-zero bias ($V_{SD} = 0.5$ μeV) where the positively sloped co-tunnelling line is very faint. The resulting values are $\mu_{lr} = 335$ μeV$\pm$ 1.5% and $t_{lr} = 39$ μeV$\pm$ 12.1%. The small value for t_{lr} confirms that, at V_M=-100μV, the two dots are weakly tunnel coupled. Assembled in matrix form $\mathbf{M}^C$ (cf. equation 1.34), the classical, electrostatic charg-

ing energies that are are given by

$$\mathbf{M}^C = \begin{pmatrix} \Delta\mu_l^C & -\Delta\mu_{lr}^C \\ -\Delta\mu_{lr}^C & \Delta\mu_r^C \end{pmatrix} = \begin{pmatrix} \Delta\mu_l^{add} - 0.4\Delta\mu_l^L & -\Delta\mu_{lr}^C \\ -\Delta\mu_{lr}^C & \Delta\mu_r^{add} - 0.4\Delta\mu_r^L \end{pmatrix} \tag{5.8}$$
$$= \begin{pmatrix} 1.14\,\text{meV} & -0.34\,\text{meV} \\ -0.34\,\text{meV} & 1.94\,\text{meV} \end{pmatrix}.$$

5.5 Left, right and interdot total capacitances

The total capacitance matrix is then given, according to equation 1.35 by

$$\mathbf{C}^{dot} = \begin{pmatrix} C_l & -C_{lr} \\ -C_{lr} & C_r \end{pmatrix} = 1/e^2 \frac{1}{det\mathbf{M}^C}\mathbf{M}^C = \begin{pmatrix} 148\,\text{aF} & -26\,\text{aF} \\ -26\,\text{aF} & 87\,\text{aF} \end{pmatrix}. \tag{5.9}$$

5.6 Local gates to dots capacitances C_{Xy}

The local gate to dot capacitances are then simply obtained by equation 1.29:

$$\mathbf{C}^{Gd} = \begin{pmatrix} C_{Ll} & C_{Rl} \\ C_{Lr} & C_{Rr} \end{pmatrix} = \mathbf{A}\mathbf{C}^{dot} = \begin{pmatrix} 20.9\,\text{aF} & 2.2\,\text{aF} \\ 6.3\,\text{aF} & 7.8\,\text{aF} \end{pmatrix} \tag{5.10}$$

5.7 Source and drain capacitances

The effect of the capacitances C_S and C_D at finite gate voltage is a translation of the triple triangle position with V_{SD} in the gate (or energy) plane. We propose a convenient method to quantify C_S and C_D from these energy shifts in the (Σ, Δ) plane. In the limit of no capacitive action of source and drain, the triangle corner labelled 2 in figure 5.10 would be the 'fixpoint' of the triangle. It is best suited for evaluation because this is the 'seed point', from which the triple triangles start growing with increasing bias. Unlike the triple triangle points 1 and 3, the position of point 2 remains unshifted simply because the triangles expands with bias. To put it the other way round, this is the only corner point that is shifted purely by the capacitive action of source and drain electrodes. The shift of triple triangle point 2 is

$$\begin{aligned} \Delta\mu^{(2)} :&= \mu^{(2)}(V_{SD}) - \mu^{(2)}(0) \\ &= \delta\Sigma^{(2)} + \delta\Delta^{(2)} \end{aligned} \tag{5.11}$$

The second equality in equation 6.1 is nothing but a transformation in the 'natural DQDot coordinates' defined in equation 1.36. $\delta\Sigma^{(2)} := \Sigma^{(2)}(V_{SD}) - \Sigma^{(2)}(0)$ and

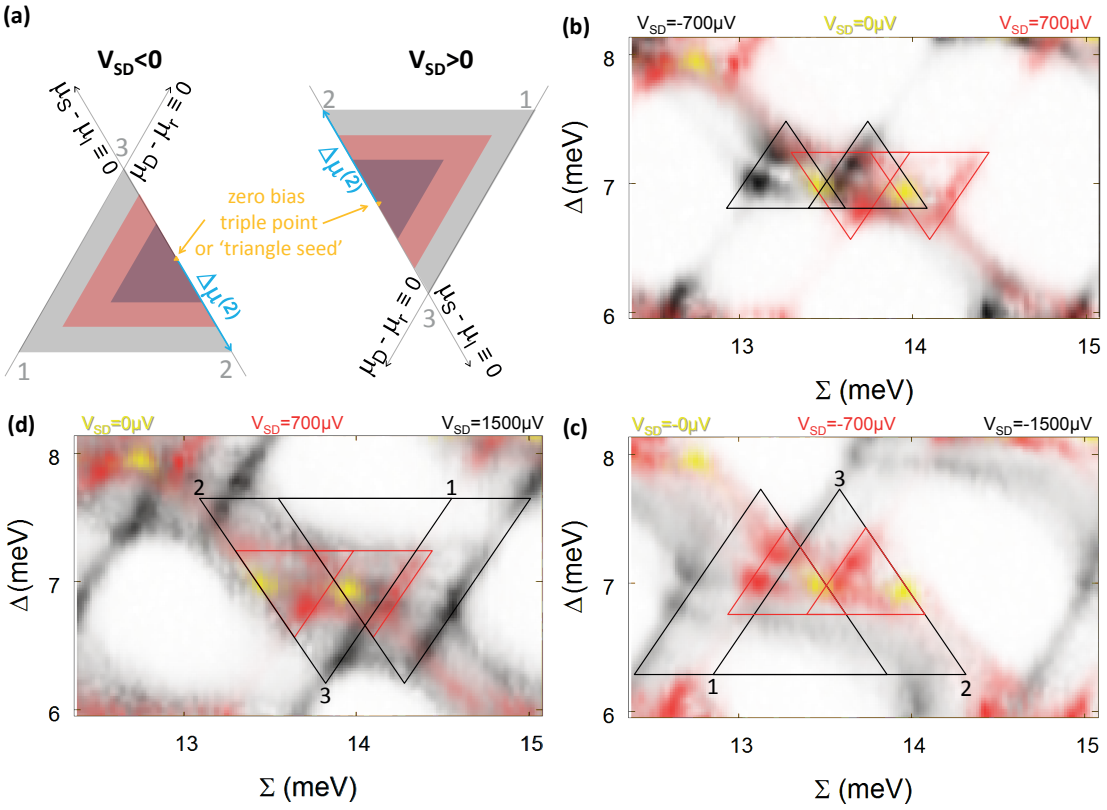

Figure 5.10: Extracting source and drain capacitances from the bias-induced shift of the triple triangles in the gate plain. The overlayed colour scales are optimised for each bias value to make the outline of the triple triangles visible. (a) Sketch of triple triangle evolution with bias. Source (drain) charging energies and capacitances can be obtained from the shift of triple triangle point 2 (1). (b-d) $\mathrm{d}I/\mathrm{d}V$ stability diagrams in the energy plane (Σ, Δ) for in arbitrary units. Equivalent plots are overlayed for different bias values V_{SD}=0 V, $\pm$700 μV and $\pm$1500 μV. (b) compares the triple triangle shift upon bias reversal with respect to the zero bias triple point (yellow point). (c) and (d) show the triple triangle evolution with increasing positive and negative bias.

$\delta\Delta^{(2)} =: \Delta^{(2)}(V_{SD}) - \Delta^{(2)}(0)$ are defined in analogy to $\Delta\mu^{(2)}$ as the coordinate shift of triple triangle cornerpoint 2 due to some bias value V_{SD} compared to zero bias (i. e. w.r.t. the triple *point*). An important point is that a triangle is shifted only if a voltage is applied, and the relevant potential differences are in this case the electrode potential relative to the adjacent quantum dot potentials $(\mu_{SD} - \mu_l)$ and $(\mu_{SD} - \mu_l)$, as our discussion considers only the nearest neighbour dot for the electrodes' capacitive action. If this either differences are zero, the corresponding capacitance does not result in a shift. Consequently, the bias-induced potential shift on the left (right) dot, using the definition of the coordinate transformation in

equation 1.36,

$$\Delta\mu_l^{(2)} := 2\delta\Sigma - \delta\Delta \tag{5.12}$$

$$\Delta\mu_r^{(2)} := 2\delta\Sigma + \delta\Delta \tag{5.13}$$

relates solely to the source (drain) capacitance C_S (C_D). In analogy to the gate efficiency coefficients one can define

$$\alpha_S := \frac{\Delta\mu_l^{(2)}}{\Delta\mu_{SD}} \tag{5.14}$$

$$\alpha_D := \frac{\Delta\mu_r^{(2)}}{\Delta\mu_{SD}}. \tag{5.15}$$

Finally, source and drain capacitances are obtained as the portion $\alpha_{S/D}$ of the respective total dot capacitance $C_{l/r}$

$$C_S = \alpha_S C_l = 76\,\mathrm{aF} \pm 6.2\% \tag{5.16}$$

$$C_D = \alpha_D C_r = 24\,\mathrm{aF} \pm 4.2\%. \tag{5.17}$$

The capacitances and procentual errors stem fom an average of the evaluation of triple triangles at ±700mV and ±1500mV bias voltage.

5.8 Summary

This chapter proposed an evaluation scheme for all charging energies and capacitances, including cross-capacitances C_{Xy} and source and drain capacitances. For the latter, a new evaluation ansatz was developed in section 5.7.
Parallely, characteristic measurements demonstrated that we have successfully fabricated and operated a CNT-based DQDot. The measurements are of high quality, e. g. the hexagonal lattice in figure 5.8, and stability with respect to electrostatic shifts and noise that typically plagues this kind of sample. On the one hand, measurements were stable in time, such that single measurements of over 20 hours duration were possible, and subsequent measurements remained comparable and consistent, even when meanwhile the measurement lines were grounded and ungrounded again. On the other hand, measurements were very stable over large parameter regions. Figure 5.7 is an example of the signal stability over a large range in the gate plane (V_L, V_R). In even larger scans (not shown), more than the excess charge number could be governed by as much as 50 electrons on both left and right dot. As no band gap was observed, the SWCNT can be assumed to be (quasi-) metallic.

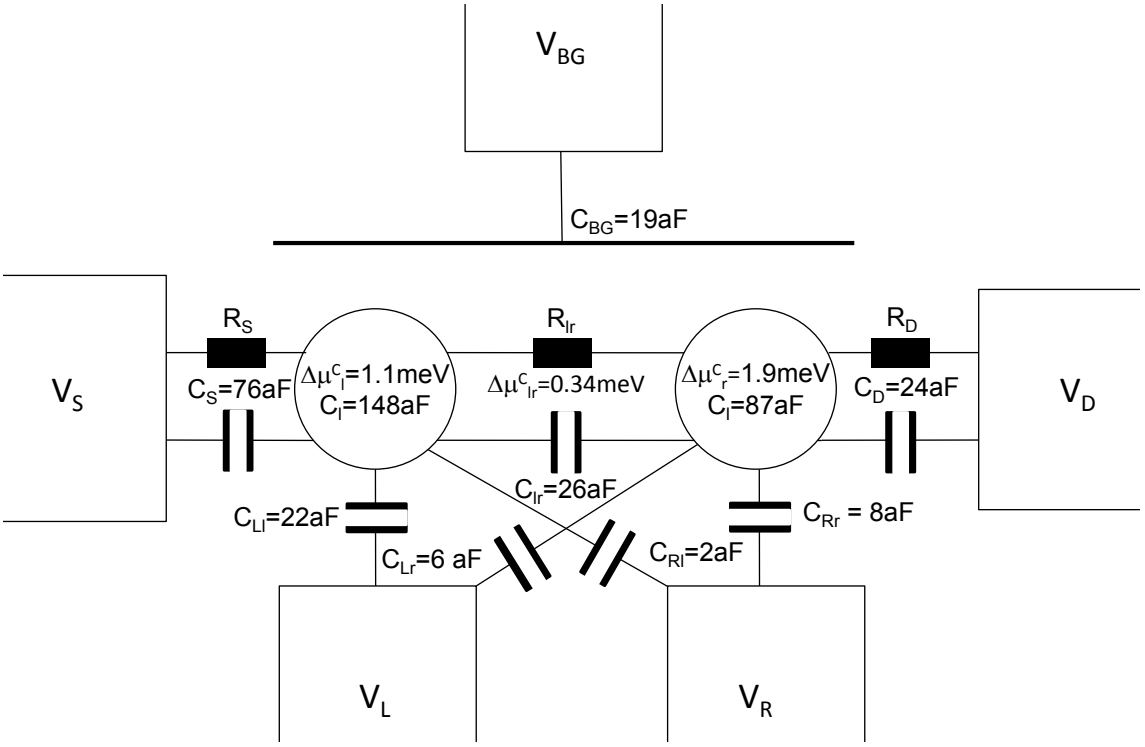

Figure 5.11: Double quantum dot circuitry with evaluated capacitances and charging energies.

The main result, the full capacitive and energetical evaluation of the SWCNT double dot is summarised in figure 5.11. The parameter values are of the same order as reported for similar samples [71, 125].
The consistency of the evaluation may be checked on the difference of total dot capacitances minus the sum of the contributing charge node capacitances (see figure 5.11). In the present case, this difference is

$$\begin{pmatrix} C_l \\ C_r \end{pmatrix} - \begin{pmatrix} C_S+ & & C_{Ll}+ & C_{Rl}+ & & & C_{lr}+ & C_{BG} \\ & C_D+ & & & C_{Lr}+ & C_{Rr}+ & C_{lr}+ & C_{BG} \end{pmatrix} = \begin{pmatrix} 3\% \\ 4\% \end{pmatrix}. \tag{5.18}$$

This means that the sum of evaluated capacitive contributors underestimates the left and right dot charging energies $\Delta\mu_{l/r} = e^2/C_{l/r}$ only by 3-4%. In an ideal case, when all capacitances can be extracted with perfect accuracy, the difference should be zero. In a realistic experimental setting, a lot of parasitic capacitances cannot be pinpointed, most prominent amongst which the capacitance of the middle gate C_M. That it is so small in the case of our sample can be taken as another indication, aside from the gate stability in even long measurement sweeps, as a merit of our sample fabrication procedure, where the *in situ* heating out and high quality Al_2O_3-

dielectric deposition in the ALD vacuum chamber. One can argue that this brings about a stable electrostatic setting, corresponding to a 'clean surface' as if the tube were not covered and in an evacuated chamber, in which the occurrence of parasitic capacitances or charge traps is suppressed.

Chapter 6

Transport spectrum of a SWCNT-based double quantum dot

Chapter 5 introduced the basic measurements on a CNT-based quantum dot. This chapter extends it by investigating higher resolution measurements. From the observed co-tunnelling features in the tunnel current and the simultaneously protocolled differential conductance, information on the the exited state spectrum of the double dot can be derived.

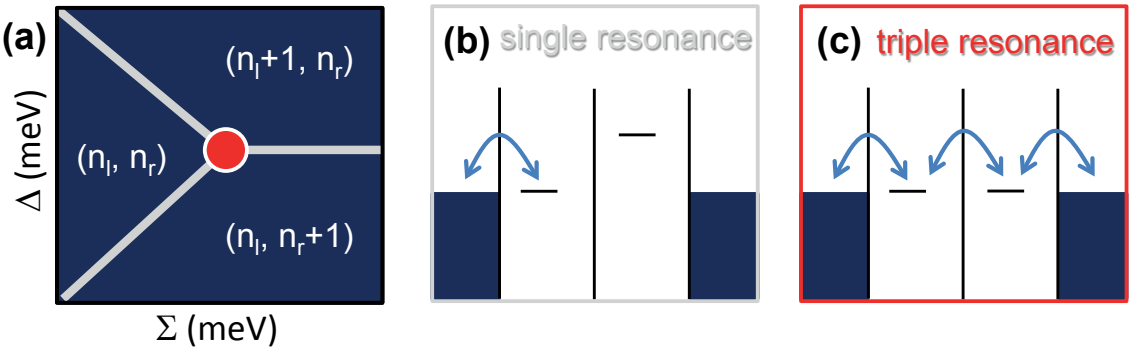

Figure 6.1: *Single* (b) and *triple* (c) resonances in a current map as a function of the gate energy coordinates (Σ, Δ) at zero bias (a) (cf. [74]). These terms denote the number of resonances on the double quantum dot considering only sequential tunneling, i. e. resonances between adjacent charge nodes. Charge nodes are source and drain electrodes or left and right quantum dots.

For the purposes of discussing the types of resonances that occur in a current map over the gate energy plane (Σ, Δ), they are categorised in *single* and *triple* resonances, following a terminology from reference [74]. The terms 'single' and 'triple'

stand for the number of simultaneous resonances on the double quantum dot at a given point in the gate energy plane (Σ, Δ) in a sequential tunnelling picture (see figure 6.1). Therefore the terminology numbers resonances of adjacent charge nodes only, i. e. resonances between the charge nodes *source-left dot*, *interdot*, and *right dot-drain*.

6.1 Single resonances: relative coupling of source and drain electrodes

6.1.1 Lead-dot single resonances

Single resonance bands at finite bias

Single resonances of a double quantum dot designate configurations in the gate energy plane (Σ, Δ) where one dot is resonant with its adjacent electrode while the other dot is not [74]. Such resonances obey either of two possible conditions which, expressed in terms of dot and electrode electro-chemical potentials, read

$$\mu_l - \mu_S = 0 \tag{6.1}$$

$$\mu_r - \mu_D = 0 \tag{6.2}$$

Current can flow through the double quantum dot via co-tunnelling [35] even where sequential tunnelling is forbidden by, e. g., Coulomb blockade. Figure 6.2 (a1) shows a map of tunnelling current I as a function of *average charging* Σ and *detuning* Δ at finite bias V_{SD}=-700 μV. The pairs of triple triangles, appearing in red contrast, are interconnected by bands of finite, lower current (blue-white contrast in figure 6.2). The width of these bands (in Σ-direction), like the dimensions of the triple triangles, is given by the size of the bias window eV_{SD}. The line scan $I(\Sigma)$ in figure 6.2 (b1) illustrates this by the spacing of the vertical blue and red dashed lines.
Figure 6.2 (a2) presents the differential conductance $\mathrm{d}I/\mathrm{d}V$ instead of the dc current over the same gate region as in figure 6.2 (a1), measured simultaneously with a lock-in amplifier (see figure 3.7). In the differential conductance map and its corresponding $\mathrm{d}I/\mathrm{d}V(\Sigma)$ line scan (figure 6.2 (b2)), the inner, exited state structure of *single resonance bands* and *triple resonance triangles* emerges more clearly than in current.

Identifying the resonances of positively and negatively sloped bands

Figure 6.3 sketches the zero bias case of the finite bias measurement in figure 6.2. In this limit, the *single resonance bands* become *single resonance lines*. Along a

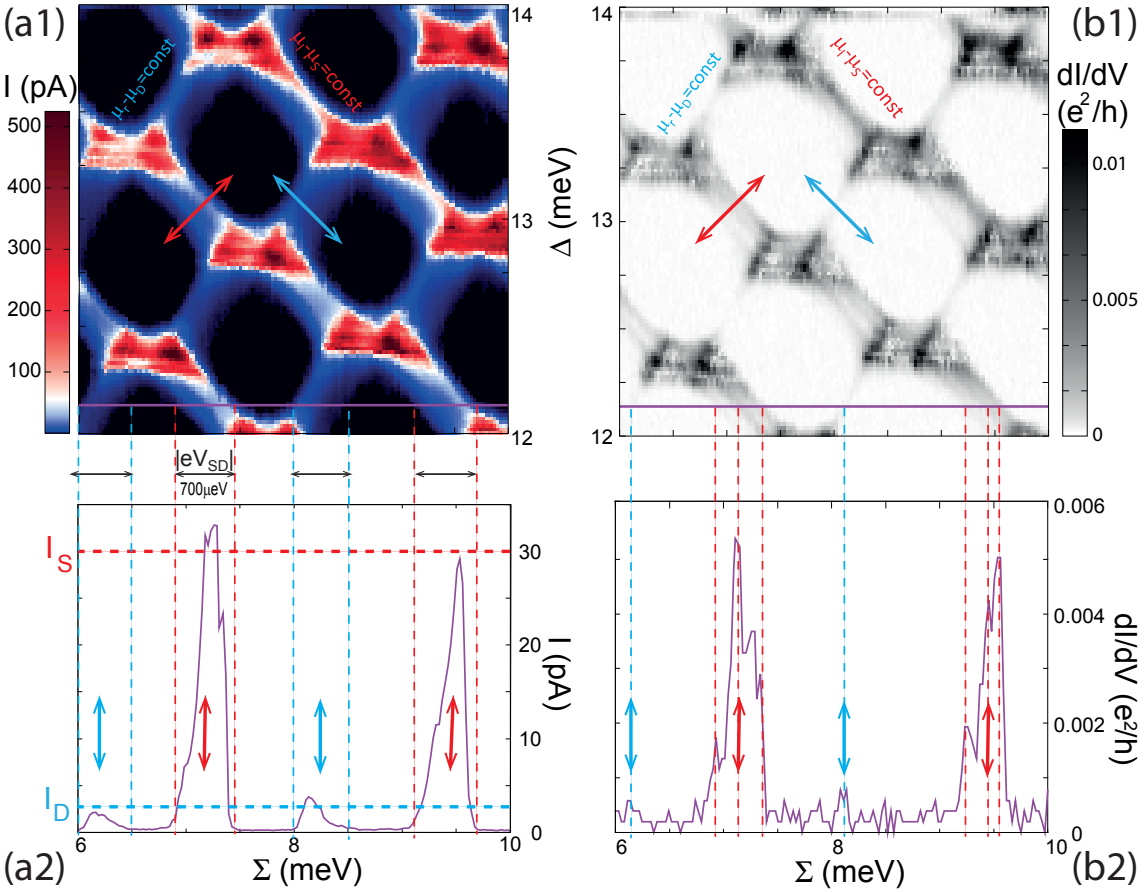

Figure 6.2: (a1) and (a2) Simultaneously measured maps of tunnel current I and differential conductance $\mathrm{d}I/\mathrm{d}V$ as a function of energy-rescaled gate coordinates (Σ, Δ) at V_{SD}=-700 μV. (a2) and (b2) Line scans $I(\Sigma)$ and $\mathrm{d}I/\mathrm{d}V(\Sigma)$ along the violet lines in (a1) and (b1) through two sets left and right dot 'single resonances'. The ac bias excitation was 10 μeV.

negatively-sloped *single resonance line* (marked by red double-headed arrows in figures 6.2 and 6.3), the source electrode is in resonance with right dot ($\mu_S - \mu_l = 0$) and charge fluctuation is only possible between source electrode and left dot ($(n_l, n_r) \rightleftharpoons (n_l+1, n_r)$). Analogously, along a positively-sloped *single resonance line* (marked by cyan double-headed arrows in figures 6.2 and 6.3), the drain electrode is in resonance with left dot ($\mu_D - \mu_r = 0$) and charge fluctuation is only possible between drain electrode and right dot ($(n_l, n_r) \rightleftharpoons (n_l, n_r+1)$). If only one dot is in resonance with its adjacent electrode, the electron number on this dot can fluctuate and current can flow via co-tunnelling processes (cf. figure 6.3 (c)).

Following reference [74], the ratio γ of *source-to-left dot* and *drain-to-right dot* coupling can be coarsely estimated by the ratio of their corresponding current or differ-

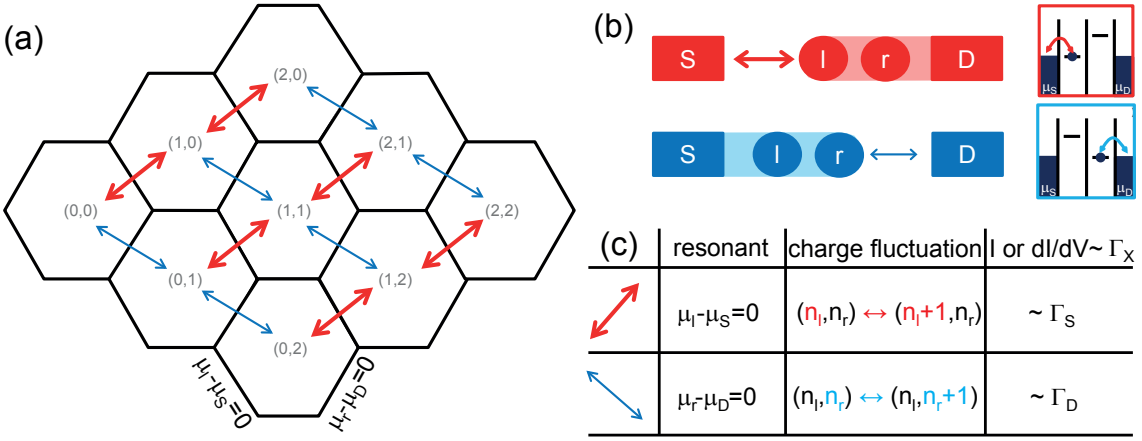

Figure 6.3: (a) Sketched map of the $I(\Sigma, \Delta)$ or $\mathrm{d}I/\mathrm{d}V(\Sigma, \Delta)$ honeycomb lattice (cf, figure 6.2). Double headed arrows indicate left and right dot single resonances. (n_l, n_r) denote the excess electron occupancy on left and right dot. (b) A simple model to describe 'co-tunneling' transport at these single resonances as quantum point contacts. (c) If one dot is in resonance with its adjacent electrode, the electrode number on the other dot can fluctuate on this dot while the charge on the other remains constant.

ential conductance.

Figure 6.2 (a2) and (b2) show line scans of the current and differential conductance traced along the violet lines in the respective two dimensional maps. There is a large asymmetry in peak heights of negatively-sloped (e. g. I_S) versus positively-sloped (e. g. I_D) single resonances in both current and differential conductance. Averaging the maximum peak current over the two periods negatively- and positively-sloped single resonances, the relative source-versus-drain coupling can be estimated to

$$\gamma = 8.2 \pm 0.7 \tag{6.3}$$

from the current data (cf. figure 6.2 (a2)) and to

$$\gamma = 9.7 \pm 1.4 \tag{6.4}$$

from the differential conductance data (cf. figure 6.2 (b2)).

This pronounced asymmetry of source over drain coupling γ is observed over a large area in gate space (Σ, Δ) (over more than 50 electrons on left and right dot), implying that the effect has but a weak gate dependence. It is also bias-independent (as evaluated over the investigated bias range $V_{SD} = -1.5, ..., 1.5$ meV) and is, in particular, not reversed (i. e. $\gamma \to 1/\gamma$) upon bias reversal, as expected for an effect that originates from asymmetric coupling of two nano-fabricated electrodes to the respective adjacent dots.

Electron temperature

Figure 6.4 (b) takes a line scan across a *single resonance* along the red line in figure 6.4 (a), scaled to energy as a function of the right dot electrochemical potential μ_r offset by $-\mu_D$. A smoothened black curve is superimposed on the raw data (black scatter). The red curve is a Gaussian fit that serves to extract the FMHW of this 'single resonance' Coulomb peak of the right dot to the drain electrode. From the FMHW, the electron temperature can be estimated to T_{el}=431 mK=37 μeV/k_{B} [20]. For comparison, the cryostat bath temperature was measured to T=280 mK=24 μeV/k_{B}.

6.1.2 Dot-dot single resonances: inter-triple point connection lines

Figure 6.4 (a) shows a map of tunnel current versus the voltages (V_L, V_R), applied to the gate fingers above left and right quantum dots. Even at zero bias excitation (V_{SD} ≈0, up to a small experimental offset $\ll k_{\mathrm{B}}T$), the low-current, few pA-scale co-tunnelling lines can be clearly resolved. The vertical texture is an artifact of the experimental scanning direction. It stems from small charge fluctuations between $I(V_R)$ line scans between two left local gate voltages V_L and $V_L + \delta V_L$ that build up the two-dimensional map $I(V_L, V_R)$. Considering that this high-resolution gate voltage scan took about 12 hours of measurement time, the electrostatic stability of this double dot measurement is remarkable.
Dot-dot single resonances give rise to co-tunnelling lines that connect each pair of triple points in the gate stability diagram figure 6.4 (a). The current is low compared to the current at the triple resonance points or at the *lead-dot* single resonance lines. An exemplary electronic configuration on the double dot along an inter-triple point pair connection line is sketched in figure 6.5, for zero bias and in the 'atomic description' of the DQDot. Along the grey line between the pair of two triple points (full and empty circles), neither of the two dots are in resonance with the electrodes. The energy diagram is sketched for an exemplary point on this line (★). As the interdot detuning is zero, the electron on the dot can fluctuate between the two dots: $(0,1) \rightleftharpoons (1,0)$. The sequential tunneling, 'atomic' model of the DQDot predicts that the system should be in Coulomb blockade here. However, a clear line appears between the dots at zero interdot detuning Δ.

Multiple interdot connection lines

Figure 6.4 (c) takes a $I(\mu_r)$ line trace along the pink and orange line in figure 6.4 (a) through the interconnection lines of two sets of triple point pairs, plotting current as a function the tunnel current against the right dot chemical potential with arbitrary

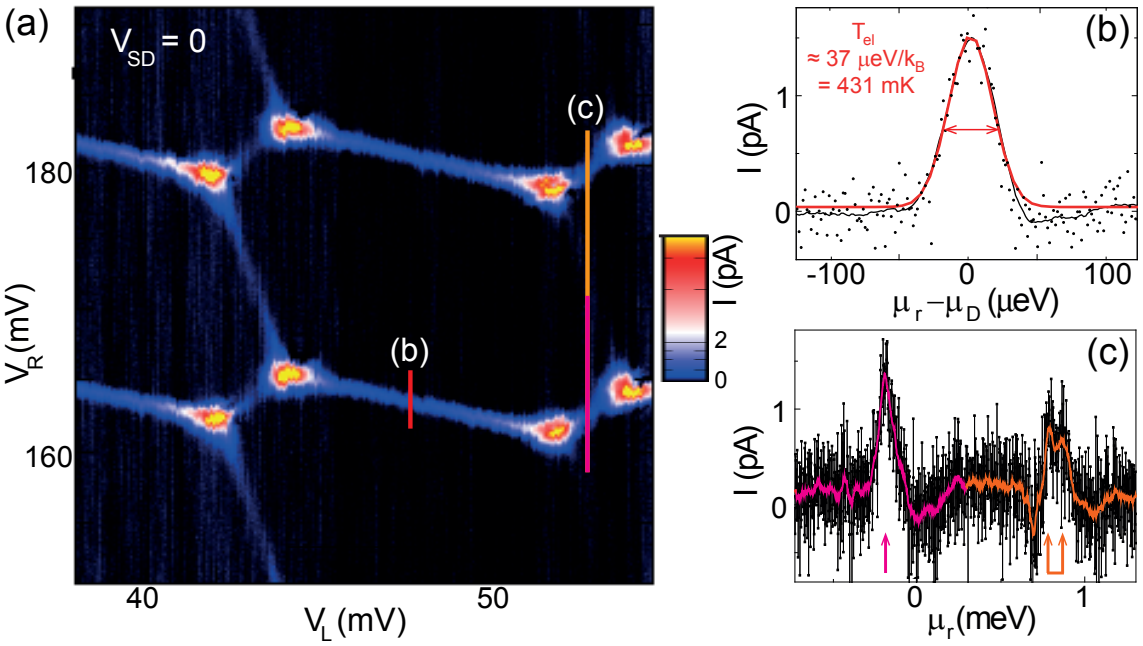

Figure 6.4: (a) Tunnel current I as a function of right and left gate voltage (V_L, V_R) at zero bias, cryostat bath temperature T=280 mK=24 μeV/k_B and 2 T. Even at zero bias, the hexagonal triple point lattice interconnected by co-tunnelling lines is visible. (b) Tunnel current line scan along the red line in subplot (a) over a 'single resonance' $(\mu_r - \mu_D = 0)$ as function of right dot chemical potential μ_r relative to the drain chemical potential. The black scatter is the raw data. The solid black line results from an FFT smoothening. The red curve is a Gaussian fit. From the FMHW of this 'single resonance' of the right dot to the drain electrode, the electron temperature can be estimated to T=431 mK=37 μeV/k_B. (c) Line scan along the pink and orange line in (a) through the interconnection lines of two triple points, plotting current as a function the tunnel current against the right dot chemical potential with arbitrary offset. The smoothened magenta line bears a single peak, the orange line a double peak split by 90 μeV.

offset. The smoothened magenta line bears a single peak, the orange line a double peak. The energy splitting of 90 μeV is of the same order as the excitation energies found here (cf. table 6.1).

A simple ansatz to explain the observation of a split interdot connection line is to appreciate that a co-tunnelling line between a triple point pair occurs not only if the ground states of left and right dot are undetuned. It can, in principle, occur whenever some ground or exited states on one dot are resonant with exited states on the other (cf. figure 6.6). Often, this double line feature was observed around zero magnetic field and ±3 T and disappeared for smaller and larger magnetic field values. It remains, however, unclear how the excitation energy is provided at nearly

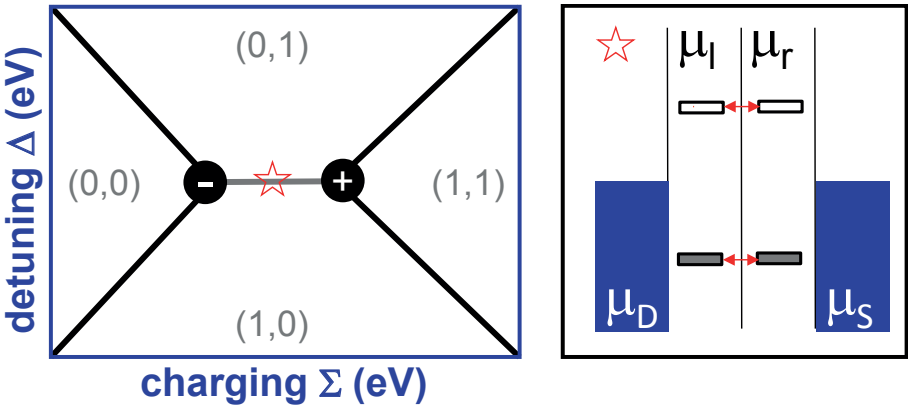

Figure 6.5: Inter-triple point pair connection line described in the 'atomic ansatz'. Along the grey line between the pair of two triple points (full and empty circles), neither of the two dots are in resonance with the electrodes. The energy diagram is skteched for an exemplary point on this line (star). As the interdot detuning is zero, the electron on the dot can fluctuate from right to left dot: $(0,1) \rightleftharpoons (1,0)$. The 'atomic ansatz' predicts that the system should be in Coulomb blockade. However, a clear line appears between the dots at zero interdot detuning Δ.

zero bias. This feature has been observed at several charge configurations in the gate plane, but no clear systematic pattern was observed that would allow more involved conclusions on the origin of the effect.

6.2 Triple resonances

In the large area $\mathrm{d}I/\mathrm{d}V(\Sigma,\Delta)$ map at finite bias V_{SD} =-700 μeV in figure 6.2 (a1), the triple triangles disclose a rich inner structure. A higher resolution scan on one triple triangle pair (presented in figure 6.7 (a)) reveals this inner structure in greater detail. The differential conductance map resolves the exited state lines more clearly than the complementary, simultaneously measured current map (figure 6.7 (b)).
In differential conductance, a peak (or, in general, extremum) feature is expected whenever an exited state starts contributing to transport. In the present experimental data, however, this 'peak structure' rather looks like 'bands' that must be understood as 'smeared-out peaks'. Besides inherent line width broadening, the peaks are further smeared out by temperature $k_{\mathrm{B}}T_{el} \approx 37\,\mu$eV, electrostatic fluctuations, noise and the ac bias excitation of here $10\,\mu$eV r.m.s. It must also be kept in mind that the experimental 'derivative of current' $\mathrm{d}I/\mathrm{d}V := I/V_{SD}^{ac}$ is but an imperfect approximation to differential conductance - for one thing, the interval V_{SD}^{ac} is finite rather than infinitesimal. For another, figure 6.7 (a) shows the derivative

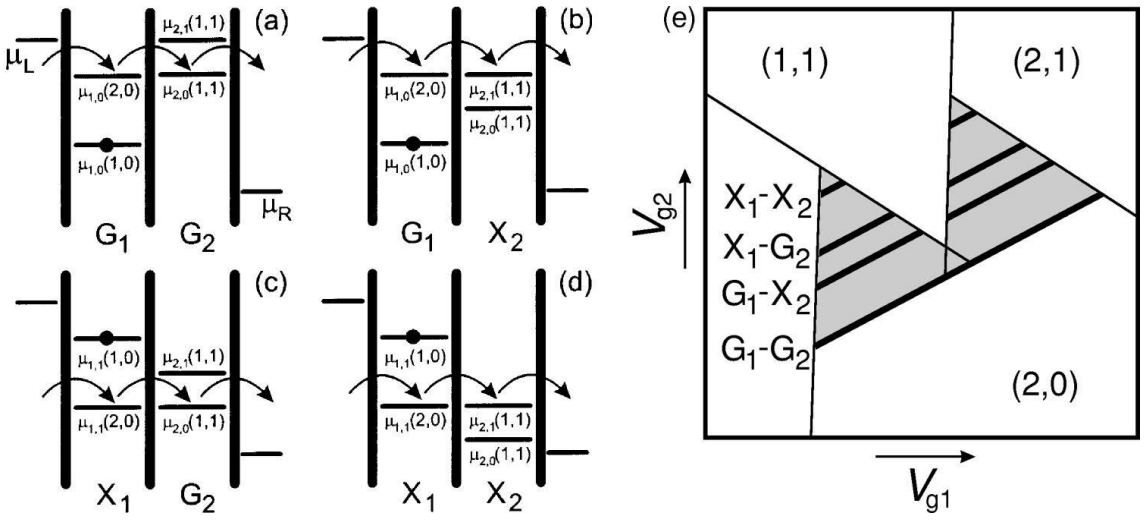

Figure 6.6: Schematic diagrams showing the possible alignments of the electrochemical potentials in the case of two levels per dot. (a) The first electrochemical potentials to align correspond to the ground states of both dots, G1 and G2. (b) When moving down the levels in the right dot, the next states to align are the ground state of the left dot, G1, and the first excited state of the right dot, X2. (c) Shifting the levels of the right dot further down results in transport through the first exited state of the left dot, X1, and the right dot ground state, G2. (d) Finally, the excited states X1 and X2 align. (e) Schematic stability diagram corresponding to the finite bias diagrams. The black solid lines within the gray triangles correspond, from bottom to top, to the level alignments shown in (a)-(d) respectively. Figure and caption taken from [26].

by a coordinate, the bias V_{SD}, in a map $\mathrm{d}I/\mathrm{d}V(\Sigma, \Delta)$ of two other, independent coordinates. Care is therefore due when ascribing a physical interpretation to features that stand for a change in tunnel current with respect to one coordinate as a function of two others. This qualitative discussion therefore adopts a phenomenological description of the data. The lines in figure 6.7 simply highlights a change in contrast. The highlighted features in the *single resonance band* mark that its width is given by the bias $\mathrm{e}V_{SD}$.
The exited state structure of a triple triangle can be charted by considering two types of resonances: *dot-lead resonances* and *dot-dot resonances*.

Dot-lead resonances

Dot-lead resonances comprise the single resonances and, in particular, all triple resonances - as all triple resonances are also single (dot-lead) resonances, It is therefore clear that the single resonance lines extend into the triple triangles. Figure 6.7 (a) demonstrates this by highlighting the positively sloped single resonance lines (red

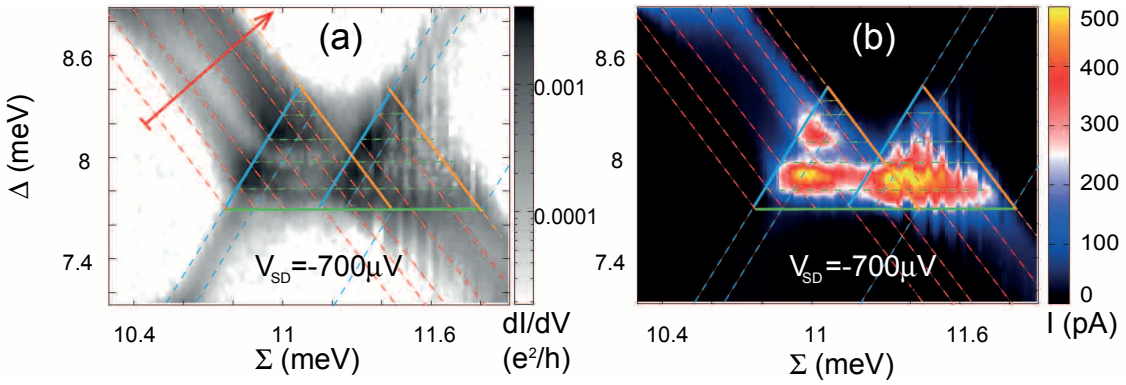

Figure 6.7: Detailed excitation structure in and around a sample triple triangle pair. (a) Differential conductance $\mathrm{d}I/\mathrm{d}V$ in logarithmic scale at constant bias eV_{SD}=- 700 μeV and zero magnetic field, as a function of gate coordinates, rescaled to energy coordinates (Σ, Δ). Red lines ($\mu_r - \mu_D = const$, labelled α through ω), cyan lines ($\mu_l - \mu_S = const$) and green horizontal lines highlight changes in contrast as a guide to the eye. Their prolongation into the triple triangle parcels out its exited state structure. (b) Same (Σ, Δ) range as in (a) showing the simultaneously recorded tunnel current I in linear scale.

and orange dashed lines) and negatively sloped ones (cyan dashed lines) on a differential conductance map of (Σ, Δ) in logarithmic scale.

A line within a *single resonance band* marks that another exited state contributes to transport through the double dot; opening up an additional transport channel. An additional transport channel does not necessarily increase the tunnel current (cf. darker area between green lines that correspond to red dashed lines γ and δ in figure 6.7 (b)).

Dot-dot resonances

Dot-dot resonances occur whenever a (ground or exited) state on the left dot is resonant with a (ground or exited) state on the right dot - and both are within the bias window. Figure 6.6 illustrates a possible spectroscopy of these horizontal lines. By definition of the gate energy coordinates (Σ, Δ), these resonances with equal left and right electro-chemical potentials $\mu_{l/r}$ have zero detuning $\Delta := \mu_r - \mu_l$ - with a constant off-set in Δ that is owed to the double role of the Δ-coordinate as a measure for interdot detuning at a given interdot charge transition $(n_l + 1, n_r - 1) \leftrightharpoons (n_l, n_r)$ and large scale energy coordinate. In the data, corresponding features resonances correspond as horizontal lines, as indicated by the green lines in figure 6.7 (a).

Constructing the triple triangle from the resonance lines

The triple triangles can be phenomenologically 'constructed' in the data by considering the different types of resonance lines. At a triple resonance states on both dots are, within the bias range, in resonance with their respective electrode and each other.
This can be reformulated by three conditions:

1. A triple point must be in a (Σ, Δ)-area where the single positively sloped resonance band (μ_S resonant with μ_l) and the negatively sloped one (μ_D resonant with μ_r) overlap.

2. Both dots must have states within the bias window eV_{SD}.

3. Inelastic sequential tunnelling is only possible via emission of boson (e. g. an acoustic phonon [127]) but not via absorption (justified by the phonon bath being 'frozen out' at cryogenic temperatures.)

The first two conditions simply restate the defining conditions for 'triple resonance' at finite bias, including inelastic tunnelling processes. If only for these conditions (modelling the double dot as two interacting atoms), the 'triple triangles' would be 'triple diamonds'; for the example of negative bias the upper diamond half would be the 'inelastic tunnelling triangle under emission' and the lower half 'inelastic tunnelling triangle under absorption'. Condition 3 confines the triple resonance area to one half of the single resonance bands overlap only, making it a triangle. The physical implication is that inelastic tunnel processes are only possible under emission of an energy quantum (i. e. a photon or phonon), but not by absorption. This statement is supported by experimental observation from here presented as well as other double dot experiments (e. g. [20, 74, 125]). From a theoretical standpoint, the absence of inelastic sequential tunnelling events under absorption is less clear. In aforementioned atomic model, it is plausible that inelastic tunnelling processes that require absorption of energy are strongly suppressed at low temperature as excitation s are 'frozen out' - which is a weaker statement than total suppression.
Above three conditions explain why sequential tunnelling through the double dot can only occur in the triangular area defined by the solid orange, cyan and green lines in figures 6.7 (a) and (b). The solid green line is called *base line of the triple triangle* because along it the ground states of left and right dot are resonant.

Bias evolution of exited state structure

Figure 6.8 (a) shows a measurement of differential conductance across a single resonance band as a function of μ_l (with $\mu_D - \mu_r = const$), where $\mathrm{d}I/\,\mathrm{d}V(\mu_l)$-traces

for different bias values are assembled into a map. Effectively, the plot shows a Coulomb diamond pattern of the left dot as if it were a single, isolated quantum dot. The diamonds are slightly skewed due to the capacitive action of source and drain electrode (cf. section 5.7). This measurement technique allows to probe the exited state structure in its bias dependence for either dot separately.
The dashed red lines in figure 6.8 (b) identify possible extrema (labelled α through ϵ) in the $\mathrm{d}I/\mathrm{d}V(V_{SD})$ line scan. The peak features are smeared out by e. g. the electron temperature or the ac bias. The extrema are related to exited states participating in transport.

Exited state energy scales

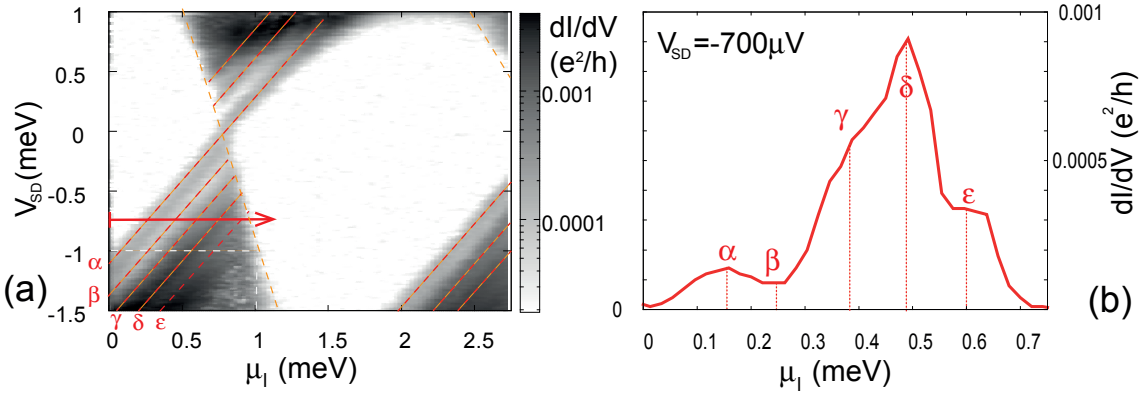

Figure 6.8: (a) Coulomb diamonds of a single *source to left quantum dot* resonance: $\mathrm{d}I/\mathrm{d}V$ plotted against bias V_{SD} and left dot chemical potential μ_l (with arbitrary offset). The line scans along the red arows in figure 6.7 (a) and figure 6.8 (a) are equivalent. (b) Line scan along the red arrow from (b1) of $\mathrm{d}I/\mathrm{d}V$ against μ_l.

Table 6.1: Exited state line spacings from figure 6.8 (b)

$\lvert\alpha-\beta\rvert$	$\lvert\beta-\gamma\rvert$	$\lvert\gamma-\delta\rvert$	$\lvert\delta-\epsilon\rvert$
90 μeV	140 μeV	110 μeV	115 μeV

Figure 6.8 (b) is a $\mathrm{d}I/\mathrm{d}V(\mu_l)$ line scan taken along the red arrow in figure 6.8 (a). The extremum-to-extremum distance provides a measure for the typical excitation energies in the here investigated SWCNT-based double quantum dot device. They are smaller by a factor of two but still of the same order as reported from a similar CNT-based double quantum dot of comparable dimensions (length of the CNT

segments acting as quantum dots $\approx 500\,\mathrm{nm}$) [19]. With these comparatively small excitation energies, the transport situation becomes complex when increasing the detuning away from the base line as more and more exited states can contribute to transport.

6.3 Asymmetry in current filling of left and right triple triangle

Throughout the data it can be observed that the left, *clockwise* triple triangle (labelled $\ominus$) has a different current pattern and level than its paired right, *counter-clockwise* triple triangle (labelled $\oplus$). The $I(\Sigma, \Delta)$ map in figure 6.9 (a) provides a typical example for this asymmetry in triple triangle 'current filling'.
In an *atomic model* of the double quantum dot - when only considering sequential tunnelling and disregarding spin effects - one would expect a symmetric current filling of a triple triangle pair. A handwaving argument can be derived from the nomenclature of left and right resonances of a pair as 'electron' and 'hole' triangles or points [26]. Two of the three areas of constant charge are the same for electron and hole triangle, e. g. $(n_l, n_r) = (1, 0)$ and $(2, 0)$ (cf. the charge state map in figure 1.10). The third charge state (n_l, n_r) is different for electron $((1, 0))$ and hole $((2, 1))$ triple resonance. The assignment of charge states assumes electrons e as charge carriers. Equivalently, one can describe charge transport in double dot in terms of holes h. The $(2e, 1e)$ charge state, e. g., can be written as $(0h, 1h)$. Considering that holes travel 'upwards in energy' and assuming $e - h$ symmetry, the transport of electron and hole triangles is equivalent. Consequently, the current pattern of e- and h-triangles should be the same:

$$e \;:\; (1e, 0e) \rightleftharpoons (2e, 0e) \rightleftharpoons (1e, 1e) \rightleftharpoons (1e, 0e) \tag{6.5}$$

$$h \;:\; (0h, 1h) \rightleftharpoons (1h, 1h) \rightleftharpoons (0h, 2h) \rightleftharpoons (0h, 1h). \tag{6.6}$$

The experimental reality breaks this e- and h-triangle symmetry, as already to be seen in figure 6.7. In the following, three mechanisms are discussed that can give rise to this current asymmetry.

Mechanism 1: Asymmetry of source versus drain impacts sequential tunneling?

The first mechanism that is possibly responsible for the *current asymmetry* is the effect of asymmetric source/drain coupling on the sequential tunneling. Its impact can be discussed with a simple rate equation ansatz. This discussion is restricted to

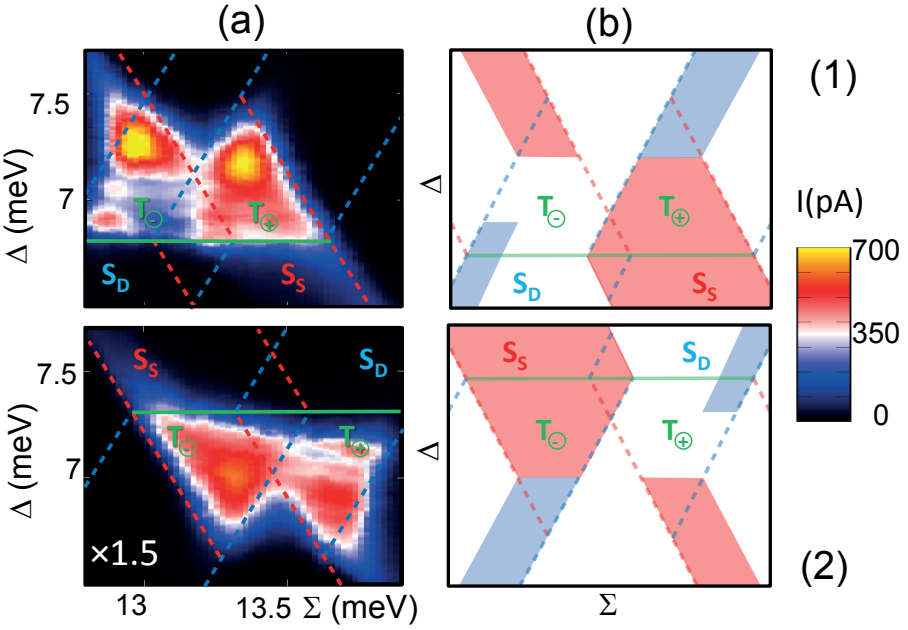

Figure 6.9: (a1) Map of the current $I(\Sigma, \Delta)$ as a function of charging and detuning coordinates, taken at V_{SD} =-700 meV and B=-3.75 T. Asymmetry in current: the current in the lower section of left and right triple triangle pair differs significantly. (b1) Illustration how co-tunnelling processes of *single resonances* can extend into the triple triangle, providing an additional co-tunnelling transport channel. An asymmetry in source (region S_S) and drain (region S_D) can thus cause a current asymmetry in left (region $T_\ominus$) and right (region $T_\oplus$) triple triangle. (a2) and (b2) as (a1) and (b2) for positive bias (V_{SD} =-700 meV).

the charge states only. The dimension of the parameter space to describe a DQDot transport process equals the number of involved states. Different spin states per charge configuration (e. g. a singlet $S(1,1)$ and the triplets $T(1,1)$ are not included as they would not add to qualitative argument while bloating the parameter space. Figure 6.10 illustrates, for an arbitrary choice of charge states (n_l, n_r), that sequential transport at each triple point ($\ominus/\oplus$) can be described as a sequence of three charge fluctuations

$$\ominus \;:\; (1,0) \rightleftharpoons (2,0) \rightleftharpoons (1,1) \rightleftharpoons (1,0) \tag{6.7}$$

$$\oplus \;:\; (2,1) \rightleftharpoons (1,1) \rightleftharpoons (2,0) \rightleftharpoons (2,1). \tag{6.8}$$

The sequence of the two paired triple triangles differs only in one charge configuration ($(1,0)$ vs. $(2,1)$). Following the scheme in figure 6.10, a master equation for all three

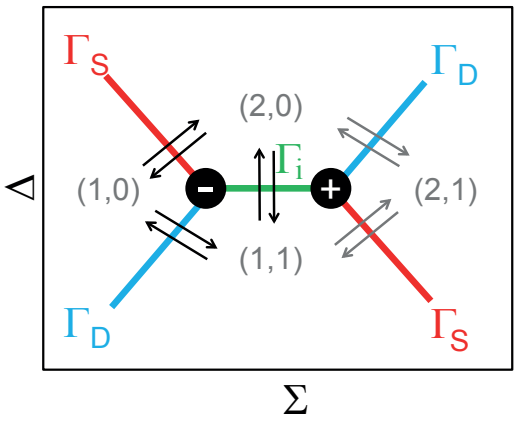

Figure 6.10: Illustration of transport at triple points labelled − and + for an example electron occupation (n_l, n_r) of the double dot at zero bias. A sequential tunnelling process can be described in terms of a cycle of three consecutive charge transitions. In this sketch, a transport cycle is represented by crossing a red, green and cyan line. The lines are colour-coded and labelled with the relevant coupling energy, i. e. source to left dot coupling Γ_S, drain to right dot coupling Γ_D and interdot coupling Γ_i.

involved charge configurations for the $\ominus$-triangle

$$\dot{P}_{10} = \Gamma_S[P_{20} - P_{10}] + \Gamma_D[P_{11} - P_{10}] \tag{6.9}$$
$$\dot{P}_{11} = \Gamma_S[P_{10} - P_{11}] + \Gamma_I[P_{20} - P_{11}] \tag{6.10}$$
$$\dot{P}_{20} = \Gamma_S[P_{20} - P_{20}] + \Gamma_I[P_{11} - P_{20}] \tag{6.11}$$

is easily derived. Densities of states and occupation probabilities of the electrodes are absorbed in the Γ. For example, the change in probabiliy $\dot{P}_{10}$ that the system is in the $(n_l, n_r) = (1, 0)$ charge state is expressed as a sum of the occupation probabilities P_{kj}, $kj \in \{10, 11, 20\}$, multiplied by the appropriate coupling energy. Reformulating the three master equations conveniently in matrix notation yields

$$\dot{\vec{P}}_{\ominus} = \mathbf{\Gamma}_{\ominus}\vec{P}_{\ominus} \tag{6.12}$$
$$\begin{pmatrix} \dot{P}_{10} \\ \dot{P}_{11} \\ \dot{P}_{20} \end{pmatrix} = \underbrace{\begin{pmatrix} -\Gamma_S - \Gamma_D & \Gamma_D & \Gamma_S \\ \Gamma_D & -\Gamma_D - \Gamma_i & \Gamma_i \\ \Gamma_S & \Gamma_i & -\Gamma_S - \Gamma_i \end{pmatrix}}_{=:\mathbf{\Gamma}_{\ominus}} \begin{pmatrix} P_{10} \\ P_{11} \\ P_{20} \end{pmatrix}$$

for the *clockwise*triple triangle ($\ominus$) . Similarly one obtains for the *counter-clockwise* triple triangle ($\oplus$)

$$\dot{\vec{P}}_{\oplus} = \mathbf{\Gamma}_{\oplus}\vec{P}_{\oplus} \tag{6.13}$$
$$\begin{pmatrix} \dot{P}_{21} \\ \dot{P}_{11} \\ \dot{P}_{20} \end{pmatrix} = \underbrace{\begin{pmatrix} -\Gamma_D - \Gamma_S & \Gamma_S & \Gamma_D \\ \Gamma_S & -\Gamma_S - \Gamma_i & \Gamma_i \\ \Gamma_D & \Gamma_i & -\Gamma_D - \Gamma_i \end{pmatrix}}_{=:\mathbf{\Gamma}_{\oplus}} \begin{pmatrix} P_{21} \\ P_{11} \\ P_{20} \end{pmatrix}.$$

Both *coupling energy matrices* are symmetric, i e. $\mathbf{\Gamma}_{\ominus/\oplus} = \mathbf{\Gamma}^T_{\ominus/\oplus}$.

Solving $\det(\mathbf{\Gamma}_{\ominus} - \gamma\mathbf{1}) = 0$ one obtains the two non-zero eigenvalues

$$\gamma_{1/2} = \sum_{X=S,D,i} \Gamma_X \pm \sqrt{\Gamma_X^2 - |\epsilon_{XYZ}|\Gamma_Y\Gamma_Z} \tag{6.14}$$

where $|\epsilon_{XYZ}|$ is the modulus of the fully anti-symmetric tensor. Note that $\gamma_{1/2}$ are invariant under the exchange $\Gamma_S \longleftrightarrow \Gamma_D$. Also, exchanging $\Gamma_S \longleftrightarrow \Gamma_D$ transforms $\mathbf{\Gamma}_{\oplus}$ into $\mathbf{\Gamma}_{\ominus}$, i. e.

$$\mathbf{\Gamma}_{\oplus} \;=\; \mathbf{\Gamma}_{\ominus}(\Gamma_S \longleftrightarrow \Gamma_D). \tag{6.15}$$

Consequently, the two matrices share the same eigenvalues. Invoking an argument from linear algebra, the two matrices are equivalent because if they are the same in one representation then in all representations. Simply put $\mathbf{\Gamma}_{\ominus}$ and $\mathbf{\Gamma}_{\oplus}$ take both the same diagonal form in their eigenbasis representations. However, the two master equations 6.13 and 6.15 act on different probability spaces; the question arises whether the probabilities P_{10} and P_{21} take the same value. Considering the steady state conditions

$$\sum_{\text{tripe triangle } \ominus/\oplus} P_{n_l n_r} = 1 \quad \Rightarrow \quad \sum_{\text{tripe triangle } \ominus/\oplus} \dot{P}_{n_l n_r} = 0 \tag{6.16}$$

and assuming that $P_{11}^{\ominus} = P_{11}^{\oplus}$ and $P_{20}^{\ominus} = P_{20}^{\oplus}$ it follows that $P_{10}^{\ominus} = P_{21}^{\oplus}$ have indeed the same probability and that the $\ominus$ and $\oplus$ probability spaces can be regarded as equivalent.
Thus, this simple rate model argumentation predicts that the sequential tunnelling is symmetric over a triple triangle pair - in contradiction to the experimental evidence (cf. figure 6.9 (a)): mechanism 1 does not explain the observed asymmetry.

Mechanism 2: Asymmetry of source versus drain impacts co-tunneling?

The second mechanism from which the current filling asymmetry within a triple triangle pair may arise also considers the asymmetry in source and drain couplings to the respective quantum dots. While before only sequential tunnelling was considered, now the effect of the relative source-versus-drain coupling on the triple triangle current via co-tunnelling processes is discussed.
As stated before in section 6.2, *dot-lead resonances* give rise to finite current outside the triple triangles. This can be ascribed to co-tunnelling processes opening up conduction channels. Experimental proof of finite current due to these *single resonances* is provided by the finite current in the (Σ, Δ)-region labelled as S_S (for drain-right dot single resonances, $I \propto \Gamma_S$) and S_D (for source-left dot single resonances, $I \propto \Gamma_D$) in figure 6.9 (a).

Now, *triple resonances*, i. e. any point within the triple triangle areas, all are in particular dot-lead resonances. Consequently, there is no reason to assume that the 'co-tunnelling channels' should close when going from a single resonance (Σ, Δ)-region, e. g. S_S, into a triple resonance one, e. g. $T_\oplus$ (cf. figure 6.9). Rephrasing this statement positively, the co-tunnelling channels are expected to extend into the triple triangles.
The ensuing question is how this co-tunnelling contribution can be quantified and to what extent it accounts for the triple triangle current asymmetry. In the previous section, section 6.2, it was demonstrated and charted how complex the inner structure of the triple triangles at finite bias can be. Here, however, it seems more conducive to give a rough quantitative estimate based on the exemplary measurement presented in figure 6.9 (a): first, an average current value is estimated for each of the (Σ, Δ)-regions $T_\ominus, T_\oplus, S_S, S_D$, yielding

$$I(T_\oplus) \approx 450 \text{ pA} \tag{6.17}$$
$$I(T_\ominus) \approx 300 \text{ pA} \tag{6.18}$$
$$I(S_S) \approx 150 \text{ pA} \tag{6.19}$$
$$I(S_D) \approx 0 \text{ pA}; \tag{6.20}$$

second, it shall be assumed that current contributions from sequential and co-tunnelling channels simply add up. The contributions $I(S_D)$ and $I(S_S)$ are outside the triple resonance areas can therefore stem only from co-tunneling. Subtracting the average currents of the single resonance regions S_D/S_S from the neighbouring triple point regions $T_\ominus/T_\oplus$ provides estimates for the sequential current contribution per region. Comparing these contributions yields

$$I(T_\oplus) - I(S_S) \approx I(T_\ominus) - I(S_D). \tag{6.21}$$

This rough argument provides an indication that the asymmetry mainly stems from lead-dot resonance co-tunnelling and the asymmetry in source versus drain coupling. This implies that, for the present data set, the sequential current contributions are indeed symmetric over a triple triangle pair.

Mechanism 3: Asymmetry due to dots acting as gate tuning the lead-dot coupling?

Reference [20] makes a similar observation of current asymmetry in a triple triangle pair in a sequential GaAs double quantum dot. As a possible cause for this asymmetry they suggest that the dot-lead couplings $\Gamma_S := \Gamma_{Sl}$ or $\Gamma_D := \Gamma_{Dr}$ depend on the charge state n_r or n_l of the *other* dot. This implies that a dot effectively acts

as a gate electrode on the coupling of the neighbouring dot to its adjacent lead. Reference [20] also observes a dependence of this asymmetry on the bias sign. In our data, a reversal of the asymmetry upon bias reversal is observed (compare figures 6.9 (1) versus 6.9 (2)). This effect is, however, is well accounted for with the previously discussed co-tunnelling contribution.

6.4 Summary

After the quantitative evaluation of the DQDot energy scales in chapter 5, this chapter undertook a more qualitative description of the transport spectrum in the SWCNT-based DQDot device in the weak interdot coupling regime, in preparation for the main results in chapter 7. In the measurements, the current I and the differential conductance $\mathrm{d}I/\,\mathrm{d}V_{SD}$ were measured simultaneously. Caution is due when interpreting the derivative $\mathrm{d}I/\,\mathrm{d}V_{SD}$ of the current by a coordinate, the bias, in a plot of two other quantities, the gate plane (Σ, Δ). However, the differential conductance data resolve some features more clearly compared to the current data. The differential conductance data are therefore helpful as supplementary information in the phenomenological description of the current through the double dot over the gate plane.
In order to structure the discussion, the features in the transport spectrum were categorised, following references [63, 74], in a sequential tunnelling picture, by counting how many adjacent charge nodes are in resonance (see figure 6.1). *Charge node* is an umbrella term comprising the two electrodes and the two quantum dots [26].

Single resonances

For *single resonances*, when only one electrode is resonant with its adjacent quantum dot, clear co-tunnelling line was observed. At finite bias, the co-tunnelling effects occurred, as expected from theory, over a band in the gate plane with a width equal to the applied bias excitation . In particular, these *single resonance bands* exhibited signatures of the exited state structure of the co-tunnelling spectrum.
Lead-dot single resonances have positive and negative slope in the gate energy plane (Σ, Δ). The current within a triple triangle pair was found to be asymmetric. Bias reversal did not reverse this asymmetry; the current at the negatively-sloped single resonances always remains higher than the positively-sloped ones. This current asymmetry was related to an asymmetric coupling of *source-left dot* coupling versus *right dot-drain* coupling. The ratio of relative coupling was roughly estimated to a factor of about 8 (cf. equation 6.3).

Dot-dot single resonances appear as horizontal lines in the gate energy plane (Σ, Δ). At some interdot charge transitions, a double or 'split' *dot-dot* single resonance line was observed, but with no significantly systematic pattern in the gate plane which would allow viable conclusions that the effect is a consequence of a particular charge configuration. Also, the effect could be suppressed by a magnetic field but reemerged at higher field values, around $B \approx 3\,\mathrm{T}$, only to be suppressed at still higher fields. At present, assigning a mechanism to these features would be speculative.

Triple resonances

The features in finite bias, non-linear transport spectrum of the *triple resonances*, i. e, the triple triangles, could be charted in the gate energy plane (Σ, Δ) by considering three contributions: the single resonance lines of *source-left dot*, *right dot-drain* and the horizontal lines that correspond to *interdot* resonances. 'Prolonging' these three types of *single resonance* lines into the triple triangle area results in a pattern that can be related to the change in current through the double quantum dot effected by the exited state structure. Typical excitation energies range around $100\,\mu\mathrm{eV}$; they are smaller by a factor 2-3 yet of the same order as reported for comparable weakly interdot-coupled double quantum dots based on CNTs [19, 35, 71] or semiconductor-based double quantum dots [28, 32, 73]. The level spacing depends also on the magnetic field (cf. e. g. [20]), which is the subject of the subsequent discussion in chapter 7.

Asymmetry of the current within a triple triangle pair

The interdot capacitance C_{lr} splits the resonances for a given interdot charge transition $(n_l + 1, n_r) \leftrightharpoons (n_l, n_r + 1)$ into a pair of triple resonances. Simple, sequential tunnelling rate equation considerations suggest that the current distribution is the same for both triple resonances. This symmetry is, however, broken in measurements on double quantum dot devices (regardless of host material, see e. g. GaAs [20], CNTs [19] or InAs nanorods [31]). The key result of this chapter is to qualitatively discriminate the contributions of sequential tunnelling and co-tunnelling to the current within the triple triangles. It was found that the asymmetry in current can be mainly attributed to asymmetric co-tunnelling stemming from asymmetric coupling of the source and drain to the double dot. Knowledge of where a significant impact of co-tunnelling is to be expected is required for a meaningful interpretation in terms of a sequential tunnelling model of the more involved measurements in chapter 7.

Chapter 7

Spin blockade spectroscopy on the interdot transitions of a SWCNT-based double quantum dot

The main results obtained from a SWCNT-based double quantum dot device are presented in the concluding chapter of this thesis. The preceding chapters serve as a preparation for these result as follows: the theory chapter 1 developed the sequential tunnelling model of a double quantum dot; relevant here is the weak interdot tunnel coupling and intermediate capacitive coupling regime where the double quantum dot behaves like 'two interacting atoms', i. e. interacting via capacitive coupling. Footing on chapter 1, chapter 5 demonstrated the experimental control over the double quantum dot device and evaluated its energy scales, allowing to present all subsequent data in physically meaningful units of energy rather than the merely metrological gate voltage values. Chapter 6 had the purpose to discriminate between the contributions of sequential tunnelling and co-tunnelling in the current through the double quantum dot to provide better notion of the validity range of the sequential tunnelling model of the double quantum dot as 'two interacting atoms'.

Upon identifying transport blockade phenomena as spin effects (section 7.1), these spin effects are used as a means of spectroscopy on the interdot spin state transition (section 7.2). After describing the evolution of these spin blockade effects with different experimental energy scales (section 7.3) within the picture of the double quantum dot as 'two interacting atoms', an exemplary effect is presented that goes beyond this approximative description (section 7.4).

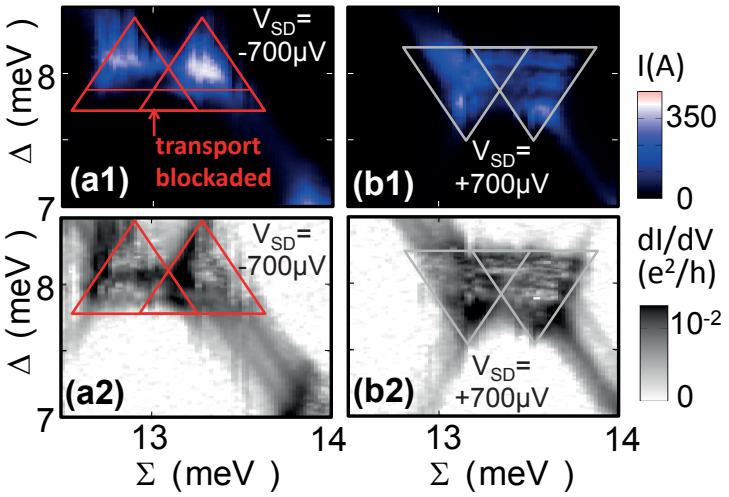

Figure 7.1: Map of (1) current $I(\Sigma, \Delta)$ and (2) $\mathrm{d}I/\mathrm{d}V(\Sigma, \Delta)$ as a function of gate energies at $B = 0$ and (a) V_{SD}=-700μV and (b) V_{SD}=+700μV bias. Superimposed on the data are colour-coded triangles, sized in height and width by the bias $|eV_{SD}|$.

At negative bias (a1), transport is blockaded at small detuning, i. e. there is a (near) zero current area within the triple triangles (highlighted with red triangles) between baseline $\Delta = 0$ and the red, horizontal line. At reverse bias (b1), there is a finite current throughout the entire triple triangles (highlighted with grey triangles). The $\mathrm{d}I/\mathrm{d}V$ data in logarithmic scale serve for a precise identification of the triple triangle boundaries.

7.1 Singlet-triplet spin blockade at zero magnetic field

In some triple triangles in a current map of the gate energy plane $I(\Sigma, \Delta)$, there are areas of drastically reduced current. An example for such a *transport blockade* is presented in figure 7.1 (a1). The triangle outlines are highlighted with a red triangle. Its dimensions are set by the bias. In the simultaneously recorded differential conductance map $\mathrm{d}I/\mathrm{d}V(\Sigma, \Delta)$ (figure 7.1 (a2)) in logarithmic scale, the triangle positions in the gate plane can be determined with higher accuracy. Their positions are then transferred back onto the conjugate current map, compensating a small, global (Σ, Δ)-shift. In the left triple triangle, termed *counter − clockwise* or *electron triangle*, there is a black area between the zero detuning base line and the thin horizontal line corresponding to current suppression to nearly zero. In the *clockwise* or *hole triangle*, there is a finite leakage current in the transport-blockaded area. For reverse bias (figure 7.1 (b1)), the entire triple triangle area is 'filled' throughout with a finite current that the colour scale translates in a blue contrast. This lifting of transport blockade upon bias reversal is characteristic for spin-blockade phenomena. The following discussion will investigate how the transport blockade phenomena can be explained by spin effects. The theoretical expectation is that spin blockade occurs only for particular charge configurations (n_l, n_r) on left and right dot. The obvious

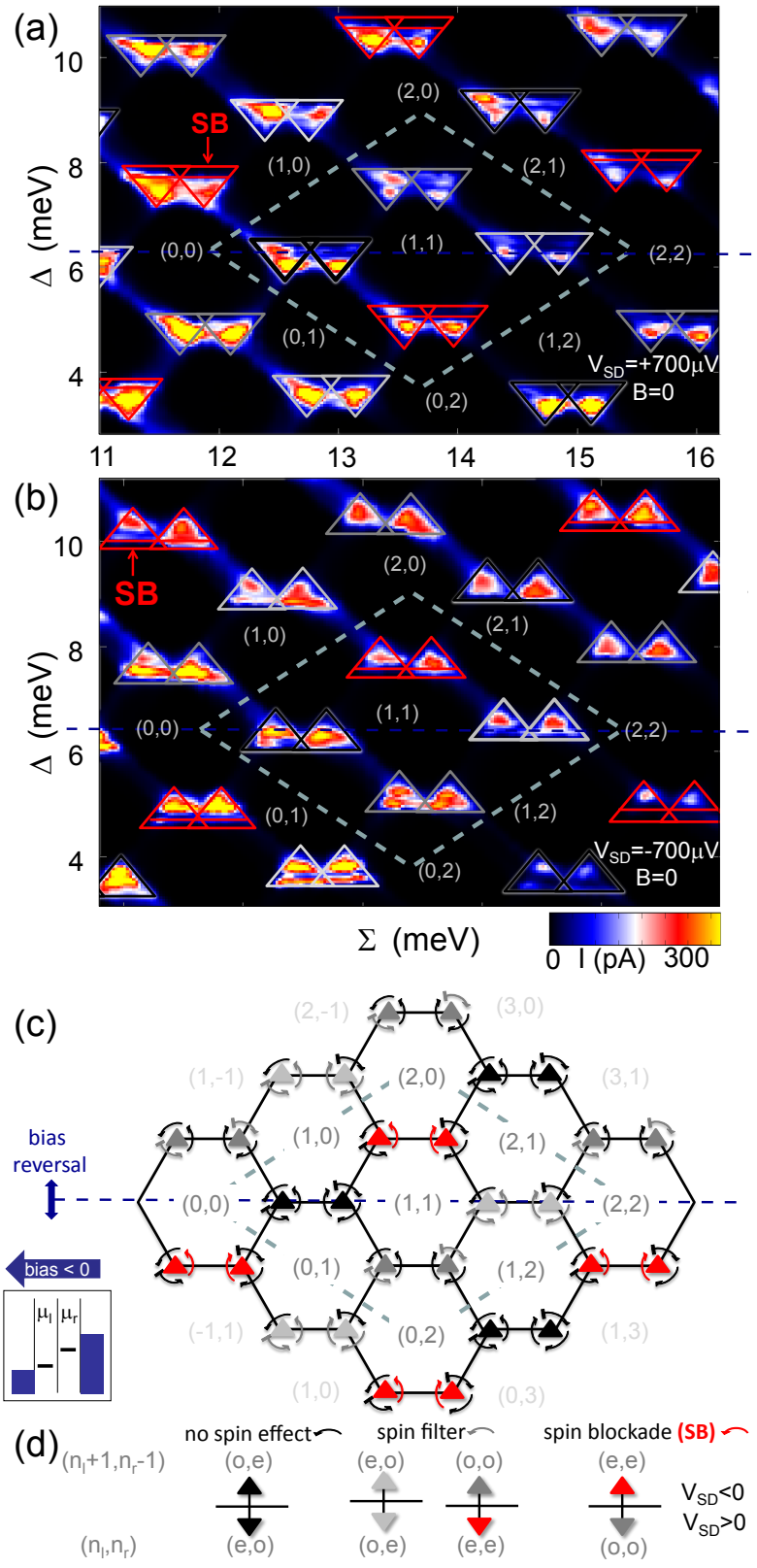

Figure 7.2: Map of current $I(\Sigma, \Delta)$ as a function of gate energies at $B = 0$ and (a) V_{SD}=+700μV and (b) V_{SD}=-700μV bias. Superposed on the data are colour-coded triangles. (c) Current pattern for different charge configurations (n_l, n_r) expected from singlet-triplet spin-blockade for $V_{SD} < 0$. Upon bias reversal, the pattern is mirrored w. r. t. the blue dashed line (and the triangles point the other way). The dashed diamond is the *unit cell of spin effects*, implying that all configurations $mod_3(n_l, n_r)$ are equivalent w. r. t. ST-spin-blockade (but not other effects governing the current). For each triple triangle, transport is described by a sequence of three tunnelling events that can involve *no spin effect*, *spin filtering* or *spin blockade (SB)*. Spin blockade, i. e. zero current in a triple triangle area, occurs only at low detuning and in absence of strong co-tunnelling (above/below the red line in the right/left triple triangles for $V_{SD} > 0 / V_{SD} < 0$).

(d) Classification of triple triangles by the interdot tunnelling event $(n_l, n_r) \rightarrow (n_l + 1, n_r\text{-}1)$. (o, e), e. g., stands for (odd, even) charge occupancy.

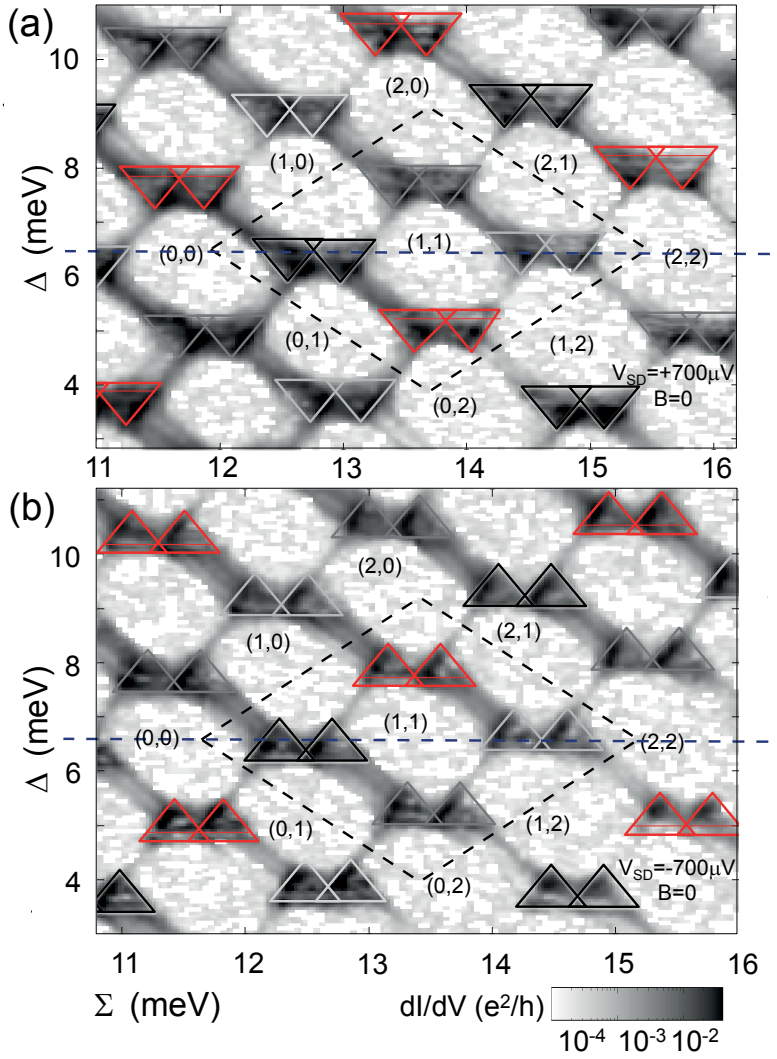

Figure 7.3: Map of differential conductance $\mathrm{d}I/\mathrm{d}V(\Sigma, \Delta)$ as a function of gate energies at $B = 0$ and (a) V_{SD}=+700μV and (b) V_{SD}=-700μV bias. Data sets (a)/(b) were recorded simultaneously with those in figures 7.2 (a)/(b). Superimposed on the data are the same colour-coded triangles (with a small, globally constant offset). The logarithmic scale features the outlines of the triple triangles and their interconnecting single resonance lines more clearly visible than in the current data (cf. figure 7.2) and confirms that colour-coded triangle outlines match the triple triangle (Σ, Δ)-areas.

next step is therefore the investigation of a wider gate energy range $I(\Sigma, \Delta)$ for a systematic pattern of spin blockade.

7.1.1 Gate map of spin blockade

Figures 7.2 (a) and (b) shows a map of current I over a wide gate region (Σ, Δ) for V_{SD}=-700 μeV and reverse bias V_{SD}=+700 μeV. Within each Coulomb-blockaded honeycomb in this gate stability lattice, the left and right dot charge state (n_r, n_l) cannot fluctuate. Superimposed on the data are equilateral triangles. Their height and base width is equal to the applied bias, $|eV_{SD}|$ =700 μeV. In these current maps with linear scale colour scale, the triple triangle positions can be less clearly pinpointed than in differential conductance maps. The positions of the triangular outlines has therefore been determined from the simultaneously recorded differential

conductance map in logarithmic scale (figures 7.3) and their position was transferred back onto the according current maps. The colour coding of the triangles categorises the charge states (n_r, n_l) by spin blockade phenomena (according to the categorisation in figures 7.2 (c) and (d)), as elaborated in the following.

An interdot charge transition $(n_r, n_l) \rightleftharpoons (n_r \pm 1, n_l \mp 1)$ (for positive ($\rightharpoonup$) and negative ($\leftharpoondown$) bias) is *spin-blockaded* if energetically allowed but forbidden by spin conservation [32, 72]. If only the charge configuration (n_r, n_l) governed the current through a double quantum dot but the spin configuration played no role, the current pattern $I(\Sigma, \Delta)$ should be symmetric upon bias reversal [61]. The experimental data in figure 7.2 evidences, however, that this bias reversal symmetry is broken. This bias asymmetry gives rise to a current rectification that is characteristic for spin blockade. Figure 7.4 presents line scans of the current I through representative triple triangles in Δ-direction to support that the current is suppressed at every other site in the triple resonance lattice and the suppression is lifted upon bias reversal. It is interesting to note that there is also a *quantitative* asymmetry w. r. t. bias for interdot transitions for which the current remains finite over the entire triple triangle area and for both bias directions (cf. second coloumn in figure 7.4). The focus of this discussion, however, lies on the bias asymmetry at interdot transitions that *qualitatively* lifts the transport suppression. Various spin blockade mechanisms can break the bias symmetry [20, 128–130, 130, 131], as elaborated in the following.

7.1.2 Mechanism of singlet-triplet spin blockade

Of relevance for the present data is the *Pauli* spin blockade, and in particular *singlet-triplet spin blockade (ST-SB)* mechanism. This effect is intrinsic to the serial double quantum dot configuration and has been observed semiconductor-based [20, 28, 29, 31, 32, 65, 72, 73, 127] and, more recently, in CNT-based [71, 97, 126] devices. The sketch in figure 7.5 recalls the basics on energies and spin singlet and triplet states of two spin-$\frac{1}{2}$ charge carriers in a confining double potential well. The current is blocked, when, due to spin selection rules, a spin on the first quantum dot (in current direction) finds no energetically accessible state for its spin orientation on the second quantum dot[1] - and does not have the energy to go back to the reservoir of its provenance. In absence of an escape mechanism for the the electron that occupies the so *trapped state* - or higher order, co-tunnelling events are negligible - the current ideally drops to zero.

[1]Note that the term *Pauli spin blockade* does not imply strict Pauli-forbiddance of non-zero spin two particle states, e. g. an $T_+(0,2) = (\uparrow\uparrow, -)$ triplet on the right quantum dot can be populated but is energetically separated by *Pauli repulsion* from the $S(2,0) = (\downarrow\uparrow, -)$ singlet.

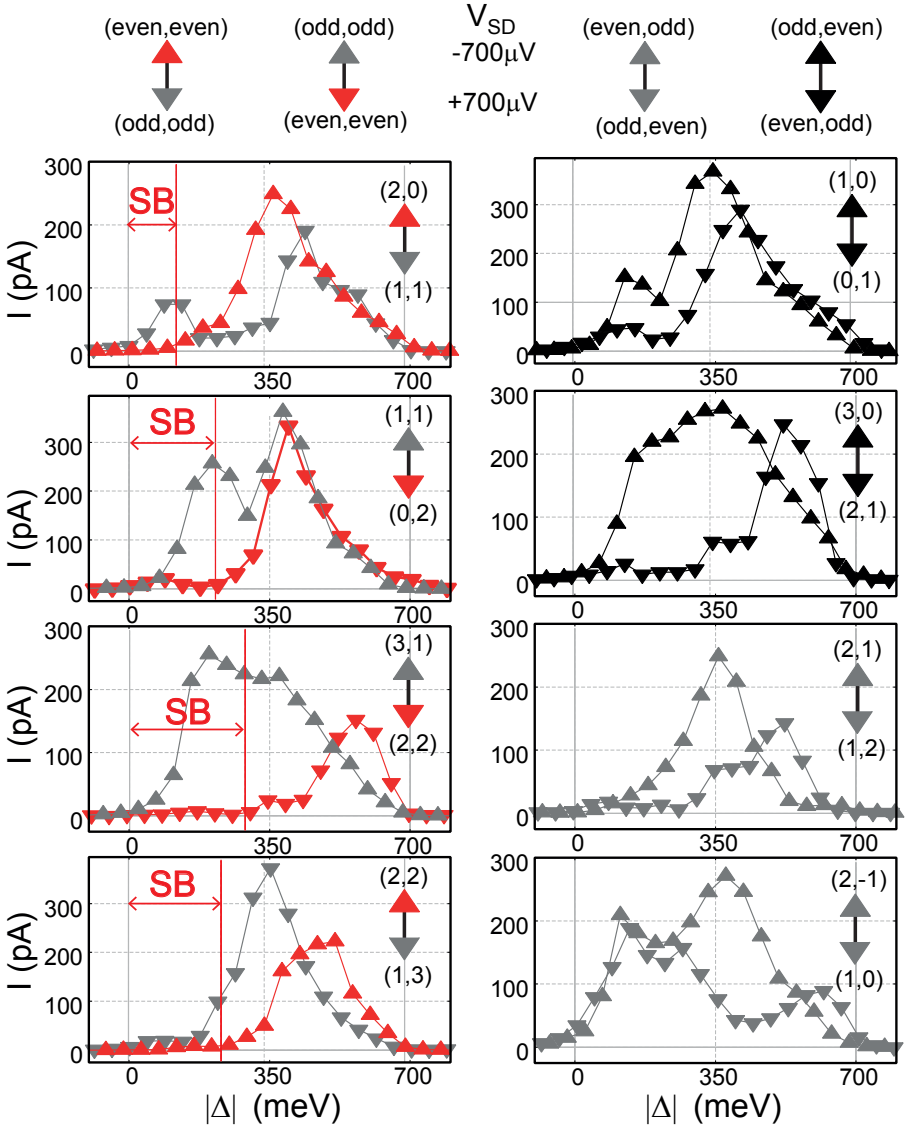

Figure 7.4: Line scans from zero detuning base line to the tip of selected triple triangles from figure 7.2. The current I is plotted as a function of interdot detuning Δ, ranging over $[0, -700]\,\mu$eV for positive bias $V_{SD} = +700\,\mu$eV (symbols $\bigtriangledown$) and $[0, +700]\,\mu$eV for negative bias $V_{SD} = -700\,\mu$eV (symbols $\bigtriangleup$). For comparability, the line traces are taken through the left (right) triangle of a pair of triple triangles for negative (positive) bias where the influence of co-tunnelling is respectively weak (for details see section 7.1.3). Two samples of each category of interdot transitions $(n_l, n_r) \rightleftharpoons (n_l + 1, n_r\text{-}1)$, as introduced in figure 7.2 (d), are presented. The colour of data point symbols and lines indicates whether spin blockade **(SB)**, no spin effect or spin filtering can be expected to occur - depending on charge configuration and bias direction - as long as the detuning Δ is smaller than the respective singlet-triplet splitting $\Delta_{ST(even,even)}$. ST-spin blockade is asymmetric upon bias reversal. Inversion of the interdot transition charge configuration results in spin blockade occurring at opposite bias direction.

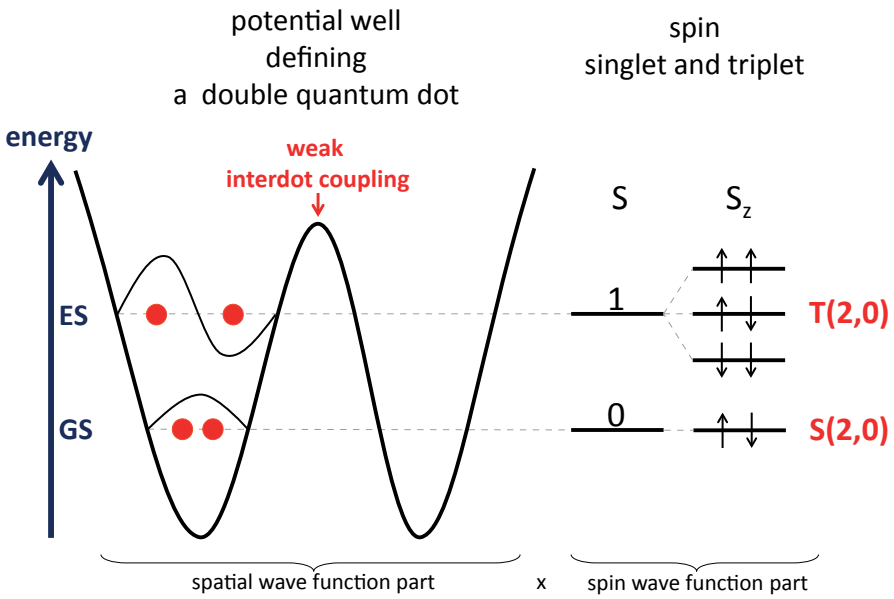

Figure 7.5: Illustration of spin singlet and triplet states and their energies of two spin-$\frac{1}{2}$-particles in a confining double well potential with total spin $S = |s_1 - s_2|, ..., |s_1 + s_2| = 0, 1$. The pairs of red dots recall that for charge configurations $(2, 0)$, the probability density of the two-electron wave function is concentrated over the site of the left quantum dot.

Upon bias reversal, current can flow. Charge carriers are subject to spin selection rules at the transition of first lead to first dot in transport direction, effecting a *spin filtering* [132] - under the condition that, in the example of figure 7.6, the $T(2, 0)$ is energetically inaccessible.
In the case of CNTs, similarly to the ST-Kondo effect (cf. chapter C), this blockade mechanism works, in principle, for the orbital isospin as well as for the electronic spin ([72, 133], see also [131]). Here, only electronic spin effects are regarded.

ST-spin blockade model and categorising by charge states (n_r, n_l)

Sequential tunnelling can be described as three subsequent tunnelling events of a charge carrier of the electrode with higher electro-chemical potential to the first dot, interdot tunneling, and the charge leaving the second dot for the other electrode. Singlet-triplet spin blockade occurs at the interdot tunnelling event, i. e. $(n_l + 1, n_r - 1) \rightleftharpoons (n_l, n_r)$ for $V_{SD} \lessgtr 0$ whenever the initial charge configuration is, for both positive and negative bias, odd on both dots and the final one is even, i. e. $(o, o) \rightarrow (e, e)$. The model of singlet-triplet spin blockade and *spin filtering* mechanism is explained in detail in figure 7.6 for the example of the $(2, 0) \rightleftharpoons (1, 1)$ interdot transition. Charge configurations of type $(o, e) \rightleftharpoons (e, o)$ or $(e, o) \rightleftharpoons (o, e)$ show no ST-spin blockade and are symmetric upon bias reversal (if this symmetry is not

broken by effects other than ST-SB). Figure 7.2 (c) categorises the charge configurations (n_l, n_r) by the occurrence of spin blockade or spin filtering for negative bias. As the current direction reverses with the bias, the equivalent sketch for positive bias is obtained by mirroring on the equal charge (n, n)-axis.

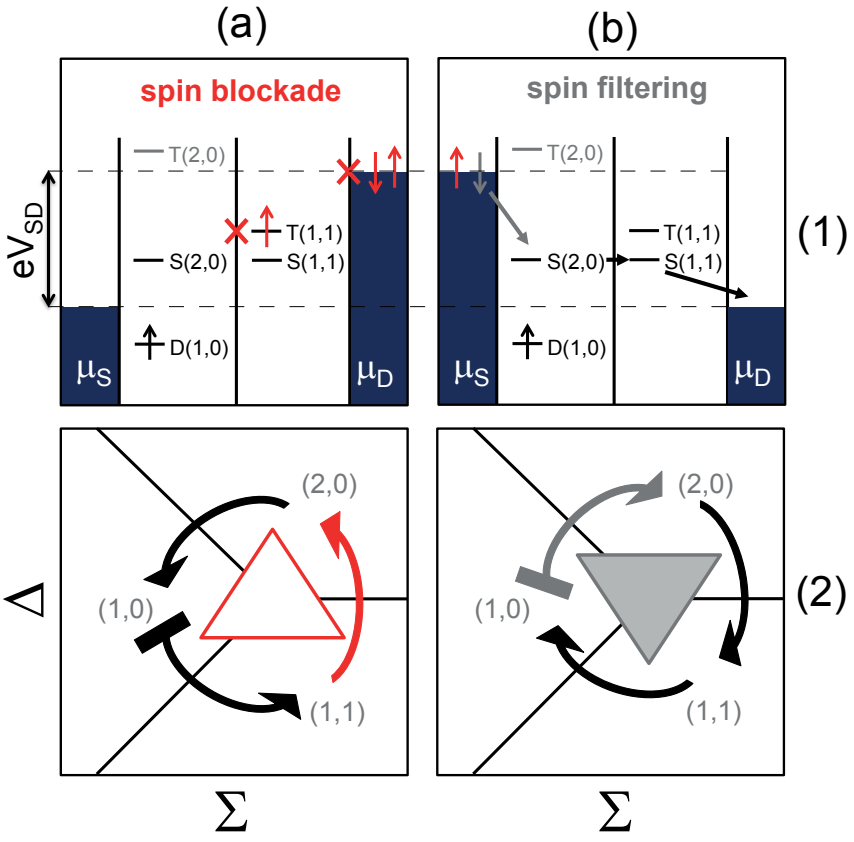

Figure 7.6: Model of singlet-triplet spin blockade and filtering mechanism: consider the charge transition between left and right quantum dot $(1,1) \rightleftharpoons (2,0)$ (cf. figure 7.2), sequential tunnelling only and assume that, e. g., a $\uparrow$-electron occupies the $D(1,0)$ doublet. (a1, a2) For negative bias, another $\uparrow$-electron will eventually tunnel into the right dot, forming a $T(1,1)$ state. This *blocking state* suppresses the current (indicated by the empty triangle in the $I(\Sigma, \Delta)$ sketch (a2)) because neither can the second $\uparrow$-electron, by spin selection rules, tunnel on into the $S(2,0)$ singlet in the left dot, nor does thermal activation suffice it make escape back to the drain electrode (indicated by the two red crosses in (a1)). Once the $T(2,0)$ triplet becomes energetically accessible, the second $\uparrow$-electron is no longer trapped the spin blockade is lifted. (a2, b2) For positive bias, only $\downarrow$-electrons can enter the left dot forming the $S(2,0)$ and can freely escape into the left dot forming the $S(1,1)$ state. While the $T(2,0)$ triplet is energetically inaccessible, $\uparrow$-electrons are blocked and the current is *spin filtered*. With the proposed state configuration in the bias window, the double quantum dot acts as a spin-polarising current rectifier.

'Unit cell' of ST-spin blockade in the gate map of current

Within this simple model, spin blockade can be assumed to be independent on the absolute charge occupancy (n_l, n_r) (e. g. [28, 134]). It rather depends on *effective charge occupancy* of the relevant charge states the filled; the "inert core levels" [134] with energies below the bias window can be neglected. As a consequence, ST spin blockade is expected to be periodic in (n_l, n_r) charge states. The discussion of the spin blockade maps $I(\Sigma, \Delta)$ can therefore be reduced to a 'unit cell' of the four interdot transitions between charge states (n, m), with $n, m = 0, 1, 2$. In figures 7.2, this unit cell is highlighted by a dashed diamond-shaped outline. Figures 7.2 (c) and (d) propose a categorisation scheme of the (n_r, n_l) charge states w. r. t. ST-spin blockade and filtering over the hexagonal gate lattice (extending a similar scheme in [20]). The occurrence of ST-spin blockade on every other triple resonance site along the hexagonal lattice is often referred to as *'simple' even-odd shell filling* [20, 71, 97]. Additional effects in the dependence of SB leakage current on a magnetic field may arise when taking into account the absolute electron number on the dots [28].

Ground and exited state spin configurations for the two-electron DQD

The model of ST-spin blockade proposed in figure 7.6 relies on a particular configuration of $(n_r, n_l) = (2, 0)$ and $(1, 1)$ singlet and triplets. Justification is due as to why the spin states on the double quantum dot should be so configured: an elementary theorem states that, without external magnetic field, a two-electron system must have a symmetric (spatial) ground state wave function [20, 135]. As the total fermionic wave function must be antisymmetric, the ground state spin wave function must then be anti-symmetric. As illustrated by figure 7.5, this implies that the spin singlet state is lower in energy than the triplet. A singlet ground state is expected (for B=0) in any situation where one quantum level contains a charge-repulsive spin pair and is not degenerate with any unfilled levels [20]. For the example of a double quantum dot with the right dot doubly occupied, i. e. $(n_l, n_r) = (2, 0)$, the ground state is a $S(2, 0)$-singlet and the $T(2, 0)$-exited state is higher in up energy by the singlet-triplet splitting $\Delta_{ST(2,0)}$. Considering a symmetric charge distribution $(n_l, n_r) = (1, 1)$ over a double dot in the *weak* interdot coupling regime (as demonstrated for the present case in figure 5.9), the $S(1, 1)$-singlet and $T(1, 1)$-triplet are *approximately* degenerate, i. e. $\Delta_{ST(1,1)} \approx 0$ [20]. In terms of the simple sketch of figure 7.5, where the interdot coupling is weak enough to describe the DQDot as 'two interacting atoms', the atomic state of the $(1, 1)$ charge configuration is composed of a priori uncorrelated single particle states on each dot.

Lifting ST-spin blockade via interdot detuning

Negative-bias blockade is lifted when the $T(2,0)$-triplet state enters the bias window (necessary condition [20]) and left and right dots are sufficiently detuned (i. e. $\Delta \geq \Delta_{ST(2,0)}$) to allow an inelastic tunnelling event $(2,0) \leftarrow (1,1)$ under emission of some bosonic energy quantum (e. g. a phonon or photon) equal to the energy mismatch (sufficient condition). Absorbative inelastic tunnelling is suppressed at low temperatures. A 'sufficient' detuning for the $T(2,0) \leftarrow T(1,1)$ tunnelling channel to open corresponds to $\Delta_{ST(2,0)}$ - under the assumption that the $T(1,1)$-triplet and $(S(1,1)$-singlet are degenerate for weak interdot coupling t_{lr}. For completeness it is noted that the argument also requires that the $S(2,0)$ and $S(1,1)$ ground states be degenerate at zero detuning - this is just the defining physical condition of the zero interdot detuning 'base line' and therefore trivially the case.

7.1.3 Identifying ST-spin blockade in the data

In the current maps presented in figures 7.2 (a) and (b), ST-spin blockade is expected in the triple resonances that are marked with red triangles. As the absolute charge number cannot be determined for this device (cf. chapter 5), one triple triangle with characteristic transport blockade is taken as a reference point. The periodicity of observed transport blockade features with the charge state is in agreement with what is expected from *even-odd shell filling*. However, current suppression to zero (black by choice of the colour scale), however, is observed not over the entire triangle but only in some areas between the zero detuning or 'base' line and 'close-by' drawn red lines. The question arises in what parameter range inside the $(o,o) \rightarrow (e,e)$-type triple triangles the state configuration required by the simple ST-spin blockade model (cf. figure 7.6) is met. The observations made on the excited state spectrum in chapter 6 answer this question, in agreement with the experimental findings of figure 7.2:

- When, e. g. for negative bias, the two quantum dots are detuned by the $S(2,0) - T(2,0)$ excitation energy $\Delta_{ST(2,0)}$, the blocking state $T(1,1)$ can be emptied by charge transition to the $T(2,0)$ triplet, lifting ST-spin blockade. Section 6.2 found a typical ground state to first exited state energy spacing of the order of $100\,\mu$eV. This is comparatively small to the triple triangle dimension $|eV_{SD}|$ =$700\,\mu$eV. The factor of about 7 of these energy scales is consistent with the distance from base line to thin red line indicated in figures 7.2 (a) and (b). The lifting of ST-spin blockade for higher detuning is ascribed in similar experiments to $T(1,1) \rightarrow T(2,0)$ transitions [20, 29, 134]. If the singlet-triplet splitting $\Delta_{ST(2,0)}$ is very small against the single particle spacing, ST-spin

blockade can even be entirely marginalised so that no spin blockade effect is observed [136].

- Section 6.3 relates a significant current asymmetry between left and right triple triangle to a current asymmetry of different 'single resonance', co-tunnelling events. The simple ST-spin blockade model, however, considers only sequential tunnelling through the double dot. Even within spin-blockaded areas, co-tunnelling is one of the mechanisms that lead to a finite leakage current (also cf. [71, 73]).

- Section 6.1 found that, in the here investigated sample, the coupling of the source electrode to the left dot is much stronger than of drain to right dot (by a factor of about 8, cf. equations 6.3 and 6.4). Near the zero detuning base line, strong co-tunnelling leakage current is expected in the left (right) triple triangle for positive (negative) bias (as illustrated in figure 6.9). Also, the present device is more transparent than similar devices that have reportedly displayed ST-spin blockade (few pA for bias values 0.5-1 meV for [71, 134]), so here, current leakage via co-tunnelling should be comparatively pronounced.

Summing up, a suppression to zero current as postulated by the simple, sequential tunnelling ST-spin blockade model (cf. figure 7.6) is expected only in the left (right) triple triangle for positive (negative) bias and at smaller interdot detuning than the $S(2,0) - T(2,0)$ energy separation Δ_{ST}. This assessment has been brought in qualitative and quantitative agreement with the experimental findings for several periods of partly spin-blockaded $(o,o) \rightarrow (e,e)$-type triple triangles: in figures 7.2 (a) and (b)), areas where ST-spin blockade can occur within the red triangular outlines below (above) the thin red lines for negative (positive) bias.
Although numerous features of reduced current are observed, none can be unambiguously attributed to spin filtering. The spin filtering mechanism requires the singlet-triplet splitting of the $(2,0)$ charge state so large that the $T(2,0)$ states are energetically above the bias window. Here, this splitting is much smaller than the bias.

7.1.4 The DQDot as a current rectifier

A fingerprint of ST-spin blockade is a pronounced asymmetry in tunnel current upon bias reversal. A double quantum dot, if operated at a triple resonance with interdot charge transition of type $(o,o) \rightarrow (e,e)$ and in the ST-spin blockade regime, can exploit this bias asymmetry to rectify the current. Current rectification is a direct consequence of the double quantum dot geometry, based on Pauli spin blockade

(see figure 7.6). No additional spin manipulation, e. g. by injecting a spin-polarised current via ferromagnetic electrodes, is required. Figures 7.7 (a) demonstrate that

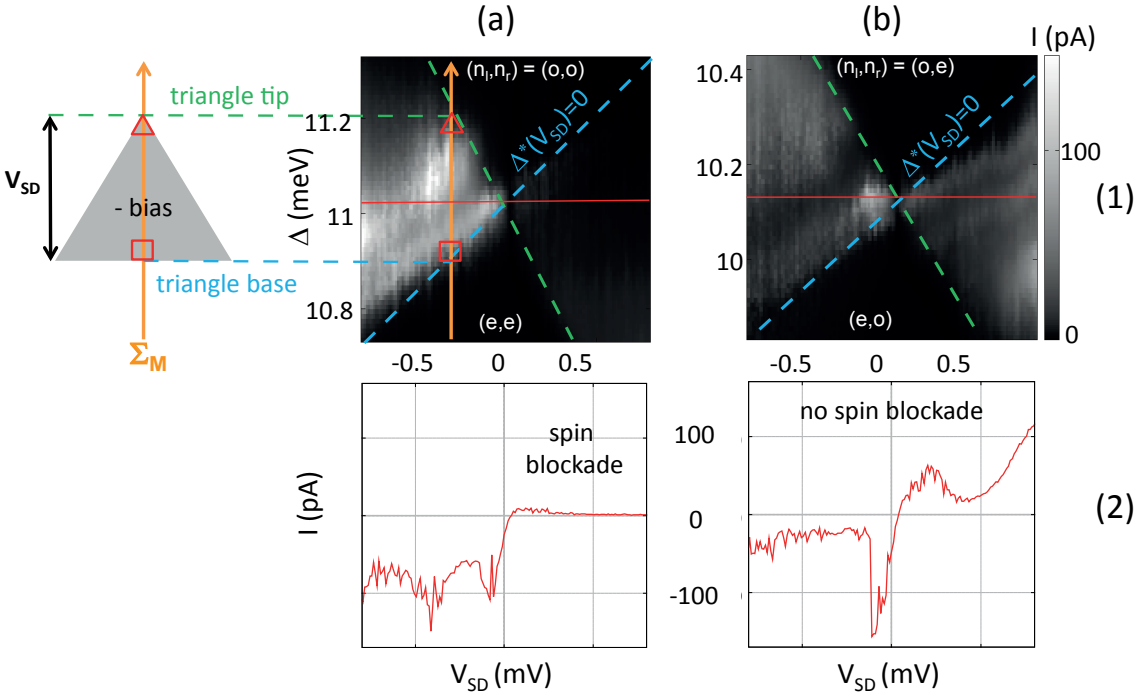

Figure 7.7: Demonstration of the double quantum dot as current recifier based on spin blockade. (a) Current I along line cuts in detuning Δ from tip to baseline of a triple triangle of transition type $(e,e) \rightleftharpoons (o,o)$ as function of bias V_{SD}. The dashed cyan 'base' (where interdot detuning $\Delta^* = 0$) and green 'tip' lines indicate the linear growth of the triangle with bias and its flip in orientation upon bias reversal. For negative bias, current flows while it is spin-blockaded for positive bias. (a2) The line trace along the red line in (a1) demonstrates that the current drops to zero for negative bias. The small leakage current peak near zero bias can be related to thermally activated escape out of the blocking state $T(1,1)$. (b1 and b2) For comparison, an equivalent measurement on triple triangle of transition type $(o,e) \rightleftharpoons (e,o)$) where the charge configurations (n_r, n_l) allow current to flow in either bias direction.

the here investigated CNT device can operate as a current rectifier. A current map is plotted as a function of bias V_{SD} and slices through a triple triangle of type $(0,2) \rightleftharpoons (1,1)$ in detuning direction Δ. The slices are taken at bias-dependent Σ-position of the *base line* middle point Σ_M

$$\Sigma_M(V_{SD}) = \Sigma_M(0) + \frac{V_{SD}}{2} \tag{7.1}$$

to ensure the line cuts to cover the full, $|eV_{SD}|$-high extent of the triple triangle, i. e. running through the middle of the zero detuning base line and the triangle

tip (illustrated in the sketch of figure 7.7) where interdot detuning is maximal for sequential tunnelling to happen for a given interdot charge transition. The bias-dependent base line and tip positions of the triangles are indicated by the cyan and green dashed lines in figure 7.7 (a1) and (b1). The model to evaluate the capacitive action of source and drain was developed at a later point in time (see section 5.7). In these measurements, this additional capacitive shift was therefore not compensated. A post-measurement correction is not possible because the 2D-data slice $I(V_{SD}, \Delta)$ out of a the 3D parameter space $I(V_{SD}, \Sigma, \Delta$ is set by the measurement - for the 'corrected slice', the data points are not recorded. This implies that, with increasing bias, the Δ-slices are increasingly off the $\Sigma(V_{SD})$-position of the triangle tip, implying that the measurement slightly underestimates the maximal Δ-range where current can flow.

On the negative bias side of figure 7.7 (a), current can flow via the effective charge transition $(0,2) \rightarrow (1,1)$, whereas on the positive bias side, the $(0,2) \nleftarrow (1,1)$ charge transition is ST-spin blockaded. Figure 7.7 (a2) is a $I(V_{SD})$-trace along the red line on figure 7.7 (a1). Typical for the characteristic IV-curve of a current rectifier, the current drops to zero for one (here: forward) biasing and has a finite value for reverse biasing. A similar ST-spin blockade IV-characteristic has been observed in a $I(\Sigma, V_{SD})$-like slice (cf. figure 5.3 (a3)) through a CNT-based DQDot phase space [97]. The small leakage current peak at low positive bias can be ascribed to thermally activated escape of electrons trapped in the $T(1,1)$ triplet back to source [20]. Statistically (even if tunnelling probabilities were skewed for spin-$\uparrow$- or $\downarrow$-electrons/holes by spin polarisation), the double dot may then be occupied in the $S(1,1)$ singlet from which the charge carrier is free to progress into the $S(0,2)$ singlet and then on to the drain, completing the charge transportation cycle. On time average, this escape mechanism out of the trapped state results in a finite leakage current [73]. With increasing bias, the energy distance of μ_S and the $T(1,1)$ energy increases. Correspondingly, the probability for thermally activated return to source electrode is gradually suppressed. Also, current is resonantly enhanced for small bias along the line trace in figure 7.7 (a2) and (b2).

For comparison, figures 7.7 (b) present the equivalent $I(V_{SD}, \Delta)$-measurement for a triple triangle with interdot charge transition type $(0,1) \rightleftharpoons (1,0)$. As the model predicts (cf. figure 7.2 (c)), current is not rectified but can flow for both forward and reverse bias.

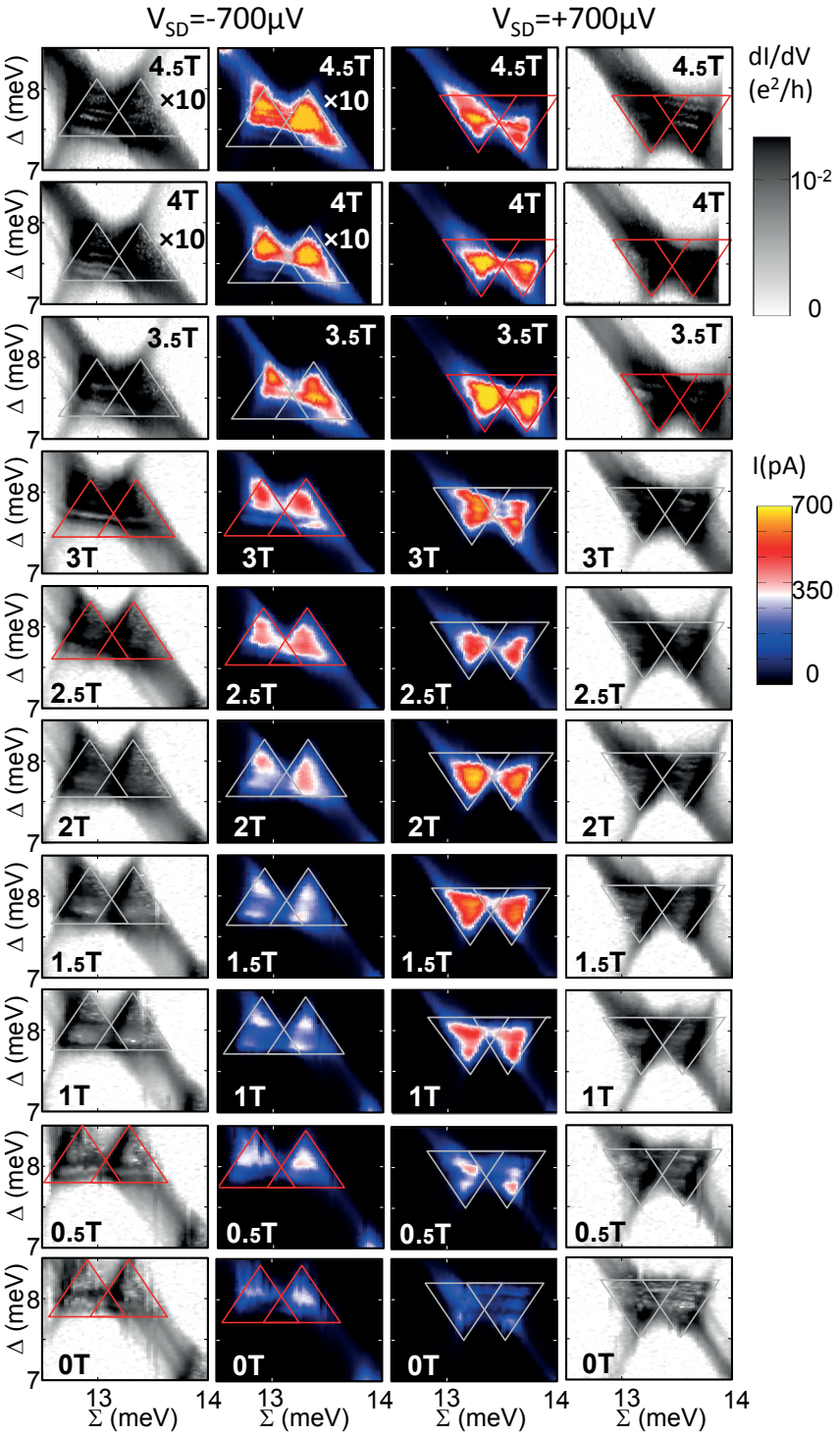

Figure 7.8: Lowest row of graphs ($B = 0$): Zoom on the $(2,0) \rightleftharpoons (1,1)$ interdot transition from the current maps $I(\Sigma, \Delta)$ in figure 7.2, supplemented by the simultaneously measured differential conductance maps $\mathrm{d}I/\,\mathrm{d}V(\Sigma, \Delta)$ (cf. figure 7.3), for $V_{SD} = \pm 700\,\mu\mathrm{V}$. Mounting in rows, the out-of-sample-plane magnetic field B increases in 0.5 T increments. Superimposed red and grey triangles have a size of $\mathrm{e}|V_{SD}|$ in Σ- and Δ-directions, outlining the triple triangles. The colour coding discriminates whether there are spin blockade features within triple triangle area or not.

7.2 Spin blockade spectroscopy on the interdot charge transition and its evolution in an external magnetic field

Even if the absolute number of excess charges on the double quantum dot can not be determined, ST-spin blockade features allow to assign *effective charge states* (n_r, n_l) to the triple resonance pattern in figure 7.2. It was shown that the discussion of ST-spin blockade can be reduced to a 'unit cell' of charge occupancies $n_r, n_l = 0, 1, 2$. For the case of two electrons in the dot (i. e. a "helium"-like quantum dot [73]), Pauli exclusion and exchange can induce a splitting between the spin singlet and triplet states that can be controlled by gates, as already demonstrated, and magnetic fields [137, 138], as shall be shown now for the present double quantum dot device.

Measurements were compared for two different magnetic field orientations along magnetically similarly easy axes of the PdNi electrodes [99]: an out-of plane perpendicular field and an in-plane perpendicular field with respect to long axis of the PdNi strips. No significant qualitative difference was observed in the data for different field orientations. The effect of ferromagnetic electrodes on the absolute Zeeman energy scale was too small to be determined. For simplicity, the magnetic field for both orientations is therefore denoted as B. Whenever the field orientation has does matter and has an impact on the data, e. g. when spin-orbit coupling comes into play, it will be explicitly emphasised.

7.2.1 Magnetic field evolution of triple triangles

The remainder of this chapter focuses on the interdot charge transition that is labelled $(2, 0) \rightleftharpoons (1, 1)$ in figure 7.2; it displays, for small detuning and zero magnetic field, ST-spin blockade for negative bias and none for positive bias, as expected for ST-spin blockade. In figure 7.8, the $I(\Sigma, \Delta; B)$-zoom on this triple resonance for $V_{SD} = \pm 700\,\mu\mathrm{V}$ shows the evolution of triple triangle current over a wide range of out-of plane magnetic fields $B = 0, 0.5, ..., 4.5\,\mathrm{T}$. The external field is perpendicular to both the SWCNT and the PdNi electrodes. The data are highly symmetric upon reversal of field orientation $|\vec{B}| \mapsto -|\vec{B}|$. The equivalent negative magnetic field measurements are therefore not shown here.
To justify the placement of the triangular outlines that mark the position of the triple triangles in the gate energy plane (Σ, Δ), the current data are supplemented by the corresponding, simultaneously measured $\mathrm{d}I/\,\mathrm{d}V(\Sigma, \Delta; B)$. The same (Σ, Δ)-range is chosen throughout figure 7.8. In this representation, it is immediately

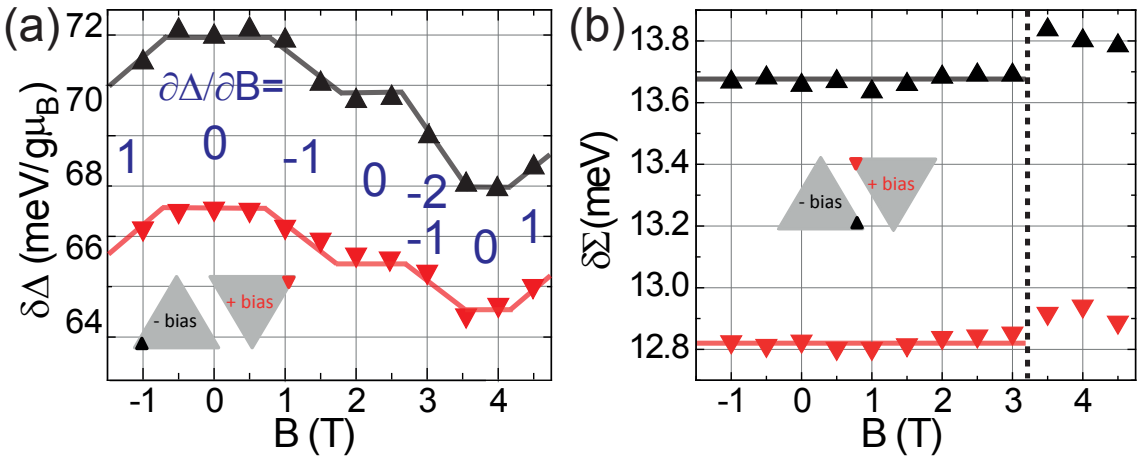

Figure 7.9: Position shift of the triple triangle 'baseline' corner points in the gate plane (Σ, Δ) with magnetic field for positive and negative bias (see sketch insets). The solid lines are manually fitted to the data points with integer slope values in units of $g\mu_B$. Blue numbers indicate the respective slopes of the line segments. (a) Magnetic field dependence of the baseline position in *interdot detuning* Δ. Discontinuities in the slope mark a change in ground state spin configuration on both or either quantum dots. (b) Magnetic field dependence of the baseline position in *average charging* Σ. Below 3.2 T, no significant B-dependence is observed.

eye-catching that the magnetic field shifts the overall position of the triple triangles in the (Σ, Δ)-plane.

A quantitative evaluation of shifts $(\delta\Delta, \delta\Sigma)$ of the zero detuning base line is provided in figure 7.9 (a, b). There is no significant shift in Σ (indicated by the linear fits with slope $\Sigma' := \frac{\partial\Sigma}{\partial B} = 0$ in figure 7.9 (b)) up to fields of about $|B| \geq 3.2\,\mathrm{T}$. For higher fields, the Σ' becomes non-zero.

The present discussion shall be confined to below 3.5 T where Σ does not depend on the magnetic field. Reference [130] proposes non-spin conserving events (or 'spin flips') to occur at higher fields. The baseline shift in detuning, shown figure 7.9 (a), has a richer structure in Δ than in Σ. Linear fits approximate the data points by intervals in B. The slopes $\Delta' := \frac{\partial\Delta}{\partial B}$ are taken as integer multiples of $g\mu_B$, where $g = 2$ is the Landé factor in CNTs [70,71] and μ_B the Bohr magneton. Figure 7.9 (a) is scaled in units of $\mathrm{eV}/g\mu_B$. In this scaling, the diagonal of the underlying grid corresponds to a slope value $g\mu_B$; the slope can thus be conveniently read off as integer multiples of the Zeeman energy scale.

To describe the observation that $\Delta' = g\mu_B n$, $n \in \mathbb{Z}$, a simple model is proposed in the following:

7.2.2 Modelling the DQDot spin state configuration

The *spin states* of the double quantum dot shall be denoted as $|X(n_l, n_r)\rangle$. $X = \langle X(n_l, n_r)| \hat{S} |X(n_l, n_r)\rangle$ stands for the total spin quantum number of the spin state, where $\hat{S}$ is the spin operator. Consider the possible spin singlet and triplet states of a double quantum dot occupied with two electrons; the normalised spin states are related to the *spin configurations* (denoted by up and down arrows) by

$$\begin{aligned} |S(2,0)\rangle &= \frac{1}{\sqrt{2}}\left[|{\downarrow\uparrow}, 0\rangle - |{\uparrow\downarrow}, 0\rangle\right] & |S(1,1)\rangle &= \frac{1}{\sqrt{2}}\left[|{\downarrow}, {\uparrow}\rangle - |{\uparrow\downarrow}\rangle\right] \\ |T_-(2,0)\rangle &= |{\downarrow\downarrow}, 0\rangle & |T_-(1,1)\rangle &= |{\downarrow}, {\downarrow}\rangle \\ |T_0(2,0)\rangle &= \frac{1}{\sqrt{2}}\left[|{\downarrow\uparrow}, 0\rangle + |{\uparrow\downarrow}, 0\rangle\right] & |T_0(1,1)\rangle &= \frac{1}{\sqrt{2}}\left[|{\downarrow}, {\uparrow}\rangle + |{\uparrow}, {\downarrow}\rangle\right] \\ |T_+(2,0)\rangle &= |{\downarrow\uparrow}, 0\rangle & |T_+(1,1)\rangle &= |{\uparrow}, {\uparrow}\rangle\,. \end{aligned} \tag{7.2}$$

This work extends the description of the ground state evolution in a magnetic field from a single [139–141] to a serial double quantum dot based on the following ansatz: the correspondence of the ground state for a *single* quantum dot is, for a double quantum dot, the interdot charge transition $X(n_l\,{+}1, n_r\,{-}1) \leftarrow Y(n_l, n_r)$ (for the example of negative bias; X, Y denote the final and initial total spin states). This means that measurements through a single quantum dot (an 'artificial atom') correspond to *level spectroscopy*, measurements through serial double quantum dots (two capacitively coupled 'artificial atoms') correspond to *interdot transition spectroscopy*.
On a single quantum dot, the energy E of a spin state $|x(n)\rangle$ changes with an external magnetic field B with a slope in the (B, E)-plane of $\frac{\partial E}{\partial B} = g\mu_{\mathrm{B}} x$, where $x = \langle x(n)| \hat{S} |x(n)\rangle$ is the spin quantum number of the single quantum dot.
This discussion investigates the double quantum dot over the plane spanned by the magnetic field B interdot detuning Δ, i. e. (B, Δ).

Model for spectroscopy on the interdot transition

In order to compute the energy dependence with magnetic field of an interdot spin state transition, an operator $\hat{\Delta}_B$ shall be introduced that acts on an interdot spin state transition of a serial double quantum dot and that measures by how much the action of a magnetic field detunes the left versus the right quantum dot in energy per Telsa. In other words, the expectation value of the operator $\hat{\Delta}_B$ with respect to a given interdot transition $|X(n_l\,{+}1, n_r\,{-}1) \leftarrow Y(n_l, n_r)\rangle$ is the slope $\Delta' = \frac{\partial \Delta}{\partial B}$:

$$\langle X(n_l\,{+}1, n_r\,{-}1) \leftarrow Y(n_l, n_r)| \hat{\Delta}_B |X(n_l\,{+}1, n_r\,{-}1) \leftarrow Y(n_l, n_r)\rangle = \frac{\partial \Delta}{\partial B} =: \Delta'. \tag{7.3}$$

For this computation, two mapping relations are required (also compare equation 1.38):
The first mapping relation requires to subtract the initial spin configuration the contribution to energy from the final one; in the example of a $S(2,0)\leftarrow T_+(1,1)$ interdot transition, the final state is $|f\rangle = |S(2,0)\rangle$ and the initial state is $|i\rangle = |T_+(1,1)\rangle$. The first mapping relation is thus

$$\begin{aligned} &\langle X(n_l+1, n_r\text{-}1) \leftarrow Y(n_l, n_r)| \,\hat{\Delta}_B\, |X(n_l+1, n_r\text{-}1) \leftarrow Y(n_l, n_r)\rangle \\ =&\{\langle X(n_l+1, n_r\text{-}1)| - \langle Y(n_l, n_r)|\} \,\hat{\Delta}_B\, \{|X(n_l+1, n_r\text{-}1)\rangle - |Y(n_l, n_r)\rangle\} \\ =&\langle X(n_l+1, n_r\text{-}1)| \,\hat{\Delta}_B\, |X(n_l+1, n_r\text{-}1)\rangle - \langle Y(n_l, n_r)| \,\hat{\Delta}_B\, |Y(n_l, n_r)\rangle\,. \end{aligned} \tag{7.4}$$

where the second equality simply uses the orthonormality of states.
The second mapping relation describes how the operator $\hat{\Delta}_B$ acts on a spin configuration $|x_l, x_r\rangle$, where x_l and x_r is the spin quantum number of left and right quantum dot respectively. In data plots with the interdot detuning Δ, as a coordinate, spin contributions of the left dot are to be subtracted from the right dot ones, e. g. $(\uparrow,\uparrow) = \uparrow - \uparrow = 0$. It is intuitive that if the chemical potentials μ_l and μ_r have the same spin dependence, the magnetic field will not detune the two quantum dots. Consequently, the slope $\Delta' := \frac{\partial \Delta}{\partial B}$ is zero - over the B-range for which the corresponding interdot transition is the 'double dot ground state'. The second mapping relation is thus

$$\langle x_l, x_r| \,\hat{\Delta}_B\, |x_l, x_r\rangle = sgn(B) g\mu_{\mathrm{B}} [x_r - x_l] \tag{7.5}$$

Examples

In a next step, the here developed model is to be applied to the interdot transitions that are relevant for the ST-spin blockade in a double quantum dot device with two effective excess charges. The calculation shall be exemplified for three interdot transitions in the case of negative bias and positive magnetic field ($sgn(B) = 1$). First, consider the singlet to singlet transition, in units of $g\mu_{\mathrm{B}}$,

$$\begin{aligned} &\langle S(2,0) \leftarrow S(1,1)| \,\hat{\Delta}_B\, |S(2,0) \leftarrow S(1,1)\rangle \\ =&\langle S(2,0)| \,\hat{\Delta}_B\, |S(2,0)\rangle - \langle S(1,1)| \,\hat{\Delta}_B\, |S(1,1)\rangle \\ =&\frac{1}{\sqrt{2}^2} \left\{ \underbrace{\langle \downarrow\uparrow, 0| \,\hat{\Delta}_B\, |\downarrow\uparrow, 0\rangle}_{0} - \underbrace{\langle \uparrow\downarrow, 0| \,\hat{\Delta}_B\, |\uparrow\downarrow, 0\rangle}_{0} - \underbrace{\langle \downarrow, \uparrow| \,\hat{\Delta}_B\, |\downarrow, \uparrow\rangle}_{+1} + \underbrace{\langle \uparrow, \downarrow| \,\hat{\Delta}_B\, |\uparrow, \downarrow\rangle}_{-1} \right\} \\ =&-1 \end{aligned} \tag{7.6}$$

where the two mapping relations (equations 7.4 and 7.5) and the relations in equation 7.2 for the respective spin states have been used. Next, consider the triplet to

singlet transition

$$\begin{aligned}
&\langle S(2,0) \leftarrow S(1,1)| \hat{\Delta}_B |S(2,0) \leftarrow T_0(1,1)\rangle \qquad (7.7)\\
=&\langle S(2,0)| \hat{\Delta}_B |S(2,0)\rangle - \langle T_0(1,1)| \hat{\Delta}_B |T_0(1,1)\rangle \\
=&\frac{1}{\sqrt{2}^2}\left\{\underbrace{\langle\downarrow\uparrow,0| \hat{\Delta}_B |\downarrow\uparrow,0\rangle}_{0} - \underbrace{\langle\uparrow\downarrow,0| \hat{\Delta}_B |\uparrow\downarrow,0\rangle}_{0} - \underbrace{\langle\downarrow,\uparrow| \hat{\Delta}_B |\downarrow,\uparrow\rangle}_{+1} - \underbrace{\langle\uparrow,\downarrow| \hat{\Delta}_B |\uparrow,\downarrow\rangle}_{-1}\right\} \\
=&0
\end{aligned}$$

Thirdly, consider the spin-blockaded transition

$$\begin{aligned}
&\langle S(2,0) \leftarrow T_+(1,1)| \hat{\Delta}_B |S(2,0) \leftarrow T_+(1,1)\rangle \qquad (7.8)\\
=&\langle S(2,0)| \hat{\Delta}_B |S(2,0)\rangle - \langle T_+(1,1)| \hat{\Delta}_B |T_+(1,1)\rangle \\
=&\frac{1}{\sqrt{2}^2}\left\{\underbrace{\langle\downarrow\uparrow,0| \hat{\Delta}_B |\downarrow\uparrow,0\rangle}_{0} - \underbrace{\langle\uparrow\downarrow,0| \hat{\Delta}_B |\uparrow\downarrow,0\rangle}_{0}\right\} - \underbrace{\langle\uparrow,\uparrow| \hat{\Delta}_B |\uparrow,\uparrow\rangle}_{0} \\
=&0
\end{aligned}$$

Table 7.1 analyses the slopes Δ' for the interdot transition classes that were categorised in figure 7.2 (d) according to the possible occurrence of spin blockade or filtering effects, using the equivalent computation from equation 1.38.

Kinks in Δ'

In single quantum dots, kinks in the magnetic field dependence of the Coulomb peak gate positions mark a change in ground state configuration [139–141]. In analogy, the present double quantum dot displays discontinuities in the derivative of gate energy coordinate Δ' w. r. t. B, marking a change in interdot transition.

Example: the interdot transition $S(2,0) \leftarrow T_+(1,1)$

Consider, for example, the first line in table 7.1, the interdot charge transition between the spin states $S(2,0) \leftarrow T_+(1,1)$ for negative bias. One electron would be transported from the right to left quantum dot - were the transition not spin-blockaded.
The initial spin states on left and right quantum dot for the (blockaded) tunnel process is given by $T_+(1,1)$ triplet, corresponding a spin-up electrons $(\uparrow,\uparrow)$ on each dot. The only energetically available final state is, though inaccessible due to spin selection rules, the $S(2,0)$ singlet, i. e. two antiparallel spins $(\uparrow\downarrow,0)$ on the left dot and none on the right dot.

Table 7.1: Possible spin states for interdot transition charge configurations for a given $\Delta(B)$ at an interdot charge transition $(2,0) \leftarrow (1,1)$ for negative bias. The dash denotes partial derivative of a given energy by the magnetic field B, e. g. $\Delta' := \partial\Delta/\partial B$. The values are in units of $g\mu_B$ for $B > 0$. For $B < 0$, the slopes change sign. Up and down arrows symbolise the spin orientation and correspond to the z-projection spin quantum numbers $\uparrow := \frac{1}{2}$ and $\downarrow := -\frac{1}{2}$. Spin flips increase the slopes by $\pm g\mu_B$.

Δ'	=	-	μ_l'	+	μ_r'	$\lvert f\rangle$	-	$\lvert i\rangle$	$X(n_l+1, n_r-1)$	$\leftarrow$	$Y(n_l, n_r)$
									$(\mathbf{e},\mathbf{e})$	$\leftarrow$	$(\mathbf{o},\mathbf{o})$
0	=	-	$(-\frac{1}{2})$	+	$(-\frac{1}{2})$	$(\uparrow\downarrow, 0)$	-	$(\uparrow, \uparrow)$	$S(2,0)$	$\nleftarrow$	$T_+(1,1)$
0	=			$\frac{1}{\sqrt{2}^2}[$			$\frac{1}{\sqrt{2}^2}[$		$S(2,0)$	$\leftarrow$	$T_0(1,1)$
		-	$(+\frac{1}{2})$	+	$(-\frac{1}{2})$	$(\downarrow\uparrow, 0)$	-	$(\downarrow, \uparrow)$			
		-	$(-\frac{1}{2})$	+	$(+\frac{1}{2})$	$+\{(\uparrow\downarrow, 0)$	-	$(\uparrow, \downarrow)\}$			
				]			]				
0	=	-	$(+\frac{1}{2})$	+	$(+\frac{1}{2})$	$(\uparrow\downarrow, 0)$	-	$(\downarrow, \downarrow)$	$S(2,0)$	$\nleftarrow$	$T_-(1,1)$
-1	=			$\frac{1}{\sqrt{2}^2}[$			$\frac{1}{\sqrt{2}^2}[$		$S(2,0)$	$\leftarrow$	$S(1,1)$
		-	$(+\frac{1}{2})$	+	$(-\frac{1}{2})$	$(\downarrow\uparrow, 0)$	-	$(\downarrow, \uparrow)$			
		-	$(+\frac{1}{2})$	+	$(-\frac{1}{2})$	$-\{(\uparrow\downarrow, 0)$	-	$(\uparrow, \downarrow)\}$			
				]			]				
+1	=	-	$(-\frac{1}{2})$	+	$(+\frac{1}{2})$	$(\uparrow\uparrow, 0)$	-	$(\uparrow, \uparrow)$	$T_+(2,0)$	$\leftarrow$	$T_+(1,1)$
0	=			$\frac{1}{\sqrt{2}^2}[$			$\frac{1}{\sqrt{2}^2}[$		$T_0(2,0)$	$\leftarrow$	$T_0(1,1)$
		-	$(+\frac{1}{2})$	+	$(-\frac{1}{2})$	$(\downarrow\uparrow, 0)$	-	$(\downarrow, \uparrow)$			
		-	$(-\frac{1}{2})$	+	$(+\frac{1}{2})$	$+\{(\uparrow\downarrow, 0)$	-	$(\uparrow, \downarrow)\}$			
				]			]				
-1	=	-	$(+\frac{1}{2})$	+	$(-\frac{1}{2})$	$(\downarrow\downarrow, 0)$	-	$(\downarrow, \downarrow)$	$T_-(2,0)$	$\leftarrow$	$T_-(1,1)$
									$(\mathbf{o},\mathbf{e})$	$\leftarrow$	$(\mathbf{e},\mathbf{o})$
+1	=	-	$(-\frac{1}{2})$	+	$(+\frac{1}{2})$	$(\uparrow, 0)$	-	$(0, \uparrow)$	$D(1,0)$	$\leftarrow$	$D(0,1)$
-1	=	-	$(+\frac{1}{2})$	+	$(-\frac{1}{2})$	$(\downarrow, 0)$	-	$(0, \downarrow)$			
									spin flip		
+1	=	-		+	(+1)	$(x, \uparrow + y)$	-	$(x, \downarrow + y)$	$\uparrow$	$\leftarrow$	$\downarrow$

Following a rationale of reference [141] (also see [140]), the magnetic field slope of a chemical potential is, by its definition, the spin of the final minus the initial spin. For the right dot this would be $0 - \uparrow = -\frac{1}{2}$ and for the left dot $\uparrow\downarrow - \uparrow = -\frac{1}{2}$ in units of $g\mu_B$. A magnetic field would thus detune the two dots, by the definition $\Delta := \mu_r - \mu_l$, with a slope of $\Delta' = -\frac{1}{2} - (-\frac{1}{2}) = 0$ - that means that a magnetic field does not detune the chemical potentials of the two quantum dot if they have the same magnetic field dependence. This is the case as long as $S(2,0) \nleftarrow T_+(1,1)$ is the

relevant charge transition. If the relevant charge transition changes, so can the slope Δ', as detailed in table 7.1, giving rise to kinks in Δ' as observed in figure 7.9 (a).

Predictions of the model to the spin states involved in interdot transitions

The prediction of the here proposed model is that triplet⇌singlet transitions, where ST-spin blockade can (but must not necessarily) occur, have zero slope $\Delta' = 0$. Transitions between charge states of same spin-multiplet type (e. g. singlet⇌singlet, doublet⇌doublet, triplet⇌triplet, ...) result in slopes $\Delta' = \pm 1$ in units of $g\mu_{\mathrm{B}}$ (with the exception of the $T_0(2,0) \rightleftharpoons T_0(1,1)$-like transitions).

Steeper slopes $\Delta' \geq \pm 2$ can be explained by additional spin flips of core electrons. The last line in table 7.1 exemplifies how a spin flip of a spin-down on the right quantum dot increases the slope by a ± 1. The model can assign possible charge transition types to a given magnetic field interval of a given slope Δ'. As the slope is only one parameter and several interdot charge transitions can produce the same slope value, this assignment is a projection onto a lower-dimensional parameter space rather than an unambiguous *one-to-one* map.

7.2.3 Map of magnetic field evolution $I(B, \Delta)$

The equivalent current data as in figure 7.8 is shown in figure 7.10 by taking a different, $I(B, \Delta; V_{SD} = \pm 700\,\mu\mathrm{eV})$- slice through the phase space. Instead of the entire triple triangles, the current I is recorded only along the line in Δ-direction from triangle tip to the middle of the zero detuning *base line*, as indicated by the green arrows in figure 7.10 (1,2) the example of zero magnetic field.

In $I(\Delta, B)$ measurement, detuning Δ was swept and B stepped (as in reference [71]) in order to avoid heating effects induced by B-sweeps (as e. g. in reference [126]). Monitoring the cryostat bath temperature, the B-steps were found small enough for the system to thermalise during the about 50 seconds $I(\Delta)$ line scan. Experimental artifacts of the scanning direction is a 'stripiness' of the data in Δ direction, i. e. signal fluctuations between line scans.

By assembling these line traces $I(\Delta)$ for magnetic fields $B \in [-4, 4]\,\mathrm{T}$, a map of the magnetic field dependence of both current and interdot transition $(n_l + 1, n_r - 1) \rightleftharpoons (n_l, n_r)$ is obtained. Simply speaking, figures 7.10 (a1, b1) (for $V_{SD} = \pm 700\,\mu\mathrm{V}$) are current bands of width $|eV_{SD}|$ in interdot detuning Δ that are Zeeman-shifted with magnetic field according to the "double dot ground state" $(n_l + 1, n_r - 1) \rightleftharpoons (n_l, n_r)$.

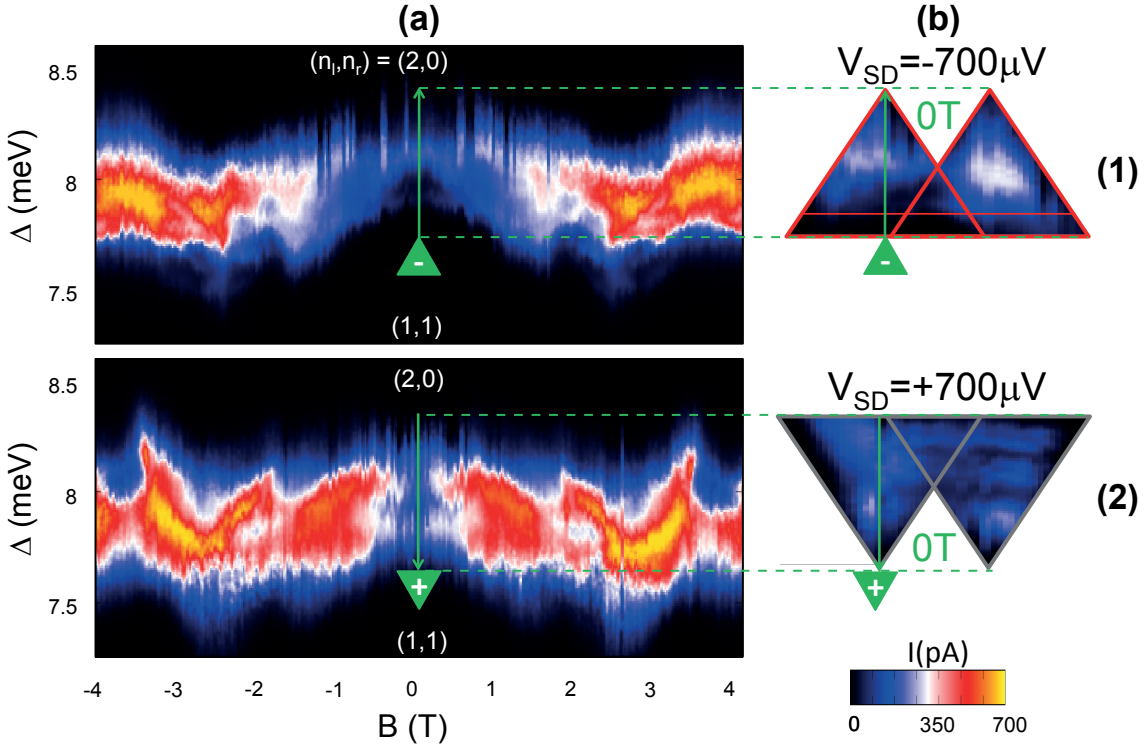

Figure 7.10: Evolution of triple triangles in a magnetic field: current I along line cuts in detuning Δ as function of an out-of plane magnetic field B for V_{SD}=-700 μV (a1) V_{SD}=+700 μV (a2). The Δ line cuts are taken through tip and baseline, as illustrated in (b1) for negative bias (with a spin -blockaded area below the red line within the ride triangular outline) and (b2) positive bias (no spin blockade, finite current within entire area of the light grey triangular outline) of a triple triangle of transition type $(e,e) \rightleftharpoons (o,o)$, using the occurrence of ST-spin blockade as a reference.

7.2.4 Rectification of base line in its magnetic field evolution

For data analysis and from a conceptual point of view, it would appreciable to disentangle the effect of the magnetic field on the "double dot ground state" $(n_l+1, n_r-1) \rightleftharpoons (n_l, n_r)$ from the current through the double dot. To compare the zero detuning line of a triple triangle in a data plot across the magnetic field range, the Δ-shift of the triple triangles must be eliminated. This can be achieved by subtraction of the shift $\delta\Delta$ - as extracted from the triangle positions (figure 7.8) in figure 7.9 (a) - from the magnetic field maps $I(B, \Delta; V_{SD} = \pm 700\,\mu\,\mathrm{eV})$ in figures 7.10. In the so transformed

detuning coordinate

$$\begin{aligned}\Delta^*(B) := \Delta(B) - \int_0^B \mathrm{d}\tilde{B}\{ & \\ & \left[\theta(\tilde{B} - \ 0)\theta(B_I - \tilde{B})\right]\Delta'_{0-I} \\ & + \left[\theta(B_I - \tilde{B})\theta(B_{II} - \tilde{B})\right]\Delta'_{I-II} \\ & +... \\ & \}\end{aligned} \tag{7.9}$$

zero interdot detuning takes zero value $\Delta^*(B) = 0$ for all B. The Roman number index $X = I, II, III, IV, ...$ in B_X denotes the magnetic field value of the X^{th} change in "double dot ground state" $(n_l + 1, n_r - 1) \rightleftharpoons (n_l, n_r)$. For example

$$\Delta'_{I-II} := \left[\frac{\partial\Delta}{\partial B}\right]_{I-II} =: g\mu_{\mathrm{B}} S_{I-II} \tag{7.10}$$

is the constant slope over a magnetic field interval $[B_I, B_{II}]$. This interval can be rephrased in terms of $g\mu_{\mathrm{B}}$ times an effective 'double quantum dot ground state spin' S_{I-II}. $S_{I-II} = 0$ ($S_{I-II} = 1$) corresponds to an effective double quantum dot singlet (triplet) "ground state". The Heaviside step functions θ were conveniently implemented in a script for the plotting software *Gnuplot*. The resulting 'rectified' maps $I(\Delta^*, B)$ are shown in figure 7.11; in this 'full set of data', $I(\Delta^*, B)$-maps are presented for $V_{SD} = \pm 700\,\mu\mathrm{V}$ and corresponding counter-clockwise and clockwise triangles, i. e.

$$\begin{aligned} V_{SD} = -700\,\mu\,\mathrm{V}: \quad & \ominus: (2,0) \leftarrow (1,1) \quad & \oplus: (2,0) \leftarrow (1,1) \\ V_{SD} = +700\,\mu\,\mathrm{V}: \quad & \oplus: (2,0) \rightarrow (1,1) \quad & \ominus: (2,0) \rightarrow (1,1) \end{aligned} \tag{7.11}$$

The triangles $\oplus$ have an overall increased current compared to the triangles $\ominus$. The main cause is, as chapter 6 made plausible, the asymmetry in *single resonance*, co-tunnelling leakage current due to the stronger source over drain coupling (applying to the triple triangles as colour-coded in red and cyan). A situation which is described by the proposed first order, sequential tunnelling model is hence found only in the triangles $\ominus$. In the $\oplus$ triangles, for instance, spin-blockaded areas would show non-zero current because they are superimposed with a finite co-tunnelling current.

If the interpretation of the (sequential tunneling) model presented in table 7.1 and its coordinate transformation $\Delta \mapsto \Delta^*$ are correct, current in figure 7.11 should occur only within the bias window that is marked by the solid orange lines. Elsewhere, the double quantum dot should be in Coulomb blockade. Checking on figure 7.11,

this is the case for $B \leq 3.2\,\mathrm{T}$. From figure 7.9 (b) it was already found that the Σ-position changes, hinting at a change of the underlying physics. There is also a drastic increase in current. A partial explanation can be obtained by appreciating that $B = 3.2\,\mathrm{T} = 370\,\mu\mathrm{eV}/g\mu_\mathrm{B}$ corresponds to half the applied bias $|\,\mathrm{e}V_{SD}| = 700\,\mu\mathrm{eV}$; starting from these field values, the blocking states $T_\pm(1,1)$ are driven out of the bias window. Note that the $I(\Delta; B)$-slices are taken through the middle Σ-position of the base line. Here, the left and right dot ground states $S(2,0)$ and $S(1,1)$ are aligned in the middle of the bias window, i. e. half the bias $|\,\mathrm{e}V_{SD}|/2 = 350\,\mu\mathrm{eV}$ away from the base line edge points (labeled 1 and 2 in figure 1.11). It is additionally assumed that, at B=0, the $T(1,1)$ and $S(1,1)$ are degenerate [20], as their probability distribution extends over both dots. Whether this rectification is a successful interpretation can also be checked in the logarithmically scaled complementary differential conductance data to figure 7.11, see figure 7.12.

7.2.5 Verification of the model by spin blockade spectroscopy

So far, it was ensured that the magnetic field dependence of the 'ground state' is correctly interpreted by the here proposed model. Next steps are to derive information on the spin state configuration and on the 'exited state' spectrum of the transport through the DQDot.

In the rectified *bias versus magnetic field*-bands $I(B, \Delta^*)$ in figure 7.12, there are many transport blockaded areas. Spin blockade can have diverse origins [20, 128–130, 130, 131] and, in particular, Pauli-spin blockade can arise from different spin state configurations (cf. [20, 73]). *Spin blockade spectroscopy* [142] - meaning that the spin blockade effect is used as a tool to probe the spin state transition spectrum on the double quantum dot - shall be used to verify whether the model can correctly describe them. To compare the predictions of model proposed in table 7.1 to the experimental findings, two exemplary features are considered.

Singlet-triplet (ST)-spin blockade at negative bias around $B = 0$

Around zero field and at small detuning, ST-spin blockade appears, for negative bias, in the $I(B, \Delta^*)$-map for both left, *counter-clockwise* (figure 7.11 (a1)) and right, *clockwise* (figure 7.11 (c1)) triple resonances of the $(2,0) \leftarrow (1,1)$ interdot transition. This standard example of a spin blockade mechanism and spin state configuration has been discussed in detail in figure 7.6. Upon bias reversal, there is a finite current over the entire triple triangle area, as expected (cf. figure 7.2). For the case of $B = 0$, the same information is contained in the positive and negative bias triangles in the gate plane $I(\Sigma, \Delta)$ (see figures 7.11 (b1) and (b2)).

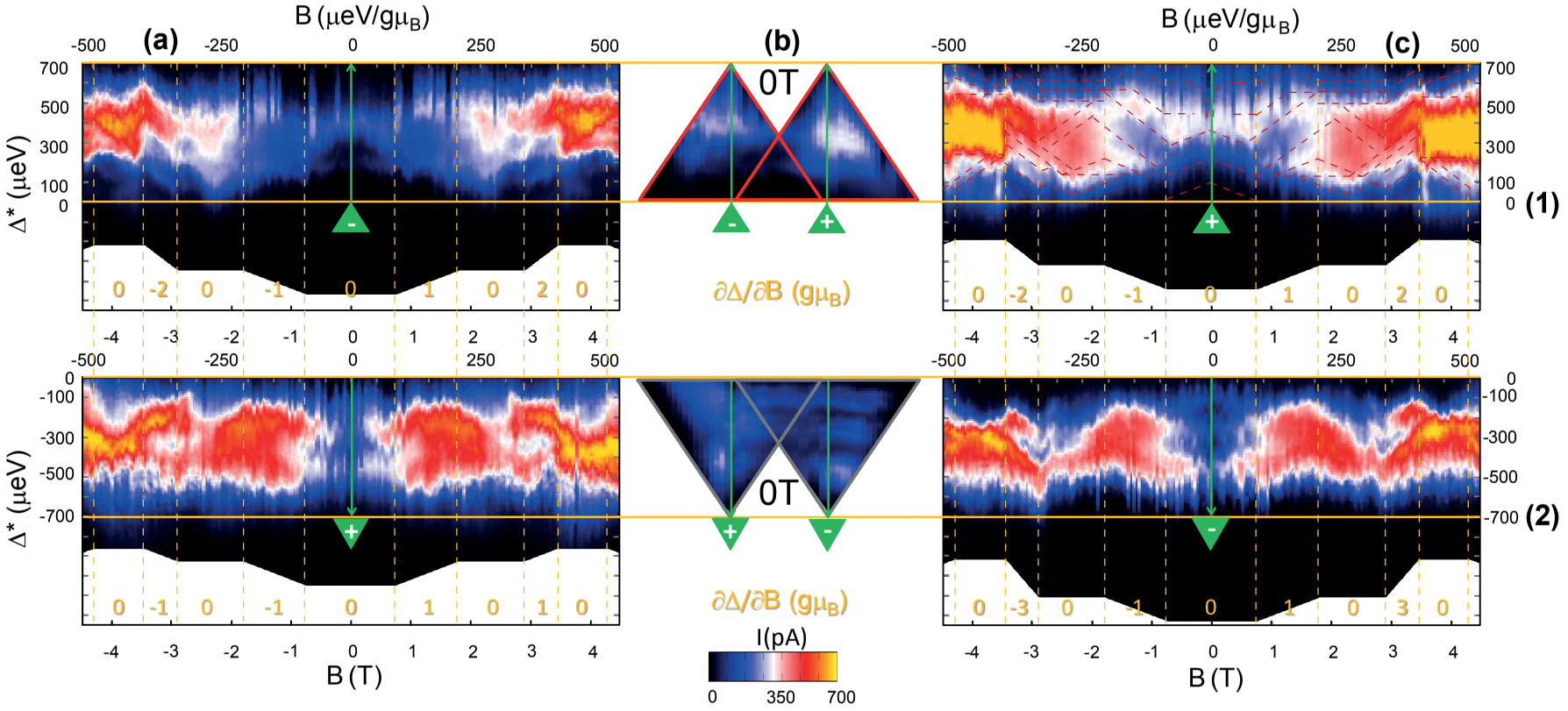

Figure 7.11: "Rectified" maps $I(B, \Delta^*)$ for counter-clockwise ($\ominus$, (a1, c2)) and clockwise ($\oplus$, (a2, c1)) triple triangles (b) of the $(2,0) \leftrightharpoons (1,1)$ interdot transition for negative (1) and positive (2) bias $V_{SD} = \mp 700\,\mu$V. The detuning coordinate $\Delta \mapsto \Delta^*$ is transformed such that, for all magnetic fields, the zero interdot detuning or 'base line' of the triple triangles are at the same Δ^*=0 value (solid orange line). This 'magnetic field evolution band' of line cuts through the center of the triple triangles is obtained by subtraction of the segment-wise 'double dot ground state' B-dependence $\frac{\partial \Delta}{\partial B} B$ according to equation 7.9. Orange numbers indicate the field dependence of the B intervals. The higher source compared to drain coupling leads to an overall increased current in the $\oplus$- compared to the $\ominus$-triple triangles over the entire B-range.

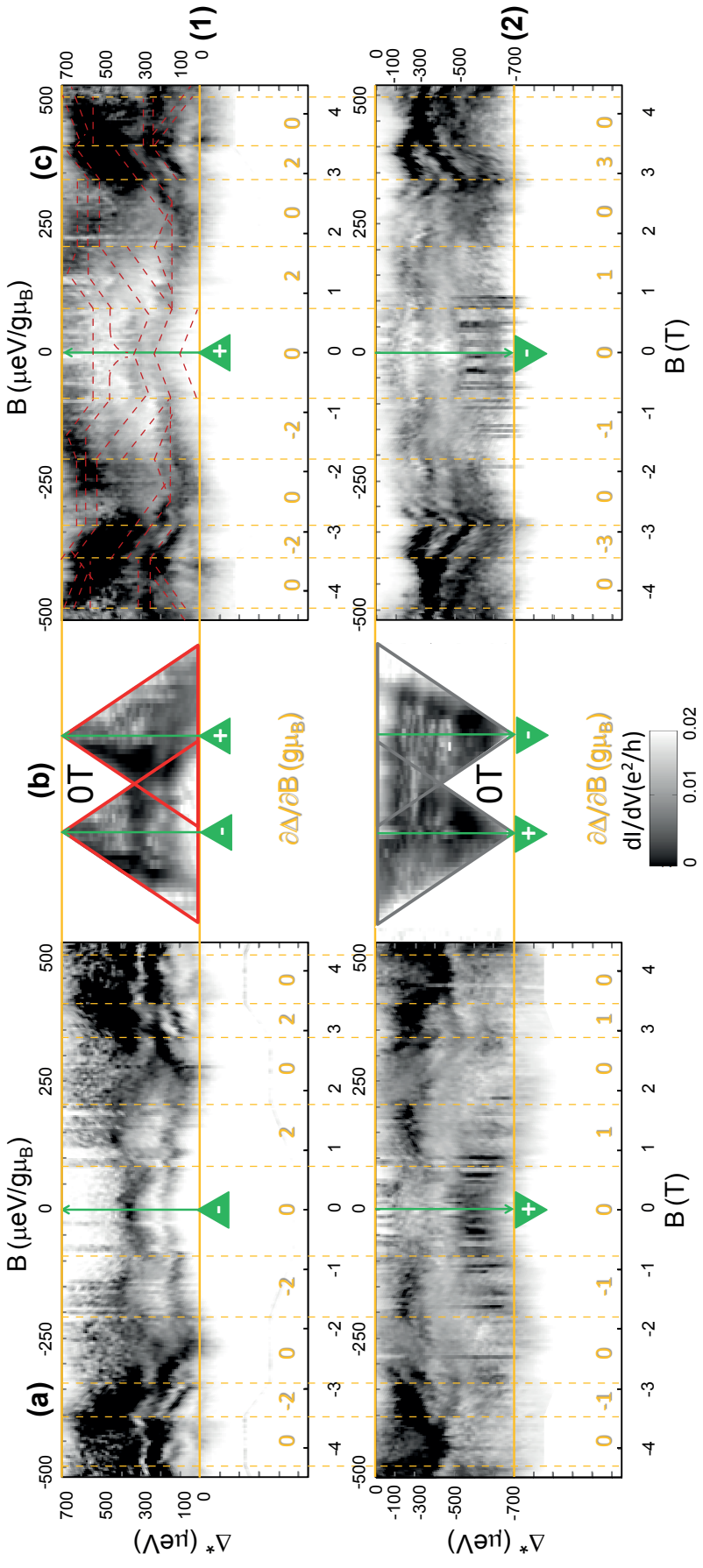

Figure 7.12: "Rectified" maps $\mathrm{d}I/\mathrm{d}V(B, \Delta^*)$ for counter-clockwise ($\ominus$, (a1, c2)) and clockwise ($\oplus$, (a2, c1)) triple triangles (b) of the $(2,0) \rightleftharpoons (1,1)$ interdot transition for negative (1) and positive (2) bias $V_{SD} = \mp 700\,\mu\mathrm{V}$. These simultaneously measured differential conductance data supplement the current data in figure 7.11, providing a check on the suggested model: if the rectification interpretation is correct, conductance features are only within the bias-wide bands (indicated by the orange lines). The model considers sequential tunnelling only. Co-tunnelling (e. g. the *single resonances*, cf. section 6.1) can give rise to features outside these bands, in the Coulomb-blockaded areas (cf. subplots (a2) and (c1)). Subplots (b1) and (b2) are greyscaled as in figure 7.8.

Triplet-singlet (TS)-spin blockade at positive bias at finite magnetic field

Consider the triple triangles in figure 7.8 for positive bias, i. e. the bias direction $(2,0) \rightarrow (1,1)$ where no ST-spin blockade should occur for zero magnetic field; transport is blockaded at higher magnetic fields $B > 3.5\,\mathrm{T}$ for low detuning Δ. Consistently, the same effect can be observed in *detuning versus magnetic field*-bands $I(B, \Delta^*)$ (figure 7.11 (c2)). This current blockade may be ascribed to *TS-spin blockade* at a transition $T(2,0) \rightarrow S(1,1)$. By symmetry (cf. figure 7.2 (d)), the situation is the same as the $(1,1) \rightarrow (0,2)$ transition for which the model of table 7.1 predicts a spin blockade effect. Reference [126] observes a similar current suppression over a comparable parameter region in a CNT-based DQDot ascribing it to a TS-spin blockade mechanism. TS-spin blockade describes the experimental findings correctly for small detuning, when the $S(1,1)$ is inaccessibly higher up in energy than $S(2,0)$ but $T_-(2,0)$ is driven below by the magnetic field. At zero detuning, however, when the $S(2,0)$ and $S(1,1)$ are in resonance, unblocking the *blocking state* $S(2,0)$. The resulting zero detuning line of finite current has been reported from GaAs-based [73] or SiGe-based [28] DQDots but is not observed here or in other CNT-based DQDot experiments [71, 126].

7.2.6 Excited state spectrum in $I(B, \Delta)$

The spectrum of three and more exited states within the $|eV_{SD}| = 700\,\mu\mathrm{eV}$ bias window is mapped out in the *bias versus magnetic field*-bands $I(B, \Delta^*)$ in its magnetic field evolution. For the example of figure 7.11 (c1), the exited state positions in detuning as a function of magnetic field, $\Delta^*(B)$, are indicated by brick red, dashed lines. In concordance with the proposed model, lines with integer multiple slopes of $g\mu_\mathrm{B}$ were matched to features in the current (see figure 7.11 (c1)). The so-placed dashed line pattern was then transferred and superposed onto the conjugate $\mathrm{d}I/\,\mathrm{d}V(\Delta^*, B)$-map (figure 7.12 (c1)). Also in $\mathrm{d}I/\,\mathrm{d}V(\Delta^*, B)$, the $\Delta^*(B)$-lines correspond to contrast features.

In the rectified detuning coordinate Δ^* (cf. equation 7.9), the lines provide information on the *relative* change in slope $\Delta'_{|ES\rangle} - \Delta'_{|GS\rangle}$ of the 'DQDot exited state' $|ES\rangle$ B-evolution with respect to that of the 'DQDot ground state' $|GS\rangle$. The subsequent discussion will focus on the first exited state $|1.ES\rangle : T(2,0) \leftarrow T(1,1)$ (slope $\Delta^{*'} = \Delta' = 1$) for the low magnetic field range ground state $|GS\rangle : S(2,0) \leftarrow T(1,1)$ (slope $\Delta^{*'} = \Delta' = 0$).

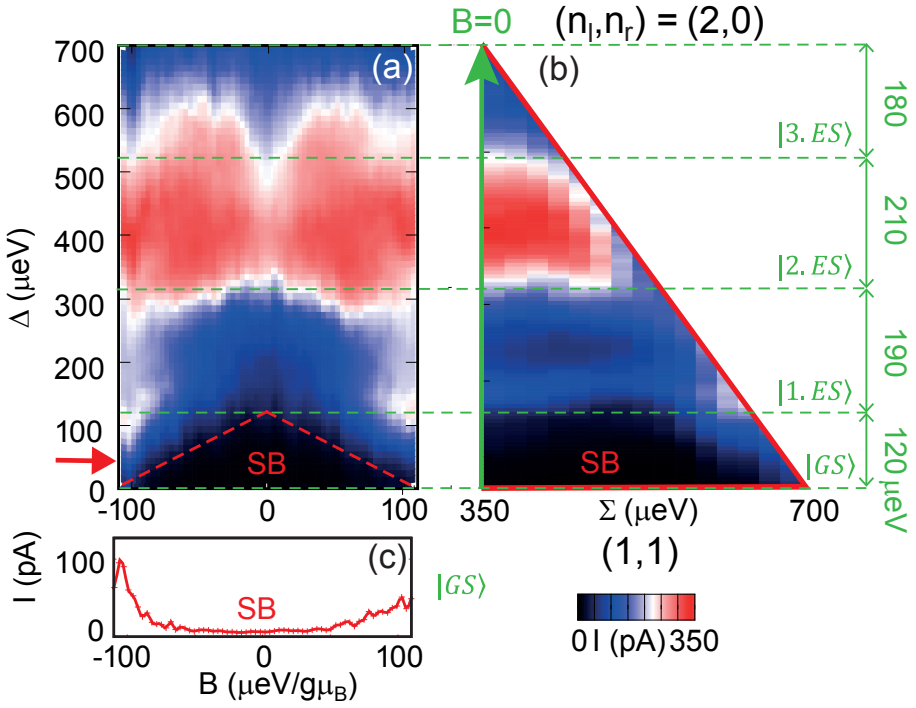

Figure 7.13: ST-spin blockade triangle around zero magnetic field and 'spin funnel' at finite detuning: (a) Map $I(\Delta, B)$ of current versus detuning Δ and inplane magnetic field B scaled in energy units. Dashed red lines mark the 'ST-spin blockade (SB) triangle'. Its extensions, measured from B=0 in both Δ and B, is given by the $(2,0)$ singlet-triplet splitting $\Delta_{ST(2,0)}$. Their slopes are $\pm g\mu_B$, consistent with a $T(2,0) \leftarrow T(1,1)$ interdot transition (cf. table 7.1)). From the fit results a Landé factor g =2. (b) *Counter-clockwise* or *electron* triple triangle at V_{SD}=-700 μeV and B=0 at the $(0,2)\nleftarrow(1,1)$ interdot transition. The data points along the green arrow correspond to the B=0-line in (a). Dashed green lines indicate the onset of exited interdot transitions and their excitation energies at B=0, e. g. the $|GS\rangle$-$|ES\rangle$ excitation $\Delta_{ST(2,0)}$=120 μeV. Only half the triangle is shown in Σ-direction. (c) Line scan $I(B)$ from the ST-spin blockade regime at small interdot detuning Δ =50 μeV. For low magnetic fields, the current through the DQDot is entirely suppressed. At higher fields, SB is lifted by as the $T(2,0) \leftarrow T(1,1)$-transition, the 'first exited state $|1.ES\rangle$', becomes energetically accessible.

7.3 Spin blockade triangles in $I(B, \Delta)$

Mechanisms to lift ST-spin blockade

The current is spin-blockaded by a *trapped state* on the double quantum dot as long as a characteristic energy barrier is not overcome. This *spin blockade energy barrier* can be surmounted, e. g. by inverting the charge state configuration via bias reversal (cf. figure 7.7 (a)), by thermal activation out of the blocking state [20], by

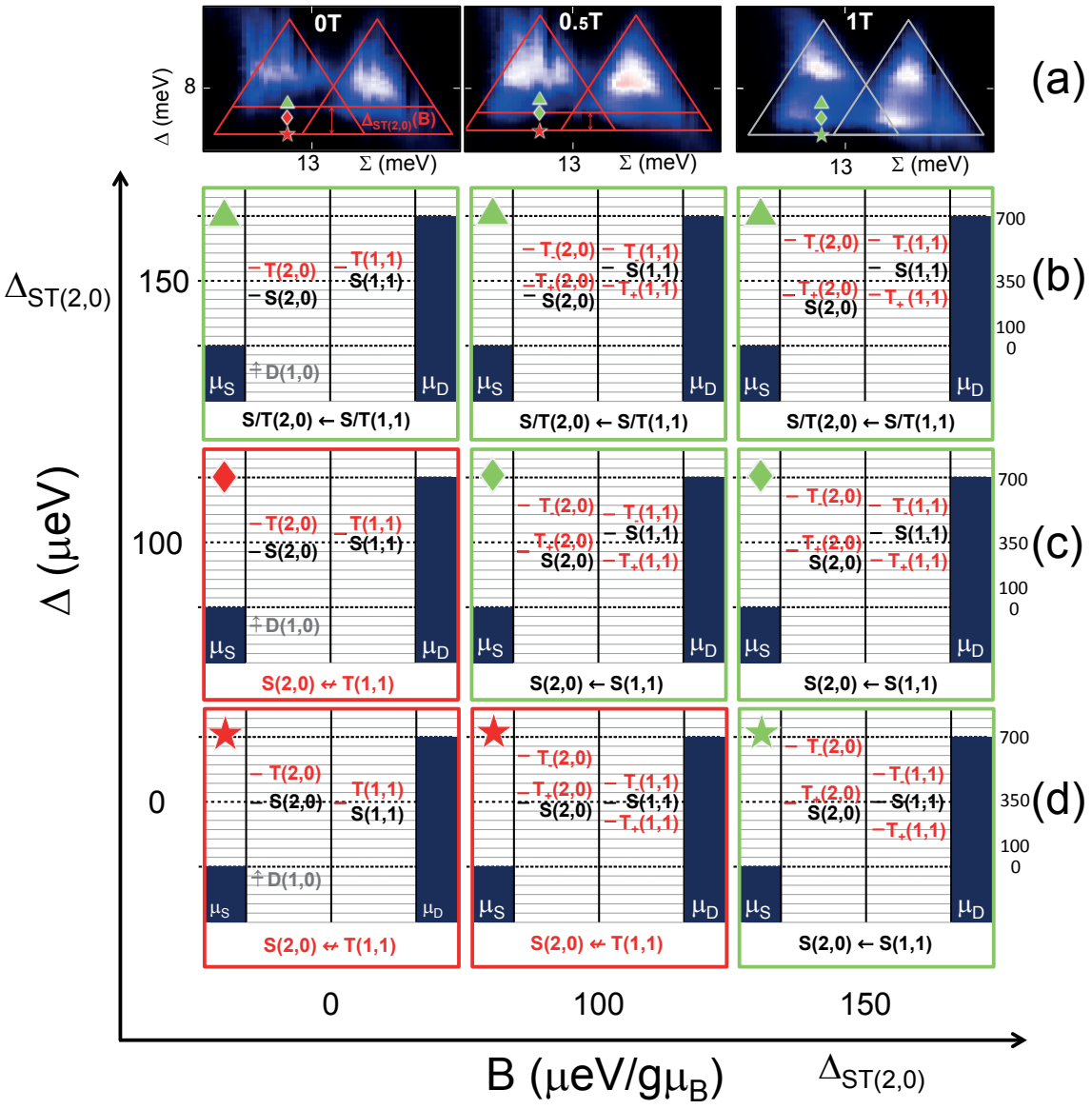

Figure 7.14: Spin state configurations (a-c2-4) in a triple triangle at an interdot transition $(2,0) \leftrightarrow (1,1)$ and V_{SD}=-700 μV (for B=0, 0.5, 1 T (a-c1)).The zero magnetic field $S(2,0)$-$T(1,1)$ splitting is $\Delta_{ST(2,0)}(B)$ ≈150 μeV (double-headed arrow in (a1)). Sketches are labelled by star, diamond and triangle for increased detuning in (a-c1) and are colour-coded for spin blockade ★♦▲ or lifted spin blockade regimes ★♦▲. (a2: ▲) When, at zero magnetic field, $\Delta \geq \Delta_{ST(2,0)}$, $T(2,0)$ is aligned with $T(1,1)$, unblocking this *blocking state*. (c4: ★) When, at zero detuning, $T_+(2,0)$ is Zeeman-shifted into resonance with $S(2,0)$, i. e. $\Delta_{ST(2,0)}(B = \Delta_{ST(2,0)}/g\mu_B) = 0$, the experimental data show lifted spin blockade throughout the triple triangle. To account for this, the simple model needs to be extended by spin flipping events and hybridisation,e. g. of $T(2,0)$ and $S(2,0)$. (b3: ♦) The ST-SB energy barrier can also be overcome by linear combinations $\alpha\Delta + (1-\alpha)B \geq \Delta_{ST(2,0)}$, $\alpha \in \mathbb{R}_+$.

spin-flipping events [71], higher order tunnelling (cf. figure 7.11 (a1) versus (c1)) or by hyperfine or spin-orbit interaction [31, 32, 71, 143]. In this section, the data are discussed only in terms of sequential tunnelling and (correspondingly) the picture of the weakly interdot-coupled DQDot as 'two interacting atoms'. Higher order effects, like co-tunnelling or spin state mixing, are set aside for the time being. Despite of these strong approximations, this scheme can describe many transport features through the double dot very accurately. Where the model is meets its limits will be exemplified in the next section (section 7.4).
For the present case of two electrons in the dot (a *helium-like* quantum dot [20]), Pauli exclusion and exchange energy induce a splitting between the spin singlet and triplet states that can be controlled by gates and magnetic fields [24, 28, 29, 137, 138]. With the right dot doubly occupied, i. e. $(n_r, n_l) = (2, 0)$, the ground state is a $S(2, 0)$-singlet and the $T(2, 0)$-exited state is higher in energy by the singlet-triplet splitting $\Delta_{ST(2,0)}$. Consequently, the detuning range in which ST-spin blockade can occur depends on the magnetic field; in this way, the magnetic field dependence of the singlet-triplet splitting $\Delta_{ST}(B)$ [20, 28] can be probed. This physical constellation could serve to use the double quantum dot to prepare a spin qubit and to perform logic gate operations [8]. The prerequisite of this use of the 'spin resource' is experimental control and precise knowledge of the parameter space. This discussion investigates in detail how the *ST-spin blockade energy barrier* $\Delta_{ST(2,0)}$ can be overcome either by detuning Δ^* or magnetic field $g\mu_{\mathrm{B}}B$ or a combination of both.

7.3.1 ST-spin blockade triangles around zero magnetic field

Figure 7.13 (a) shows a current map $I(B, \Delta)$ as a function of detuning and a magnetic field B; B is applied in the sample plane and perpendicularly to the PdNi electrodes, i. e. along an easy magnetisation axis of the strips (for details on the magnetic properties of the PdNi electrodes as fabricated here see [99]).
Dashed green lines indicate the onset of zero magnetic field exited 'states' $|1.ES\rangle$ through $|3.ES\rangle$ across figures 7.13 (a) and (b).

Lifting ST-spin blockade by detuning only at $(B, \Delta) = (0, \Delta_{ST(2,0)})$

Figure 7.13 (a) can be understood as line cuts $I(\Delta)$ from triple triangle tip to base line centre, assembled over a range of magnetic fields into a $I(B, \Delta)$-map. To give an example, the zero field $I(\Delta; B = 0)$-line trace is indicated by the green arrow in figure 7.13 (c), where half $\ominus$-triple triangle for the $(2, 0) \leftarrow (1, 1)$ interdot transition and at $B = 0$ is shown. Its lowest portion, from zero detuning $\Delta = 0$ to

$\Delta_{ST(2,0)}$ =120 μeV is spin-blockaded (SB). At (and above) $\Delta = \Delta_{ST(2,0)}$, the $T(2,0)$ triplet is aligned with (and drops below) the *trapping state* $T(1,1)$; current can flow because the $T(2,0) \leftarrow T(1,1)$ interdot transition is allowed by spin selection rules.
The $I(B)$-line trace emphasises that for $0 \leq \Delta \leq \Delta_{ST(2,0)}$, the current across the double quantum dot is suppressed (SB, figure 7.13 (c)).
Treading along the *coloumns* in figure 7.14 (a1) it is demonstrated for $B = 0$ how ST-spin blockade occurs for zero (cf. sketch 7.14 (a4), ★) and low detuning (cf. sketch 7.14 (a3), ♦) and is lifted when the $T(2,0)$ and $T(1,1)$ triplets are detuned into (cf. sketch 7.14 (a2), ▲) and beyond resonance.

Lifting ST-spin blockade by magnetic field only at $(B, \Delta) = (\mp\Delta_{ST(2,0)}, 0)$

The range of figure 7.13 (a) covers the exited spectrum of the entire $|eV_{SD}|$ = |-700 μeV|- wide bias window in the interdot detuning Δ. In B, the range is confined to the 'ground state' $S(2,0) \nleftarrow T(1,1)$. At $g\mu_B B = \pm\Delta_{ST(2,0)}(0)$, spin blockade is lifted as the singlet-triplet splitting $\Delta_{ST(2,0)}(g\mu_B B = \Delta_{ST(2,0)}) = 0$ is compensated. At these values, the $T_{\mp}(2,0)$ triplet is resonant with the $S(2,0)$ singlet.
Over the magnetic field range in figure 7.13 (a), the 'ground state' exhibits no change in Δ with B, i. e. $\frac{\partial\Delta}{\partial B} = 0$, in agreement with the model in table 7.1. In this interval, the raw data are therefore unaffected by the rectification interpretation (see section 7.2.4) and the detuning coordinate is equivalent to the transformed coordinate $\Delta^* \equiv \Delta + const \ \forall \ g\mu_B B \in \left[-\Delta_{ST(2,0)}(B=0), \Delta_{ST(2,0)}(B=0)\right]$. Increasing B reduces $\Delta_{ST(2,0)}$.
Treading along the *lines* in figure 7.14, e. g. from figure 7.14 (a) via (b) to (c), it is demonstrated how with increasing B the *bias current threshold* [20] is gradually brought closer to the zero-detuning triple triangle 'base line' (to be read off the Δ-distance of points ★ and ▲/♦, see sketches 7.14 (a4)/(b4)) until coinciding when the splitting reaches zero (sketch 7.14 (c4), ★). A red line marks this bias current threshold and its Δ-distance to the baseline corresponds to the singlet-triplet splitting $\Delta_{ST(2,0)}(B)$. Similar dependencies of the singlet-triplet splitting in the magnetic field have been reported from previous DQDot experiments [20,24,28,29,72,137,144] and theoretical work [27, 133].
The spin constellation schematic in figure 7.14 (c4), can, by comparison with the experimental findings in figure 7.14 (c1), identify the condition for spin blockade lifting at zero detuning: the $T(2,0)$ must be in resonance with the $S(2,0)$ (or below in energy). However, being based on the simple spin blockade model that neglects spin flips and that the double quantum dot system may be more accurately described by an eigenbasis of mixed states [32] (e. g. mixing $T(2,0)$, $S(2,0)$, $T(1,1,)$, $S(1,1)$,...), it is beyond these schematics to explain how spin blockade is lifted.

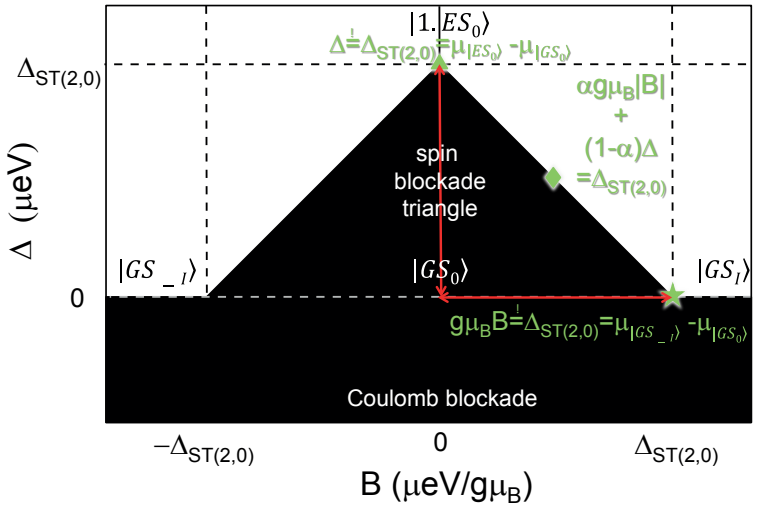

Figure 7.15: Sketch of a *spin blockade triangle* in $I(B, \Delta)$. Consider the point of zero detuning and magnetic field in the $(B, \Delta) = (0, 0)$ plane, in a region with spin blockade. The sketch is drawn for negative bias V_{SD}. Black areas stand for zero and white ones for finite current through the double dot. To overcome the spin blockade, an energy must be supplied by either positive detuning Δ (▲) or a magnetic field $\pm g\mu_B B$ (▼) or a (linear) combination of both (♦) , of at least the *spin blockade energy barrier*, e. g. $\Delta_{ST(2,0)}$ for ST spin blockade. These conditions give rise to a *spin blockade triangle*.

For example, according to schematic 7.14 (c4, ★), the triplets $T_-(1,1)$ and $T_+(1,1)$ should be blocking states, in contradiction with the experimental findings. It may not be without reason that sketches like in figure 7.14 of how spin are often omitted in literature [20, 28, 29, 73]. They are discussed here in order to demonstrate the predictive limits of this commonly used model of the double quantum dot as 'two interacting atoms'.

Lifting ST-spin blockade by a linear combination $g\mu_B B + \Delta \geq \Delta_{ST(2,0)}$

A black-contrasted triangular area of suppressed current is observed in around zero detuning and field in figure 7.13 (a). The sketch in figure 7.15 explains this *spin blockade triangle*: consider the point of zero detuning and magnetic field in the $(B, \Delta) = (0, 0)$ plane, in a region with spin blockade. The sketch is drawn for negative bias V_{SD}. Black areas stand for zero and white ones for finite current through the double dot. As already seen in the data (cf. figure 7.13 (a)), to overcome the spin blockade, an energy must be supplied by either positive detuning Δ (▲) or a magnetic field $\pm g\mu_B B$ (▼) or a (linear) combination of both (♦)

$$\Delta_{ST(2,0)} \stackrel{!}{=} \alpha\Delta + (1-\alpha) g\mu_B |B|, \ \alpha \leq 1 \tag{7.12}$$

of at least the *spin blockade energy barrier*, e. g. $\Delta_{ST(2,0)}$ for ST spin blockade. Along this line the double dot 'ground state' transition changes from $S(2,0) \leftarrow T(1,1)$ to $S/T(2,0) \leftarrow S/T(1,1)$. That Δ and B can be linearly combined to the threshold to lift the spin blockade is an experimental finding. The sides of this equal-sided triangle have slopes

$$\frac{\partial \Delta}{\partial B} = \pm g \mu_{\mathrm{B}} \tag{7.13}$$

with $g = 2$. Similar total suppression of spin blockade by a magnetic field has been observed, e. g., in GaAS-based double quantum dots [24,73] and in another group-IV (Si/SiGe)-based DQDots [28] $g = 2.1 \pm 0.2$.
These conditions give rise to a *spin blockade triangle*, in analogy to a electrostatically blockaded *Coulomb blockade diamonds* in the (gate, bias)-plane or a *Coulomb blockade hexagons* in the (Σ, Δ)-plane. For negative detuning Δ, the system is driven outside the triple triangle area, i. e. into normal Coulomb blockade.

7.3.2 Double spin blockade triangle: spin re-orientation of lower-level spins

Figure 7.16 (a) shows a current map $I(B, \Delta)$ for the interdot charge transition $(2,0) \leftarrow (1,1)$ at negative bias V_{SD} =-700μeV. The range is confined to the first 'double dot exited state' $|1.ES_0\rangle \equiv |GS_{\pm I}\rangle := T(2,0) \leftarrow T(1,1)$ in magnetic field B and for the first three exited states in detuning Δ. The 'double dot ground state' $|GS_0\rangle := S(2,0) \nleftarrow T(1,1)$ is identified by spin blockade spectroscopy [32,142]. In agreement with the proposed model of magnetic field dependence of the interdot transition spin state configuration in Δ-coordinate, the slope $\Delta' = \frac{\partial \Delta}{\partial B}$ is zero. Therefore, the effective detuning $\Delta^* \equiv \Delta$ is here equivalent to the untransformed 'raw data' detuning Δ.
As already seen in figure 7.13 (a), there is a *spin blockade triple triangle* at low detuning stemming from ST-spin blockade. Figure 7.16 ★ and ♦ illustrates this for $B = 0$. This spin blockade is lifted once, by detuning or magnetic field, the $T(2,0) \leftarrow T(1,1)$ and interdot channels become energetically accessible. As a direct consequence, the $S(2,0) \leftarrow S(1,1)$ channel is also unblocked (cf. figure 7.16 ▲ for B). According to table 7.1, the $T(2,0) \leftarrow T(1,1)$ transition has a slope of $\Delta' = \pm 1$ in units of $g\mu_{\mathrm{B}}$; these slopes define the equilateral sides of the ST-spin blockade triangle. The change from black to blue contrast in the colour scale of figure 7.16 (a) marks the onset of a small but finite tunnel current through the double dot and is highlighted by red, $\pm g\mu_{\mathrm{B}}$-sloped lines. Experimental artifacts in the data are some line scans $I(\Delta)$ where the signal is 'shifted up' due to some electrostatic fluctuation. At higher detuning $\Delta > \Delta_{ST(2,0)} \approx 113\,\mu$eV, the double dot is driven into a second

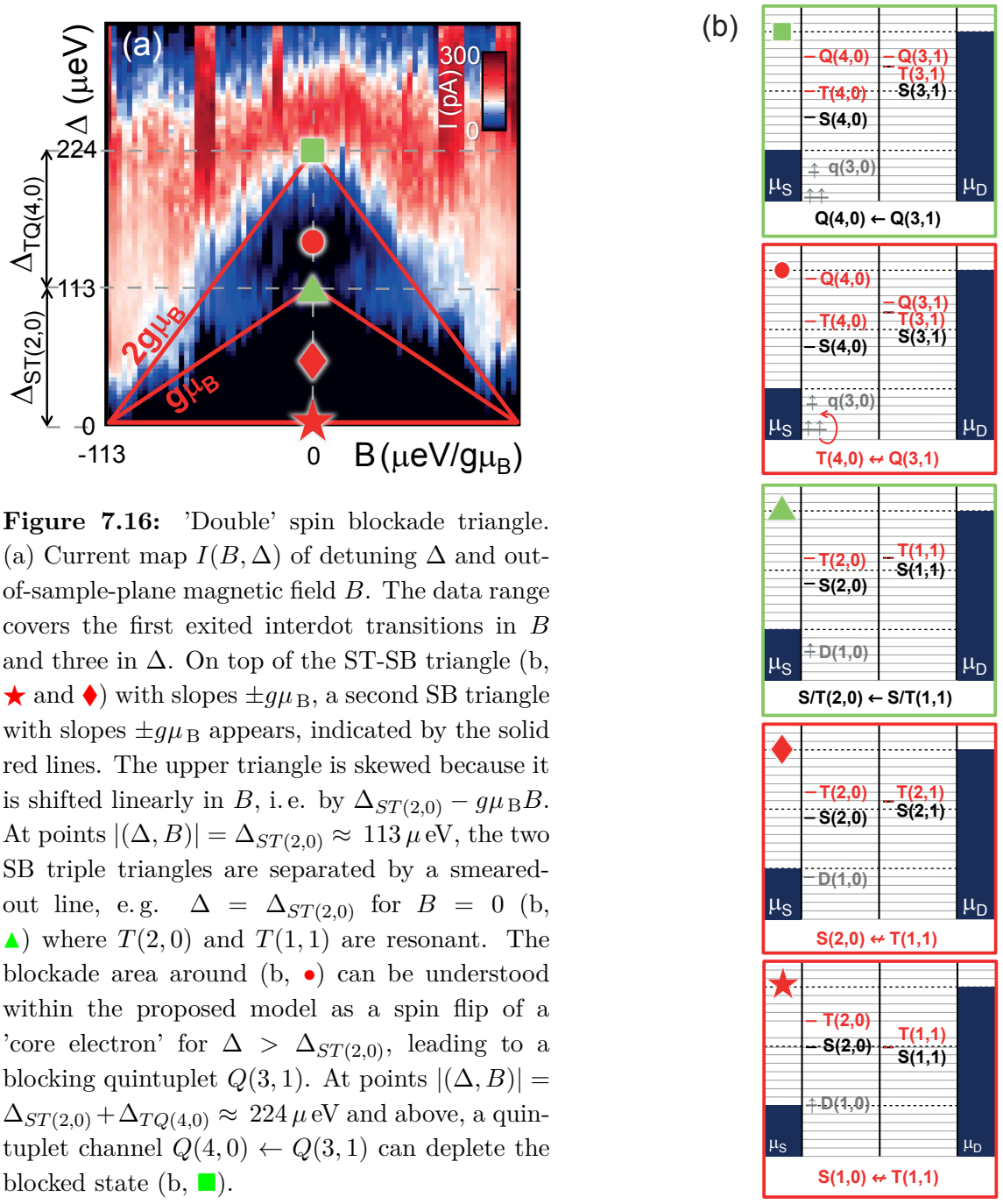

Figure 7.16: 'Double' spin blockade triangle. (a) Current map $I(B, \Delta)$ of detuning Δ and out-of-sample-plane magnetic field B. The data range covers the first exited interdot transitions in B and three in Δ. On top of the ST-SB triangle (b, ★ and ♦) with slopes $\pm g\mu_B$, a second SB triangle with slopes $\pm g\mu_B$ appears, indicated by the solid red lines. The upper triangle is skewed because it is shifted linearly in B, i. e. by $\Delta_{ST(2,0)} - g\mu_B B$. At points $|(\Delta, B)| = \Delta_{ST(2,0)} \approx 113\,\mu$eV, the two SB triple triangles are separated by a smeared-out line, e. g. $\Delta = \Delta_{ST(2,0)}$ for $B = 0$ (b, ▲) where $T(2,0)$ and $T(1,1)$ are resonant. The blockade area around (b, ●) can be understood within the proposed model as a spin flip of a 'core electron' for $\Delta > \Delta_{ST(2,0)}$, leading to a blocking quintuplet $Q(3,1)$. At points $|(\Delta, B)| = \Delta_{ST(2,0)} + \Delta_{TQ(4,0)} \approx 224\,\mu$eV and above, a quintuplet channel $Q(4,0) \leftarrow Q(3,1)$ can deplete the blocked state (b, ■).

region of blockaded current (see figure 7.16 ●). Above $\Delta > 224\,\mu$eV, this transport blockade is also lifted (cf. figure 7.16 ■) making way to a markedly increased tunnel current. The red contrast in the colour scale of figure7.16 (a), indicative of increased current, follows well the red lines with slopes $\pm 2g\mu_B$.

This second blockade region can be regarded as a another spin blockade triangle

Table 7.2: Quintuplet-triplet (QT)-spin blockade at an interdot charge transition $(4,0) \leftarrow (3,1)$ for negative bias - or a $(2,0) \leftarrow (1,1)$ interdot charge transition where one core electron on the left dot undergoes a spin flip, increasing the spin on the left dot by one. In the latter case, the slopes Δ' are to be increased by +1 with respect to the $S(2,0) \leftarrow T_+(1,1)$ ground interdot transition (cf. the experimental findings in figure 7.16). The dash denotes partial derivative of a given energy by the magnetic field B, e. g. $\Delta' := \partial\Delta/\partial B$. The values are in units of $g\mu_{\mathrm{B}}$ for $B > 0$. For $B < 0$, the slopes change sign. Up and down arrows symbolise the spin orientation and correspond to the z-projection spin quantum numbers $\uparrow := \frac{1}{2}$ and $\downarrow := -\frac{1}{2}$. Spin flips increase the slopes by $\pm g\mu_{\mathrm{B}}$.

Δ'	=	-	μ_l'	+	μ_r'	$\lvert f\rangle$	-	$\lvert i\rangle$	$X(n_l+1, n_r-1)$	$\leftarrow$	$Y(n_l, n_r)$
									$(\mathbf{e},\mathbf{e})$	$\leftarrow$	$(\mathbf{o},\mathbf{o})$
0 +1	=	-	$(-\frac{1}{2})$	+	$(-\frac{1}{2})$	$(\uparrow\uparrow\uparrow\downarrow, 0)$	-	$(\uparrow\uparrow\uparrow, \uparrow)$	$T_+(4,0)$	$\leftarrow$	$Q_{++}(3,1)$
1 +1	=	-	$(+\frac{1}{2})$	+	$(-\frac{1}{2})$	$(\uparrow\uparrow\uparrow\uparrow, 0)$	-	$(\uparrow\uparrow\uparrow, \uparrow)$	$Q_{++}(4,0)$	$\leftarrow$	$Q_{++}(3,1)$

on top of the ST-spin blockade one, appreciating that the base line of the upper triangle is marked by the $T(2,0) \leftarrow T(1,1)$ interdot transitions that have a finite slope $\Delta' = \pm g\mu_{\mathrm{B}}$ in the $I(B,\Delta)$-map. The upper triangle is skewed because it is shifted linearly in B, i. e. by

$$\Delta_{ST(2,0)} - g\mu_{\mathrm{B}} B.$$

The triangular shape can be retrieved when subtracting the 'baseline slopes of the upper SB-triangle from its lateral slopes', i. e.

$$\pm 2g\mu_{\mathrm{B}} - \pm g\mu_{\mathrm{B}} = \pm g\mu_{\mathrm{B}}$$

- which is the same *relative* slope of baseline versus equilateral triangle sides (or equivalently: respective $|ES\rangle$ versus $|GS\rangle$) as in the underneath ST-spin blockade triangle.

Note that this reduction in tunnel current is also present in the measurements shown previously (see figures 7.15 (a), (b) and (c) or figures 7.11 (a1) and (b1)). In order to build up the discussion by going from simpler to more complex effects, it was not explicitly mentioned then. While this blockade effect is reproducible, it is not equally pronounced in each measurement. An incomplete spin blockade manifests in a leakage current through the double dot [32]. In this sense, figure 7.16 presents a particularly pregnant measurement of $I(B,\Delta)$ of this effect.

The ensuing question is what spin state configuration gives rise to the upper of this 'double decker' spin blockade triangles. Here, it shall be investigated how this observation can be described within the proposed model of table 7.1. First it must

be noted that slopes $\Delta' = \pm 2g\mu_B$ or greater, as observed in figure 7.16, can occur, according to the model, only by spin flipping events of the 'core' electrons (cf. section 7.1.2). Until this point, where only ground and first exited interdot transition were discussed, it was a descriptively good approximation that the 'core' electrons are 'inert'. Consider now, for instance, a flip of a 'core' spin occurring above $g\mu_B B + \Delta \geq \Delta_{ST(2,0)}$. This flip of a 'core spin' is indicated by the red, curved arrow in figure 7.16 ●. The maximal number of unpaired spins is, as a result, increased by two, to a maximal overall spin S =2 for the double dot system. A total spin of two corresponds to quintuplet states $Q(3,1)$ or $Q(4,0)$ with five possible z-projection values $S_z \in \{-2,-1,0,1,2\}$. In this notation, (x,y) stands for the number of relevant spins rather than the effective number of excess charges on the double quantum dot; $T(2,0)$ and $Q(4,0)$, for example, do not differ in charge distribution but only in spin configuration.

Higher than triplet spin states (and in particular non-singlet ground states) have been previously reported for 'artificial atoms' formed in quantum dots [145, 146] and their occurrence has been brought in agreement with Hund's rule. Also in double quantum dots higher spin states have been reported [20, 126]. In particular, reference [20] ascribes features of suppressed transport to *doublet-quadruplet spin blockade* (for a different interdot transition type than discussed here).

In the present case, the upper triple triangle can be described in terms of *triplet-quintuplet spin blockade*. As discussed previously, a triplet state with both electrons on the same dot, i. e. $T(2,0)$ are higher than the triplet state $T(1,1)$ with charges distributed over both dots. In analogy, the quintuplets $Q(4,0)$ should be higher up in energy than the $Q(3,1)$-quintuplets. Employing the same argument as for ST-spin blockade, eventually the, e. g., $Q_{++}(3,1) = (\uparrow, \uparrow\uparrow\uparrow)$ will be occupied and acts a blocking state as long as the $Q_{++}(4,0) = (0, \uparrow\uparrow\uparrow\uparrow)$ is energetically inaccessible. This situation is illustrated in figure 7.16 ● and in table 7.2. The blockade is lifted when the $Q_{++}(4,0)$-quintuplet is brought to level with the blocking state $Q_{++}(3,1)$ (or below) Starting from this point, current can flow via the quintuplet interdot transition $Q(4,0) \leftarrow Q(3,1)$. The energy barrier to overcome this triplet-quintuplet spin blockade $\Delta_{TQ(4,0)}$ is the energy difference of states between $Q(4,0)$ and $T(2,0)$. Left and right quantum dots need to be detuned $\Delta = \Delta_{ST(2,0)} + \Delta_{TQ(4,0)} \approx 224\,\mu$eV or above to lift the blockades (cf. figure 7.16 ■).

Conceptionally, this experiment demonstrates a controlled change of a few-electron, trapped spin state by a combination of electrostatic and magnetic tuning.

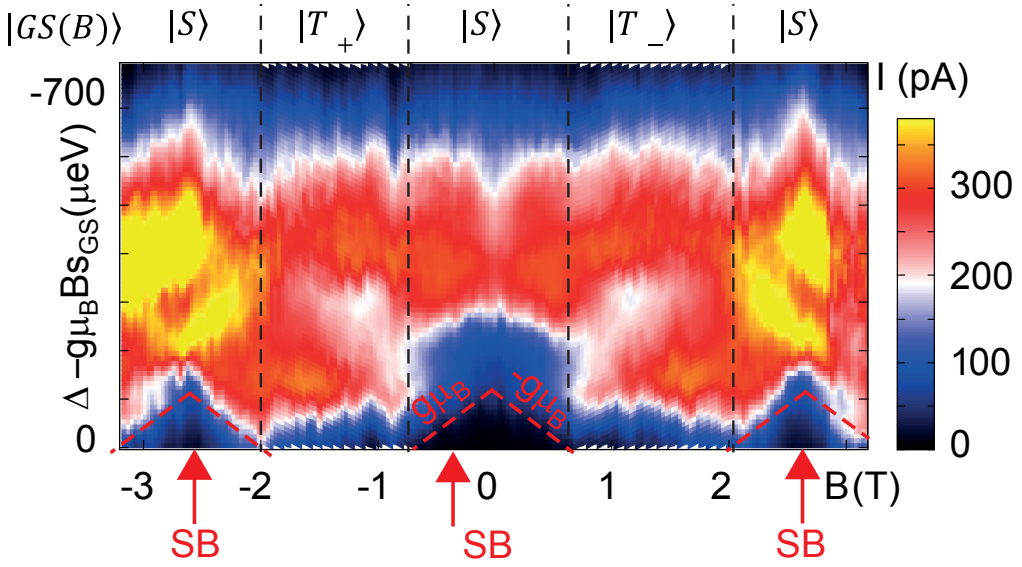

Figure 7.17: Spin blockade triangles at finite and zero in-plane magnetic fields: the map $I(\Delta, B)$ from figure 7.13 (a) over a larger magnetic field range $[-3.2, 3.2]$ T. Whenever the interdot transition $(2,0) \rightleftharpoons (1,1)$ has zero slope $\Delta' := \frac{\partial \Delta}{\partial B} = 0$ (denoted as singlet "effective DQD ground state" $|S\rangle$), a 'transport blockade triangle' is observed, around zero field (as already seen in figure 7.13 (a), and additionally around ± 2.75 T. Note that, along with the overall current, the leakage current in the blockaded triangles is higher at finite than at the low magnetic field. Dashed red lines outline the 'transport blockade (SB) triangles'. The slopes are $\pm g\mu_B$ for all three triangles. It is feasible that the finite B-triangles stem, e. g., from a S^*T^*-spin blockade, where S^* and T^* denote some exited singlet and triplet state that are driven into the bias window by the magnetic field. In the regions of effective triplet 'DQD ground states' $|T_\pm\rangle$ (with $\Delta' = \pm 1$), transport is unimpeded over the the entire detuning range $0 \geq \Delta \geq |V_{SD}| = |\text{-}700\,\mu\text{eV}|$.

7.3.3 Spin blockade triangles at finite magnetic field

Figure 7.17 shows the map $I(\Delta, B)$ from figure 7.13 (a) over a larger magnetic field range $[-3.2, 3.2]$ T.

The discussion now focuses on the spin blockade features that appear symmetrically in magnetic field around $B = \pm 2.75$ T. The finite field-spin blockade triangles are highlighted similarly as the zero field spin blockade triangle with $\pm g\mu_B$-sloped, red dashed lines and are labelled **SB**.

That spin blockade can appear also at finite magnetic fields has been theoretically predicted and experimentally observed. Reference [130] makes the theoretical proposal that SB at higher fields can arise, e. g. from mixed states while triplets are unblocked by non-spin-conserving processes (in the presence of strong spin-orbit coupling). Experimentally, spin blockade has been reported at high field up to 8 T [126].

Whenever the the interdot transition $(2,0) \rightleftharpoons (1,1)$ has zero slope $\Delta' := \frac{\partial \Delta}{\partial B} = 0$ (denoted as singlet "effective DQD ground state" $|S\rangle$), a 'transport blockade triangle' is observed, around zero field (as already seen in figure 7.13 (a), and additionally around $\pm 2.75\,\mathrm{T}$. Note that, along with the overall current, the leakage current in the blockaded triangles is higher at finite than at the low magnetic field. The slopes are $\pm g\mu_{\mathrm{B}}$ for all three triangles. It is feasible that the finite B-triangles stem, e. g., from a S^*T^*-spin blockade, where S^* and T^* denote some exited singlet and triplet state that are driven into the bias window by the magnetic field. In principle, there can be mixed or higher spin states, e. g. a quintuplet $Q(n_l, n_r)$, with $n_l + n_r = 4$ and spin=2, when a 'core' electron on a dot would flip [130]. In the regions of effective triplet 'DQD ground states' $|T_{\pm}\rangle$ (with $\Delta' = \pm 1$), transport is unimpeded over the the entire detuning range $0 \geq \Delta \geq |V_{SD}| = |\text{-}700\,\mu\,\mathrm{eV}|$.

The leakage current is increased at finite field compared to small field. One possible origin of increased leakage current is, as already discussed, the increased overall conductance with at higher magnetic fields and, in particular, higher co-tunnelling currents. Another may be enhanced rates for spin flipping events at higher fields that can unblock blocking spin states on the double dot (e. g. $T_+(1,1) = (\uparrow,\uparrow) \rightarrow S(1,1) = (\uparrow,\downarrow)$). Nonetheless, the spin blockade is less clearly pronounced on the $I(B,\Delta)$-map than the zero field one. Therefore the finite magnetic field triangle shall be counterchecked and verified by two independent, complimentary measurements. Because the data are highly symmetric in magnetic field, only the example of the spin blockade triangle at positive, finite field is treated (cf. figure 7.17).

Verification 1: spin blockade pattern on a large scale gate energy map $I(\Sigma, \Delta; B = +3\,\mathbf{T})$

If spin selection rules were at the origin of the finite transport blockade triangle in figure 7.17, a pattern of spin blockade should appear on a larger scale gate energy map of current as was observed at the beginning of this chapter for zero field (see figure 7.2). The large scale maps at zero magnetic field in figure 7.2 measured again within the positive magnetic field SB triangle (in figure 7.17), for a $B = 3\,\mathrm{T}$. The measurement is presented in figure 7.18 (a) and (b) for positive and negative bias $V_{SD} = \pm 700\,\mu\mathrm{eV}$.
The red triangular outlines in figure 7.18 mark the interdot transitions of type $(o,o) \rightarrow (e,e)$ (o= odd, e= even charge occupancy on a dot (cf. categorisation in figure 7.2 (d)). At this type of interdot transition, ST-spin blockade is expected. Indeed, areas of blockaded transport are observed in the red-outlined triple triangles

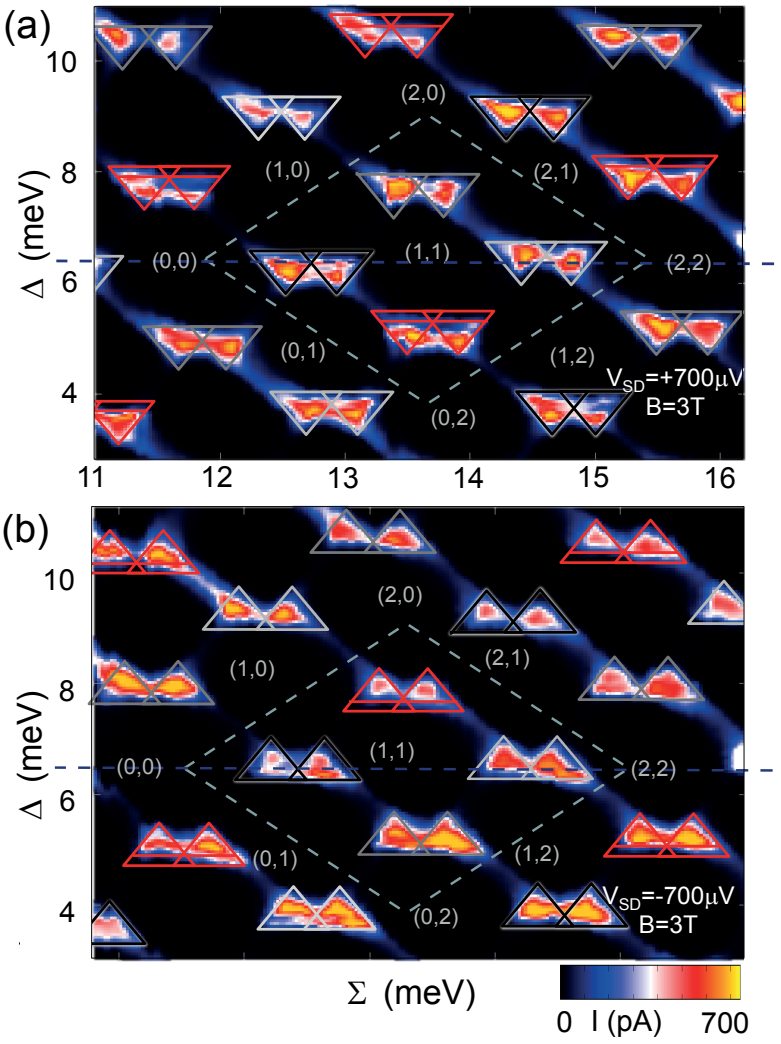

Figure 7.18: Map of current $I(\Sigma, \Delta)$ as a function of gate energies at an in-plane magnetic field $B = 3\,\mathrm{T}$ and (a) V_{SD}=+700 μV and (b) V_{SD}=-700μV bias. The same data range is shown as in figures 7.2 (a)/(b). For the particluar choice of the magnetic field around $\pm 3\,\mathrm{T}$, the same configuration of colour-coded triangles fits the data (adapted to the magnetic field induced shifts in (Σ, Δ)). Owing to the increased current at higher magnetic fields, the colour scale is twice as large as in figure 7.2.

(between base line and the thin red lines within the triple triangles) but not in the black- and grey-outlined ones. The pattern corresponds - similarly to the zero bias case in section 7.1 - to the 'even-odd' shell filling that is characteristic for S*T*-spin blockade. S* ans T* denote some exited singlet and triplet states respectively that form the 'double dot effective ground state', e. g. $|GS_{II}\rangle$: $S^*(2,0) \nleftarrow T^*(1,1)$. The distance from triple triangle base line to parallel line within the triangles corresponds to the exited singlet-triplet splitting $\Delta_{S^*T^*(2,0)}$.

Verification 2: gate energy map over the SB triangle magnetic field range $I(\Sigma, \Delta; 2\ \mathbf{T} \leq B \leq +3.75\ \mathbf{T})$

The $I(B, \Delta^*)$ maps are assembled from line scans $I(\Delta)$ for different magnetic fields B. Taking this slice through the parameter space incurs a number of operations

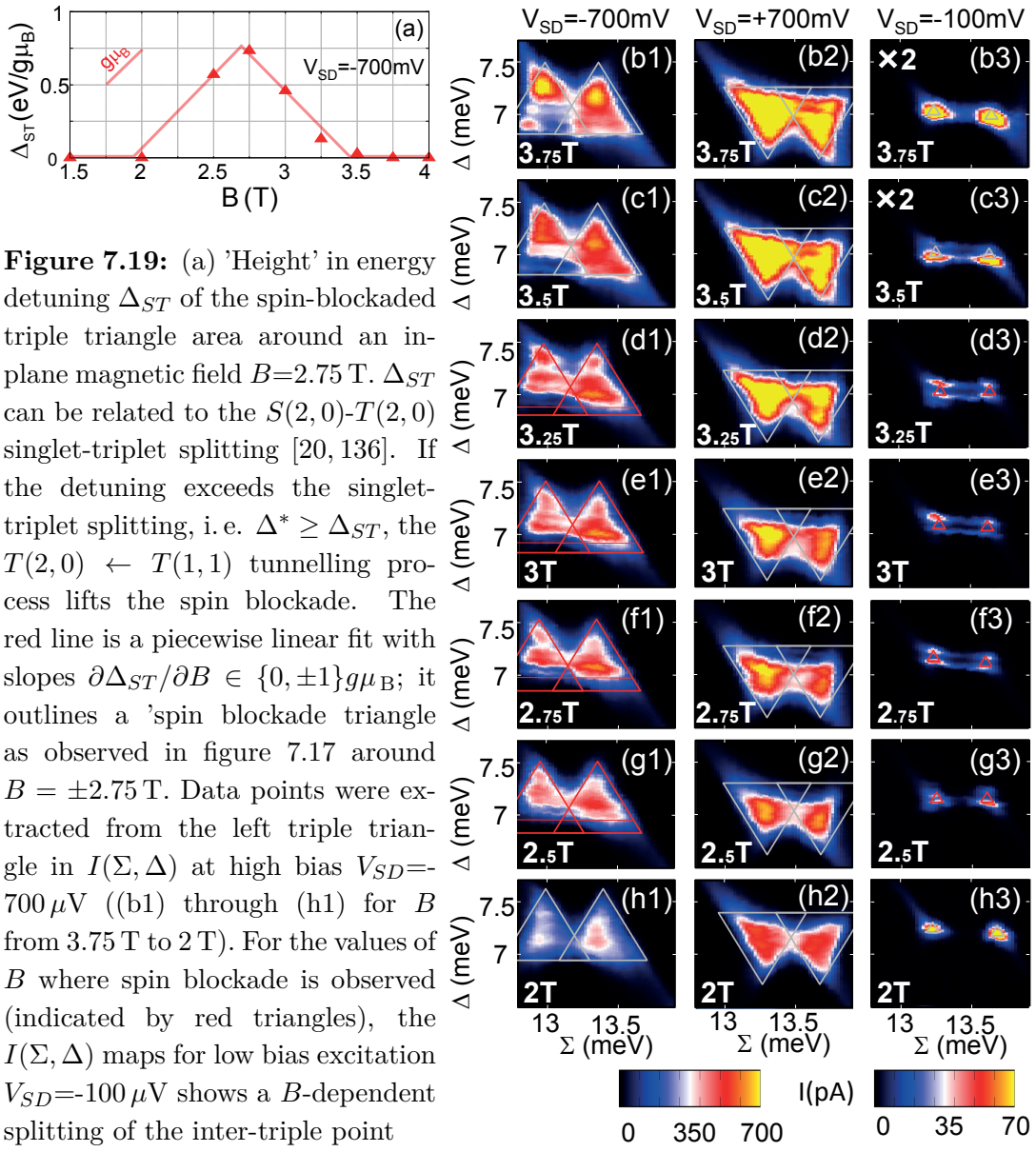

Figure 7.19: (a) 'Height' in energy detuning Δ_{ST} of the spin-blockaded triple triangle area around an in-plane magnetic field B=2.75 T. Δ_{ST} can be related to the $S(2,0)$-$T(2,0)$ singlet-triplet splitting [20, 136]. If the detuning exceeds the singlet-triplet splitting, i. e. $\Delta^* \geq \Delta_{ST}$, the $T(2,0) \leftarrow T(1,1)$ tunnelling process lifts the spin blockade. The red line is a piecewise linear fit with slopes $\partial\Delta_{ST}/\partial B \in \{0, \pm 1\} g\mu_B$; it outlines a 'spin blockade triangle as observed in figure 7.17 around $B = \pm 2.75$ T. Data points were extracted from the left triple triangle in $I(\Sigma, \Delta)$ at high bias V_{SD}=-700 μV ((b1) through (h1) for B from 3.75 T to 2 T). For the values of B where spin blockade is observed (indicated by red triangles), the $I(\Sigma, \Delta)$ maps for low bias excitation V_{SD}=-100 μV shows a B-dependent splitting of the inter-triple point connection line ((b2) through (h2)) for B from 3.75 T to 2 T). This splitting ($\approx$ 100 μeV) is of the order of the bias and Δ_{ST} at V_{SD}=-700 μV and B=0, as shown in (a). The data for corresponding negative B (and also zero field) are equivalent (not shown).

and interpretations that can distort the experimental data and lead to misinterpretations; for instance, the middle point of the triple triangle base line Σ_M must be determined in the data (within some accuracy limit < 1), and it is assumed that its value is unaffected by magnetic field. Taking line cuts $I(\Delta)$ discards the redundant information of the full triple triangles that allows to estimate the effect of random

artifacts due to charge fluctuations or co-tunneling. Also, the position of the base line, i. e. the transformation $\Delta \mapsto \Delta^*$ (see equation 7.9) is based on the model presented in table 7.1 grounding on the empirical determination of the $I(\Sigma, \Delta)$ for a feasible number of magnetic field values.
Therefore, the second counter-check on whether the triangular blockade features in the $I(B, \Delta^*)$ can be related to spin blockade takes a look back at the full gate space (Σ, Δ) over a magnetic field range that covers the finite magnetic field spin blockade triangle in figure 7.17 with 0.25 T-increments, presented in figures 7.19 (b-h1). Red triangles indicate the values of B where spin blockade is observed. The quantity of interest is characteristic energy scale for ST-spin blockade, i. e. the $S^*(2,0)$-$T^*(2,0)$-splitting Δ_{ST} [20, 136]; this *energy barrier* sets the maximum detuning range over which spin blockade remains in place.
Figure 7.19 (a) plots the values of Δ_{ST} against the magnetic field B as extracted from the Δ-distance of the two horizontal red lines in figures 7.19 (b-h1). The red line is a guide to the eye with slopes $\partial\Delta_{ST}/\partial B \in \{0, \pm 1\} g\mu_B$; it retraces accurately the outline of the spin blockade triangle observed in figure 7.17 around $B = \pm 2.75$ T. Figure 7.19 (a) is a confirmation that the finite field triple triangle in $I(B, \Delta)$ in figure 7.17 are a genuine physical effect rather than an artifact of measurement process or data interpretation. The data for corresponding negative B (and also zero field) are, by symmetry in B, equivalent and therefore not shown.
In figure 7.19 (b2-h2), it is confirmed that upon bias reversal from V_{SD}=-700 μV to V_{SD}=+700 μV the transport blockade effect vanishes and current can flow over the entire triple triangle area, supporting that the blockade is indeed a spin effect.

Small bias splitting of the triple triangle interconnection line

An interesting observation is made in the equivalent data at small bias excitation (see figure 7.17); for the values of B where spin blockade occurs for $V_{SD} = -700\,\mu$eV, the inter-triple triangle connection line splits for small bias excitation s $V_{SD} = -100\,\mu$eV. Comparing the $I(\Sigma, \Delta; V_{SD} = -100\,\mu\,\text{eV})$-maps (figures 7.17 (b-h3)) where spin blockade occurs (indicated by red triangular outlines in figures 7.17 (d1)-(g1)) with those without spin blockade (indicated by grey triangular outlines in figures 7.17 (b1), (c1) and (h1)), one observes:

- In the triple triangle areas, the overall current is drastically reduced at low bias whenever there is spin blockade at high bias.
- The low bias triple triangles, though the triangular shape is barely recognisable, appear split in Δ-direction with a 'gap' of reduced conductance in the middle.

- Correspondingly, the co-tunnelling line that interconnects the triple triangle pair is also split. The current is (possibly resonantly) enhanced compared to where there is no spin blockade at high bias.

- This splitting ($\approx 100\,\mu$eV) is of the order of both the bias and Δ_{ST} at V_{SD}=-700 μV and B=0, as shown in (a). However, it does not display a magnetic field dependence. Furthermore, the lower interconnection line is at zero detuning $\Delta = 0$ while the upper one is at positive detuning equal to the bias $\Delta \approx +|\,\mathrm{e}V_{SD}| = 100\,\mu$eV, leading to conclude that the lines occur when the minimal and maximal conditions on detuning for sequential tunnelling are met. However, a splitting of the same order ($\approx 90\,\mu$eV, cf. figure 6.4 (c)) has been observed at (near) zero dc bias excitation , suggesting that the splitting would be bias-independent, as e. g. a ground to exited state splitting Δ_{ST} is. Even though the dc bias excitation is zero, there are still thermal excitation (electron temperature T=431 mK=37 μeV/k_B, see figure 6.4 (b)) and a small ac bias excitation (10 μV rms, required for lock-in operation to measure $\frac{\mathrm{d}I}{\mathrm{d}V}$).

The origin of the split inter-triple triangle connection line can not be unambiguously assigned to either ground to exited state splitting Δ_{ST} (because it does not display the expected magnetic field dependence) or the size of the bias window (because the splitting occurs also at zero dc bias excitation , and because resonant enhancement of current is plausible for zero detuning $\Delta = 0$ but not for maximal detuning $\Delta = |eV_{SD}|$). Why this inter-triple triangle connection line splits and why its enhancement coincides with the occurrence of spin blockade is an interesting field for future research efforts.
On a final note on this splitting, it shall be discriminated from inter-triple triangle connection line splitting feature that appear very similar but are different in detail and origin. A similar effect has been observed (e. g. [20, 26]). The origin of the interdot line splitting observed there is either a consequence of microwave irridiation (which can be excluded here) or has been attributed to a (not further specified) 'high bias'-regime [26]. The effect is, however, fundamentally different to what is observed here. Reference [26] reports finite-current inter-triple point lines at positive *and* negative detuning (i. e. at $\pm h\nu$ where ν is the microwave frequency); this implies that the current is carried by inelastic tunnel processes not only by emission but also by absorption; at low T, where should this energy come from; in the 'atomic' picture, excluding absorption gives rise to half-filled diamonds in $I(\Sigma, \Delta)$, i. e. triangles. Furthermore, the second line in the present experiments occurs for *positive* detuning, thus neither explanation in reference [26] applies.
In a 'molecular' description of the double quantum dot, all tunnelling processes are resonant via molecular states, so there is no distinction between absorption

and emission inelastic tunnelling (thus there is a priori no reason why there should be triangles rather than diamonds). A fully molecular description of the double quantum dot is work in progress, in cooperation with Andrea Donarini, Universität Regensburg.

7.4 Lifting ST-spin blockade by ST-mixing

The 'atomic', sequential tunnelling model of a double quantum dot is an approximation of great predictive power despite of its relative simplicity. Up to this point in the discussion, it served well to explain the majority of features in the experimental data. It remains, however, an approximation that cannot reproduce all experimental features of a real double quantum dot device. The co-tunnelling features, for instance, are beyond the scope of the sequential tunnelling model that treats the double dot as two *interacting artificial atoms* (see chapter 6).

To demonstrate the limits of the 'atomic', sequential tunnelling model, this section comments on an example of a measured transport blockade feature that effectively requires a description of the double quantum dot as an *artificial molecule*. The intention of this section is merely to point out an example that the 'atomic picture' can not validly explain. While a qualitative explanation of this effect is hinted at, developing a theory for a full scale theoretical analysis is a project for consecutive work. An good starting point is provided in a recent theoretical work on spin-orbit effects in carbon nanotube double quantum dots [147].

7.4.1 Spin funnels in $I(B, \Delta)$

In figure 7.20 (a), there is an area of reduced leakage current through the double quantum dot around zero magnetic field and for finite detuning $400\,\mu\text{eV} \geq \Delta \geq 620\,\mu\text{eV}$. Unlike all previously discussed features, the outline of this reduced current area is not linear but has a non-zero curvature. For increasing detuning Δ and increasing magnetic field strength $|B|$, the width of this area widens symmetrically around B=0. The current suppression becomes more pronounced with higher interdot detuning, as can be seen from the three line traces $I(B; \Delta = const.)$ in figure 7.20 (b); their detuning positions are marked by colour-coded arrows in figure 7.20 (a). Owing to its shape, a similar feature in an equivalent measurement of the current $I(B, \Delta)$ on a Ga/GaAs-based double quantum dot was called '*spin funnel*' [20, 65]. Reference [28] labels such features (referring to an experimental setup without microwave irridiation, cf. [20]) as 'anomalous spin blockade'.

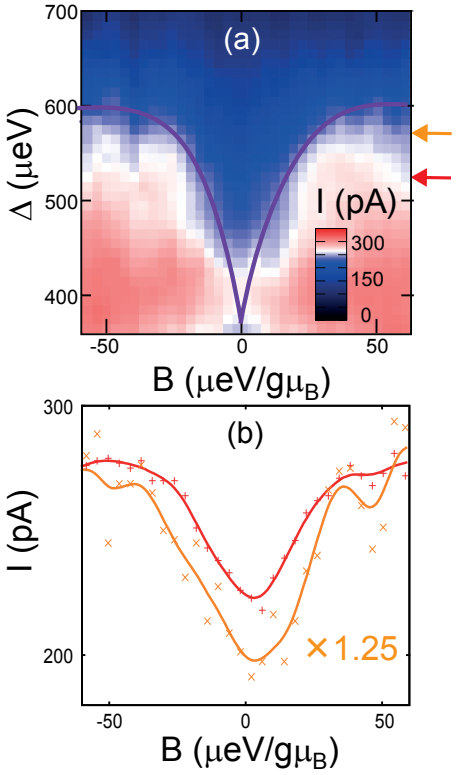

Figure 7.20: (a) Detail of figure 7.13 (a): map of the current as a function of interdot detuning Δ and in-plane magnetic field B, showing a *spin funnel* feature at finite detuning, opening with increasing detuning. The 'funnel' is highlighted by the violet curved lines as a guide to the eye. (b) Line scans $I(B)$ through the *'spin funnel'*-like anomalous transport blockade feature at finite detuning and around B=0, for interdot detuning Δ=530 μeV and Δ=570 μeV. The Δ-value of the line scans is indicated in (a) by colour-coded arrows. The orange line scan is scaled up with a factor of 1.25.

Similar 'spin funnel' features in literature

Similar *spin funnel* features have been observed in double quantum dots formed within Ga/GaAs [20], InAs nanorods [31,32] and also in ^{12}CNTs [71,126] and ^{13}CNTs [71] devices. The spin funnel presented here is distinguished from those reported before in two ways; first, it occurs at finite detuning rather than at zero to low detuning; second, the funnel widens as the two quantum dots are further detuned rather than being maximally spread for zero detuning and narrowing with increasing detuning (compare figure 7.21 (c1) versus (c2)).
This discussion focuses on the ^{12}CNT device in [71] (interdot coupling $t_{lr} = 50\,\mu$eV) because it is the most comparable with the here investigated ^{12}CNT device ($t_{lr} = 39\,\mu$eV). Taken from [71], a measurement of the leakage current I_{dd} as a function of a magnetic field B aligned in parallel to the CNT axis and of detuning Δ is shown in figure 7.21 (c1).

7.4.2 Lifting spin blockade by singlet-triplet-mixing

ST-spin blockade relies on an energetic separation of a singlet and triplet spin state for an appropriate charge configuration (n_l, n_r). In the present example, this *energy barrier* is the singlet-triplet splitting $\Delta_{ST(2,0)}$ between the $S(2,0)$ and $T(2,0)$ states.

Consider now a physical situation where the double quantum dot system is no longer accurately described by these 'atomic' states; the system eigenstates are rather mixed states with respect to the basis of 'atomic' states. Consider, in particular, that the system eigenstates can be mixed from singlet and triplet states. Whenever the eigenstates have both singlet and triplet components, there is no trapped state anymore (e. g. $T_+(1,1)$) and ST-spin blockade mechanism is lifted. It is equivalent to say that ST-mixing enables spin relaxation processes to lift ST-spin blockade [20, 28, 32].

7.4.3 Qualitative model of the spin funnel

Qualitatively modelling a typical spin funnel

The exact mixing depends on the microscopic properties of the spin-orbit interaction in the material system hosting the double quantum dot [32] and on the details of confinement [148]. The aim here is, however, only a qualitative description of the funnel features. Transport through a double quantum dot is commonly modelled by mixing of 'atomic' states [20, 32, 126, 130]. Reference [20] proposes a simple model that can qualitatively reproduce the spin funnel in figure 7.21 (c1). This discussion follows and adapts this model.

Assume that the singlet states $S(2,0)$ and $S(1,1)$ hybridise for small detuning Δ such that the energy $E(\Delta)$ of the mixed singlet state follows the cyan line, as sketched in figure STmixing (a1). Assume further that the pure triplet states $T(1,1)$ are still eigenstates of the system such their energy dependence with detuning $E(\Delta)$ is linear. Also, in the examples at hand, the interdot transition $(2,0)\leftarrow(1,1)$ is biased negatively. Consequently, current flows only at positive detuning.

At zero magnetic field, where the triplet states are energetically degenerate, the $T(1,1)$ intersect with the mixed singlet at finite detuning. The intersection point is marked by a dark red circle in figure 7.21 (a1). At this point in energy, there can be resonantly enhanced ST-mixing [28] and hence ST-spin blockade lifting. In a next step, this point is 'transferred' into the current map as a function of magnetic field and detuning $I(B,\Delta)$, as illustrated in the sketch (figure 7.21 (b1)) of the measurement shown in figure 7.21 (c1).

At finite magnetic field, the triplet states split by $\pm g\mu_{\mathrm{B}}$, resulting in a second intersection ot the $T_+(1,1)$ with the mixed singlet, indicated by the dark red star in figure 7.21 (a1). Similarly transferring this point onto the sketch of the measurement, one obtains a second point in $I(B,\Delta)$ where ST-spin blockade is lifted due to ST-mixing at low detuning and finite magnetic field. Repeating this procedure for many magnetic fields recovers the *spin funnel* form, indicated by the violet, curved line

in figure 7.21 (b1). Upon reversal of the magnetic field, the physical situation is symmetrical, and correspondingly the triplets $T_+(1,1) \leftrightarrow T_-(1,1)$ are interchanged. The resulting curved outline in figure 7.21 (b1) is in good qualitative agreement with the experimentally observed spin funnel feature, equally highlighted by curved, violet lines in figure 7.21 (c1).

Adapted model to the here observed spin funnel

The *spin funnel* in here presented data differs from those observed in literature [20, 32, 71] in two ways: first, the spin funnel appears not at zero but finite interdot detuning; second, the funnel opens upwards, with increasing detuning, rather than downwards (compare e. g. figures 7.21 (c1) and 7.21 (c2)).
The qualitative model from reference [20] can be adapted in a simple way to qualitatively explain the here observed spin funnel by assuming that the triplet states $T(1,1)$ are shifted in energy with respect to the mixed singlet states. This shift is indicated by the big black arrow in figure 7.21 (a2). Employing the same rationale as before, ST-spin blockade is lifted at zero magnetic field and small detuning where triplet state intersects with the singlet state due to resonantly enhanced ST-mixing. This point is marked by a dark red circle in figure 7.21 (a2). At finite magnetic field, there is a second intersection of $T_+(1,1)$ with the mixed singlets at finite detuning, marked by the dark red star. Considering additional magnetic field values retraces a spin funnel that opens towards increasing interdot detuning.
Including an offset in Δ, the adapted model reproduces the experimentally observed spin funnel qualitatively. In principle, a similar argumentation holds if the spin blockade mechanism is not based on singlet and triplet spin states but on other spin states. While the qualitative argument remains valid, specific spin blockade mechanism cannot be unambiguously attributed to the here observed spin funnel feature.

7.4.4 Possible escape mechanisms out of the trapped states

From the magnetic field dependence of spin blockade, information on electron spin relaxation mechanisms can be gained [71, 130, 149]. A lifted or an incomplete spin blockade manifests in a leakage current through the double dot [32]. This current is due to processes that enable transitions out of the trapped triplet states $T(1,1)$. To give an example, the spin funnel originates from singlet-triplet state mixing. Up to this point in discussion, there was no mention by what physical mechanisms trapped states can be depleted. Two mechanisms than can lead to spin relaxation have been reported in literature: hyperfine interaction and spin-orbit coupling.

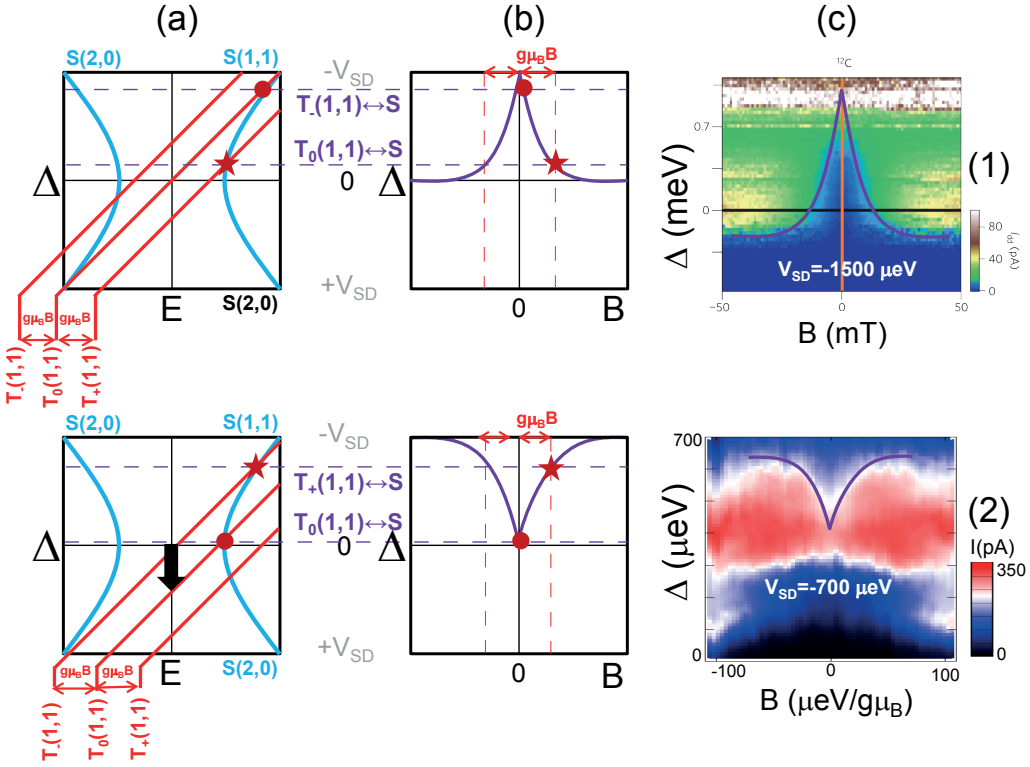

Figure 7.21: Lifting spin blockade by spin state mixing. (a1) Energy dependence $E(\Delta)$ of mixed singlet states and triplet states of the interdot charge transition $(0,2) \rightleftharpoons (1,1)$ on interdot detuning Δ and magnetic field B, following a model from reference [20]. (b1) Sketch of a spin funnel feature in a map of the current $I(B,\Delta)$ as derived from the intersections of triplet and mixed singlet states in (a1), where SB is lifted due to ST-mixing. (c1) Example of experimentally observed spin funnel in $I(B,\Delta)$ of a ^{12}CNT-based DQDot, taken from reference [71]. The spin funnel is highlighted by curved violet lines. The black and orange lines mark line cuts presented in [71] that are not shown here. (a2) Adapted model of singlet and triplet energy dependence $E(\Delta)$. (b2) Sketch of the spin funnel in $I(B,\Delta)$ as derived from the adapted model in (a2). (c2) Spin funnel feature at finite detuning, opening with increasing detuning. The violet lines highlight the funnel feature, in qualitative agreement with the adapted model.

Hyperfine interaction

If the material hosting the double quantum dot possesses a nuclear spin, the hyperfine interaction can mix different $(1,1)$ states [31, 32, 65, 71]. The CNT used in the present experiments was CVD-grown from a carbon feedstock with natural isotope distribution in which the zero nuclear spin ^{12}C-isotope is by far predominant (98.9% [24]). The net nuclear spin can therefore assumed to be close to zero and consequently hyperfine interaction effects to be negligibly small. The other natural

carbon isotope, ^{13}C, has an odd number of hadrons in its nucleus and consequently a net nuclear spin of $\frac{1}{2}$. Comparative measurements on ^{12}CNT and ^{13}CNT-based double quantum dots have substantiated experimentally that hyperfine interaction is negligible in ^{12}CNT [71].
Also, the effect of hyperfine spin state mixing is manifested in a qualitatively different feature compared to the spin funnel; hyperfine interaction typically leads to a finite leakage current for zero detuning and magnetic field that is suppressed by a small increase in either energy scale (cf. [31, 32, 71, 143]).

Spin-orbit interaction

Due to spin-orbit interaction the $(1,1)$ eigenstates of the double quantum dot can become superpositions of spin triplets and the singlet states [28, 147]. Within the mixed state eigenbasis that then describes the double quantum dot, transitions between different $(1,1)$ spin states become possible that would violate spin selection rules in the 'atomic' state basis (e. g. $S(1,1)$, $T(1,1)$,...). These observations were understood theoretically in terms of non-spin-conserving interdot tunnelling caused by spin-orbit coupling [130,131,150]; reference [130] predicts, e. g., that spin-orbit interaction can also lift spin blockade by hybridising triplet $T(1,1)$ states with $S(0,2)$. In particular, the spin funnel feature has been ascribed to spin-orbit coupling [32,61, 71, 130]. Spin-orbit interaction is present and cannot be neglected in CNTs [61, 62, 151, 152]. Experimental evidence was recently provided that spin-orbit interaction is not negligible also in the tubes are not ultraclean either, i. e. in presence of disorder [153]. Amongst the potential sources of disorder are, in the present case, charge traps in the Al_2O_3 gate oxide that covers the entire device surface (cf. section 3.2) or adsorbates.
The orbital momentum of a charge carrier on a carbon nanotube can be visualised as the charge carrier encircling the tube with clockwise or counter-clockwise helicity [41, 131, 151]. In this simple picture, it is intuitive that a magnetic field parallel to the tube axis 'tunes' the orbital mometum [61, 62] while a perpendicular field exercises no Lorentz force.
In the compared experiments of reference [71] (cf. figure 7.21 (c1)), the field was aligned in parallel to the CNT axis. The observed spin funnel feature was ascribed to spin relaxation due to spin-orbit coupling.
In the present experimental setup, the magnetic field is applied in the sample plane and perpendicularly to the PdNi electrodes, i. e. along an easy magnetisation axis of the strips (see chapter 4). The angle between the CNT and PdNi electrodes, and therefore the CNT and $B_\perp$, is about 21°. With respect to the CNT, the magnetic field has thus a co-axial component $B_\perp = B_\perp^{CNT} \cos 21° + B_{||}^{CNT} \sin 21°$. The maps of

current over the plane of interdot detuning Δ and magnetic field were measured for two orientation of the magnetic field, the above mentionned $B_\perp$ and $B_\odot$. $B_\odot$ refers to an out-of sample plane orientation, where the magnetic field is perpendicular to both the PdNi electrodes and the CNT - with zero co-axial field component. Indeed, the spin funnel feature is observed only in $I(B_\perp, \Delta)$ (see figure 7.21 (c2)) but not in $I(B_\odot, \Delta)$ (see figure 7.10 (a1)), supporting that spin orbit coupling is at the origin of the spin funnel effect.

7.5 Summary

At the heart of this chapter is an effect called *Pauli spin blockade*, a current-blocking mechanism that is inherent to double quantum dots in serial configuration. As its name suggests, the interdot charge transport in the DQDot is suppressed despite of energetically available states that would allow transport because transition into them is forbidden by spin selection rules. As a consequence, a spin becomes *trapped* on one quantum dot. From the perspective of the trapped spin, there is an energetically available state to proceed to the next dot - but only the opposite spin orientation is admitted.

Section 7.1 identifies and substantiates Pauli-spin blockade features in the tunnel current through the double quantum dot at certain interdot charge transitions. The principle of Pauli spin blockade is exemplified by the mechanism of singlet-triplet spin blockade. On a side note, it demonstrates how a serial double quantum dot acts as a current rectifier by virtue of Pauli-spin blockade.

Section 7.2 makes use of the occurrence of Pauli-spin blockade features an their evolution in a magnetic field to do spectroscopy on the spin states of the interdot charge transitions. For this purpose, and in extension of models of magnetic field dependence of single quantum dot ground states, a simple model is proposed that relates the experimental features to spin configurations of the interdot charge transitions according to their evolution with magnetic field. In this way, the spectrum of ground and exited interdot transitions can be probed.

Section 7.3 concentrates on specific Pauli-spin blockade features, dubbed here *spin blockade triangle*, that provide a direct experimental demonstration that spin blockade can be lifted by several energy scales or a combination thereof. Investigated energy scales are in particular the interdot detuning energy Δ and the magnetic field $g\mu_{\mathrm{B}}B$. These spin blockade triangles can also be observed for higher spin

states than singlets and triplets as well as for finite magnetic fields. Experimentally, the observation of 'double SB-triangle' demonstrates a controlled trapping and release of a trapped spin state by a combination of electrostatic and magnetic tuning.

In conclusion, section 7.4 comments on a spin blockade phenonemon, dubbed *spin funnel*, that is beyond the simple description of the double dot as 'two interacting atoms'. In order to qualitatively explain this spin funnel, the double dot system is to be described with eigenstates mixed from the atomic states. Singlet-triplet spin blockade, for example, foots on an energetic separartion of a spin singlet and its corresponding spin triplet state. Consequently, singlet-triplet spin blockade is lifted when eigenstates are mixed from both singlet and triplet atomic states.

Knowledge of the 'spin blockade triangle' in $I(B, \Delta)$ can be useful control and process spin-embedded information by combinations of electrostatic and magnetic means on future spintronics devices.

Conclusion

Synopsis

This thesis investigates how the tunnel current through clean, single-walled carbon nanotube-based quantum dot systems is influenced by spin phenomena. Its focus lies on Pauli spin blockade effects. Such spin blockade effects are experimentally observed here in the clear-cut transport spectrum of a serial double quantum dot specimen in the regime of capacitive and weak tunnel interdot coupling. With a simple model, based on a sequential tunnelling description of the double quantum dot as 'two interacting artificial atoms', spin blockade is used as a means of spectroscopy on spin and charge interdot transtitions. This *spin blockade spectroscopy* reveals the evolution of the interdot transitions with different energy scales. How spin blockade can be lifted by combinations of different energy scales is directly observed as triangular, transport-blockaded regions in maps of the current as a function of interdot detuning Δ and the magnetic field $g\mu_{\mathrm{B}}B$. These *spin blockade triangles* (in analogy to *Coulomb diamonds* in current maps as a function of a gate voltage and the bias) occur also at finite detuning and symmetrically at finite magnetic fields. Controllable trapping of single spins by means of spin blockade requires an accurate characterisation of its energy scales. The present results can provide a working point for spin blockade in a double quantum dot that is used as a *module* in forthcoming, more complex spintronics circuits. Two other potential *spintronics modules*, based on a spin valve configuration and on Kondo effects, are also investigated. The next conclusive step is to integrate these *spintronics modules*, together with a superconducting electrode acting as a *Cooper-pair spin splitter* and spin state preparation by irradiation, into a *spin lab on a chip* built from SWCNT-based quantum dot systems. Such a spin lab provides a suitable model system for fundamental research interests. At the same time, it may inspire novel solid state spintronics or quantum computing applications.

Along this line and towards these results, the chapters of this thesis provide the following contributions:

Summary

Chapter 1 reviews the concepts of electronic transport through transistors based on quantum dot systems. Multiple quantum dots can behave like *interacting artificial atoms* or *artificial molecules*, depending on their capacitive and tunnelling inter-coupling. At low temperature, transport through quantum dot devices can be energetically inhibited due to Coulomb repulsion of the charge carriers, often called Coulomb blockade. In particluar, chapter 1 proposes a matrix ansatz which formulates the description of the serial double quantum dot in the weak interdot coupling regime in matrix notation. In this notation, the relations take the analogous form to the scalar relations of a single quantum dot, with matrices on $\mathbb{R}^2 \times \mathbb{R}^2$. The ansatz here yields the same relations as reported in literature [20, 24, 26]. The cross-capacitances (e. g. C_{Lr}, the action of the left local gate L onto the right quantum dot r) are easily implemented in this description, providing the theoretical basis to accurately translate the experimental gate voltages into the physically relevant energy scales of the quantum dot system. A self-consistent method is proposed to extract the gate voltage to energy conversion factors only from the dimensions of the triple triangles in $I(V_L, V_R)$, with the bias voltage acting as reference to absolute energy scales. The advantage of this method is its inherent independence of any quantum mechanical effects (cf. e. g. [125]).

Chapter 2 reviews how electronic transport can be confined in all-carbon molecules, down to one-dimensional confinement in carbon nanotubes. Quantum dots can be implemented in carbon nanotubes by (e. g.) electrostatic definition of a CNT segment that is short against the coherence length scales. The electronic properties and energy dispersion of CNT-based quantum dots are specified.

Chapter 3 describes how a serial double quantum dot can be implemented in a SWCNT-based device and suitable measurement setup. In the course of the work leading to this thesis, the fabrication techniques for clean, high quality single walled carbon nanotube synthesis and SWCNT-based transistor fabrication have been set up at the University of Regensburg, leading to the locally first observation of TMR, Kondo and spin blockade effects in such devices.

Chapter 4 provides a micromagnetic characterisation of ferromagnetic contact electrodes with respect to their suitability for carbon nanotube-based spin valves. Dif-

ferent thin-film electrode designs, varying shapes and materials, are characterised for a clear, mono-domain magnetisation reversal and a shape-dependent difference in coercive field that is large enough for the magnetic switching of parallel to antiparallel relative magnetisation orientation to be resolved in experiment. The second aspect of investigation is the interface resistance of the different materials to SWCNTs. Single and multi walled carbon nanotube-based spin valves based on these ferromagnetic electrode designs have been experimentally demonstrated in previous work [55].

Chapter 5 demonstrates a clearly defined stability diagram of a double quantum dot in the weak tunnelling and capacitive interdot coupling regimes, measured on a SWCNT-based device. Furthermore, a high tunability of the interdot coupling has been demonstrated; forthcoming spintronics applications may rely on control over the interdot coupling. Footing on the matrix description developed in chapter 1, a consistent guideline is developed to evaluate the electrostatic energy scales of a double quantum dot. In particular, a new scheme is proposed to independently extract the source and drain capacitances from the shift of the triple triangles in the gate plane. Knowledge of absolute physical energy scales is the prerequisite for quantitative comparison with theoretical simulations and calculations. On a technical note, it was also found highly useful to implement the gate voltage to energy-conversion directly into the computerised (here: *PERL*-based) measurement scripts; this allows to 'measure the sample directly in physical energy coordinates' rather than in gate voltages that vary between individual samples and measurement setups. The benefit of this proceeding is a direct feedback on the physical situation in absolute energy scales during the measurement process, allowing to efficiently identify interesting features in parameter space and focusing on them. Often the coordinates of physical interest depend multiple experimental parameters. For example, the energy coordinate *interdot detuning* $\Delta = \Delta(V_L, V_R; V_{SD}, B)$ depends of the local gate voltages V_L and V_R, the bias V_{SD} and the magnetic field B. More involved measurement 'slices' through the parameter space in physical coordinates, e. g. measuring the current $I(V_{SD}, \Delta)$ as a function of bias and interdot detuning, require therefore the implementation of all relevant dependencies of physical and experimental parameters directly in the measurement scripts. If the 'slice' through the parameter space is not measured in a physically meaningful way, the data points required for correction have not been recorded. In the here suggested measurement scheme, conversely, the raw experimental parameters can be simultaneously recorded with the physical ones; this information is thus not 'lost' in the sense that the energy conversion can still be corrected at a later point in time.

Chapter 6 describes the phenomena in the transport spectrum of the weakly interdot coupled double quantum dot in the picture of 'two interacting atoms'. On the basis of a simple categorisation of features into single (co-tunneling) and triple (sequential tunneling) resonances, the exited state structure of the finite bias *triple triangles* measurements can be qualitatively understood. Typical excitation energies are around 100 μeV. A strong asymmetry in current between two types of single resonances can be related to asymmetric coupling of the source and drain electrodes to their adjacent quantum dots, and a coarse estimate on he relative tunnel couplings can be derived. Also, a third kind of single resonance, a co-tunnelling line that interconnects the paired triple resonances, is observed. In some experimental situations, a splitting of this resonance into a double line is observed. Its origin must be subject to further investigation. The important input of chapter 6 for understanding the subsequent main results is to discriminate effects of co-tunnelling and sequential tunneling, providing a validity range of the sequential tunnelling description of the double quantum dot as 'two interacting atoms'.

Chapter 7 presents the main results of this thesis, building up on the findings of the previous chapters. The underlying spin effect is called *Pauli spin blockade*, a current-blocking mechanism that is inherent to double quantum dots in serial configuration. As its name suggests, the interdot charge transport in the DQDot is suppressed despite of energetically available states that would allow transport – but the interdot transition is instead forbidden by spin selection rules. As a consequence, a single spin becomes *trapped* on one quantum dot. Pauli-spin blockade features are identified in the tunnel current through the double quantum dot at certain interdot charge transitions. The principle of Pauli spin blockade is exemplified by the mechanism of singlet-triplet spin blockade. On a side note, it demonstrates how a serial double quantum dot acts as a current rectifier by virtue of Pauli-spin blockade. The occurrence of Pauli-spin blockade features an their evolution in a magnetic field is used to do spectroscopy on the spin states of the interdot charge transitions. For this purpose, and in extension of models of magnetic field dependence of single quantum dot ground states, a simple model is proposed that relates the experimental features to spin configurations of the interdot charge transitions according to their evolution with magnetic field. In this way, the spectrum of ground and exited interdot transitions can be probed. Specific Pauli-spin blockade features, dubbed here *spin blockade triangle*, provide a direct experimental demonstration that spin blockade can be lifted by several energy scales or a combination thereof. Investigated energy scales are in particular the interdot detuning energy Δ and the magnetic field $g\mu_{\mathrm{B}}B$. These *spin blockade triangle* can also be observed for higher spin states than singlets and triplets as well as for finite magnetic fields. Experimentally, the observation

of 'double SB-triangle' demonstrates a controlled trapping and release of a trapped spin state by a combination of electrostatic and magnetic tuning. In conclusion, another spin blockade phenomenon is , dubbed *spin funnel*, that is beyond the simple description of the double dot as 'two interacting atoms'. In order to qualitatively explain this spin funnel, the double dot system is to be described with eigenstates mixed from the 'pure' atomic states. Singlet-triplet spin blockade, for example, foots on an energetic separation of a spin singlet and its corresponding spin triplet state. Consequently, singlet-triplet spin blockade is lifted when eigenstates are mixed from both singlet and triplet atomic states.
Knowledge of the 'spin blockade triangle' in $I(\Delta, B)$ can be useful control and process spin-embedded information by combinations of electrostatic and magnetic means on future spintronics devices.

Appendix A

Synthesis of SWCNT by CVD

Catalyst composition

Based on the original recipe from [58], the catalyst is suspended in 30 ml of methanol with the following composition:

Table A.1: Specifications of the catalyst ingredients for CVD growth of CNTs (after a recipe from [58])

Ingredient (powder)	quantity	company/product specification
$MoO_2(acac)_2$	4-10 mg (best 8.5 mg)	Fluka Chemie AG/EC No. 2338995
$Fe(NO_3)_3.9H_2O$	40 mg	Aldrich Chemical Company Inc. Al 08705 BS, 22,774-9 [17524-05-9]
Al_2O_3	30 mg	Degussa GmbH Kontrolnummer 2024 mean particle size 14 nm
methanol	30 ml	J.T. Baker /UN 1230, 8045 1l

Before each use, the catalyst solution is to be sonicated for at least 30 min (60 min before first use). A catalyst suspension should be used no longer than 2-3 months.

Catalyst deposition on a chip

- Clean sample surface (e. g. SiO_2 or Si_3N_4 membranes) thorougly: oxygen plasma (about 5 min), warm acetone bath, sonicate in warm acteone (cave: membranes break), rinse with propanol.

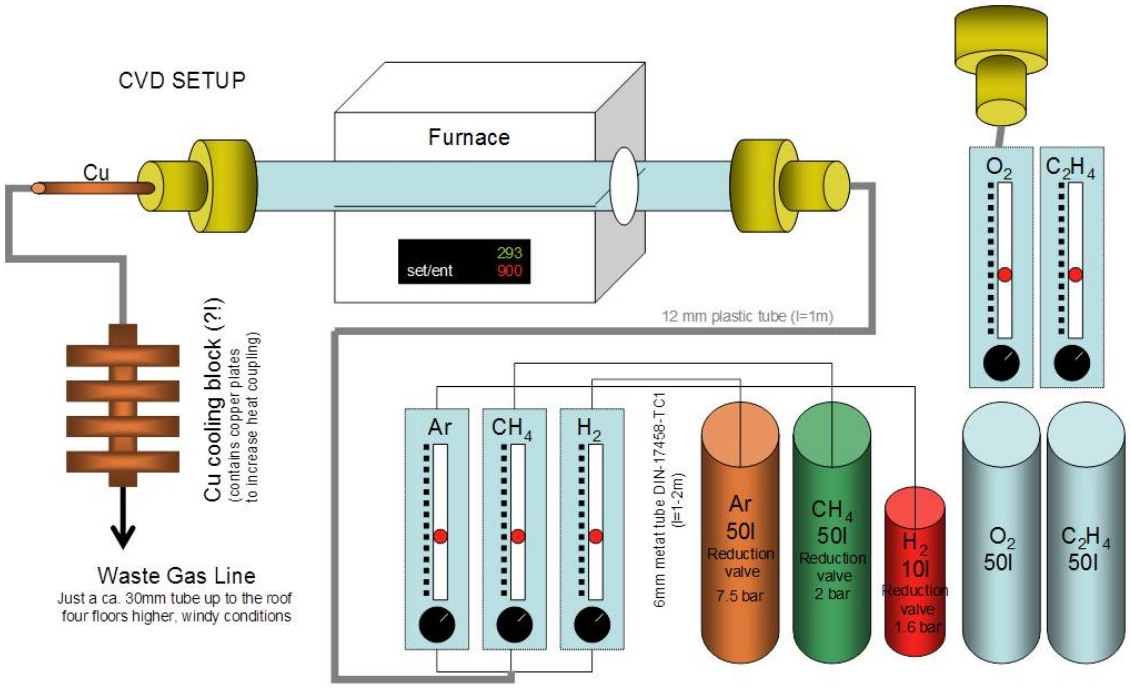

Figure A.1: Schematic CVD setup for SWCNT growth.

- Spin-coat a double resist layer PMMA (polymere chain length 200K/concentration 7%, resist thickness about 300 nm)/PMMA(950K/2%, about 50 nm). The thicker the resist, the easier the subsequent lift-off.

- EBL-pattern a mask with *catalyst islands* of about 2 μm in diameter where SWCNT growth is desired.

- Take up catalyst solution with pipette (cleaned with acetone then methanol), deposit a few drops on sample, wait 1-2 s, then vigoursly blow with N_2 until the sample is dry; blow in diagonal direction over the sample to prevent a drop at the sample border from sedimenting excess catalyst.

- Bake sample for 5 min at 150°C.

- Pick up the sample on an edge with tweezers, hold it above the surface of warm acetone in a beaker rinse vigorously with a acetone spray bottle (to wash of excess catalyst on the resist) while dipping the sample into the acetone, the stir for at least 1 min. Rinse with propanol (not methanol - it solves the MoO_2 catalyst component, foiling the CNT growth).

SWCNT growth process

- Place sample at the middle of the quartz tube, place quartz tube in the tubular furnace (Lindberg/Blue M, model number TF55030C-1), then fasten the valves airtight (even small amounts of oxygen foil the CNT growth).
- Rinse all gas lines (H_2 (5.0), Ar (4.6), CH_4 (2.5)) for 2 min.
- Switch on furnace and set target temperature to 900°C.
- When target temperature is reached, set H_2 flow rate to 700 ml/min.
- Close Ar flow.
- Open CH_4 flow at 520 ml/min for 10-15 min (CNT tube starts).
- Stop CH_4 flow after 10-15 min (CNT tube ends).
- Leave H_2 flow rate at 700 ml/min, set Ar flow to 13 ml/min and open the lid of the furnace to let it cool down.
- At room temperature, open quartz tube and retrieve the sample.

Servicing the CVD system

- *Only a used quartz tube is a good quartz tube* - for high yield of CNT growth, do a few 'dummy runs' (without sample) on a new quartz tube. Experience has shown that 'CVD process contamination' needs to be reasonably 'fresh', so CNT growth is better when the CVD system is used frequently (few days or less before a CNT growth run).
- To clean the quartz tube, heat it on air (open ends) at 900-1000)°C to burn organic waste.
- The rest pressure in the process gas bottles can hamper the CNT growth. At low bottle pressures, the contamination intake of gases increases relatively.

Appendix B

Characterisation of SWCNTs by TEM diffraction

B.1 Transport and diffraction experiments on one sample design

Knowledge of the band structure of the CNT is an important input for theoretical understanding and simultation of data obtained from a carbon nanotube-based device. As developed in section 2.3, the electronic structure of a CNT is fully characterised by its chiral indices (n, m). The arising experimental challenge is to measure the chiral indices on the same CNT that the later transport experiments will be performed on. From the Coulomb blockade pattern in transport measurements they cannot be extracted unambiguously. Likewise, typical atomic force microscope (AFM) can only measure one parameter, the CNT diameter, where a set of two, (n, m), is to be determined, and within the margin of experimental error lie many possible chiral indices with widely differing electronic properties. AFM, transmission electron microscope (TEM) or scanning tunnelling microscope (STM) with atomic resolution are able to directly image the CNT molecule in the positional space such that the chiral indices can simply be read off by counting the hexagon periods along a unit cell. Access to such high resolution microscopes is mostly not readily available and they often impose requirements on the sample that can not be met by samples destined for transport experiments. One feasible technique would be Raman spectroscopy.

This appendix presents another method: the chiral indices of a CNT can be determined from its reciprocal space images. Suitable electron diffraction images can be measured in a TEM. Its great advantage over all above mentioned methods is

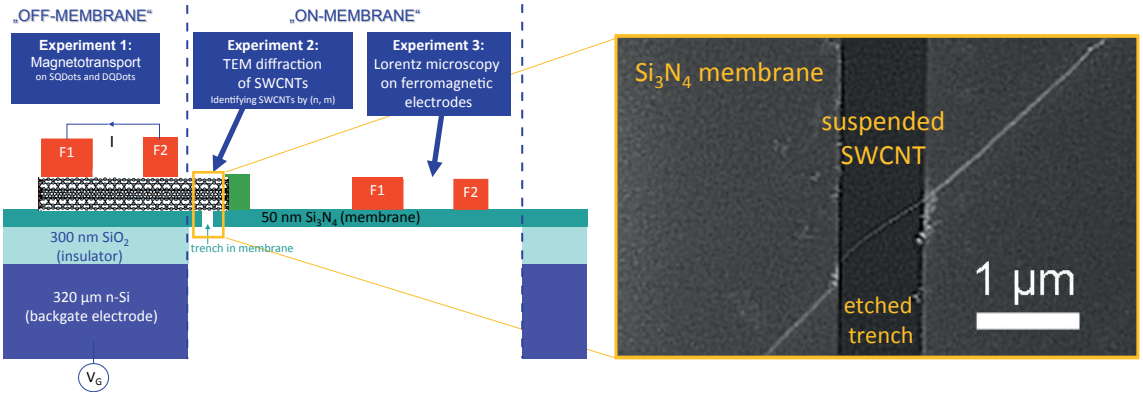

Figure B.1: Side view sketch of our integrated sample setup for TEM diffraction and transport measurement: For transmission electron microscopy, a carbon nanotube is grown from an amorphous, low stress PECVD Si_3N_4 membrane, optimally over an etched trench to eliminate substrate scattering (experiment 2). On solid substrate, the highly doped Si substrate, in conjunction with the insulating SiO_2 and Si_3N_4 layers, serves as a backgate for any kind of CNT transport sample, here e. g. a 2-terminal SWCNT lateral spin valve (experiment 1). TEM Lorentz microscopy can characterise the domain structure of the ferromagnetic electrodes $F1$ and $F2$ (experiment 3). Blow-up: SEM micrograph side view of a SWCNT suspended over a CHF_3/O_2 dry-etched trench in the membrane.

that it alone can directly look *into* the tube, either directly from the spatial image or the specifics of the diffraction pattern, allowing to unambiguously discriminate between single, double or multi wall carbon nanotubes or bundles of CNTs, see e. g. figure B.3 (b). Transmission electron microscopy requires at he investigated object to reside on some grid or membrane. To resolve the object of interest, i. e. a mere two atomic monolayers of a CNTs, suitable substrates are thin, have low scattering probabilities with electrons of energies defined by the TEM acceleration voltage and be aperiodic to average out lattice refraction effects.

This appendix presents experiments stemming from a cooperation with the group of Prof. Joseph Zweck who provided the TEM expertise. The presented TEM measurements on our homegrown carbon nanotubes were performed by their Christian Huber. The contribution of this work was to develop a sample setup that integrates TEM diffraction and electronic transport measurements on the very same tube and produce them. Figure B.1 presents this setup. The catalyst is deposited onto the membrane such that some CNTs will grow onto the solid substrate. To eliminate the noise from the 50 nm amorphous, low-stress PECVD Si_3N_4, a trench was CHF_3/O_2 dry-etched into the membrane. The rationale of the integrated sample design is illustrated in figure B.2: the catalyst dot is deposited onto the membrane and behind a slit, so those CNTs that lie on the backgatable substrate must also lie suspended over

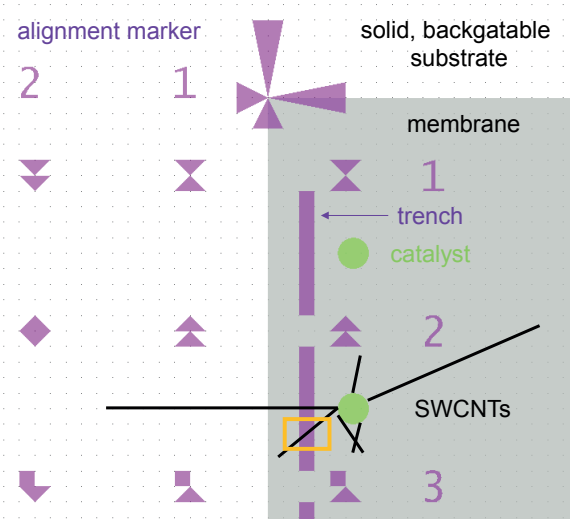

Figure B.2: Basic idea of integrated sample setup for TEM and electron transport measurements: The catalyst dot is deposited onto the membrane and behind a slit, so those CNTs that lie on the backgatable substrate must also lie suspended over a trench. The area of the orange square corresponds to the SEM image in figure B.1.

a trench. The requirement for a backgate in the transport measuremts is fulfilled by the highly doped Si wafer that is electrically insulated from CNT and electrodes by 300 nm of thermal SiO_2.
Commercially unavailable, the membrane design was developed from scratch and custom made the California-based company *appnano* from an n-doped Si wafer. The standard technique to produce membranes on by KOH wet edging. An unassuming yet crucial process parameter is the dopant of the Si substrate; while $n-$Si can be KOH-etched, $p-$Si oddly is an etch stop for KOH. Dry etching through a p-doped Si wafers of the enormous thickness of 320 μm (compared to a bare 50 nm of membrane film thickness) proved production-wise demanding and brought about unsatisfactory results in terms of membrane strain, definition and stability. Our group has, however, experienced issues with n-doped Si losing its conductance at cryogenic temperatures. The cause for this potentially lies within the dopant.
As figure B.1 indicates, the benefit of this integrated design is that all experiments presented in this thesis could be performed on a single, individual CNT: from CNT quantum dots (experiment 1, chapter 5 following) over magnetic domain probing and engineering of the ferromagnetic electrodes (experiment 3, part 4) to retrieving the CNT chiral indices by TEM diffraction (experiment 2, this section).

B.2 CNT chiral indices from TEM diffraction

From the diffraction patterns obtained by TEM measurements, supported by high resolution images and computational methods, it is possible to derive the chiral indices (n, m). Data, evaluation and description of this subsection is based on work by Christian Huber under supervision of Prof. Josef Zweck, Universität Regensburg.

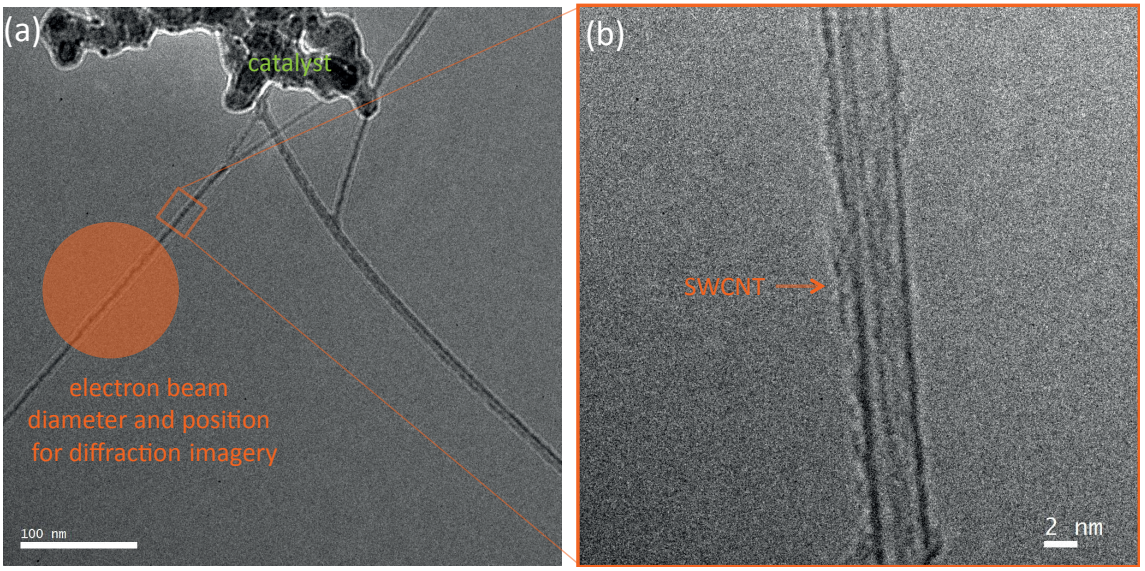

Figure B.3: Real space TEM images of SWCNTs: (a) TEM image showing a SWNTs on the left side of the image. To the right one finds a thicker, probably multi-walled CNT. The red circle represents the electron beam spot size and position for taking the below diffraction image. (b) High resolution TEM image of a CNT. Its diameter is approximately 3.2 nm.

Measurement technique

A CNT is illuminated by an electron beam, as illustrated in figure B.3 (a). Using a small condenser aperture (30 μm), it is possible to achieve a near-parallel illumination with a diameter of only 100 nm (see figure B.4). The diffraction pattern of the CNT ermerges in the back focal plane of the objective lense and can be recorded by a CCD-camera in the microscope. While the electron beam is focused on the CNT, amorphous carbon contaminates the tube. Cooling the sample during the TEM measurements to liquid nitrogen temperature significantly reduced the deposition of amorphous carbon onto the investigated CNT such that an evaluable diffraction patterns could be recorded; among sources of the carbon contamination are residual carbon-containing gases or lithography resist (poly-methyl methacrylate, PMMA) in the TEM vacuum chamber that are decomposed by the electron beam.

On the features in the diffraction image

The CNT can be imagined as a double graphene layer of infinite extension in one and finite extension in the other plane direction with strong curvature. Each graphene layer the electron beam transverses gives rise to six diffraction maxima per order that are the corner points of its hexagonal Brioullin zone. In figure B.4, the first order

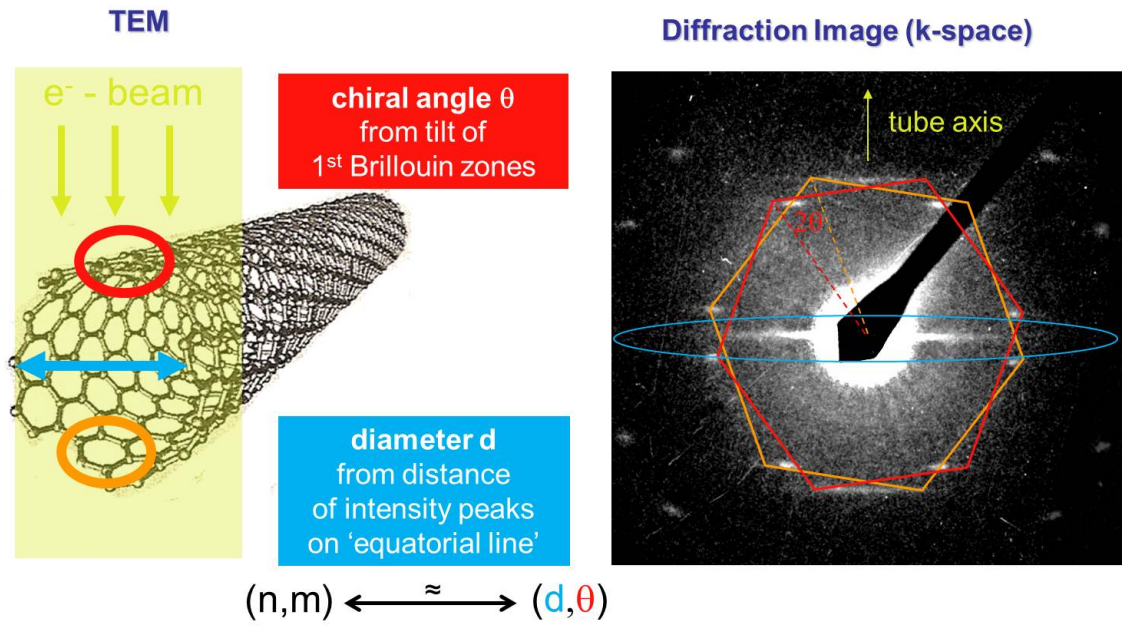

Figure B.4: Basic principle of TEM diffraction on SWCNTs. The CNT is effectively a finite graphene bilayer with curvature. The first (and higher) Brioullin zones are tilted by twice the CNT's chiral angle with respect to each other. By fitting the zeroth order *equatorial line* to Bessel functions the diameter can be extracted. The diffraction image taken by Elsa Thune.

peaks are outlined with a red/orange hexagon for the upper/lower graphene layer. Positional space unit cells and correspondingly the two Brioullin zone images are rotated by twice the chiral angle 2θ against each another [154]. The zeroeth order diffraction peaks lie along the so-called *equatorial line*, as indicated by the blue ellipse in figure B.4. Stemming from the cylindrical CNT symmetry, the intensity distribution and peak spacing can be developed in Bessel functions with the tube diameter d as fit parameter. With (d, θ) extracted, one can isomorphically conclude to the chiral indices (n, m) of a CNT segment.

Taking into account an experimental margin of error, one can narrow down to few possible combinations of (n, m). Plausibility considerations and possibly some additional input, e. g. from transport measurements whether the tube is quasi-metallic or semiconducting, further enhances the accuracy.

Greater experimental accuracy than with this intuitive evaluation scheme can be obtained with the following scheme:

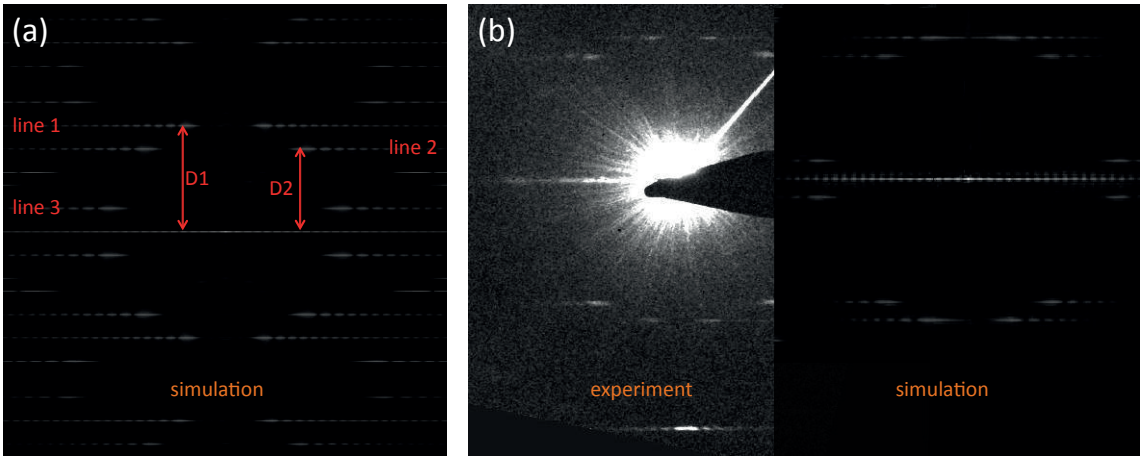

Figure B.5: Reciprocal space TEM images of SWCNTs: (a) Simulated diffraction pattern for the chiral indices (24,11). The principal layer lines are index with lines 1, 2 and 3. D1 and D2 are the corresponding layer line spacings. (b) Matching the simulated diffraction image (right-hand side) to the experimental on (left-hand side) allows to extract the chiral indices of a SWCNT. The tube's structure is thus fully characterised.

Evaluation of the chiral indices (n, m) from *layer lines*

The diffraction pattern of a SCWNT shows a specific *layer line* structure. A simulation for the chiral indices $(24, 11)$ is presented in figure B.5 (a). The spacing of the layer lines as well as the intensity distribution of each layer line is closely related to the chiral indices of the tube. The main diffraction spots can be assigned to reflections from graphene layers tilted against each other by twice the chiral angle θ. The broadening of the spots is caused by the helical structure of the tube. It has been shown that the intensity distribution of each layer line is proportional to the square modulus of a Bessel function [155, 156]. For a tube with chiral indices (n, m) the order of the Bessel-Function is equal to n for layer line $l2$ and m for $l1$ (figure B.5 (a)). The layer line spacing $D1$ and $D2$ is defined by the chiral angle θ.
The chiral indices can be determined by analysing the layer-line spacings and the order of the Bessel function of the layer lines. Additionally, the information on the CNT diameter can be determined from calibrated high resolution transmission electron microscope pictures and by fitting the equatorial line in the diffraction pattern. A tilt angle between the electron beam and the tube has a significant effect on the diffraction pattern [157]. As a consequence the spacing of the layer lines as well as the intensity distribution of each layer line is slightly changed. To obtain the chiral indices accurately the influence of a tilt angle has to be considered. In this way the chiral indices of a CNT shown in figure B.3 (b) can be determined with good accuracy.

Figure B.5 (b) shows an experimental image along with the matching simulation; from it the chiral indices are found to be $(29, 19)$. A tilt angle of $\approx 20°$ has been taken into account.

Appendix C

Four-fold symmetry and Kondo effects in a SWCNT quantum dot

This chapter presents data measured on a SWCNT single quantum dot with two ferromagnetic electrodes $F1$ and $F2$. A similar sample of identical design is shown in figure C.1 (a). The ferromagnet used is 40 nm of $Pd_{60}Fe_{40}$ as investigated in section 4.2.

This dicussion is deliberatly restricted to a phenomenological description of the data. An in-depth, quantitative study on the Kondo effect in CNT-based quantum dots with ferromagnetic electrodes will be published shortly in the PhD thesis of Markus Gaaß [158], who continued the work on this topic.

C.1 Four-fold degenerate pattern in Coulomb diamonds

Figure C.1 (b) shows a stability diagramme, where the differential conductance is mapped out as a function of bias and the backgate voltage potential. As electrode material, $Pd_{60}Fe_{40}$ was used. At a relatively high temperature of T=1.8 K =155 μeV/k_B, a clear Coulomb diamond pattern appears. Additional finite bias line features can, by comparison with figure 1.3, be identified as co-tunnelling lines and exited states where additional conductance channels are opening up. Note that the sketch in figure 1.3 shows the tunnel current through a quantum dot, whereas the data in figure C.1 (b) represents the derivative of the current by the bias voltage. Consequently, where a surface of increased current is marked in the sketch, only its outlines are expected in the $\mathrm{d}I/\mathrm{d}V(V_{SD}, V_G)$ plot, as detailed in figure C.4 (a). With a maximum differential conductance close to twice the quantum conductance

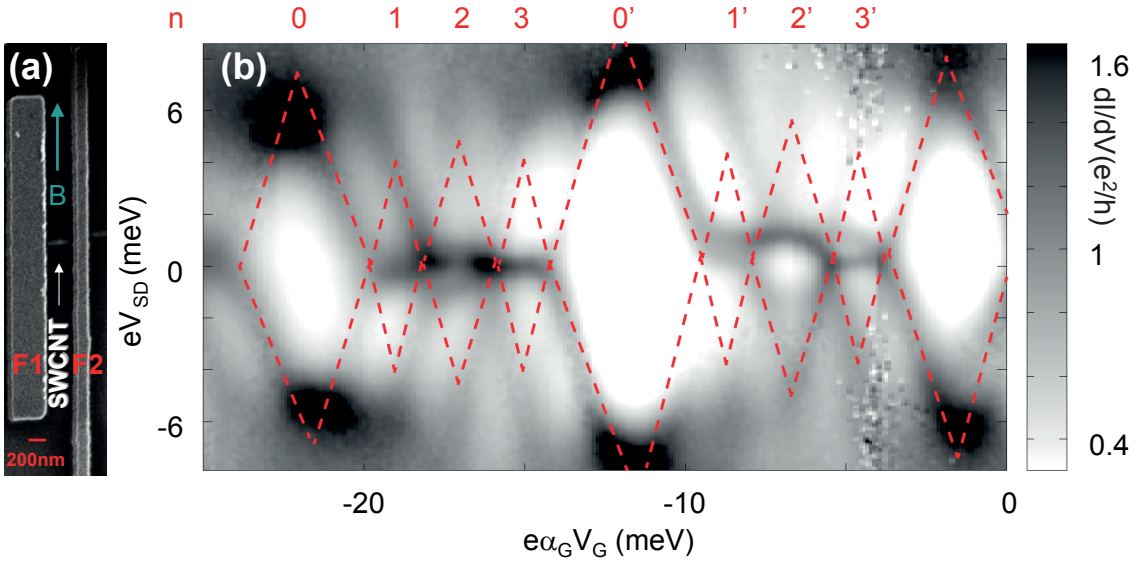

Figure C.1: (a) SEM micrograph of a similar SWCNT quantum dot sample with ferromagnetic $Pd_{60}Fe_{40}$ electrodes. (b) Stability diagram of differential conductance $\mathrm{d}I/\mathrm{d}V$ plotted as a function of bias V_{SD} and backgate energy $e\alpha_G V_G$ (with the gate efficiency α_G), measured at T=1.8 K=155 μeV/k_B. An external field of 200 mT perpendicular to the SWCNT and parallel to the ferromagnetic $PdFe$ electrodes aligns the magnetisations of the contacts $(M_{F1}, M_{F2}) = \uparrow\uparrow$ co-linearly. The Coulomb blockade pattern shows two periods of *big-small-small-small* Coulomb diamonds, highlighted with red dashed lines. This four-fold symmetry is a fingerprint of SWCNTs with both spin and orbital degeneracies intact. Each *small* diamonds exhibits zero bias anomalies of increased non-zero conductance.

e^2/h (cf. figure C.1), this SWCNT quantum dot operates close to the unitary limit of quantum conductance four a energetically four-fold degenerate SWCNT device ($4e^2/h$). In this parameter range of high electrode transparencies to the CNT, the quantum dot is expected to be still in the Coulomb blockade regime but close enough to the Fabry-Pérot regime to exhibit e. g. Kondo effects, as already mentionned in section 2.4.

As a guide to the eye, the Coulomb diamond outlines are highlighted with red dashed lines in figure C.1. In good agreement with figure C.4, two full periods can be made out; each period consists of one big Coulomb diamond, where a new shell of four energy-degenerate electronic states starts populating, followed by three smaller diamonds of roughly equal size. The pattern allows to assign the diamonds with a value n that corresponds to the mod_4 of the excess electron number on the SWCNT. A bandgap of a semiconducting nanotube marks the gate region with zero excess electrons on the dot. Counting the diamonds away from the gap, the absolute

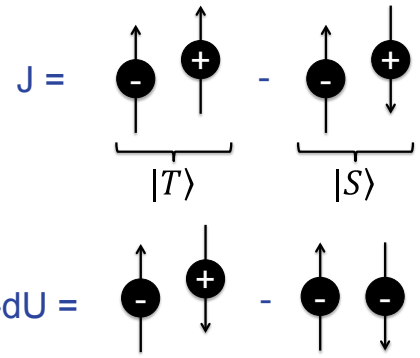

Figure C.2: Illustration of SWCNT energy corrections to four-fold degeneracy. Each state is characterised by a spin quantum number (marked by either up or down arrow for spin $\frac{1}{2}$ or $-\frac{1}{2}$) and an orbital quantum number (denoted as $+$ or $-$ for clockwise or counter-clockwise trajectory around the CNT cylinder). J is the (spin) singlet-triplet splitting, δ the orbital mismatch and dU the electrostatic charging energy of a doubly occupied orbital versus two singly occupied ones.

excess electron number can be determined. For this sample, presumably because its SWCNT is quasi-metallic, no bandgap is observed and so the absolute electron number remains unknown.

Table C.1: Four-fold degeneracy: (a) Addition energies for the first period $n = 0, 1, 2, 3$ of Coulomb diamonds in figure C.1. (b) Proposed parameter set of coupling energies as detailed in section 2.4 (cf. figure 2.7). All values are scaled to the level spacing $\Delta\mu^L \approx 3.0\ meV$.

(a)	valley	0	1	2	3
	addition energies $\Delta\mu_i$	4.9 meV	1.65 meV	1.95 meV	1.65 meV

(b)		$\Delta\mu^L$	J	dU	δ
	coupling energies $[\Delta\mu^L]$	1	0.07	0.01	0.18

Energy contributions that can cause the deviation in size of the three smaller diamonds have been discussed in section 2.4 and are illustrated in figure C.2. The 'middle' diamonds labelled with occupancy $n = 2, 2'$ in figure C.1 (b) are slightly larger (by $\delta - J - 2dU$) than the equal-sized flanking diamonds with odd occupancy $n = 1, 3, 1', 3'$.

From the electrode spacing of about 280 nm, the level spacing in the nanotube can estimated to $\Delta\mu^L \approx 3.0\ meV$ via equation 2.44. The electrostatic charging energy was $\Delta\mu_C \approx 1.4$ meV. Table C.1 (a) presents the addition energies of the first period of four Coulomb diamonds presented (labelled $0, 1, 2, 3$ in figure C.1, i. e. their zero bias widths in gate energy $e\alpha_G V_G$). Table C.1 (b) proposes a parameter set for the

coupling energies, as detailed in section 2.4 (cf. figure 2.7) that matches the data to an accuracy below 1%. The condition for four-fold periodicity in the SWCNT Coulomb pattern, $\delta \leq \Delta\mu^L/2$ [140] is satisfied. Note that the data were taken not at zero but a small finite magnetic field (B=200 mT) - which is small compared to typical energy scales but safely above typical coercive fields of the ferromagnetic electrodes (below 50 mT) known from similar samples of identical design. The rationale for this measure was to define a controlled relative magnetisation orientation of ferromagnetic source electrodes. At zero field, this could not be achieved in TMR calibration measurements.

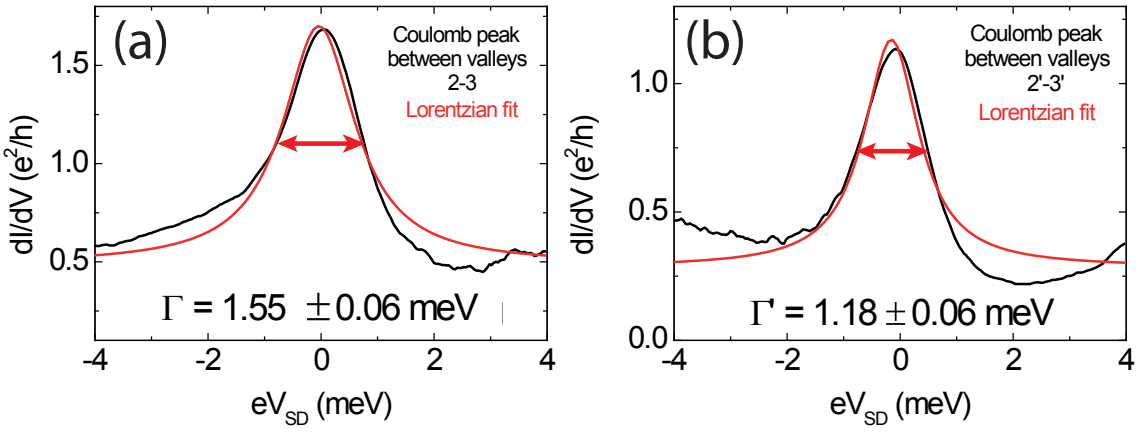

Figure C.3: The resonance width of a Coulomb peak in $\mathrm{d}I/\mathrm{d}V(V_{SD})$ is obtained from width parameter of a Lorentzian fit. Resonance width Γ (and also conductance) are higher for the first four-fold degenerate period of Coulomb diamonds ((a) Γ=1.55±0.06 meV) compared to the second period ((b) Γ'=1.18±0.06 meV), as denoted in figure C.1. The values were obtained from the Coulomb peaks between valleys $2, 3$ and $2', 3'$ respectively.

The coupling energy Γ in equation is given by the resonance width of a Coulomb peak. Given that the zero bias conductance for period $n = 0, 1, 2, 3$ (max. $1.6e^2/h$) is significantly higher than for the period $n = 0', 1', 2', 3'$ (max. $1.2e^2/h$), Γ is extracted for each period separately, as demonstrated in figure C.3. Consistently, the coupling energy is higher for the first period (Γ =1.55 meV) than for the second (Γ' =1.18 meV).

C.2 Spin-$\frac{1}{2}$, orbital and ST-Kondo effects

The zero bias anomallies occur in figure C.1 (b) for every Coulomb diamond with partially occupied shells (i. e. all apart from $n = 4, 4'$). Some of these anomalies are actually split into a double peak on a small bias scale and are rougly symmetric

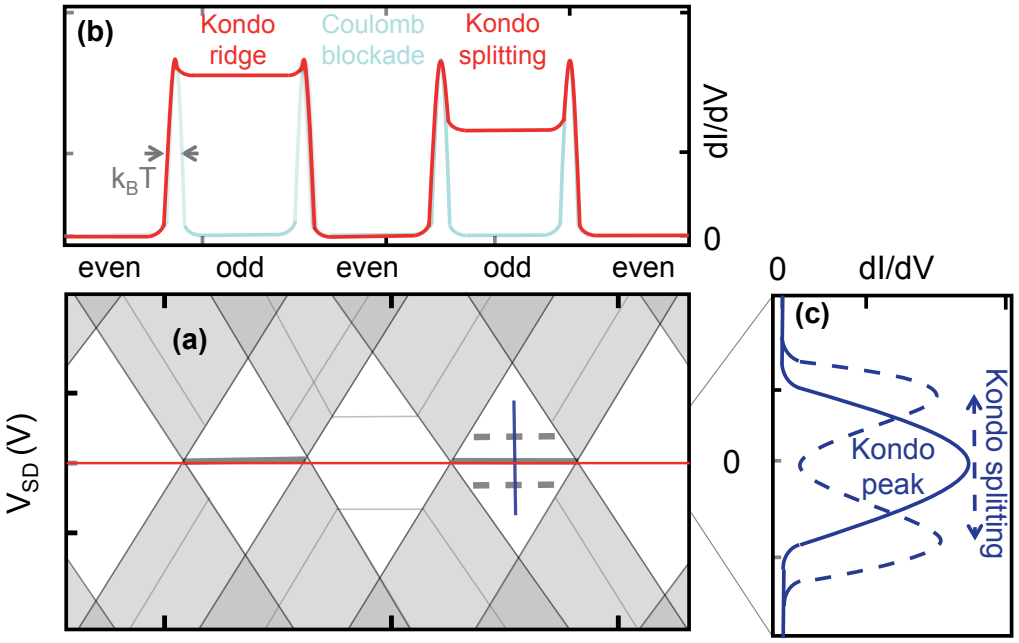

Figure C.4: (a) Idealised sketch of a stability diagram $\mathrm{d}I/\,\mathrm{d}V(V_G, V_{SD})$. The gate voltage range corresponds to one period of four Coulomb diamonds in the experimental data of figure C.1 (b). The finite differential conductance areas in the (V_G, V_{SD}) have been greyshaded. This accounts, put in a simple picture, for inleastic co-tunnelling transport mechanisms that render the current through the dot non-constant and hence the differential conductance non-zero. (b) Idealised sketch of zero bias line traces of conductance as function of the gate voltage, $\mathrm{d}I/\,\mathrm{d}V(V_G)$, taken along the red semitransparent line in subfigure (a). Three scenarios are colour-coded. Cyan trace: Basic Coulomb peaks without any zero bias anomalies. Red trace: Two Kondo 'ridges' in each valley with odd excess electron occupancy. Dashed red trace: As subfigure (a) indicates with a dashed black line, the Kondo ridge splits in bias direction. Consequently, the zero bias conductance in the corresponding valley drops. (c) Idealised sketch of line traces of conductance as function of the bias, $\mathrm{d}I/\,\mathrm{d}V(V_{SD})$ at fixed gate, taken along the orange semitransparent line in subfigure (a). Blue trace: A Kondo peak around zero bias. Dashed blue trace: Under the effect of e. g. an external magnetic field, split 'double' Kondo peaks appear at positive and negative bias of same magnitude.

around zero bias. The remainder of this chapter confines itself to the region around the zero bias line which is marked by the semitransparent red line in figure C.4 (a). All anomalies can be attributed to Kondo effects. They are one of the archetypical phenomena of may-body physics and result from the exchange interaction between a single localised spin and a bath of conduction electrons (cf. [158]). The relevant Kondo effects will be briefly introduced in the following.

C.2.1 Zero and small bias anomalies

Every Coulomb diamond in figure C.1 (b) bears a conductance anomaly at or around zero bias, apart from the diamonds that correspond to completely filled shell (excess electron numbers $n = 0, 0'$ on the quantum dot). These lines of finite conductance, where a simple sequential tunnelling picture would predict Coulomb-blockade, can be ascribed and accounted for by the aforementioned Kondo effects. The two periods of Coulomb diamonds in figure C.1 (b), i. e. $n = 0, 1, 2, 3$ and $n' = 0', 1', 2', 3'$, are distinctly different in the structure of their (near) zero bias anomalies. In the following, both periods will be investigated in more depth by studying the line traces $\mathrm{d}I/\,\mathrm{d}V(V_G)$ and $\mathrm{d}I/\,\mathrm{d}V(V_{SD})$ through each anomaly.

Evaluation of period $n = 0, 1, 2, 3$

Figure C.5 (a) highlights a small bias range zoom on the first period of four Coulomb diamonds in figure C.1 (b).
The 'odd' Coulomb-blockade valleys ($n = 1, 3$) show, in the zero bias gate trace $\mathrm{d}I/\,\mathrm{d}V(V_G)$ (cf. figure C.5 (b)) no drop to zero conductance but rather a line of finite conductance with roughly linear slope. This compares well to a *Kondo ridge* (b) like it is sketched in figure C.4 (b). The 'conjugate' line traces in bias $\mathrm{d}I/\,\mathrm{d}V(V_{SD})$ (cf. figures C.5 (c) and (e) for $n = 1, 3$) each display correspondingly a single *Kondo peak* as sketched in figure C.4 (c).
The 'even' Coulomb-blockade valley ($n = 2$) shows a dip in the zero bias $\mathrm{d}I/\,\mathrm{d}V(V_G)$ (cf. figure C.5 (b)). Still, the conductance does not drop to zero as expected in the Coulomb blockade regime. The 'conjugate' line trace in bias $\mathrm{d}I/\,\mathrm{d}V(V_{SD})$ (cf. figure C.5 (d) for $n = 2$) reveals a double peak, both asymmetric in peak height and around zero bias. This corresponds qualitatively to a *split Kondo peak* as idealtypically sketched in figures C.4 (b) and (c).

Evaluation of period $n' = 0', 1', 2', 3'$

Figure C.6 (a) highlights a small bias range zoom on the second period of four Coulomb diamonds in figure C.1 (b).
All 'odd' and 'even' Coulomb-blockade valleys ($n' = 1', 2,' 3'$) show, in the zero bias gate trace $\mathrm{d}I/\,\mathrm{d}V(V_G)$ (cf. figure C.6 (b)) a drop in conductance compared to the Coulomb resonances but still remain at finite $\mathrm{d}I/\,\mathrm{d}V$ values. These drops are very pronounced in valleys $n' = 2', 3'$ but less so in valley $n' = 1'$, comparing well to the case of a *split Kondo ridge* (b) as sketched in figure C.4 (b).
The 'conjugate' line traces in bias $\mathrm{d}I/\,\mathrm{d}V(V_{SD})$ (cf. figures C.6 (c), (d) and (e) for $n' = 1', 2', 3'$ respectively) display correspondingly a double, *split Kondo peak* each,

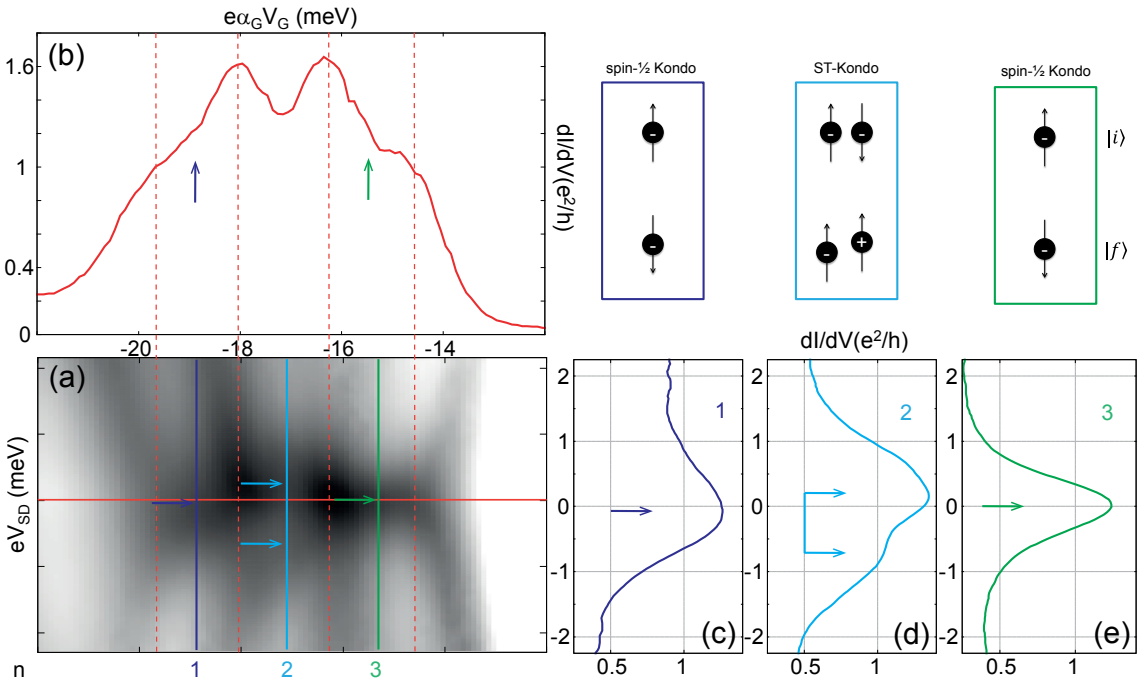

Figure C.5: Kondo ridges: (a) Low bias $\mathrm{d}I/\mathrm{d}V(V_G, V_{SD})$ zoom on the first period of four diamonds in figure C.1 (b) with excess electron numbers $n = 0, 1, 2, 3$. Format and notation mirror those in sketched figure C.4. (b) Red trace: $\mathrm{d}I/\mathrm{d}V(V_G)$ linescan along the red line in subfigure (a). The Kondo ridges appear in the odd valleys $n = 1, 3$, marked by the blue and green arrows respectively. (c) Blue trace: A single Kondo peak in the $\mathrm{d}I/\mathrm{d}V(V_{SD})$ line scan at zero bias in (odd) valley 1. (d) Cyan trace: A double Kondo peak in the $\mathrm{d}I/\mathrm{d}V(V_{SD})$ line scan around zero bias in (even) valley 2. (e) Green trace: A single Kondo peak in the $\mathrm{d}I/\mathrm{d}V(V_{SD})$ line scan at zero bias in (odd) valley 3. The correspondingly colour-coded frames ascribe possible Kondo mechanisms to each valley $n = 1, 2, 3$.

as sketched in figure C.4 (c). While the peak heights are asymmetric for all valleys, both 'odd' valleys ($n' = 1', 3'$) have their split peaks symmetrically distributed around zero bias while they are highly asymmetric for the 'even' valley ($n' = 2'$). The splitting in valley $n' = 2'$ is also very large compared to those in the adjacent 'odd' valleys ($n' = 1', 3'$) and also the even valley $n = 2$ in the first Coulomb diamond period (cf. figure C.5 (d)).

To ascribe possible underlying Kondo mechanisms to the investigated zero bias anomalies and to identify the contributions to the split Kondo peaks, the next section will undertake a coarse quantitative analysis of the Kondo splittings. Of particular interest is whether an effect of the ferromagnetic electrodes on the Kondo

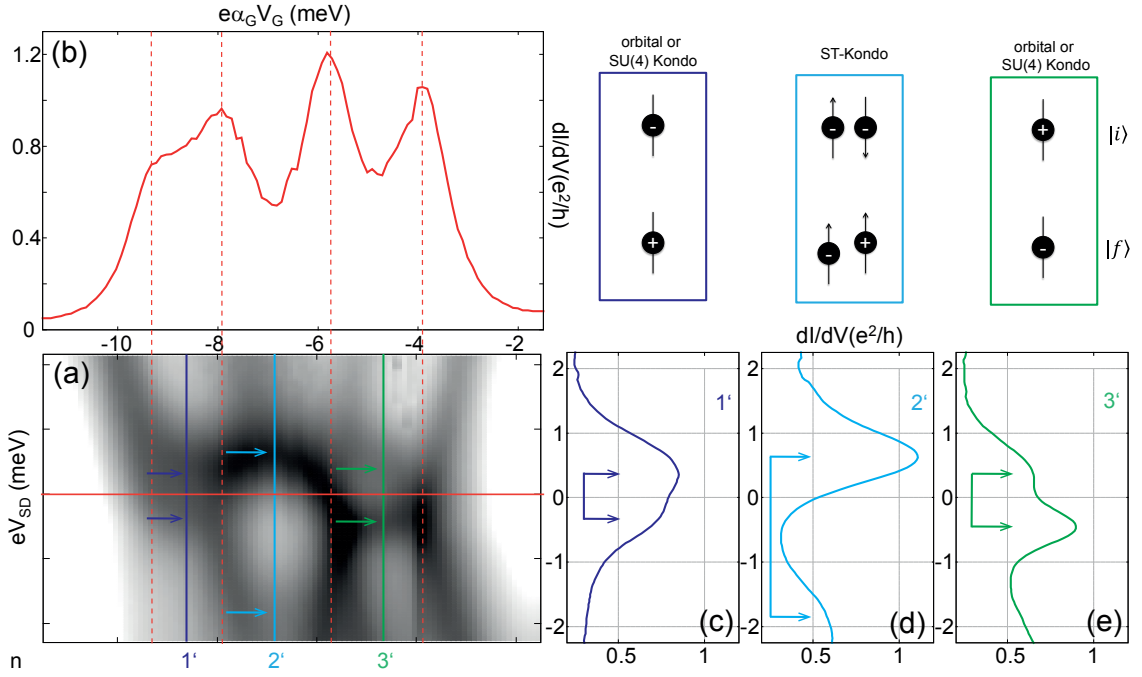

Figure C.6: (a) Low bias $\mathrm{d}I/\mathrm{d}V(V_G, V_{SD})$ zoom on the second period of four diamonds in figure C.1 (b) with excess electron numbers $n = 0', 1', 2', 3'$. For this period, the bias offset differs by 0.6 meV with respect to the period $n = 0, 1, 2, 3$ which has been corrected in this graph, similarly to [159]. (b) Red trace: $\mathrm{d}I/\mathrm{d}V(V_G)$ line scan along the red line in subfigure (a). Between the Coulomb peaks, marked by the dashed red lines, the conductance shows dips, corresponding to the dip between a split Kondo resonance: (c) Blue trace: A split Kondo peak in the $\mathrm{d}I/\mathrm{d}V(V_{SD})$ line scan at zero bias in (odd) valley $1'$. (d) Cyan trace: A large Kondo splitting in (even) valley $2'$, asymmetric around zero bias. (e) Green trace: A split Kondo peak in the $\mathrm{d}I/\mathrm{d}V(V_{SD})$ line scan at zero bias in (odd) valley $3'$. The correspondingly colour-coded frames ascribe possible Kondo mechanisms to each valley $n' = 1', 2', 3'$.

splitting can be traced.

C.2.2 Review of relevant Kondo effects

Figure C.4 (a) shows an idealised sketch of a stability diagram $\mathrm{d}I/\mathrm{d}V(V_G, V_{SD})$. Its range corresponds to one period of four Coulomb diamonds in the experimental data in figure C.1 (b). The finite differential conductance areas in the (V_G, V_{SD}) have been greyshaded. This accounts, put in a simple picture, for inelastic co-tunnelling transport mechanisms that render the current through the dot non-constant and hence the differential conductance non-zero.

Sequential tunnelling Coulomb blockade in linear response

The blue line is simple case single electron sequential tunnelling at zero bias. Here conductance is non-zero only if a single particle state has its corresponding electrochemical potential aligned to the Fermi level of source and drain electrodes. The Coulomb blockade diamonds are thus truly 'void of current' and appear as white areas with dark outlines.

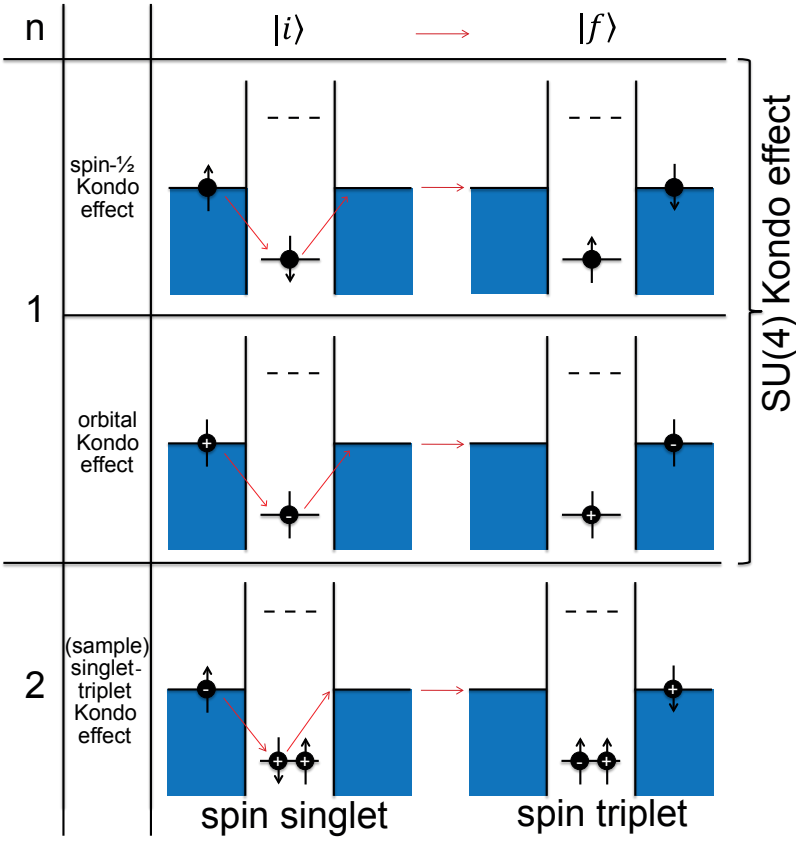

Figure C.7: Illustration of spin and orbital Kondo effects: In table form, the number of electrons n on the quantum dot is plotted against the initial and final states ($|i\rangle$ and $|f\rangle$) on the dot for each Kondo process.

Spin-$\frac{1}{2}$ and orbital Kondo effects

The simplest Kondo system consists of a single electrons localised, e. g., on a quantum dot. The Kondo effect also requires some at least two-fold energetic ground state degeneracy of a single localised electron that couples to a Fermi sea by means of a Heisenberg-like exchange interaction [160]. In the present case, the wave function of a single electron on the quantum dot would hybridise with many-body wave

function of source and drain electrodes. Through higher order tunnel processes, this allows current to resonantly flow within the Coulomb diamond areas which, in a mere sequential tunnelling picture, should be Coulomb-blockaded. These Kondo effects appear as a zero bias conductance feature in every Coulomb diamond with odd occupancy, as figure C.4 (a) sketches. In a $\mathrm{d}I/\,\mathrm{d}V(V_G)$ at zero bias (cf. figure C.4 (b), red line), the Kondo feature manifests, in the simplest case, as a *Kondo ridge*. The 'conjugate' line trace $\mathrm{d}I/\,\mathrm{d}V(V_{SD})$ at fixed gate potential through the Kondo feature (cf. figure C.4 (c), blue line) features a characteristic *Kondo peak*.
In principle, any degeneracy in the ground state of the localised can lead to a Kondo effect. In the present, both the electronic spin ($\pm\frac{1}{2}$) and the orbital pseudo-spin ($+/-$) can give rise to Kondo effects. As each spin-$\frac{1}{2}$ and orbital obey an SU(2) symmetry, when both effects occur simultaneously, they can be written to obey a SU(4)=SU(2)$\otimes$SU(2) symmetry, motivating the name *SU(4)-Kondo effect* [70]. Figure C.7 illustrates the different Kondo processes. Consider the case of one excess electron on the quantum dot; three excess electrons on the dot is the equivalent case of a single hole on the dot, so the Kondo process is analogous to the $n = 1$ case. A (pseudo-)spin-flip co-tunnelling process connects the two states of opposite respective (pseudo-)spin. The flipping spins can be either spin-$\frac{1}{2}$ or the orbital chirality quantum number or both at the same time. The tunnelling processes onto and from the dot, indicated by the two red arrows, are to be understood as simultaneous. The Kondo process may be characterised the electron that tunnels from the source electrode onto the dot and the electron - of at least one opposite spin - co-tunnelling from dot to drain electrode. Equivalently, the Kondo process is characterised by the spin configuration on the quantum dot 'before' (initial state $|i\rangle$) and 'after' (final state $|f\rangle$) the co-tunnelling event. The possible combinations of initial and final states are summarised by the blue (spin-$\frac{1}{2}$ Kondo), red (orbital Kondo) and violet (SU(4) Kondo) arrows in figure C.8 (a).

Singlet-Triplet (ST) Kondo effect

The singlet-triplet (ST)-Kondo effect occurs for two electrons in the dot. In this situation, two degeneracies are required for Kondo processes to occur, both the one between two-particle (spin) singlet and triplet states and also the orbital degeneracy. As figure C.7 illustrates, the ST-Kondo process effectively is much like a simple spin-$\frac{1}{2}$ Kondo effect. For two electrons on the dot, however, this process would be Pauli-forbidden were it not for the additional orbital degeneracy. Consequently, a ST-Kondo process requires a single flip in orbital momentum in addition to the electronic spin flip. Hence, the ST-(TS-)Kondo effect requires two electrons with parallel (anti-parallel) spin and same (opposite) orbital momentum on the dot as an

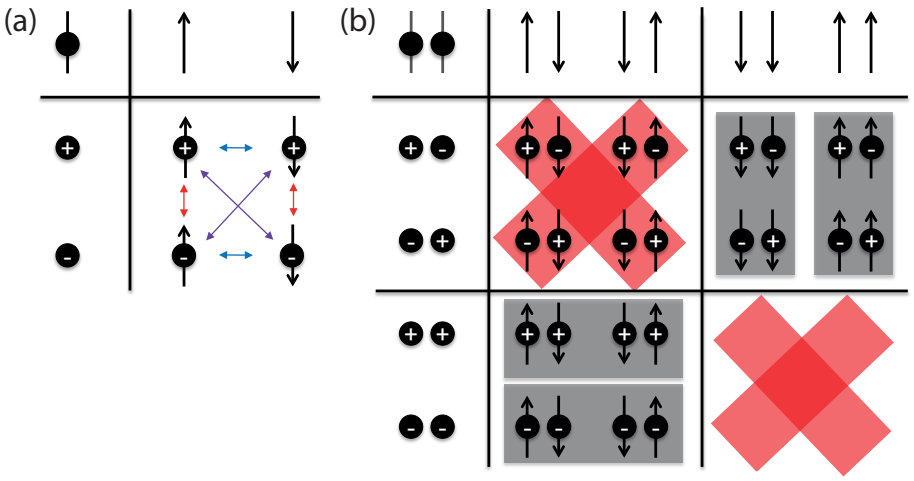

Figure C.8: Phase spaces of possible initial and final states for (a) one charge carrier (3 electrons correspond to one hole, spin-$\frac{1}{2}$ and/or orbital Kondo effects) and two charge carriers (ST-Kondo effect). All possible configurations of orbital momentum (clockwise +, counter-clockwise -) and spin states (up or down, $\pm\frac{1}{2}$) provide four Kondo channels contributing to the tunnel current (see configurations within grey rectangles, which are quantum mechanically indistinguishable and hence count only for one channel). Spin configurations on red rectangles cannot give rise to ST-Kondo effects by Pauli-prohibition.

initial state and yields the reversed situation as a final state. Measurements of both constellations have been reported [70].
Figure C.8 (b) sumarises all possible configurations of orbital momentum (clockwise +, counter-clockwise -) and spin (up, down) states. As each spin up and down and clockwise and counter-clockwise orbits are quantum mechanically indistinguishable, configurations paired within the underlying rectangles count as one channel. Spin configurations on red rectangles cannot give rise to ST-Kondo effects by Pauli-prohibition. The number of grey rectangles in figure C.8 (b) reveals that four Kondo channels contribute to the tunnel current, each with up to the quantum conductance e^2/h. The Kondo conductance is thus enhanced compared to an only two-fold degenerate Kondo system [70, 86].

C.2.3 Kondo splitting

The Kondo splitting Δ_K may be quantified by considering three contributions:

$$\Delta_K = \Delta_K^{spin} + \Delta_K^{orb} + \Delta_K^{FM} \tag{C.1}$$

accounting for spin effects (Δ_K^{spin}), orbital effects (Δ_K^{orb}) and the influence of the ferromagnetic contacts (Δ_K^{FM}).

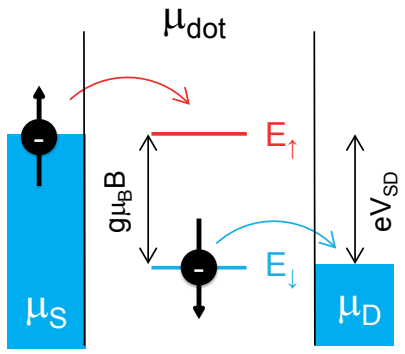

Figure C.9: Energy scales and conditions for the spin down Kondo peak of a Zeeman-split spin-$\frac{1}{2}$ Kondo resonance caused by a magnetic field. The energy difference of spin up energy level $E_\uparrow$ and spin down energy level $E_\uparrow$ is given by ΔE_Z, i. e. twice the Zeeman energy of a spin-$\frac{1}{2}$. The two tunnelling events for spin up and down electrons are not to be understood sequentially, but simultaneously. For resonant transport to occur via the 'Kondo channel', the bias must provide an energy exactly equal to the Kondo splitting Δ_K.

Spin and orbital contributions to Kondo splitting

Spin and orbital contributions

$$\begin{aligned} \Delta_K^{spin} &= \Delta_K^{spin}(\vec{B}^{ext}) + \Delta_K^{spin}(\vec{B}^{stray}) \qquad \text{(C.2)} \\ &= [g\mu_{\mathrm{B}} B^{ext} + g\mu_{\mathrm{B}} B^{stray}]\Delta s^{spin} \\ \Delta_K^{orb} &= \Delta_K^{orb}(B_{||}^{ext}) + \Delta_K^{orb}(B_{||}^{stray}) + \delta\Delta s^{orb} \qquad \text{(C.3)} \\ &= [\mu_{\mathrm{orb}} B^{ext} + \mu_{\mathrm{orb}} B^{stray} + \delta]\Delta s^{orb}, \end{aligned}$$

depend on both external magnetic field and the stray field of the ferromagnetic electrodes, proportional to twice the corresponding spin or orbital quantum number, i. e. $\Delta s^{spin} = 1$ and $\Delta s^{orb} = 2$. Figure C.9 illustrates this for the example of a Zeeman-split spin-$\frac{1}{2}$ Kondo peak. The orbital mismatch $\delta = 0.18\Delta\mu^L = 0.54$ meV was determined in table C.1 The above expression for Δ_K^{orb} is using the approximation $\delta - dU \approx \delta$ as $dU \ll \delta$.

The spin degeneracy can be lifted by a magnetic field B. The orbital degeneracy can be lifted by applying a magnetic field $B_{||}$ parallel to the CNT axis. In the present experiment, $B_{||}$ is $B_{ext}\sin(30°)$.

A comparable experiment on a SWCNT quantum dot with highly transparent non-ferromagnetic electrodes [70] suggests that higher magnetic field strengths are necessary to lift the orbital degeneracy. As our data set lacks a B-dependence, we cannot directly reproduce this finding but shall assume it to be correct for our case. For the same reason, we cannot determine μ_{orb} directly but have to rely on the value from reference [70], who have found that $\mu_{orb} \approx 13\mu_{\mathrm{B}}$. The contribution of the ferromagnetic electrode stray fields is typically in the few mT range and can thus be neglected.

The spin (orbital) splitting contribution due to the small external magnetic field is 0.024 meV (0.64 meV). It accounts only for a mere 1-3% (11-14%) of the measured splitting for valleys $n = 2, 1', 2', 3'$. The experimentally found distance in energies between these split Kondo peaks are summarised in table C.2.

Contributions of the ferromagnetic electrode to Kondo splitting

$\Delta_K^{FM}(P, V_G)$ depends on the polarisation P of the ferromagnet and on the gate voltage along the split ridge. At the middle of the ridge this spltting contribution drops to zero, forming an x-shaped modulation of the split Kondo peaks along V_G [161]. While there is a slight gate dependence, e. g. in the split Kondo ridges of valley $2'$ and $3'$, such an x-crossing is not observed in the present data. This suggests that $\Delta_K^{FM}(P, V_G)$ is small against other contributions. In order to further justify neglecting $\Delta_K^{FM}(P, V_G)$, all line traces $\mathrm{d}I/\,\mathrm{d}V(V_{SD})$ are purposefully taken at the centres of the Coulomb valleys, where $\Delta_K^{FM}(P, V_G)$ is theoretically expected to be zero [158].
The contribution $\Delta_K^{FM}(M)$ depends on the magnetisation M of the ferromagnetic electrodes. M can take values from zero to 1 for maximum magnetisation. If, e. g. the screened $3d$ orbitals account for the ferromagnetism of a metal, and the 5 orbitals are each half-occupied with a, say, spin-up electrons, then M=100%. As will be shortly published and derived in detail [158], the magnetisation contribution to the splitting of a Kondo ridge has the dependence

$$\Delta_K(M) = \frac{\Gamma}{\pi}\, ln\frac{1-M}{1+M}. \tag{C.4}$$

This energy contribution is always zero or negative because, by the structure of equation C.4, the argument of the logarithm is always $\leq$1. 'Negative' means that this energy contribution is antigonal to other effects that can split Kondo resonances, effectively offsetting the Kondo resonances in a $\mathrm{d}I/\,\mathrm{d}V(V_{SD}, B)$-plane.

C.3 Discussion

Four-fold symmetry

A clear four-fold symmetry is observed in figure C.1 (b), indicating that there both orbital and spin degeneracies of the SWCNT segment are unbroken. The orbitals (clockwise (+) and counterclockwise (−)) are energetically separated by a finite δ=0.54 meV=0.18$\Delta\mu^L$. Still, the four-fold symmetry in the Coulomb diamond pattern remains intact as long as it is small against the level spacing $\Delta\mu^L$ ($\delta \ll \Delta\mu^L$), as in the present case (cf. table C.1). Moreover. the occurrence of this clear

four-fold symmetry is a confirmation that the CNT consists indeed only of a single shell. Kondo effects can arise from either degeneracy (cf. figure C.7). The clear four-fold degenerate Coulomb diamond pattern (shown for two consecutive periods in figure C.1 (b)) is also a quality fingerprint of our CVD-grown SWCNTs (cf. CNT-based quantum dot fabrication (cf. chapter 3).

Kondo temperature

The *Kondo temperature* T_K is the characteristic energy scale of the Kondo effect. It marks the maximum of competing energy scales, e. g. the electron temperature or orbital splitting, up to which a Kondo effect can occur. T_K can be extracted from the data as the FMHW of a given Kondo peak. The FMHW of the Kondo peak in valley $n = 3$ yields a Kondo temperature value of T_K=1.13 meV/k_B ≈13 K, which is an order of magnitude above the cryostat bath temperature (1.8 K). Within this data set, no temperature dependence is available. This singlular, very high value for T_K must be understood as an upper bound. It has, however, often been reported, that the four-fold degeneracy in the SU(4)-Kondo [70,86] and ST-Kondo [70] effects leads to a Kondo temperature much higher than in the ordinary spin-$\frac{1}{2}$ case. Revolving this argument, the high Kondo temperature provides an additional support that the investigated sample indeed exhibits SU(4) Kondo effects. Also note that even for finite orbital splitting δ, as in in the present case, SU(4)-Kondo effects can occur under the condition that the orbital splitting is smaller than than the characteristic Kondo temperature energy scale, i. e. $\delta < k_\mathrm{B}T_K$ (valid at zero or small magnetic fields) [70]. This condition is fulfilled for the presented datas set.

Ascribing Kondo mechanisms to the zero bias anomalies

Table C.2 presents the energy distances of the Kondo peaks in all investigated valleys. The values were extracted from the respective bias line scans in figures C.5 and C.6. In order to ascribe Kondo mechasims to each bias anomaly, table C.2 compares the measured splittings with the spin-$\frac{1}{2}$ and orbital contributions Δ_K^{spin} and Δ_K^{orb}. The appropriatly colour-coded ascribations of Kondo meachnisms are placed over the $\mathrm{d}I/\,\mathrm{d}V(V_{SD})$ line scans for each valley in figures C.5 and C.6.

In the two valleys of the first period with odd excess electron occupacy ($n = 1, 3$, cf. figures C.5 (c) and (e)), no Kondo splitting is observed. One can attribute the ordinary spin-$\frac{1}{2}$ Kondo effect to these resonances, as the small spin splitting, Δ_K^{spin}=0.024 meV, is small against the bath temperature T=1.8 K=0.155 meV/k_B and therefore not resolvable.

Table C.2: Kondo splittings from experiment compared to the expected spin-$\frac{1}{2}$ and orbital contributions to Kondo splitting.

valley		1	2	3	1'	2'	3'
Kondo mechanism		spin-$\frac{1}{2}$	ST	spin-$\frac{1}{2}$	SU(4)	ST	SU(4)
Δ_K measured	(meV)	0	0.89	0	0.68	[2.6]	0.76
-Δ_K^{spin}	(meV)	0.024	0.024	0.024	0.024	0.024	0.024
-Δ_K^{orb}	(meV)		1.17		1.17	1.17	1.17
=	(% of Δ_K)	n/a	-33%	n/a	-62%	[54%]	-41%

The two valleys with half-filled shell ($n = 2$, cf. figure C.5 (d) , and $n' = 2'$, cf. figure C.6 (d)) both exhibit a pronounced Kondo splitting. As the singlet-triplet splitting J is small against the orbital splitting δ, the singlet is lower in energy than the triplet and thus the ground state. The only feasible process underlying these split resonances is therefore a ST Kondo effect.
The two oddly occupied valleys in the second Coulomb diamond period ($n' = 1', 3'$, cf. figures C.6 (c) and (e)) also show a clear Kondo spllitting. Any SU(4) Kondo effect that involves a flip in orbital momentum can be at its origin (cf. red or violet arrows in figure C.8 (a)), given that only $\Delta_K^{orb} > k_{\mathrm{B}}T$.
SU(4) and ST Kondo effects have been observed in many CNT-based quantum dots with non-ferromagnetic electrodes (e. g. [70, 86, 162]). In particlular, figures C.6 (a) and (b) are comparable and in striking agreement with figures 3 (b) and (a) from reference [70].

Influence of the ferromagnetic electrodes on the Kondo splitting

The measured Kondo splittings Δ_K for valleys $n = 2, 1', 2', 3'$ are quantitatively compared to the theoretically contributions Δ_K^{spin} and Δ_K^{orb}. in table C.2. In the bottom line of the table, the differences between measurement and expectation are presented as percentage values of the respective Δ_K. All splittings are overestimated by -33% to -62%. Only the splitting $n' = 2'$ is much larger than the energy range of other splittings and is underestimated by +54%. Considering additionally the pronounced asymmetry of the split peaks, additional effects may be at the origin of this splitting (cf. figures C.6 (d)). While the nature of these effects remains

speculative, resonance $n' = 2'$ clearly does not compare well with the other three split Kondo peaks $n = 2, 1', 3'$ and shall be exluded from further considerations.

Table C.3: Tentative estimate of the influence of the ferromagnetic electrodes on the Kondo splitting. As the magnetisation M is unknown, it is used as a fitting parameter to satisfy equation C.1.

valley	2	1'	3'		
quantity				average	deviation
M	67%	91.2%	83%	80.4%	±6.8%
$\Delta_K^{FM}(M)$ (meV)	-0.3	-0.46	-0.35	-0.37	±0.08

Up to this point, the influence of the ferromagnetic electrodes on the Kondo splitting, $\Delta_K^{FM} \approx \Delta_K^{FM}(M)$, has not been taken into account. Apart from the coupling energies Γ and Γ' (that were extracted for each period separately from figures C.3 (a) and (b)), the only remaining input parameter in equation C.4 is the magnetisation M. In our present data set, his parameter for our particular amorphous, thin-film $Pd_{70}Fe_{30}$ has not been determined from independent characterisation experiments.

In order to provide an, if very tentative, estimate of $\Delta_K^{FM}(M)$ nonetheless, two steps are undertaken: First, it shall be assumed that equation C.1 covers all relevant contributions to Kondo splitting. Then the difference of the observed Kondo Δ_K splitting and the spin-$\frac{1}{2}$ and orbital contributions is given by $\Delta_K^{FM}(M) = \Delta_K - \Delta_K^{spin} - \Delta_K^{orb}$. Second, M shall be used as a fitting parameter rather than an input parameter.
The fitting values of the magnetisation M that reduce the difference of measured splitting and Δ_K^{spin}, Δ_K^{orb} and $\Delta_K^{FM}(M)$ to zero are presented in table C.3. The mean value is $\langle M \rangle$=80.4% with a reasonably small scatter $\delta \langle M \rangle$=6.8%, which is about an order of magnitude above reasonable values [57, 99]. The result of this rough estimate may be carefully interpreted as an indication that the ferromagnetic electrodes indeed impact the Kondo splitting, but a broader data base is required to solidify this claim.

Electrostatic control of spin states via Kondo effects [161] makes SWCNT-based quantum dot transistors with ferromagnetic electrodes a potential building block for forthcoming spintronics devices.

Appendix D

Example of other transport blockade effects

Figure D.1 gives an example of a blockade effect other than the Pauli-spin blockade discussed previously. The tunnel current $I(V_{SD}, \Delta)$ is measured as a function of bias and the interdot detuning, repeated for different magnetic fields. The magnetic field is aligned in the sample plane; it is perpendicular to the length of the PdNi electrodes and in a 69° angle with respect to the carbon nanotube. This slice through the parameter space effectively corresponds to two half Coulomb diamonds, 'meeting' at a triple resonance of the double quantum dot.

The spin blockade effect occurs at an interdot transition of type

$$(odd, even) \rightleftharpoons (even, odd)$$

for which no Pauli spin blockade is expected in either bias direction. At zero magnetic field, there is bo spin blockade, as expected (see figure D.1 (a3)). At $B = 3\,\mathrm{T}$, the transport for negative bias is blockaded but unimpeded for positive bias (see figure D.1 (a2)). For lower or higher magnetic fields around 3 T, this blockade is lifted (see figure D.1 (b2) for 2 T and (c1) for 4 T). This effect is symmetric in magnetic field (not shown).

An asymetric effect with magnetic field is observed at very low fields. Note the pronounced difference in current structure and zero bias triple point position for the small field change from 0 mT to -40 mT. As typical magnetisation reversal fields $B^{coercive}$ of our ferromagnetic PdNi electrodes are around $\pm 40\,\mathrm{mT}$ (cf. [55, 99]), this feature may be related to a spin valve-like current switch.

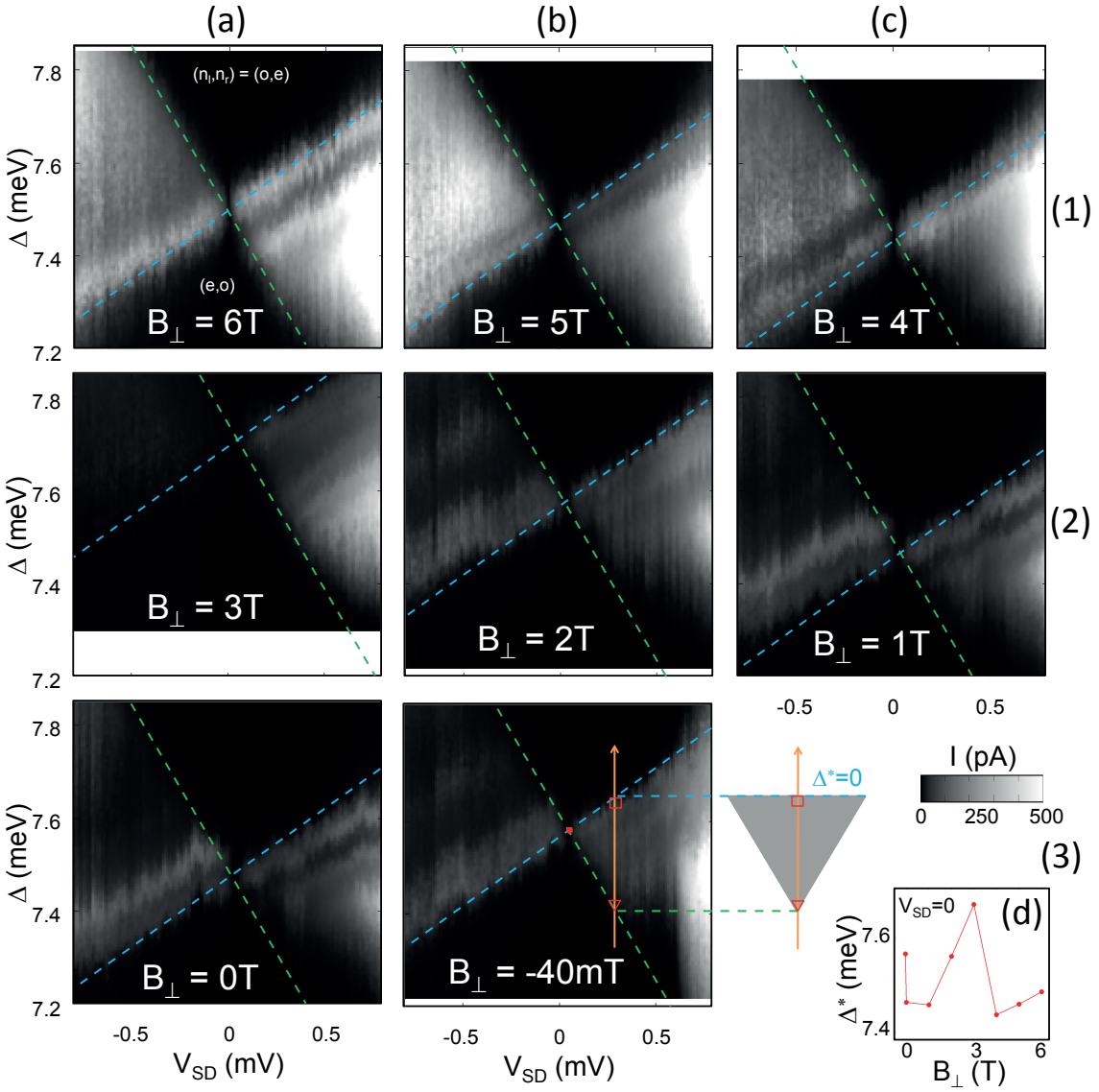

Figure D.1: (a1-c2) Current I along line cuts in detuning Δ from tip to baseline of a triple triangle of transition type $(o,e) \rightleftharpoons (e,o)$ as function of bias V_{SD}. The measurement was repeated for values of B=6 T towards -40 mT. The simple sequential tunneling, atomic model of singlet-triplet spin blockade (cf. figure 7.6) predicts current flowing for both positive and negative bias. At 3 T and (-3 T, not shown) and negative bias, however, current is blockaded. (d) Δ-position of zero bias triple point (e. g. red point in (b3)) as a function of magnetic field.

Acknowledgments

Many have helped and supported me during the inspiring, challenging time of research that ends with this thesis. I feel deeply grateful and priviliged to have worked with such excellent people. To name a few, thanks are owed to...

- Prof. Dr. Christoph Strunk for entrusting me with research and technical projects in this fascinating field of experimental physics.
- Dr. Andreas Hüttel for introducing me into the art of understanding and measuring double quantum dot devices and his thorough proof-reading of this thesis.
- Prof. Dr. Dieter Weiss, at whose chair I had the opportunity to research with an excellent infrastructure and within his competent and helpful team.
- Drs. Ben Stahl and Andi Rogl who greatly helped and supported me, most importantly with well-placed socratic questions to sharpen my points in this thesis. And for having me. You are friends.
- My collegues and friends Dr. Florian Otto, Tom Geiger, Markus Gaaß, Dr. Emiliano Pallechi, David Kalok, Silvia Schmidmeier, Daniel Steininger, Matrin Obstbaum and Daniel Schmid for the great time inside and outside academia. Thanks are to be detailled over (hopefully many) drinks drained together.
- Dr. SungHo Jhang for the good company, advice and many clean tubes grown and worked upon together.
- Drs. Jonathan Eroms and Elisabeth Reiger for support, advice and encouragement on academic issues and, more importantly, on how to handle babies.
- Dr. Andrea Donarini for recalling me how much fun a good discussion about physics can be (and the baby talk, too).
- Prof. Dr. Kicheon Kang for all his patient, calm and impressingly precise advice - and the nice chats about children and other non-academic matters of importance.
- Dr. Ondrej Vavra for the good time, advice and always being around when there was ”need for a strong man (who doesn’t ask too many questions)”.

- Prof. Dr. Herre van der Zant, Prof. Dr. Alberto Morpurgo and Dr. Benoit Witkamp for hosting me at Delft Technical University to teach me how to grow good tubes.

- Thomas Haller, Michael Weigl, Cornelia Linz and Uli Gürster for all the friendly and competent technical expertise - I have really learnt much from from you. The same goes for the electronic and mechanical workshop, to name two for many: Dieter Riedl and Norbert Sommer.

- Claudia Rahm and Elke Haushalter for their guiding hand through the administrative jungle. You did make things more friendly, go more smoothly and you did make a difference.

- the co-founders and co-workers of the "Alumniverein der physikalischen Fakultät der Uni Regensburg", Tobias Sonnleitner, Florian Sanftl, Ina Schneider, Matthias Heise, Dr. Gernot Deinzer, Johannes Leiner and above mentioned Drs. Rogl, Stahl, Otto, Pallecchi, Kalok, Obstbaum and Geiger. It was a privilege working with you (in the sense: it was really cool pulling up projects together!). Thanks to our always supportive presidents Profs. Schäfer, Richter, Wegscheider and Weiss. And of course to the irreplacable Ulla Turba.

- an meine Eltern Tilde und Rainer. Mit Eurem unerschütterlichen Vertrauen habt Ihr mich getragen. Danke für die aufbauenden Worte, als ich sie brauchte, und die Kraft, wohlmeinende Ratschläge zurück zu halten, als ich sie mal nicht brauchen konnte. Ohne Eure Unterstützung hatte ich die Promotion nicht zu Ende führen können. In diesem Sinne auch vielen Dank an meine Schwester Niloka Sabrina und meine zweiten Eltern Walter und Rosi.

- til mine svigerforeldere Astri og Jon Oddvar som kom helt fra Norge bare på være stede ved forsvarelsen av mitt doktorarbeit. Det satte jeg veldig stor pris på.

- Physics. I want to thank you too. You have been a demanding and no easy lover: capricious and elusive in experiment, rigorously analytical in theory, often seemingly contradictive but - no matter how hard I argued - always right in the end.

- Aina, mon épouse, partenaire, amante, amie, mère de mes enfants. Tu as fait plus que me soutenir dans ce temps intense et souvent ardu, cettes nuits et ces weekend solitaires et perdus au cours des semaines et des années dans la salle blanche, au labo, perdues aux pensées. Tu l'as partagé avec moi. C'est, de façon, autant ton doctorat que le mien. Je sais pourtant que les titres te valent moins que le temps passé ensemble, et j'en suis tellement content!

- Damian, my son and joy and most important result of Ph.D. time.

Curriculum Vitæ

Dominik Oliver Preusche-Rogstad

* Heidelberg, 4. February 1977

married, one child

dominik.preusche@cantab.net

Doctorate in Experimental Physics	2006-2011	Universität Regensburg
Studies of Physics	1999-2006	Universität Regensburg
Studies in Applied Mathematics	2002-2003	University of Cambridge, UK
Professional Education	1997-1999	Deutsche Bank AG
Social Service	1996-1997	CSP, Montpellier, France
School	1983-1996	KFG, Heidelberg
	1994	Lycée Jean Monnet Monpellier, France
Scholarships		Studienstiftung des deutschen Volkes
	2002-2003	DAAD

Bibliography

[1] W. Pauli. 'Exclusion principle and quantum mechanics.' In 'Nobel Lecture,' (1945).

[2] G. E. Uhlenbeck and S. Goudsmit. 'Spinning electrons and the structure of spectra.' Naturwissenschaften, 47:953 (1925).

[3] G. Binasch, P. Grünberg, F. Saurenbach and W. Zinn. 'Enhanced magnetoresistance in layered magnetic structures with antiferromagnetic interlayer exchange.' Phys. Rev. B, 39 (7):4828 (1989).

[4] M. N. Baibich, J. M. Broto, A. Fert, F. N. Van Dau, F. Petroff, P. Etienne, G. Creuzet, A. Friederich and J. Chazelas. 'Giant Magnetoresistance of (001)Fe/(001)Cr Magnetic Superlattices.' Phys. Rev. Lett., 61 (21):2472 (1988).

[5] S. M. Thompson. 'The discovery, development and future of GMR: The nobel prize 2007.' Journal of Physics D: Applied Physics, 41 (9):093001 (2008).

[6] 'Nobel prize in physics 2007: The discovery of giant magnetoresistance.' (2007). Class for Physics of the Royal Swedish Academy of Sciences.

[7] J. S. Moodera, J. Nowak and R. J. M. van de Veerdonk. 'Interface magnetism and spin wave scattering in ferromagnet-insulator-ferromagnet tunnel junctions.' Phys. Rev. Lett., 80 (2941) (1998).

[8] D. Loss and D. P. DiVincenzo. 'Quantum computation with quantum dots.' Physical Review A, 57 (1):120 (1998).

[9] M. N. Leuenberger and D. Loss. 'Spintronics and quantum computing: switching mechanisms for qubits.' Physica E, 452–457(6) (2001).

[10] J. M. Kikkawa and D. D. Awschalom. 'Lateral drag of spin coherence in gallium arsenide.' nature, 397:139 (1999).

[11] S. A. Wolf, D. D. Awschalom, R. A. Buhrman, J. M. Daughton, S. von Molnár, M. L. Roukes, A. Y. Chtchelkanova and D. M. Treger. 'Spintronics: A spin-based electronics vision for the future.' Science, 294 (5546):1488 (2001).

[12] S. A. Wolf, A. Y. Chtchelkanova and D. M. Treger. 'Spintronics: a retrospective and perspective.' IBM J. Res. Dev., 50:101 (2006).

[13] L. E. Hueso, J. M. Pruneda, V. Ferrari, G. Burnell, J. P. Valdes-Herrera, B. D. Simons, P. B. Littlewood, E. Artacho, A. Fert and N. D. Mathur. 'Transformation of spin information into large electrical signals using carbon nanotubes.' Nature, 445 (7126):410 (2007).

[14] I. Zutic, J. Fabian and S. Das Sarma. 'Spintronics: Fundamentals and applications.' Rev. Mod. Phys., 76 (2):323 (2004).

[15] J. A. Katine, F. J. Albert, R. A. Buhrman, E. B. Myers and D. C. Ralph. 'Current-driven magnetization reversal and spin-wave excitations in Co/Cu/Co pillars.' Phys. Rev. Lett., 84 (14):3149 (2000).

[16] M. A. Nielsen and I. L. Chuang. *Quantum Computation and Quantum Information (Cambridge Series on Information and the Natural Sciences)* (Cambridge University Press, 2004), 1st edn.

[17] R. C. Ashoori. 'Electrons in artificial atoms.' Nature, 379 (6564):413 (1996).

[18] R. H. Blick, R. J. Haug, J. Weis, D. Pfannkuche, K. v. Klitzing and K. Eberl. 'Single-electron tunneling through a double quantum dot: The artificial molecule.' Phys. Rev. B, 53 (12):7899 (1996).

[19] S. Sapmaz, P. Jarillo-Herrero, L. P. Kouwenhoven and H. S. J. van der Zant. 'Quantum dots in carbon nanotubes.' Semiconductor Science and Technology, 21 (11):S52 (2006).

[20] A. C. Johnson. 'Charge sensing and spin dynamics in gaas quantum dots.' Ph.D. thesis, Havard University (2005).

[21] P. Otellini. 'La ley de Moore sigue confirmándose.' Tech. rep., Intel (2009).

[22] G.-E. Moore. 'Cramming more components onto integrated circuits.' Electronics, 38 (8) (1965).

[23] M. Dubash. 'Moore's law is dead, says Gordon Moore.' Tech. rep., Techworld (2005).

[24] A. K. Hüttel. 'Gekoppelte Quantenpunkte im Bereich niedrigster Elektronenzahlen.' Ph.D. thesis, LMU München (2005).

[25] J. Zheng, P. R. Nicovich and R. M. Dickson. 'Highly Fluorescent Noble-Metal Quantum Dots.' Annual Review of Physical Chemistry, 58 (1):409 (2007).

[26] W. G. van der Wiel, S. De Franceschi, J. M. Elzerman, T. Fujisawa, S. Tarucha and L. P. Kouwenhoven. 'Electron transport through double quantum dots.' Rev. Mod. Phys., 75 (1):1 (2002).

[27] D. Schroer, A. D. Greentree, L. Gaudreau, K. Eberl, L. C. L. Hollenberg, J. P. Kotthaus and S. Ludwig. 'An electrostatically defined serial triple quantum dot charged with few electrons.' PHYS.REV.B, 76:075306 (2007).

[28] N. S. Lai, W. H. Lim, C. H. Yang, F. A. Zwanenburg, A. Morello and A. S. Dzurak. 'Pauli spin blockade in a highly tunable silicon double quantum dot.' cond-mat, arXiv:1012.1410v1 (2010).

[29] C. B. Simmons, T. S. Koh, N. Shaji, M. Thalakulam, L. J. Klein, H. Qin, H. Luo, D. E. Savage, M. G. Lagally, A. J. Rimberg, R. Joynt, R. Blick, M. Friesen, S. N. Coppersmith and M. A. Eriksson. 'Pauli Spin Blockade and Lifetime-Enhanced Transport in a Si/SiGe double quantum dot.' (2010).

[30] F. A. Zwanenburg, A. A. van Loon, G. A. Steele, C. E. W. M. van Rijmenam, T. Balder, Y. Fang, C. M. Lieber and L. P. Kouwenhoven. 'Ultrasmall silicon quantum dots.' Journal of Applied Physics, 105 (12):124314+ (2009).

[31] A. Pfund, I. Shorubalko, K. Ensslin and R. Leturcq. 'Spin-state mixing in InAs double quantum dots.' Phys. Rev. B, 76 (16):161308 (2007).

[32] S. Nadj-Perge, S. M. Frolov, J. W. W. van Tilburg, J. Danon, Y. V. Nazarov, R. Algra, E. P. A. M. Bakkers and L. P. Kouwenhoven. 'Disentangling the effects of spin-orbit and hyperfine interactions on spin blockade.' Physical Review B, 81 (20):201305+ (2010).

[33] S. Neubeck, L. A. Ponomarenko, F. Freitag, A. J. M. Giesbers, U. Zeitler, S. V. Morozov, P. Blake, A. K. Geim and K. S. Novoselov. 'From one electron to one hole: Quasiparticle counting in graphene quantum dots determined by electrochemical and plasma etching.' Small, 6 (14):1469 (2010).

[34] A. Javey, J. Guo, Q. Wang, M. Lundstrom and H. Dai. 'Ballistic carbon nanotube field-effect transistors.' Nature, 424 (6949):654 (2003).

[35] N. Mason, M. J. Biercuk and C. M. Marcus. 'Local Gate Control of a Carbon Nanotube Double Quantum Dot.' Science, 303 (5658):655 (2004).

[36] A. Eliasen, J. Paaske, K. Flensberg, S. Smerat, M. Leijnse, M. R. Wegewijs, H. I. Jørgensen and J. Monthioux, M.and Nygaard. 'Transport via coupled states in a C_{60} peapod quantum dot.' Physical Review B, 81 (15):155431+ (2010).

[37] L. V. Radushkevich and V. M. Lukyanovich. Zurn. Fisic. Chim., 26:88 (1952).

[38] S. Iijima and T. Ichihashi. 'Single-shell carbon nanotubes of 1-nm diameter.' nature, 363:603 (1993).

[39] R. Saito, G. Dresselhaus and M. S. Dresselhaus. *Physical Properties of Carbon Nanotubes* (Imperial College Press, 1998).

[40] C. T. S. Reich and J. Maultsch. *Carbon Nanotubes* (Wiley-VCH, 2004).

[41] J.-C. Charlier, X. Blase and S. Roche. 'Electronic and transport properties of nanotubes.' Rev. Mod. Phys., 79 (2):677 (2007).

[42] E. Thune and C. Strunk. *Quantum Transport in Carbon Nanotubes* (Springer, Berlin, 2005).

[43] S. Koller, L. Mayrhofer and M. Grifoni. 'Spin transport across carbon nanotube quantum dots.' New J. Phys., 9:348 (2007).

[44] 'Nobel prize in physics 2010: Graphene.' (2010). Class for Physics of the Royal Swedish Academy of Sciences.

[45] P. Avouris, Z. Chen and V. Perebeinos. 'Carbon-based electronics.' nature nanotechnology, 2:605 (2007).

[46] Z. Chen, J. Appenzeller, Y.-M. Lin, J. Sippel-Oakley, A. G. Rinzler, J. Tang, S. J. Wind, P. M. Solomon and P. Avouris. 'An integrated logic circuit assembled on a single carbon nanotube.' Science, 311 (5768):1735 (2006).

[47] S. Rosenblatt, H. Lin, V. Sazonova, S. Tiwari and P. L. McEuen. 'Mixing at 50 GHz using a single-walled carbon nanotube transistor.' Applied Physics Letters, 87 (15) (2005).

[48] N. Chimot, V. Derycke, M. F. Goffman, J. P. Bourgoin, H. Happy and G. Dambrine. 'Gigahertz frequency flexible carbon nanotube transistors.' Applied Physics Letters, 91:15 (2007).

[49] V. Sazonova, Y. Yaish, H. Ustunel, D. Roundy, T. A. Arias and P. L. McEuen. 'A tunable carbon nanotube electromechanical oscillator.' Nature, 431 (7006):284 (2004).

[50] A. K. Hüttel, G. A. Steele, B. Witkamp, M. Poot, L. P. Kouwenhoven and H. S. J. van der Zant. 'Carbon Nanotubes as Ultrahigh Quality Factor Mechanical Resonators.' Nano Letters, 9 (7):2547 (2009).

[51] G. A. Steele, A. K. Huttel, B. Witkamp, M. Poot, H. B. Meerwaldt, L. P. Kouwenhoven and H. S. J. van der Zant. 'Strong Coupling Between Single-Electron Tunneling and Nanomechanical Motion.' Science, 325 (5944):1103 (2009).

[52] B. Lassagne, D. Garcia-Sanchez, A. Aguasca and A. Bachtold. 'Ultrasensitive Mass Sensing with a Nanotube Electromechanical Resonator.' Nano Letters, 8 (11):3735 (2008).

[53] M. S. Dresselhaus, G. Dresselhaus, R. Saito and A. Jorio. 'Exciton photophysics of carbon nanotubes.' Annual Review of Physical Chemistry, 58 (1):719 (2007).

[54] J. P. Cleuziou, W. Wernsdorfer, V. Bouchiat, T. Ondarcuhu and M. Monthioux. 'Carbon nanotube superconducting quantum interference device.' Nature Nanotechnology, 1 (1):53 (2006).

[55] D. Preusche, S. Schmidmeier, E. Pallecchi, C. . Dietrich, A. K. Huettel, J. Zweck and C. Strunk. 'Characterisation of ferromagnetic contacts to carbon nanotubes.' Journal of Applied Physics, 084314 (2009).

[56] S. Sahoo, T. Kontos, J. Furer, C. Hoffmann, M. Graber, A. Cottet and C. Schönenberger. 'Electric field control of spin transport.' Nature Physics, 1 (2):99 (2005).

[57] H. T. Man, I. J. W. Wever and A. F. Morpurgo. 'Spin-dependent quantum interference in single-wall carbon nanotubes with ferromagnetic contacts.' Phys. Rev. B, 73 (24) (2006).

[58] J. Kong, H. T. Soh, A. M. Cassell, C. F. Quate and H. Dai. 'Synthesis of individual single-walled carbon nanotubes on patterned silicon wafers.' Nature, 395 (6705):878 (1998).

[59] Z. Ghorannevis, T. Kato, T. Kaneko and R. Hatakeyama. 'Growth of Single-Walled Carbon Nanotubes from Nonmagnetic Catalysts by Plasma Chemical

Vapor Deposition.' Japanese Journal of Applied Physics, 49 (2):02BA01+ (2010).

[60] Z. W. Pan, S. S. Xie, B. H. Chang, C. Y. Wang, L. Lu, W. Liu, W. Y. Zhou, W. Z. Li and L. X. Qian. 'Very long carbon nanotubes.' Nature, 394 (6694):631 (1998).

[61] F. Kuemmeth, H. Churchill, P. Herring and C. Marcus. 'Carbon nanotubes for coherent spintronics.' Materials Today, 13 (3):18 (2010).

[62] F. Kuemmeth, S. Ilani, D. C. Ralph and P. L. McEuen. 'Coupling of spin and orbital motion of electrons in carbon nanotubes.' Nature, 452 (7186):448 (2008).

[63] L. G. Herrmann, F. Portier, P. Roche, A. L. Yeyati, T. Kontos and C. Strunk. 'Carbon nanotubes as cooper-pair beam splitters.' Phys. Rev. Lett., 104 (2):026801 (2010).

[64] L. Hofstetter, S. Csonka, J. Nygård and C. Schönenberger. 'Cooper pair splitter realized in a two-quantum-dot Y-junction.' Nature, 461 (7266):960 (2009).

[65] A. C. Johnson, J. R. Petta, J. M. Taylor, A. Yacoby, M. D. Lukin, C. M. Marcus, M. P. Hanson and A. C. Gossard. 'Triplet-singlet spin relaxation via nuclei in a double quantum dot.' nature, 435:925 (2005).

[66] S. Nadj-Perge, S. M. Frolov, E. P. A. M. Bakkers and L. P. Kouwenhoven. 'Spin-orbit qubit in a semiconductor nanowire.' Nature (London), 468 (2011).

[67] C. Strunk. 'Boosting magnetoresistance in molecular devices.' Science, 306:63 (2004).

[68] A. Cottet and T. Kontos. 'Spin Quantum Bit with Ferromagnetic Contacts for Circuit QED.' Physical Review Letters, 105 (16):160502+ (2010).

[69] T. Fliessbach. *Statistische Physik* (Spektrum Akademischer Verlag, 1999).

[70] P. Jarillo-Herrero, J. Kong, H. S. J. van der Zant, C. Dekker, L. P. Kouwenhoven and S. De Franceschi. 'Orbital Kondo effect in carbon nanotubes.' Nature, 434 (7032):484 (2005).

[71] H. O. H. Churchill, A. J. Bestwick, J. W. Harlow, F. Kuemmeth, D. Marcos, C. H. Stwertka, S. K. Watson and C. M. Marcus. 'Electron nuclear interaction in ^{13}C nanotube double quantum dots.' Nature Physics, 5 (5):321 (2009).

[72] K. Ono, D. G. Austing, Y. Tokura and S. Tarucha. 'Current rectification by pauli exclusion in a weakly coupled double quantum dot system.' Science, 297 (5585):1313 (2002).

[73] A. C. Johnson, J. R. Petta, C. M. Marcus, M. P. Hanson and A. C. Gossard. 'Singlet-triplet spin blockade and charge sensing in a few-electron double quantum dot.' Phys. Rev. B, 72 (16):165308 (2005).

[74] L. Herrmann. 'Carbon nanotubes as Cooper pair beam splitters.' Ph.D. thesis (2010).

[75] L. Guan, K. Suenaga and S. Iijima. 'Smallest carbon nanotube assigned with atomic resolution accuracy.' Nano Letters, 8 (2):459 (2008). PMID: 18186659.

[76] www.chemistry.ohio state.edu.

[77] http://cwx.prenhall.com/petrucci/medialib.

[78] B. Stojetz. 'Interplay of bandstructure and quantum interference in multiwall carbon nanotubes.' Ph.D. thesis, University of Regensburg (2004).

[79] C. F. G. Cuniberti and K. Richter. *Electronic Transport in Mesoscopic Systems* (Cambridge University Press, 1995).

[80] W. Liang, M. Bockrath, D. Bozovic, J. H. Hafner, T. M. and H. Park. 'Fabry-perot interference in a nanotube electron waveguide.' nature, 411:665 (2001).

[81] P. J. Fabian. 'Festkörper- Theorie II: Mesoskopische Physik.' lecture course (2006).

[82] S. Datta. *Electronic Transport in Mesoscopic Systems (Cambridge Studies in Semiconductor Physics and Microelectronic Engineering)* (Cambridge University Press, 1997).

[83] A. Javey, J. Guo, Q. Wang, M. Lundstrom and H. Dai. 'Ballistic carbon nanotube field-effect transistors.' Nature, 424 (6949):654 (2003).

[84] S. Sapmaz, P. J. Herrero, J. Kong, C. Dekker, L. P. Kouwenhoven and H. S. J. van der Zant. 'Electronic excitation spectrum of metallic carbon nanotubes.' Physical Review B, 71 (15):153402+ (2005).

[85] M. R. Buitelaar, T. Nussbaumer and C. Schönenberger. 'Quantum dot in the kondo regime coupled to superconductors.' Phys. Rev. Lett., 89 (25):256801 (2002).

[86] J. Paaske, Rosch, A., P. Wolfle, N. Mason, C. M. Marcus and J. Nygard. 'Non-equilibrium singlet-triplet kondo effect in carbon nanotubes.' Nature Physics, 2 (7):460 (2006).

[87] C. T. Inc. 'Carbon nanotubes, production methods for carbon nanotubes including arc discharge, laser, chemical vapor deposition and ball milling.' azonano.com (2006).

[88] D. Schmid. 'Growth of ultraclean carbon nanotubes for low temperature transport measurements.' Master's thesis, Universität Regensburg (2010).

[89] Z. H. Li, M. Wang, X. Q. Wang, H. B. Zhu, H. M. Lu and Y. Ando. 'Synthesis of large quantity single-walled carbon nanotubes by arc discharge.' Chinese Physics Letters, 19 (1):91 (2002).

[90] B. I. Yakobson and R. E. Smalley. 'Fullerene nanotubes: C1,000,000 and beyond.' American Scientist, v85 (n4):p324 (1997).

[91] S. Inoue, T. Nakajima, K. Nomura and Y. Kikuchi. 'Growth Mechanism and Selective Synthesis of SWNTs.' (2006).

[92] M. Marchand, C. Journet, D. Guillot, J.-M. Benoit, B. I. Yakobson and S. T. Purcell. 'Growing a Carbon Nanotube Atom by Atom: And Yet It Does Turn.' Nano Letters, 9 (8):2961 (2009).

[93] Z. Jin, H. Chu, J. Wang, J. Hong, W. Tan and Y. Li. 'Ultralow feeding gas flow guiding growth of large-scale horizontally aligned single-walled carbon nanotube arrays.' Nano Letters, 7 (7):2073 (2007).

[94] N. Inami, M. Ambri Mohamed, E. Shikoh and A. Fujiwara. 'Synthesis-condition dependence of carbon nanotube growth by alcohol catalytic chemical vapor deposition method.' Science and Technology of Advanced Materials, 292+ (2007).

[95] A. Ural, Y. Li and H. Dai. 'Electric-field-aligned growth of single-walled carbon nanotubes on surfaces.' Applied Physics Letters, 81 (18):3464 (2002).

[96] I. B. Babić, J. Furer and C. Schönenberger. 'Suitability of carbon nanotubes grown by chemical vapor deposition for electrical devices.' cond-mat/0406626 v1 (2004).

[97] M. R. Buitelaar, J. Fransson, A. L. Cantone, C. G. Smith, D. Anderson, G. A. C. Jones, A. Ardavan, A. N. Khlobystov, A. A. R. Watt, K. Porfyrakis

and G. A. D. Briggs. 'Pauli spin blockade in carbon nanotube double quantum dots.' Phys. Rev. B, 77 (24):245439 (2008).

[98] J. Biberger. 'Transportphänomene in mesoskopischen 2 DEG- Strukturen unter dem Einfluss inhomogener Streufelder von Nanomagneten.' Ph.D. thesis (2007).

[99] D. Steininger, D. Preusche, M. Ziola, M. Kiessling, M. Sperl, A. K. Hüttel, G. Bayreuther and C. Strunk. 'Electric and magnetic characterization of PdNi contact electrodes.' in preparation.

[100] F. Otto. 'Nonlinear vortex transport in mesoscopic channels of amorphous NbGe.' Ph.D. thesis, Universität Regensburg (2009).

[101] S. Schmiedmeier. 'Mikromagnetische Charakterisierung von ferromagnetischen Kontaktelektroden.' Master's thesis, Universität Regensburg (2007).

[102] S. Sahoo, T. Kontos, C. Schönenberger and C. Sürgers. 'Electrical spin injection in multiwall carbon nanotubes with transparent ferromagnetic contacts.' Appl. Phys. Lett., 86 (11):112109 (2005).

[103] J.-R. Kim, H. M. So, J.-J. Kim and J. Kim. 'Spin-dependent transport properties in a single-walled carbon nanotube with mesoscopic co contacts.' Phys. Rev. B, 66 (23):233401 (2002).

[104] B. Zhao, I. Mönch, T. Mühl, H. Vinzelberg and C. M. Schneider. 'Spin-dependent transport in multiwalled carbon nanotubes.' J. Appl. Phys., 91 (10):7026 (2002).

[105] M. Sperl. ' Temperaturabhängigkeit der Magnetisierung in ultradünnen epitaktischen Fe Co- Schichten mit verschwindender Kristall- Anisotropie.' Master's thesis, Universität Regensburg (2004).

[106] P. D. R. Gross and D. A. Marx. 'Spinelektronik (vorlesungsskript zur vorlesung im ss 2004).' Ph.D. thesis, Walther-Meissner-Institut, Lehrstuhl für Technische Physik (2004).

[107] F. Bensch. 'Der magnetische phasenübergang und das einsetzen des ferromagnetismus bei dünnen eisenschichten auf galliumarsenid.' Ph.D. thesis, Universität Regensburg (2001).

[108] W. Nolting. *Quantentheorie des Magnetismus*, vol. 1 (Teubner-Verlag Stuttgart, 1986).

[109] R. Pulwey. 'Magnetkraftuntersuchungen an ferromagnetischen Nanostrukturen.' Master's thesis, Universität Regensburg (1999).

[110] M. Schlapps. 'Transportexperimente an Nanostrukturierten (Ga, Mn) As - Schichten.' Master's thesis, Universität Regensburg (2005).

[111] J. Chapman. 'Transmission electron microscopies of magnetic microstructures.' Journal of Magnetism and Magnetic Materials, 200 (1-3):729 (1999).

[112] C. Lim. 'Lorentz microscopy investigation of the free layer reversal in CoFe and Co top spin-valves.' Journal of Magnetism and Magnetic Materials, 238 (2-3):301 (2002).

[113] T. Uhlig and J. Zweck. 'Direct observation of switching processes in permalloy rings with lorentz microscopy.' Phys. Rev. Lett., 93 (4):047203 (2004).

[114] A. Hubert and R. Schäfer. *Magnetic Domains* (Springer, 1998), 1st edn.

[115] A. Javey, J. Guo, Q. Wang, M. Lundstrom and H. Dai. 'Ballistic carbon nanotube field-effect transistors.' Nature, 424 (6949):654 (2003).

[116] A. Cottet, T. Kontos, S. Sahoo, H. T. Man, M. S. Choi, W. Belzig, C. Bruder, A. F. Morpurgo and C. Schönenberger. 'Nanospintronics with carbon nanotubes.' Semic. Sci. and Techn., 21 (11):S78 (2006).

[117] R. D. Gomez, T. V. Luu, A. O. Pak, K. J. Kirk and J. N. Chapman. 'Domain configurations of nanostructured permalloy elements.' J. Appl. Phys., 85 (8):6163 (1999).

[118] E. Shalyguina, K. H. Shin and N. M. Abrosimova. 'Size dependence of magnetic properties of permalloy microstripe arrays.' Journal of Magnetism and Magnetic Materials, 239:252 (2002).

[119] J. Yu, U. Rüdiger, L. Thomas, S. S. P. Parkin and A. D. Kent. 'Micromagnetics of mesoscopic epitaxial (110) fe elements with nanoshaped ends.' J. Appl. Phys., 85 (8):5501 (1999).

[120] K. J. Kirk, J. N. Chapman and C. D. W. Wilkinson. 'Lorentz microscopy of small magnetic structures (invited).' J. Appl. Phys., 85 (8):5237 (1999).

[121] M. Huber (2005). Unpublished work.

[122] M. R. McCartney and D. J. Smith. Scanning Microscopy, 11:335 (1997).

[123] H. Aurich, A. Baumgartner, F. Freitag, A. Eichler, J. Trbovic and C. Schonenberger. 'Permalloy-based carbon nanotube spin-valve.' Applied Physics Letters, 97 (15):153116 (2010).

[124] I. W. H.T. Man and A. Morpurgo. 'Spin-dependent quantum interference in single-wall carbon nanotubes with ferromagnetic contacts.' cond-mat/0512505 v1 (2005).

[125] M. R. Gräber, W. A. Coish, C. Hoffmann, M. Weiss, J. Furer, S. Oberholzer, D. Loss and C. Schönenberger. 'Molecular states in carbon nanotube double quantum dots.' Physical Review B - Condensed Matter and Materials Physics, 74 (7) (2006).

[126] S. J. Chorley, G. Giavaras, J. Wabnig, G. A. C. Jones, C. G. Smith, G. A. D. Briggs and M. R. Buitelaar. 'Single spin detection with a carbon nanotube double quantum dot.' cond-mat (2010).

[127] T. Fujisawa, T. H. Oosterkamp, W. G. van der Wiel, B. W. Broer, R. Aguado, S. Tarucha and L. P. Kouwenhoven. 'Spontaneous emission spectrum in double quantum dot devices.' Science, 282 (5390):932 (1998).

[128] D. Weinmann, W. Häusler and B. Kramer. 'Spin blockades in linear and nonlinear transport through quantum dots.' Phys. Rev. Lett., 74 (6):984 (1995).

[129] A. K. Hüttel, H. Qin, A. W. Holleitner, R. H. Blick, K. Neumaier, D. Weinmann, K. Eberl and J. P. Kotthaus. 'Spin blockade in ground-state resonance of a quantum dot.' Europhys. Lett., 62 (5), 62:712 (2003).

[130] J. Danon and Y. V. Nazarov. 'Pauli spin blockade in the presence of strong spin-orbit coupling.' Physical Review B (Condensed Matter and Materials Physics), 80 (4):041301+ (2009).

[131] S. Weiss, E. I. Rashba, F. Kuemmeth, H. O. H. Churchill and K. Flensberg. 'Spin-orbit effects in carbon-nanotube double quantum dots.' Physical Review B, 82 (16):165427+ (2010).

[132] C. S. Peca, L. Balents and K. J. Wiese. 'Fabry-perot interference and spin filtering in carbon nanotubes.' Phys. Rev. B, 68 (20):205423 (2003).

[133] A. Pályi and G. Burkard. 'Hyperfine-induced valley mixing and the spin-valley blockade in carbon-based quantum dots.' Phys. Rev. B, 80 (20):201404 (2009).

[134] T. Hatano, S. Amaha, T. Kubo, S. Teraoka, Y. Tokura, J. A. Gupta, D. G. Austing and S. Tarucha. 'Transport properties of two laterally coupled vertical quantum dots in series with tunable interdot coupling.' Applied Physics Letters, 97 (6):062108 (2010).

[135] N. W. Ashcroft and N. D. Mermin. *Solid State Physics* (Thomson Learning, 1976).

[136] G. A. Steele, G. Gotz and L. P. Kouwenhoven. 'Tunable few-electron double quantum dots and Klein tunnelling in ultraclean carbon nanotubes.' Nature Nanotechnology, 4 (6):363 (2009).

[137] L. P. Kouwenhoven, T. H. Oosterkamp, M. W. S. Danoesastro, M. Eto, D. G. Austing, T. Honda and S. Tarucha. 'Excitation spectra of circular, few-electron quantum dots.' Science, 278 (5344):1788 (1997).

[138] A. Kogan, G. Granger, M. A. Kastner, D. Goldhaber-Gordon and H. Shtrikman. 'Singlet–triplet transition in a single-electron transistor at zero magnetic field.' Phys. Rev. B, 67 (11):113309 (2003).

[139] E. Pallecchi. 'Multiwall carbon nanotube josephson junctions with niobium contacts.' Ph.D. thesis (2009).

[140] S. Moriyama, T. Fuse, T. Yamaguchi and K. Ishibashi. 'Spin effects in single-electron transport through carbon nanotube quantum dots.' Phys. Rev. B, 76 (4):045102 (2007).

[141] J. A. Folk, C. M. Marcus, R. Berkovits, I. L. Kurland, I. L. Aleiner and B. L. Altshuler. 'Ground state spin and coulomb blockade peak motion in chaotic quantum dots.' Physica Scripta, Volume 2001:26 (2001).

[142] M. Pioro-Ladrière, M. Ciorga, J. Lapointe, P. Zawadzki, M. Korkusiński, P. Hawrylak and A. S. Sachrajda. 'Spin-blockade spectroscopy of a two-level artificial molecule.' Phys. Rev. Lett., 91 (2):026803 (2003).

[143] F. H. L. Koppens, J. A. Folk, J. M. Elzerman, R. Hanson, L. H. W. van Beveren, I. T. Vink, H. P. Tranitz, W. Wegscheider, L. P. Kouwenhoven and L. M. K. Vandersypen. 'Control and detection of singlet-triplet mixing in a random nuclear field.' Science, 309 (5739):1346 (2005).

[144] R. C. Ashoori, H. L. Stormer, J. S. Weiner, L. N. Pfeiffer, K. W. Baldwin and K. W. West. 'N-electron ground state energies of a quantum dot in magnetic field.' Phys. Rev. Lett., 71 (4):613 (1993).

[145] S. Tarucha, D. G. Austing, T. Honda, R. J. van der Hage and L. P. Kouwenhoven. 'Shell filling and spin effects in a few electron quantum dot.' Phys. Rev. Lett., 77 (17):3613 (1996).

[146] L. H. W. van Beveren, R. Hanson, I. T. Vink, F. H. L. Koppens, L. P. Kouwenhoven and L. M. K. Vandersypen. 'Spin filling of a quantum dot derived from excited-state spectroscopy.' New Journal of Physics, 7 (1):182 (2005).

[147] S. Weiss, E. I. Rashba, F. Kuemmeth, H. O. H. Churchill and K. Flensberg. 'Spin-Orbit Effects in Carbon-Nanotube Double Quantum Dots.' arxiv.org (2010).

[148] V. N. Golovach, A. Khaetskii and D. Loss. 'Spin relaxation at the singlet-triplet crossing in a quantum dot.' Phys. Rev. B, 77 (4):045328 (2008).

[149] F. H. L. Koppens, C. Buizert, I. T. Vink, K. C. Nowack, T. Meunier, L. P. Kouwenhoven and L. M. K. Vandersypen. 'Detection of single electron spin resonance in a double quantum dot.' Journal of Applied Physics, 101 (8):081706 (2007).

[150] M. Busl, C. López-Monís, R. S'anchez, J. Inarrea and G. Platero. 'Spin dynamics in double quantum dots in the spin blockade regime.' Physica E: Low-dimensional Systems and Nanostructures, 42 (3):643 (2010).

[151] S. H. Jhang, M. Marganska, Y. Skoursi, D. Preusche, B. Witkamp, M. Grifoni, H. van der Zant, C. Strunk and J. Wosnitza. 'Spin-orbit interaction in chiral carbon nanotubes probed in pulsed magnetic fields.' Phys. Rev. B, 82:041404 (2010).

[152] S. H. Jhang, M. Margaska, Y. Skourski, D. Preusche, M. Grifoni, J. Wosnitza and C. Strunk. 'Direct observation of band-gap closure for a semiconducting carbon nanotube in a large parallel magnetic field.' Phys. Rev. Lett., 106 (9):096802 (2011).

[153] T. S. Jespersen, K. Grove-Rasmussen, J. Paaske, K. Muraki, T. Fujisawa, J. Nygaard and K. Flensberg. 'Gate-dependent spin-orbit coupling in multi-electron carbon nanotubes.' nature physics (2011).

[154] J. C. Meyer, M. Paillet, G. S. Duesberg and S. Roth. 'Electron diffraction analysis of individual single-walled carbon nanotubes.' Ultramicroscopy, 106:176 (2006).

[155] L. Qin. 'Electron diffraction from carbon nanotubes.' Rep. Prog. Phys., 69:2761 (2006).

[156] S. Amelinckx, A. Lucas and P. Lambin. 'Electron diffraction and microscopy of nanotubes.' Rep. Prog. Phys., 62:1471 (1999).

[157] J.-M. Zuo, I. T. Kim, A. Celik-Aktas and J. Tao. 'Quantitative structural analysis of individual nanotubes by electron diffraction.' Z. Kristallogr., 222:625 (2007).

[158] M. Gaass, A. K. Hüttel, K. Kang, I. Weymann, J. von Delft and C. Strunk. 'Universality of the Kondo effect in quantum dots with ferromagnetic leads.' submitted for publication (2011).

[159] J. H. Grove-Rasmussen, K. and P. Lindelof. 'Fabry-perot interference, kondo effect and coulomb blockade in carbon nanotubes.' Physica E: Low-dimensional Systems and Nanostructures, 40:92 (2007).

[160] A. C. Hewson (Cambridge University Press, 1993).

[161] J. R. Hauptmann, J. Paaske and P. E. Lindelof. 'Electric-field-controlled spin reversal in a quantum dot with ferromagnetic contacts.' Nature Physics, 4 (5):373 (2008).

[162] B. Babić, T. Kontos and C. Schönenberger. 'Kondo effect in carbon nanotubes at half filling.' Phys. Rev. B, 70 (23):235419 (2004).